



HAL
open science

Understanding the oxygen evolution reaction (OER) for Co based transition metal oxides / hydroxides in alkaline electrolytes

Yan Duan

► **To cite this version:**

Yan Duan. Understanding the oxygen evolution reaction (OER) for Co based transition metal oxides / hydroxides in alkaline electrolytes. Material chemistry. Sorbonne Université; Nanyang Technological University (Singapour), 2021. English. NNT : 2021SORUS416 . tel-03701201

HAL Id: tel-03701201

<https://theses.hal.science/tel-03701201v1>

Submitted on 21 Jun 2022

HAL is a multi-disciplinary open access archive for the deposit and dissemination of scientific research documents, whether they are published or not. The documents may come from teaching and research institutions in France or abroad, or from public or private research centers.

L'archive ouverte pluridisciplinaire **HAL**, est destinée au dépôt et à la diffusion de documents scientifiques de niveau recherche, publiés ou non, émanant des établissements d'enseignement et de recherche français ou étrangers, des laboratoires publics ou privés.

Sorbonne Université

Nanyang Technological University

Ecole doctorale 397 Physique & Chimie des Matériaux

Chimie du Solide et Energie

**Comprendre la réaction de libération d'oxygène (OER) pour les
oxydes / hydroxydes de métaux de transition à base de Co dans les
électrolytes alcalins**

Par Yan Duan

Thèse de doctorat de Physique & Chimie des Matériaux

Dirigée par Alexis Grimaud avec Jason Zhichuan Xu

Présentée et soutenue publiquement le 19 mars 2021

Devant un jury composé de :

Grimaud, Alexis

Xu, Jason Zhichuan

Chen, Zhong

Laberty-Robert, Christel

Zonging, Shao

Ning, Yan

Directeur de thèse

Codirecteur de thèse

Président du jury

Membre du jury

Rapporteur

Rapporteur

Dédicace

Remerciements

Foremost, I would like to thank my parents.

Firstly, I would like to express my sincere gratitude to my supervisor Dr. Alexis Grimaud and Dr. Jason Xu for their continuous support during my studies. The research work done here would not be possible without their support. I would also like to thank them for their extensive scientific guidance provided to these works. I received a great amount of knowledge about scientific principles related to these works from their teachings, and these principles became invaluable for in-depth understandings.

Secondly, I would like to thank ERI@N management for their financial support during my pursuit for my higher degree. Thanks Prof. Claude Guet, Prof. Bo Liedberg and Prof Souhir Boujday for NTU-Sorbonne joint programme. Thanks Ms. Huang Minying, Ms. Si Bachir Hakima and Thieullent Gael for their continuous help.

I would like to extend my gratitude to all the technical staff in Espace, inorganic lab, organic lab and FACTS lab for computer fixing and equipment training. I would like to thank Prof Jean-Marie Tarascon, Dr. Daniel Alves Dalla Corte, Dr. Gwenaëlle Rouse and Dr Sathiya Mariyappan for sharing their lab and equipment.

I would also like to thank my colleagues in NTU and Collège de France for their guidance on various aspects of the project. Their insight and hands-on guide allowed these works to manifest as these complete forms.

Finally, I would like to thank my friends who accompanied and spiritually supported me during my PhD studies.

Sommaire

Remerciements.....	1
Sommaire	1
Introduction.....	1
1 Chapter 1	1
1.1 Hypothesis/Problem Statement.....	2
1.2 Objectives and Scope.....	4
1.3 Dissertation Overview	5
1.4 Findings and Outcomes/Originality.....	6
1.5 Reference	7
2 Chapter 2.....	9
2.1 Background for OER	10
2.2 Performance evaluation for OER catalysts.....	11
2.2.1 Overpotential.....	11
2.2.2 Specific activity vs mass activity.....	11
2.2.3 Turnover frequency.....	12
2.3 Transition metal oxides/hydroxides as catalyst materials for OER	12
2.3.1 Perovskite oxides	14
2.3.2 Spinel oxides.....	15
2.3.3 Layered hydroxides.....	16
2.3.4 Fundamentals of electronic structure.....	17
2.4 Mechanism of OER.....	19
2.4.1 Concerted proton-electron transfer (CPET).....	19
2.4.2 Non-concerted proton-electron transfer.....	24
2.4.3 Multi-metal transition metal oxides/hydroxides as OER catalyst.....	28
2.4.4 Influence by electrolyte cation species	29
2.5 Reference	30
3 Chapter 3.....	39
3.1 Material synthesis	40
3.1.1 Sol gel methods.....	40
3.1.2 Thermal decomposition methods.....	41
3.1.3 Solid state synthesis	41
3.1.4 Electrodeposition methods.....	42
3.2 Characterization	43
3.2.1 Electrochemical Characterization	43
3.2.2 Structural Characterization	45
3.3 Reference	55
4 Chapter 4.....	61
4.1 Introduction.....	62
4.2 Experimental Methods.....	64
4.2.1 Material synthesis	65
4.2.2 Material Characterizations	65
4.2.3 Electrochemical Tests	65

4.2.4 DFT Calculations	66
4.3 Results and Discussions	66
4.3.1 Material characterizations	66
4.3.2 Electrochemical test	72
4.3.3 X-ray absorption spectroscopy studies	73
4.3.4 Magnetic studies	76
4.3.5 DFT calculations	80
4.3.6 Interplay between Co^{3+} spin configuration and Co 3d-O 2p covalency	81
4.4 Summary	82
4.5 Reference	82
5 Chapter 5	85
5.1 Introduction	85
5.2 Experimental Methods	88
5.2.1 Material synthesis	89
5.2.2 Material Characterizations	89
5.2.3 Electrochemical Tests	89
5.2.4 DFT Calculations	91
5.3 Results and Discussions	92
5.3.1 Material characterizations	92
5.3.2 Electrochemical studies	96
5.3.3 Characterization after electrochemical study	98
5.3.4 Reaction mechanism	105
5.3.5 DFT Calculation	114
5.4 Summary	118
5.5 Reference	119
6 Chapter 6	127
6.1 Introduction	127
6.2 Experimental methods	130
6.3 Results and Discussions	139
6.3.1 $\text{La}_{1-x}\text{Sr}_x\text{CoO}_{3-\delta}$ perovskite series	139
6.3.2 Cobalt oxyhydroxide films	146
6.3.3 Fe-containing cobalt oxyhydroxide films	147
6.4 Summary	151
6.5 Reference	152
7 Chapter 7	158
7.1 Implications	159
7.2 Recommended Future Work 1	160
7.2.1 Experimental details	160
7.2.2 Preliminary results	161
7.3 Recommended Future Work 2	165
7.3.1 Experimental details	166
7.3.2 Preliminary results	166
7.4 Recommended Future Work 3	167
7.4.1 Experimental details	167
7.4.2 Preliminary results	167

7.5 References.....	168
Conclusion	171
Table des illustrations	173
Table des tableaux.....	181

Introduction

The development of efficient electrocatalysts to lower the overpotential of oxygen evolution reaction (OER) is of fundamental importance in improving the overall efficiency of fuel production by water electrolysis. Among a plethora of catalysts being studied on, transition metal oxides / hydroxides that exhibit reasonable activity and stability in alkaline electrolyte have been identified as catalysts to potentially overpass the activity of expensive Ir- and Ru- based oxides. Understanding the oxygen evolution reaction (OER) for transition metal oxides / hydroxides in alkaline electrolytes paves the way for better design of low cost and highly efficient electrocatalysts. As discussed by Trasatti, “A true theory of electrocatalysis will not be available until activity can be calculated a priori from some known properties of the materials”. Substantial efforts have been devoted to understanding the factors that determine the OER activity and searching for activity descriptors. Different parameters have been studied throughout the years and descriptors including enthalpy of transition from a lower to higher oxide states, the binding energy of surface oxygen, the number of $3d$ electron for bulk transition metal cations, e_g occupancy number of transition metal cations and covalency bonding transition metal ions to oxygen have been reported as OER activity descriptors. However, for some very active transition metal oxides / hydroxides, their surface can be changed when interacting with the surrounding electrolyte. Hence, interfacial descriptors, examples including surface redox transition from lower to higher oxidation state of the oxide precedent to OER, the potential of zero charge or the change in a work function on the adsorption through the water layer have been developed. This dissertation, with three different work on Co-based oxides / hydroxides, studies and deepens the understanding of the bulk properties, surface properties of materials and interfacial properties on OER. Firstly, with Fe substitution, it addresses tuning the e_g configuration of metal cations in LaCoO_3 where adjusting the metal $3d$ oxygen $2p$ covalency can bring benefits to the OER performance. Secondly, with Ni substitution in ZnCo_2O_4 , it demonstrates a change in relative position of O p -band and M_{Oh} d -band centre which induces a change in stability as well as the possibility for lattice oxygen to participate in the OER. Stable $\text{ZnCo}_{2-x}\text{Ni}_x\text{O}_4$ with small amount of Ni substitution follows adsorbates evolving mechanism (AEM) under OER conditions. Lattice oxygen participate (LOM) in the OER of metastable $\text{ZnCo}_{2-x}\text{Ni}_x\text{O}_4$ with larger amount of Ni substitution. Lattice oxygen participating mechanism would give rise to the continuous

formation of oxyhydroxide as surface-active species and consequently enhance the OER activity. Finally, with $\text{La}_{1-x}\text{Sr}_x\text{CoO}_3$ series, CoOOH and Fe-containing CoOOH as examples, the impact of the electrolyte has been explored by the study of reaction kinetics parameters. With a better understanding of how material properties and dynamic environment influence the OER activity and mechanism, we can obtain more efficient OER catalysts for better energy infrastructure.

Chapter 1

Introduction

Understanding the oxygen evolution reaction (OER) for transition metal oxides in alkaline electrolytes paves the way for designing better low cost and highly efficient electrocatalysts. Chapter 1 presents the significance to probe the mechanism of electrocatalysts by studying how the material properties are correlated to the OER performance in the fundamental research on OER oxide electrocatalyst. With Co based transition metal oxides/hydroxides as examples, through fundamentals on materials properties, various material characterization techniques and DFT modeling, multi-dimensional material properties can be fully understood. The findings of the impact on OER activity by intrinsic bulk properties, surface evolution and the interaction with water surroundings shed light on rational design on electrocatalysts.

1.1 Hypothesis/Problem Statement

The combustion of fossil fuels has brought up severe issues related to environmental pollution. Besides, the reserve for fossil fuels is not able to fulfill the worldwide energy demand. Hence, environmentally friendly sustainable energies are in great need. Hydrogen is one of the green energies which can be consistently produced by a clean way through water electrolysis. The current limitation related to the overall efficiency of water electrolysis lies in the large overpotential of the anode side, which is the oxygen evolution reaction (OER).¹ As for any reaction, the reaction rate is correlated to the activation energy barrier following a so-called linear free energy relationship; this barrier can be decreased by the use of a catalyst.² IrO₂ and RuO₂ have been used in industry to minimize the overpotential on the anode. However, their high cost but more importantly low abundance has hampered the large-scale deployment of water electrolyzers.³ Researchers have thus focused on searching for cost friendly electrocatalysts such as transition metal oxides/hydroxides to improve the efficiency for OER reaction. In order to rationally design highly active electrocatalysts, understanding the OER mechanism on the surface of different electrocatalysts is of prime importance. For a typical OER process in alkaline solution, a four-step reaction happens on the surface of a metal oxide/hydroxide catalyst, which involves the consecutive formation of different intermediates. The optimal binding energy of these intermediates gives rise to optimized OER activity.⁴ As the binding strength of these intermediates are governed by the electronic structure of the metal oxides, adjusting the electronic structure proves a powerful strategy to tune the OER activity. Hence, studies have found that when decreasing the e_g occupancy of the transition metal oxides, the binding energy increases. When e_g occupancy is around 1.2, the catalyst exhibits the best OER activity.³ Besides, the energy level of oxygen also influences the binding strength of the intermediates. When the oxygen level is increased, the metal and oxygen covalency is enhanced,⁵ leading to an increased OER activity. However, when the oxygen energy level is too closed to the Fermi energy, catalysts are found to be unstable and their surface undergoes surface evolution. An operando study has revealed that the surface evolution of Ba_{0.5}Sr_{0.5}Co_{0.8}Fe_{0.2}O₃ (BSCF)⁶ with the leaching of the soluble species (Ba²⁺, Sr²⁺) and metal cations (Co²⁻³⁺ and Fe²⁻³⁺) into the solution that redeposit back to the surface, resulting in the formation of an

oxyhydroxide layer.⁷ This new layer contributes to the high OER activity of BSCF. For these surface reconstructed OER catalysts, including $\text{La}_{1-x}\text{Sr}_x\text{CoO}_{3-\delta}$ (LSCO) ($x > 0.5$), LaNiO_3 , $\text{ZnFe}_{0.4}\text{Co}_{1.6}\text{O}_4$ etc.,⁸⁻¹⁰ a pH dependent phenomenon has been observed in alkaline solution. When the pH value is increased from 12.5 to 14, the OER activity increased. This has been found to be a result from kinetically limited proton transfer, following a so-called non-concerted proton-electron transfer.¹¹ Besides that, the OER kinetics is found to be dependent on the nature of the alkaline cations in the electrolyte for many transition metal hydroxide electrocatalysts such as $\text{Ni}(\text{Fe})\text{OOH}$. With different cation species in the electrolyte, the OER activity of the catalyst can be adjusted. A DFT modeling has found the cation insertion into the layered structure to form a $\text{Ni}(\text{Fe})\text{-OO}^- \text{-} \text{M}^+$ intermediate which can change the electronic structure of the OER catalysts.¹² Operando study by Raman also found that by using cation with bigger size, such as Cs^+ , there is better stabilization to the $\text{Ni}\text{-OO}^- \text{-} \text{Cs}^+$ intermediate, hence better OER activity.¹³

In this thesis, Co based transition metal oxides/hydroxides is focused on. Tailoring the electronic structure can be rationalized by substitutions strategies in existing transition metal oxides/hydroxides. Co-based oxides/hydroxides have been identified as active towards OER, which structure provides large freedom for the engineering of the electronic structure. With the aid of fundamentals in physical chemistry, various material characterization techniques and DFT modeling, the materials properties of the structure tailored Co based transition metal oxides/hydroxides can be fully revealed. These properties include intrinsic bulk properties, surface evolution and the interaction with water surroundings. The performance of these materials in alkaline electrolyte including OER activity and long-term stability can be observed by conducting electrochemical experiments. By establishing the correlation between the material properties and the electrocatalytic properties, the mechanism for the electrocatalysts will be uncovered. The hypothesis is tested in Chapter 4 to Chapter 6 through three studies on Co-based transition metal oxides/hydroxides as OER catalysts. In the Chapter 4, through Fe substitution, the electronic structure of perovskite LaCoO_3 is tuned, which results in enhanced OER activity. Here, the properties of the $\text{LaCo}_{1-x}\text{Fe}_x\text{O}_3$ are investigated with the help of X-ray Powder Diffraction (XRD), Fourier-transform infrared spectroscopy (FTIR), scanning electron microscopy (SEM), X-ray absorption spectroscopy (XAS), Superconducting Quantum Design (SQUID) and Density functional theory (DFT) modeling. In the Chapter 5, through Ni substitution, the oxygen in spinel oxide ZnCo_2O_4 becomes more active, which leads to surface

reconstruction, adjusted OER mechanism and enhanced activity. The investigation on the intrinsic bulk properties of $\text{ZnCo}_{2-x}\text{Ni}_x\text{O}_4$ is to some degree more complicated than $\text{LaCo}_{1-x}\text{Fe}_x\text{O}_3$ series. This is due to its spinel structure which involves the consideration of site occupancy of the metal cations. The hard XAS studies and soft XAS studies contribute to the structure determination of the bulk and the surface. Besides, the intrinsic bulk properties and surface evolution are studied by electrochemical studies, XRD, X-ray photoelectron spectroscopy (XPS), Transmission electron microscopy energy-dispersive X-ray spectroscopy (TEM-EDS), Electron energy loss spectroscopy (EELS), X-ray magnetic circular dichroism (XMCD) and DFT calculation. In the Chapter 6, with LSCO and Co(Fe)OOH as examples, the physical origin for their interactions with water surroundings have been investigated by kinetic parameter. Temperature dependent experiments were carried out to extrapolate the kinetic parameters of the reaction and facilitate the investigation on the correlation between the OER activity of these materials and the electrolyte composition. A good understanding of the OER for Co based transition metal oxides/hydroxides in alkaline electrolytes would aid the rational design of highly active electrocatalysts. The findings are not limited to the design Co based transition metal oxides/hydroxides as OER catalysts. They could shed lights on the other types of electrocatalysts design for CO_2 , HER, etc., applications as well.

1.2 Objectives and Scope

The objective of this thesis is to understand how electrocatalysts work with the example of Co based transition metal oxides/hydroxides as OER catalysts in alkaline electrolytes. First, we aim to reveal the impact of electronic structure on the OER activity of Co-based materials. By a Fe substitution, the Co-O covalency has been enhanced in LaCoO_3 . This goes together with the changed spin state and metallic feature of the $\text{LaCo}_{0.9}\text{Fe}_{0.1}\text{O}_3$. Subsequently, by introduction of Ni into ZnCo_2O_4 , the energy level of oxygen becomes higher than metal cations, which leads to a destabilization of the surface. Surface characterizations confirm the aggregation of Ni on the surface to form an oxyhydroxide layer, which is the result of high activity. Thirdly, the mechanism of the surface evolution of the $\text{ZnCo}_{2-x}\text{Ni}_x\text{O}_4$ is investigated by changing its concentration of electrolyte. To get more insights on the electrolyte dependent OER activity of the active materials, an in-depth exploration is further conducted by a temperature dependent

study for LSCO and Co(Fe)OOH catalysts. The relationship between the OER activity and the kinetic parameters such as activation energy and pre-exponential factor is established.

1.3 Dissertation Overview

The thesis addresses the role of material properties including intrinsic, surface and interfacial properties on the OER of Co based transition metal oxides / hydroxides in alkaline electrolytes.

Chapter 1 presents the significance to probe the mechanism of electrocatalysts by studying how the material properties are correlated to the OER performance in the fundamental research on OER oxide electrocatalyst. With Co based transition metal oxides/hydroxides as examples, through fundamentals on materials properties, various material characterization techniques and DFT modeling, multi-dimensional material properties can be fully understood. The findings of the impact on OER activity by intrinsic bulk properties, surface evolution and the interaction with water surroundings shed light on rational design on electrocatalysts.

Chapter 2 reviews the literature concerning the catalysts designs. The benchmarking parameters for measuring the performance of OER catalysts are evaluated. Among a plethora of materials as candidates for OER catalysts, transition metal oxides/hydroxides are highlighted. Their structural features and usage as OER catalysts have been reviewed. In addition, the physical and chemical fundamentals for the materials behind the catalytic phenomenon are presented. The growing understandings of the mechanisms underlying the OER on the surface of different catalysts have been elaborated. The significance for the study on the interaction between the catalyst and its water surrounding has been discussed.

Chapter 3 discusses the preparation methods for Co based transition metal oxides / hydroxides studied in this thesis as OER catalysts have been demonstrated. The working principles for the characterization techniques utilized in this thesis are explained and the reasons for their usage are stated. The setups for electrochemical studies have been illustrated. The data analysis techniques have been explained.

Chapter 4 elaborates the role of e_g filling and covalency on OER of Co based transition metal oxide $\text{LaCo}_{1-x}\text{Fe}_x\text{O}_3$.

Chapter 5 focuses on the role of oxygen energy level on the surface stability of $\text{ZnCo}_{2-x}\text{Ni}_x\text{O}_4$. It elaborates the surface activation by the change in electronic structure. The mechanism understanding on surface reconstructed $\text{ZnCo}_{2-x}\text{Ni}_x\text{O}_4$ are revealed. The impact of water surrounding on the $\text{ZnCo}_{2-x}\text{Ni}_x\text{O}_4$ is discussed.

Chapter 6 discusses the interplay between the electrolyte dependent OER activity with the kinetic parameters. The physical origin of the interaction between electrode with the water surroundings has been uncovered.

Chapter 7 draws together the threads of the thesis. The hypotheses are tested, and the goals are met. This thesis presents investigations on Co-based transition metal oxides/hydroxides as OER catalysts in alkaline solutions. It demonstrates how the intrinsic properties, surface properties and interfacial properties tune the mechanism and the kinetics of the OER. The understandings from these studies shine light on future catalysts improvements and design. Future research directions that can help to gain more insights on the understandings of surface electrochemistry are proposed. In the future, the gap existing in our understanding between the starting catalysts and the surface for the reconstructed materials will be bridged. The surface of the catalysts under exposure to different electrolytes environments will be explored. Extrinsic stimulations that can tune the intrinsic, surface and interfacial properties will be investigated.

1.4 Findings and Outcomes/Originality

This research led to several novel outcomes by:

1. Demonstrating OER activity enhancement by substitution strategies in Co-based materials.
2. Identifying the critical role of tuning the electronic structure of Co based oxides/hydroxides towards highly active electrocatalysts.

3. Demonstrating different OER mechanisms for different Co-based materials based on their electronic structures.
4. Establishing a relationship between change in Co-O covalency with the surface evolution of Co-based electrocatalysts.
5. Elaborating the electrolyte dependent OER activity for highly active Co-based transition metal oxides/hydroxides.
6. Elucidating the physical origin of the interfacial property between electrode and electrolyte by a kinetic parameter study.

1.5 Reference

- (1) Hong, W. T.; Risch, M.; Stoerzinger, K. A.; Grimaud, A.; Suntivich, J.; Shao-Horn, Y. Toward the Rational Design of Non-Precious Transition Metal Oxides for Oxygen Electrocatalysis. *Energy Environ. Sci.* **2015**, *8* (5), 1404–1427. <https://doi.org/10.1039/C4EE03869J>.
- (2) Hong, W. T.; Risch, M.; Stoerzinger, K. A.; Grimaud, A.; Suntivich, J.; Shao-Horn, Y. Toward the Rational Design of Non-Precious Transition Metal Oxides for Oxygen Electrocatalysis. *Energy Environ. Sci.* **2015**, *8* (5), 1404–1427. <https://doi.org/10.1039/C4EE03869J>.
- (3) Suntivich, J.; May, K. J.; Gasteiger, H. A.; Goodenough, J. B.; Shao-Horn, Y. A Perovskite Oxide Optimized for Oxygen Evolution Catalysis from Molecular Orbital Principles. *Science* **2011**, *334* (6061), 1383–1385.
- (4) Hammer, B.; Nørskov, J. K. Theoretical Surface Science and Catalysis—Calculations and Concepts. In *Advances in Catalysis*; Elsevier, 2000; Vol. 45, pp 71–129. [https://doi.org/10.1016/S0360-0564\(02\)45013-4](https://doi.org/10.1016/S0360-0564(02)45013-4).
- (5) Grimaud, A.; May, K. J.; Carlton, C. E.; Lee, Y.-L.; Risch, M.; Hong, W. T.; Zhou, J.; Shao-Horn, Y. Double Perovskites as a Family of Highly Active Catalysts for Oxygen Evolution in Alkaline Solution. *Nature communications* **2013**, *4*, 2439.
- (6) Fabbri, E.; Nachttegaal, M.; Binninger, T.; Cheng, X.; Kim, B.-J.; Durst, J.; Bozza, F.; Graule, T.; Schäublin, R.; Wiles, L.; Pertoso, M.; Danilovic, N.; Ayers, K. E.; Schmidt, T. J. Dynamic Surface Self-Reconstruction Is the Key of Highly Active Perovskite Nano-Electrocatalysts for Water Splitting. *Nature Mater* **2017**, *16* (9), 925–931. <https://doi.org/10.1038/nmat4938>.
- (7) Suntivich, J.; Perry, E. E.; Gasteiger, H. A.; Shao-Horn, Y. The Influence of the Cation on the Oxygen Reduction and Evolution Activities of Oxide Surfaces in Alkaline Electrolyte. *Electrocatalysis* **2013**, *4* (1), 49–55. <https://doi.org/10.1007/s12678-012-0118-x>.
- (8) Grimaud, A.; Diaz-Morales, O.; Han, B.; Hong, W. T.; Lee, Y.-L.; Giordano, L.; Stoerzinger, K. A.; Koper, M. T.; Shao-Horn, Y. Activating Lattice Oxygen Redox Reactions in Metal Oxides to Catalyse Oxygen Evolution. *Nature chemistry* **2017**, *9* (5), 457.

- (9) Yang, C.; Batuk, M.; Jacquet, Q.; Rouse, G.; Yin, W.; Zhang, L.; Hadermann, J.; Abakumov, A. M.; Cibin, G.; Chadwick, A. Revealing PH-Dependent Activities and Surface Instabilities for Ni-Based Electrocatalysts during the Oxygen Evolution Reaction. *ACS Energy Letters* **2018**, *3* (12), 2884–2890.
- (10) Zhang, R.; Pearce, P. E.; Duan, Y.; Dubouis, N.; Marchandier, T.; Grimaud, A. The Importance of Water Structure and Catalyst-Electrolyte Interface on the Design of Water Splitting Catalysts. *Chem. Mater.* **2019**, *acs.chemmater.9b02318*. <https://doi.org/10.1021/acs.chemmater.9b02318>.
- (11) Hong, W. T.; Stoerzinger, K. A.; Lee, Y.-L.; Giordano, L.; Grimaud, A.; Johnson, A. M.; Hwang, J.; Crumlin, E. J.; Yang, W.; Shao-Horn, Y. Charge-Transfer-Energy-Dependent Oxygen Evolution Reaction Mechanisms for Perovskite Oxides. *Energy & Environmental Science* **2017**, *10* (10), 2190–2200.
- (12) Zaffran, J.; Stevens, M. B.; Trang, C. D. M.; Nagli, M.; Shehadeh, M.; Boettcher, S. W.; Caspary Toroker, M. Influence of Electrolyte Cations on Ni(Fe)OOH Catalyzed Oxygen Evolution Reaction. *Chem. Mater.* **2017**, *29* (11), 4761–4767. <https://doi.org/10.1021/acs.chemmater.7b00517>.
- (13) Garcia, A. C.; Touzalin, T.; Nieuwland, C.; Perini, N.; Koper, M. T. M. Enhancement of Oxygen Evolution Activity of NiOOH by Electrolyte Alkali Cations. *Angew. Chem. Int. Ed.* **2019**. <https://doi.org/10.1002/anie.201905501>.

Chapter 2

Literature Review

The demand for clean energy and the challenges remaining for the production of green hydrogen by water electrolysis stimulate the search for highly active OER electrocatalysts. In this chapter, the benchmarking parameters for measuring the performance of OER catalysts are evaluated. Among a plethora of materials as candidates for OER catalysts, transition metal oxides/hydroxides are highlighted. Their structural features and usage as OER catalysts have been reviewed. In addition, the physical and chemical fundamentals for the materials behind the catalytic phenomenon are presented. The growing understandings of the mechanisms underlying the OER on the surface of different catalysts have been elaborated. The significance for the study on the interaction between the catalyst and its water surrounding has been discussed.

2.1 Background for OER

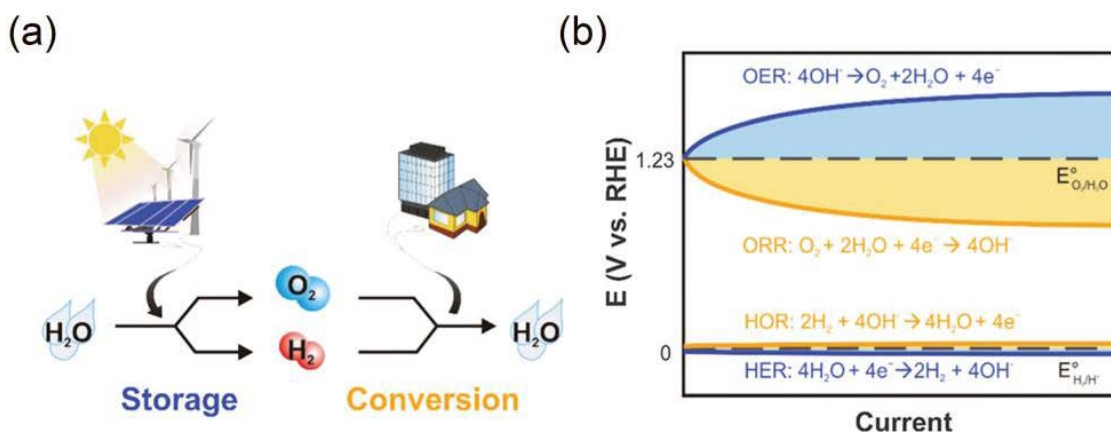
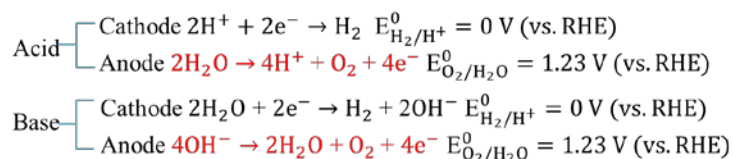
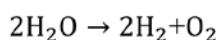


Figure 2.1 (a) Oxygen electrochemistry application for energy storage and conversion. (b) Reaction formulas for OER, ORR, HOR and HER. The overpotentials of the reactions. The figures are adapted from Ref 1.

The overconsumption of fossil fuels has caused severe environmental issues such as the ever-growing concentration of greenhouse gases and atmospheric pollution. Besides, the depleted fossil fuels cannot meet the increasing energy demand worldwide anymore. It is thus urgent to switch to clean energy vectors that can be produced from sustainable sources. Hydrogen fuel is one of such green energy vectors. While hydrogen is currently generated at more than 95% by the reforming of natural gas or oil, the cleanest way to produce hydrogen is through water electrolysis. The advantage for water splitting to produce hydrogen is the yields of clean product without by-products¹. Below, the half-reactions at the cathode and anode sides during water electrolysis in both acidic and alkaline solutions are written, with hydrogen evolved at the cathode and oxygen at the anode.



With platinum-based catalysts, the hydrogen evolution proceeds at a high rate.¹ However, the efficiency of water electrolysis has been severely hampered by the large overpotential of oxygen

evolution. To improve the sluggish reaction kinetics of OER, hence the overall efficiency for fuel production, noble metal-based compounds (i.e. IrO_2 and RuO_2) are used as electrocatalysts. However, their elemental scarcity and high cost force for the search of non-precious transition metal-based oxides/hydroxides as alternatives.^{2,3} Transition metal oxides/hydroxides are more stable when used in alkaline solutions.

2.2 Performance evaluation for OER catalysts

In order to evaluate the performance of transition metal oxides/hydroxides as OER catalysts, we look into their activity and stability. To measure the OER activity and stability of a catalyst, there are mainly three electrochemical methods: cyclic voltammetry (CV), chronoamperometry (CA), and chronopotentiometry (CP). Detailed experimental setup and measurements are shown in Chapter 3.2.1 Electrochemical Characterization section. There are a few parameters that can be obtained from these electrochemical measurements.

2.2.1 Overpotential

The OER is thermodynamically feasible above the half-cell potential of 1.23V. However, due to the slow kinetics of the OER, a large deviation from this thermodynamical potential is required to yield appreciable anodic current. Ruthenium oxide, as the best-known catalysts for OER, requires 0.4V overpotential at a current density of $1.5\text{A cm}^{-2}_{\text{geo}}$. The best-known transition metal oxide catalyst is nickel-iron-cobalt oxide, which requires an overpotential around 0.4V at $10\text{mA cm}^{-2}_{\text{geo}}$.¹

2.2.2 Specific activity vs mass activity

Mass activity of the catalysts are obtained by normalising the current densities by the mass loading on the working electrode. However, OER is a surface reaction and only the atoms on the surface participate to the reaction. Other atoms underneath the surface do not contribute to the reaction. Hence, mass activity does not represent the intrinsic activity of the catalyst. A more accurate way to report the “true” activity of a catalyst is to normalise the current density by

surface area to obtain a specific activity, as surface area can reflect the real number of active sites on the surface.⁴ Surface area of transition metal oxides obtained by Brunauer-Emmett-Teller (BET) methods and ECSA methods are elaborated in Chapter 3.2.1 Electrochemical Characterization and Chapter 3.2.2 Structure Characterization sections.

2.2.3 Turnover frequency

The turnover frequency (TOF) reflects the number of reaction products generated per active site per unit of time. Figure 2.2 compares the TOF of oxide catalysts with the natural catalyst OEC used in the OER process in photosynthesis II.

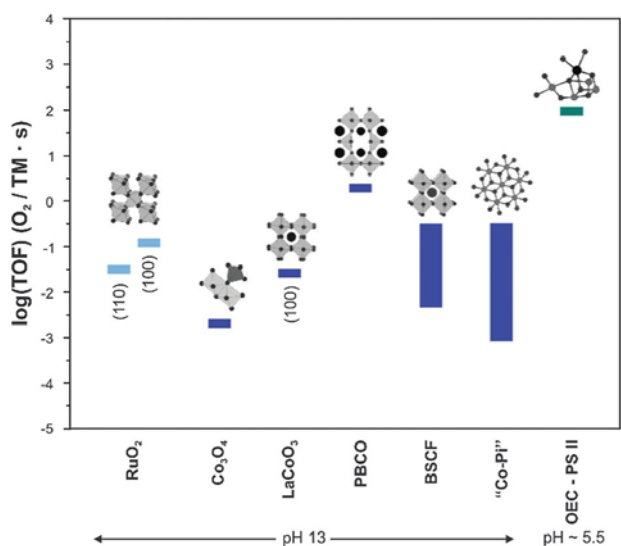


Figure 2.2 TOF of different oxides materials and the natural catalyst OEC. This figure is adapted from Ref 1.

2.3 Transition metal oxides/hydroxides as catalyst materials for OER

Table 2.1 Oxides used as catalysts materials.

Rutile-type	RuO ₂ , IrO ₂ , MnO ₂ , PbO ₂ , PtO ₂ , OsO ₂ , ReO ₂	Mixed oxides with SnO ₂ , TiO ₂ , Fe ₂ O ₃
-------------	---	---

		Doped oxides SnO ₂ , MnO ₂ , PbO ₂
Spinel-type	Co ₃ O ₄ MCo ₂ O ₄ M=Ni, Mn, Cr... Fe ₃ O ₄ MFe ₂ O ₄ M=Ni, Co, Mn...	Doped oxides Co ₃ O ₄
Perovskite-type	NiM ₂ O ₄ M=La, Pr, Nd M' _{1-x} Sr _x MO ₃ M=Mn, Co, Fe, Ni M'=La, Nd	
Other oxides	NiO _x , PdO, M _x WO ₃ , Bi ₂ M ₂ O ₇ M=Rh, Ru Li _{0.5} Pt ₃ O ₄ , SrPd ₃ O ₄ , ABO ₂ A=Pt, Pd, Ag, Cu B=Co, Cr, Ru, Ir ABO ₄ •xMO ₂ A=Al, Rh B=Sb, Nb, Ta M=Ru, Ir	

A plethora of materials have been used as catalysts materials. Co based transition metal oxides have attracted much attention. Ba_{0.8}Sr_{0.2}Co_{0.5}Fe_{0.5}O₃ has been found as a better catalyst than IrO₂.² Co³⁺ at octahedral site is quite active for OER.⁵⁻⁷ Six-coordinated Co can exist in various crystal structures, such as spinel structure oxides (e.g. ZnCo₂O₄), delafossite structure oxides (e.g. LiCoO₂), perovskite (e.g. LaCoO₃) and rock salt structure (CoO) are shown in Figure 2.3. Figure 2.3 Crystal structure of spinel structure oxides (e.g. ZnCo₂O₄), delafossite structure oxides (e.g. LiCoO₂), perovskite (e.g. LaCoO₃) and rock salt structure (CoO) with CoO₆.

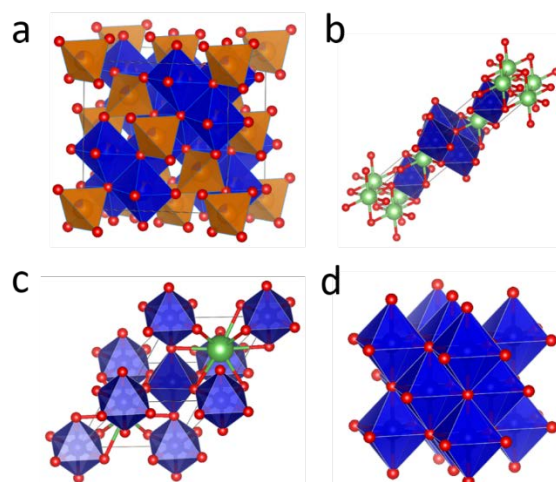


Figure 2.3 Crystal structure of spinel structure oxides (e.g. ZnCo₂O₄), delafossite structure oxides (e.g. LiCoO₂), perovskite (e.g. LaCoO₃) and rock salt structure (CoO) with CoO₆.

2.3.1 Perovskite oxides

Perovskite oxides have a general formula of ABO₃, where A-site cations are typically electropositive cations which are larger than B-site cations. B sites are typically occupied by transition metals or main group ions.⁸ A-site cations are in a 12-coordinate framework of corner-shared BO₆ octahedra.⁹ The structure of perovskite oxide and the possible coupling of A, B cations are shown in Figure 2.4.

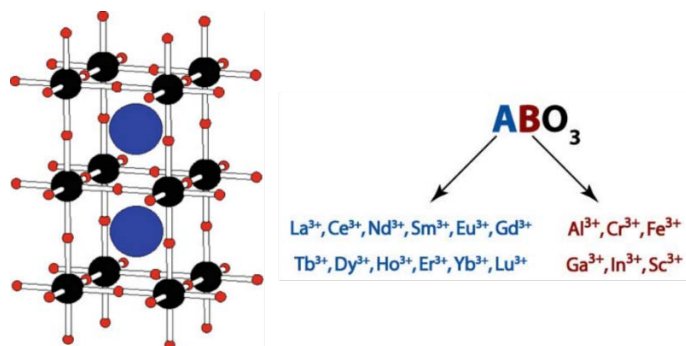


Figure 2.4 Structure of perovskite oxide.

Creating a combination of multimetals in the A sites and B sites for perovskite is able to modify the valence state and electronic structure of the catalyst. This provides some degree of freedom to tune the crystal structure and control the oxygen vacancy level as well.¹⁰⁻¹⁴ The feasibility for the

multimetal perovskite is based on two parameters, one is the Goldschmidt tolerance factor t , the other being the octahedral factor μ .¹⁵ t is calculated from the ratio of ionic radii:

$$t = \frac{r_A + r_O}{\sqrt{2}(r_B + r_O)}$$

where r_A and r_B are the ionic radii of cations at A and B sites, and r_O is the ionic radius of oxygen. For a stable perovskite structure to be formed, t should lie in the range of 0.8-1. If $t = 1$, an ideal cubic structure with the larger cation A and smaller cation B is formed. For t within the range of 0.9-1, a cubic structure forms. Examples are SrTiO_3 and BaTiO_3 .¹⁶ For $t > 0.8$ and < 0.9 , an orthorhombic or rhombohedral structure is formed. If $t < 0.8$ or $t > 1.0$, the cation A is too small or too big to be adjusted to BO_6 octahedron framework, which ends up in an alternative structure.

The octahedral factor μ is the ratio between ionic radii of B and oxygen:

$$\mu = \frac{r_B}{r_O}$$

μ should lie in the range of 0.44–0.72 for a stable BO_6 octahedron to form.

2.3.2 Spinel oxides

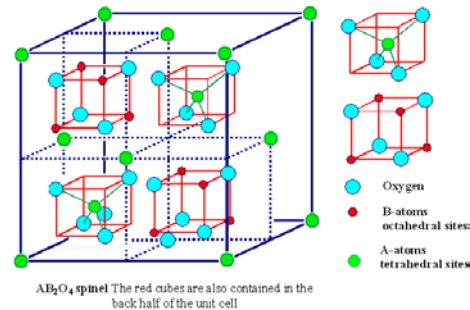


Figure 2.5 Structure of spinel oxide. This figure is adapted from Ref 17.

Spinel oxides have a general formula AB_2O_4 :



where A-site cations are typically charged as 2+ at tetrahedral sites, sometimes can be charged as 3+, while B-site cations are normally charged as 3+ at octahedral sites.¹⁸ Depending on how the cations occupy the octahedral and tetrahedral sites, either normal or inverted spinel structure is formed. The parameter λ represents the degree of inversion. For a normal spinel structure, where $\lambda=0$, all the A^{2+} cations occupy tetrahedral sites and all the B^{3+} cations occupy octahedral sites.

Examples are Co_3O_4 , MgCo_2O_4 and ZnCo_2O_4 .¹⁹ In the inverse spinel structure, A^{2+} occupies the octahedral sites, while B^{3+} cations are partially in the tetrahedral sites and partially in the octahedral sites. Examples are NiCo_2O_4 , MnCo_2O_4 and FeCo_2O_4 .²⁰ By modifying the $\text{M}_{\text{Td}}\text{-O}$ and $\text{M}_{\text{Oh}}\text{-O}$ bond lengths by metal cation substitution or doping, unit cell parameters and oxygen fractional coordinate can be changed.²¹ However, no influence on $\text{M}_{\text{Oh}}\text{-O}$ bond lengths can be induced by substitution of tetrahedral cations. M_{Td} has a $\bar{4}3\text{m}$ symmetry with six equivalent unshared edges and no angular freedom. Cation substitution in Td site can only adjust the $\text{M}_{\text{Td}}\text{-O}$ bond length. M_{Oh} has a $\bar{3}\text{m}$ symmetry, with six unshared edges, pertaining to the faces perpendicular to the threefold axis, and six shared edges. The cation substitution in Oh site can modify the $\text{M}_{\text{Oh}}\text{-O}$ bond lengths as well as the $\text{O-M}_{\text{Oh}}\text{-O}$ angle. This altered $\text{O-M}_{\text{Oh}}\text{-O}$ angle can further result in modified $\text{M}_{\text{Td}}\text{-O}$ bond length.²²

2.3.3 Layered hydroxides

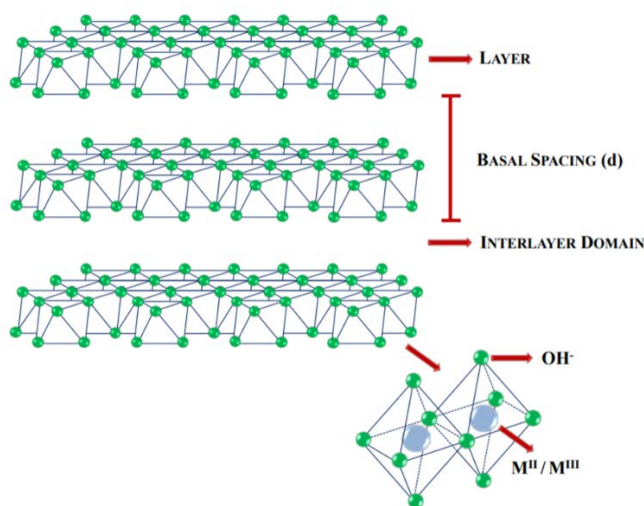


Figure 2.6 Structure of layered hydroxides. This figure is adapted from Ref 23.

Layered hydroxides have a formula of $\text{M}^{2+}_{(1-x)}\text{M}^{3+}_x(\text{OH})_2$. The metal cations stay in the octahedral site in a six-fold coordination. Most of the layered hydroxides exhibit hexagonal unit cell. The hydroxides with $\text{M}^{2+}/\text{M}^{3+}$ ratio equal to 1 display an orthorhombic phase.²⁴

2.3.4 Fundamentals of electronic structure

Electronic structure is vital in determining the physical and chemical properties of transition metal oxides/hydroxides. For a perovskite or a hydroxide structure, first-row transition metal cations with d^4 - d^7 electronic configurations normally occupy the octahedral sites. The cations in octahedral sites generally determine the physical properties of the materials.⁹

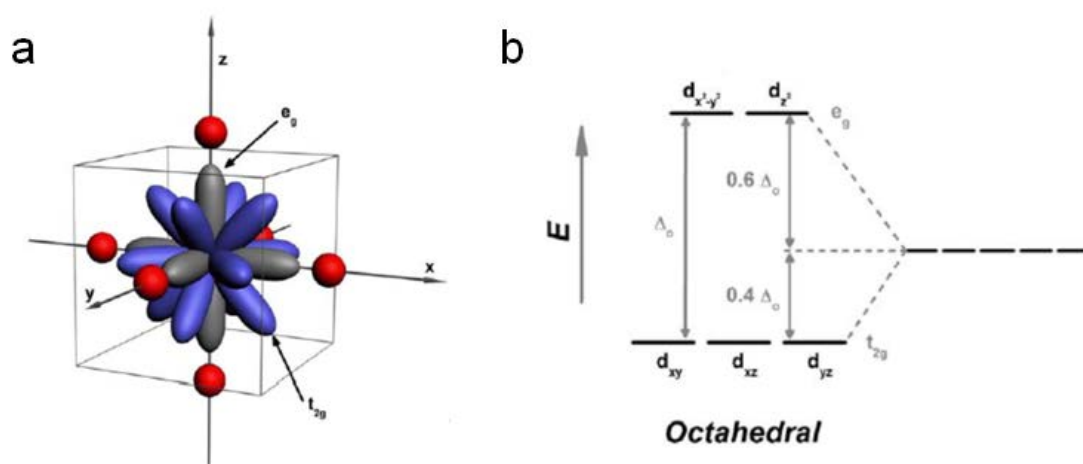


Figure 2.7 (a) Spatial arrangement of oxygen ligands with respect to the d orbitals in the octahedral crystal field. (b) degenerate d orbitals in octahedral crystal field. This figure is adapted from Ref 25.

In crystal structure, the cations are exerted repulsion force by the negatively charged oxygen around them (Figure 2.7a).²⁶ As the ligand approaches the metal ion, a loss of degeneracy can be promoted. The electron of the ligand can be attracted and get closer to some d -orbitals while repelled from others. The ligands which are closer to the d -orbitals normally have higher energy than those further away. This leads to a splitting in energy for d -orbitals. In octahedral environment, the d_{z^2} and $d_{x^2-y^2}$ experience the most repulsion and undergo destabilization, thus forming the so-called e_g levels. Instead, the d_{xy} , d_{yz} and d_{xz} orbitals do not directly overlap with oxygen orbitals, thus less repulsion leads to relatively stabilization in energy. The t_{2g} formed by d_{xy} , d_{yz} and d_{xz} has relatively lower position than e_g ones (Figure 2.7b). The metal d orbitals electrons can partially describe the electron in bands formed in crystal. The ionic-covalent metal-oxygen bond shall also be considered to accurately describe the electronic structure.

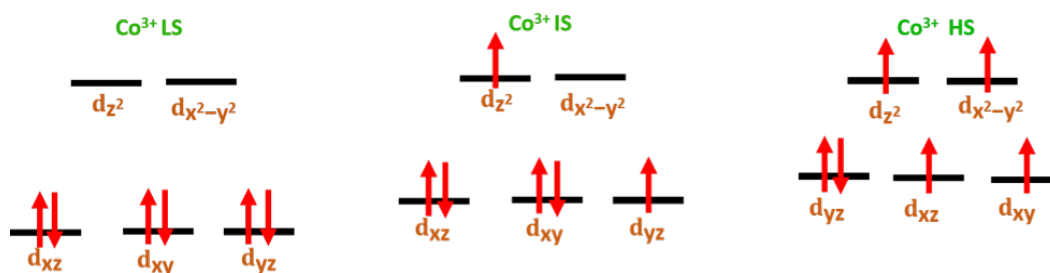


Figure 2.8 Scheme of low spin state, intermediate spin state and high spin state of Co^{3+} .

The high or low spin state is determined by the splitting energy which is a competition between the crystal field splitting energy of the $3d$ states of the Co ions and the Hund's rule intra-atomic exchange energy. With LaCoO_3 as an example, the splitting energy of the Co ions is rather small: 10 meV. The spin state transition can thus be induced by thermo-excitation. In LaCoO_3 , Co^{3+} exists in low spin ($t_{2g}^6 e_g^0$, $S = 0$) state at low temperature (< 90 K). As the temperature increases, a transition from low spin state to intermediate spin state ($t_{2g}^5 e_g^1$, $S = 1$) occurs at 90 K²⁷, before to transition to the high spin state ($t_{2g}^4 e_g^2$, $S = 2$) state at 500 K.^{28,29} The spin state of Co^{3+} in LaCoO_3 at room temperature is considered as either intermediate spin states³⁰ or a mixture of high spin and low spin states^{31,32}. While for a normal spinel ZnCo_2O_4 , Co^{3+} remains in low spin ($t_{2g}^6 e_g^0$, $S = 0$) state.¹⁹

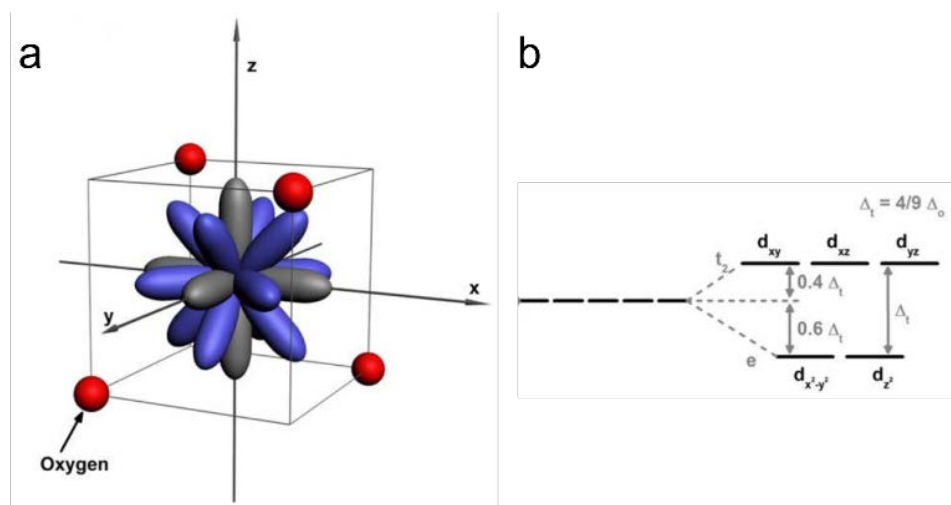


Figure 2.9 (a) Spatial arrangement of oxygen ligands with respect to the d orbitals in the tetrahedral crystal field. (b) degenerate d orbitals in tetrahedral crystal field. This figure is adapted from Ref 25.

In a spinel structure, first-row transition metal cations can occupy the tetrahedral sites as well. In a tetrahedral environment, ligands approach more closely the d orbitals between the axis rather than the orbitals on the axis. The higher energy orbitals are the opposite ones as in the case of octahedral geometry (Figure 2.9). Furthermore, as the ligands do not approach the orbitals directly, the energy splitting is lower than that in octahedral geometry.

2.4 Mechanism of OER

2.4.1 Concerted proton-electron transfer (CPET)

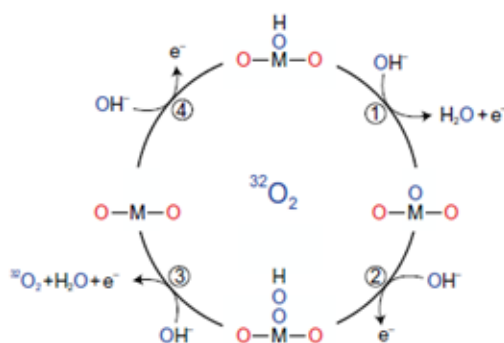


Figure 2.10 Traditional mechanism of OER process in which the concerted proton–electron transfers are involved on the metal sites. The oxygen in blue are originated from electrolyte, whereas oxygen in red is the oxygen contributed from the oxide lattice. This figure is adapted from Ref 33.

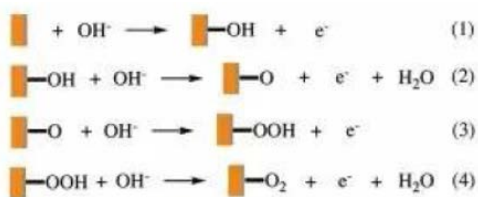


Figure 2.11 Four steps CPET reactions.

Figure 2.10 and Figure 2.11 depict the traditional four steps OER process in which four consecutive concerted proton-electron transfers occur on the surface of metal sites in alkaline solution. After being exposed to the electrolyte, OH^- is adsorbed on the surface of the metal oxide catalyst. Then, another OH^- molecule react with the adsorb *OH to form water and leave a M-O bond on the oxide surface. A third OH^- the react to form M-OOH. Then, OOH* reacts with

another OH⁻ to leave M-OO. Finally, OO* desorbs from the surface and releases in the form of oxygen. The reaction free energies for these four steps can be calculated as following:

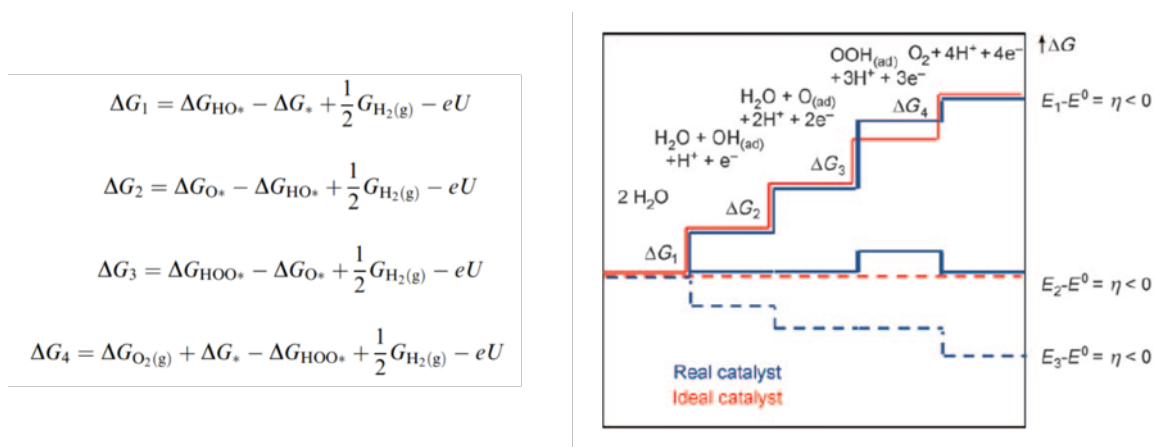


Figure 2.12 Reaction free energies for four CPET steps. (left) This figure is adapted from Ref 34. Reaction free energy of real catalysts and ideal catalysts under three different OER potentials. (right) This figure is adapted from Ref 35.

The OER on a catalyst is limited by these four reaction steps. The overpotential of the OER for the catalyst is determined by the most positive value among ΔG_1 , ΔG_2 , ΔG_3 and ΔG_4 . Previous belief was that the rate limiting step in OER is either the strong adsorption of OOH_{ads} or the weak adsorption of O_{ads} species. Nevertheless, the rate limiting steps for different catalysts vary from each other. Since ΔG_1 and ΔG_4 rarely acts as the rate-determining step, a so-called volcano plot was constructed based on the difference in the free binding energy between O^* and OH^* to capture the OER kinetics for different catalysts (Figure 2.13).

Figure 2.13 Volcano plot. This figure is adapted from Ref 36.

2.4.1.1 Electronic structure affecting OER performance

The change in electronic structure parameters such as covalency and e_g configuration can adjust the adsorbate binding strength. Thus, the electronic structure determines the OER activity.

2.4.1.1.1. e_g configuration

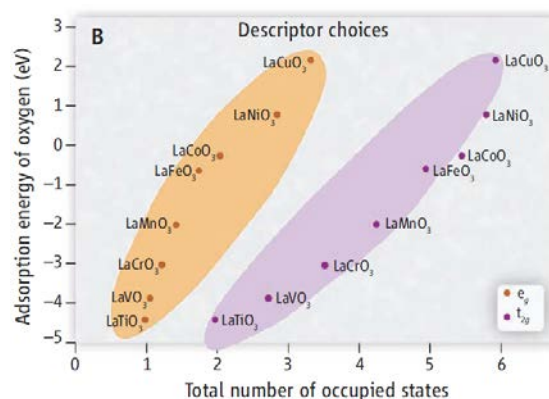


Figure 2.14 (a) Correlation between OER activity and the occupation of e_g orbital for different perovskite materials. (b) adsorption energy of oxygen vs. e_g occupation. These figures are adapted from Ref 37.

The intermediates are bonded with oxygen, hence S. Trasatti et.al proposed M-O binding energy as a descriptor for OER.³⁸ The formation of *OH and *O can be promoted when M-O bind

energy is enhanced. However, the formation of *OOH is hindered when M-O bond too strong. Hence, an optimal M-O is required for high efficiency of the OER reaction. Nørskov et. al. first found the interplay between M-O binding energy and e_g where increasing occupancy of e_g orbital occupancy leads to stronger O binding energy. (Figure 2.14b)³⁹ Shao-Horn et al. proposed that e_g occupancy number could quantify the M-O binding energy. A correlation between e_g and OER activity have been established. A compound with metal cation of $e_g \sim 1.2$ possesses the greatest OER activity.² As shown in Figure 2.14, BSCF with e_g occupancy of 1.2 has the best OER activity among those perovskites. LaCoO_3 possesses a bit larger e_g than BSCF. Through adjusting the size of the catalysts, the e_g configuration can be tuned. As reported by Zhou et. al, by tailoring the size of LaCoO_3 , its e_g can be adjusted to ~ 1.2 which give the best OER activity.³¹ Examples of B site substitution for Co have shown their ability in OER enhancement. For example, Mn and Ni have been widely used to partially replace Co and endow the charge redistribution between two B sites metal elements. When Mn substitutes part of Co, Mn^{4+} and Co^{2+} are generated as a consequence of electron transfer from Mn^{3+} to Co^{3+} via O^{2-} ions.⁴⁰ While Ni is doped in LaCoO_3 , Ni^{3+} ions act as electron donors to the Co^{3+} ion by contributing its electron on e_g band.³⁰ Under these scenarios, double exchange interaction plays a pivotal role in change of electron occupancy on e_g and t_{2g} , hence boosting the OER performance.⁴¹ The metal substitution induced lattice strain also changed the spin state and e_g configuration.

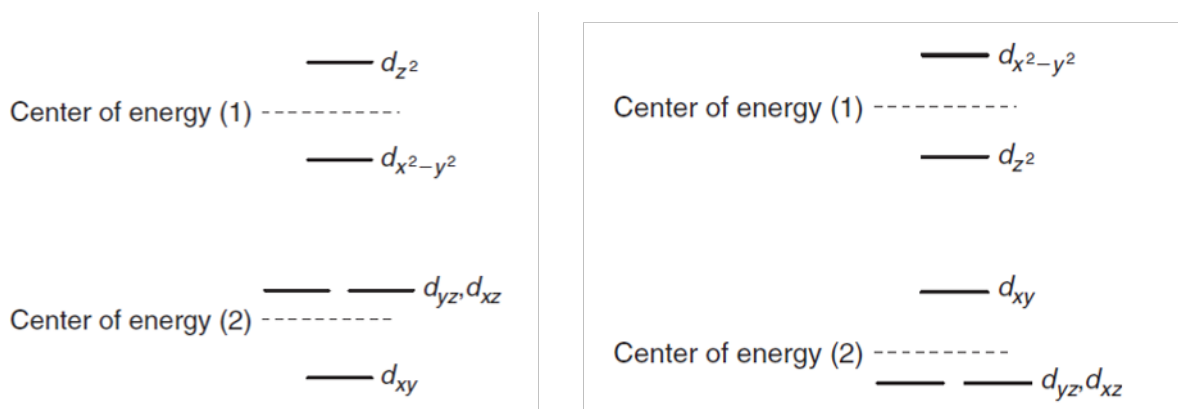


Figure 2.15. Compression on z axis (left) and elongation on z axis (right). This figure is adapted from Ref 42.

As discussed above, the orbital experiencing more repulsion will become more destabilized and tends to be higher in energy. When compression force is exerted on the z axis, the repulsion on

d_{z^2} is the maximal. $d_{x^2-y^2}$ is at a relatively lower position to balance with the energy of d_{z^2} . d_{yz} and d_{xz} experience more repulsion than d_{xy} , thus, they are located at the upper and lower position of the centre of energy 2. Similarly, the plot in Figure 2.15 for the case of elongation on z axis can be plotted.

2.4.1.1.2. Covalency

Studies have found out that the OER activity was correlated with the location of oxygen 2p orbital centre (with the Fermi level as reference).⁴³⁻⁴⁵ Grimaud et al. found that the potentials for the four steps reaction can be lowered as the metal-oxygen covalency is enhanced.³³ The metal-oxygen hybridization is affected by the choice of metal cations. Metal cations substitution and their different oxidation states modify the number of *d* electrons and the electronegativity of the metal cations. The increase in electronegativity moves the metal *d* states close to O 2p states and increase the metal-oxygen hybridization in perovskite.⁴⁶ Much research bolstered the hypothesis that optimizing cobalt valence state can promote OER activity. This is because the change in oxidation states in metal cations also change their covalency. The valence state of B cations can be tuned when substituting A site cation with a lower valence state element.⁴⁴ Mefford et al. introduced Sr²⁺ cation into La³⁺ which induce in promotion of Co³⁺ to Co⁴⁺. This lifts the O 2p center, enhance the covalency between metal 3d and O 2p orbitals,^{47,48} hence to promote the OER process.⁴⁵ Therefore, methods were proposed to enhance the OER activity in Co based perovskites. Initially, their OER performances were normally enhanced by change of synthesis methods or conditions to enlarge surface area, choice of different transition metal oxides, metal cations substitution in the transition metal oxides, etc. However, bringing the perspectives of electronic structures, these novel strategies boosted the performance by either change the covalency or the e_g configurations of the metal cations in the transition metal oxides. The covalence of the oxide framework can be increased not only by cation substitution of a more electronegative metal, but also by replacing oxygen with less electronegative ligands (such as S, Se or Te).⁴⁹ The anion substitution is not discussed in this thesis. This can be explored in the future research work.

2.4.2 Non-concerted proton-electron transfer

2.4.2.1 Surface reconstruction

When the O p-band center get too close to E_F , materials such as BSCF82, SCF82 and BSCE46 become unstable under OER conditions.⁵⁰ Though not perfectly stable, they exhibit very good OER activities. With BSCF82 as an example, a surface amorphization have been observed under TEM after OER reaction in alkaline solution.⁵¹ With the aid of operando XAS, Fabbri et.al. found that $\text{Co}^{2+}/\text{Co}^{3+}$ and $\text{Fe}^{2+}/\text{Fe}^{3+}$ dissolved together with the leaching of Ba^{2+} and Sr^{2+} . Then, $\text{Co}^{2+}/\text{Co}^{3+}$ and $\text{Fe}^{2+}/\text{Fe}^{3+}$ re-deposited back to the surface of the catalysts to form a layer of $(\text{Co/Fe})\text{O}(\text{OH})$.(Figure 2.16)⁵² This new surface contributes to high OER activity of BSCF82.

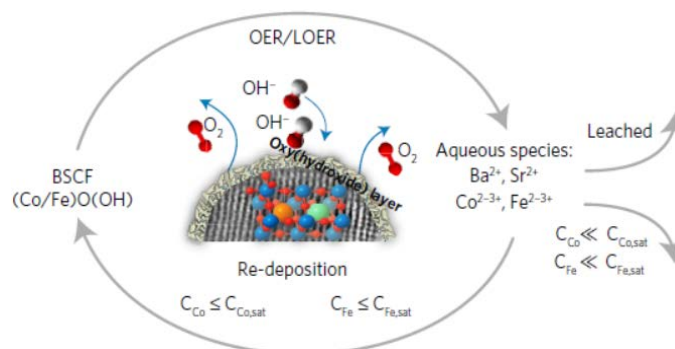


Figure 2.16 Dissolution and re-deposition mechanism for BSCF82. This figure is adapted from Ref 52.

2.4.2.2 Lattice oxygen mechanism

For some very active but unstable catalysts, such as LSCO, a new mechanism (Figure 2.17) emerged. By employing isotopic labelling, more than 14 nm ^{18}O was evolved after ^{18}O -labelling, which indicates the participation of lattice oxide in the OER.³³

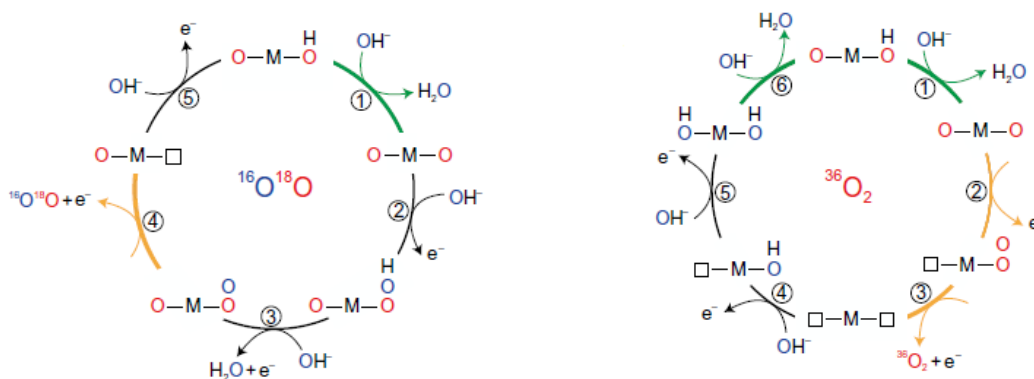


Figure 2.17 Evolved OER mechanisms which involve non-concerted proton–electron transfer. The illustration on the left involves OER that evolve $^{34}\text{O}_2$ and $^{36}\text{O}_2$ is evolved on the right. The same processes as in concerted proton-electron transfer have been marked in yellow and green. These figures are adapted from Ref 33.

2.1.1.1.1. Cationic and anionic redox reaction

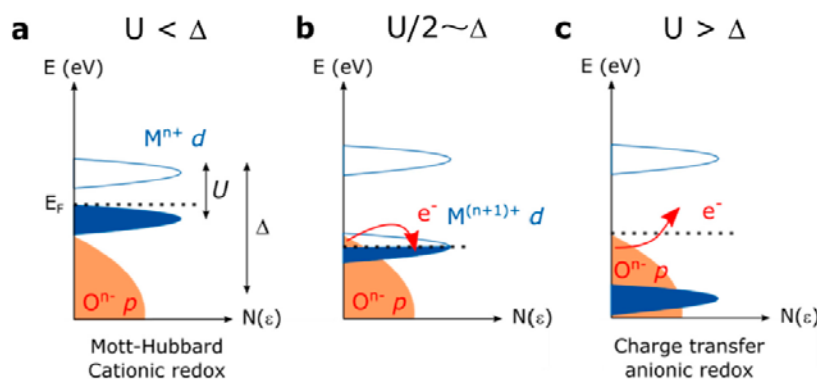


Figure 2.18 Zaanen-Sawatzki-Allen (ZSA) framework for the electronic structure of transition metal oxides. These figures are adapted from Ref 26.

The differentiation between cationic and anionic redox reaction is based on the relative magnitude of charge transfer gap Δ (the electronegativity between the cation and anion) and Coulomb inter-site repulsion U (the energy between occupied and unoccupied metallic states). Figure 2.18a illustrates Mott-Hubbard cationic redox reaction with $U < \Delta$. Figure 2.18c demonstrates charge transfer anionic redox reaction with $U > \Delta$. The intermediate case is shown in Figure 2.18b.

When oxygen species in a compound are redox active, they can contribute to the OER activities as well.⁴⁸ This is the case when there is strong M 3d and O 2p overlap,⁴⁹ leading to the formation

of ligand holes. As lattice oxygen take part to the OER process, ligand vacancies are formed on the metal oxides.²⁶ Other factors such as substitution can also induce oxygen deficiency.⁴⁵ When these ligand holes are formed, the metal 3d and oxygen 2p overlap is large. These ligand holes modify the active redox centre on the surface of catalysts. As reached in Chapter 2.4.1, Shao-Horn et. al. demonstrated the oxygen p band relative to Fermi level in perovskite as a descriptor in 2013.⁴⁹ Shifting the oxygen p band centre closer to Fermi level can promote the OER activity by triggering the lattice oxygen redox reaction.^{50,53,54} (Figure 2.19)

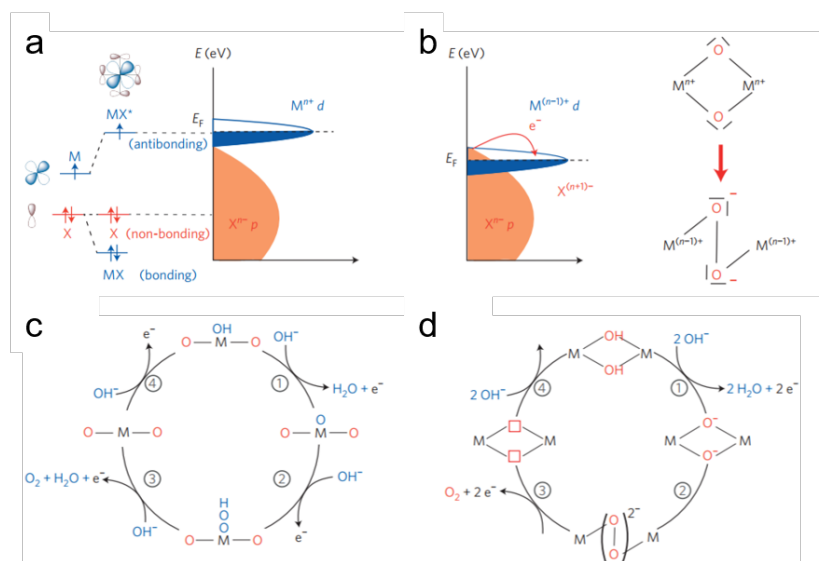


Figure 2.19 (a) (c) Metal cations as active sites without oxygen deficiency. (b) (d) Oxygen deficiency participates in the OER process. These figures are adapted from Ref 26.

2.4.2.3 pH-dependence phenomenon

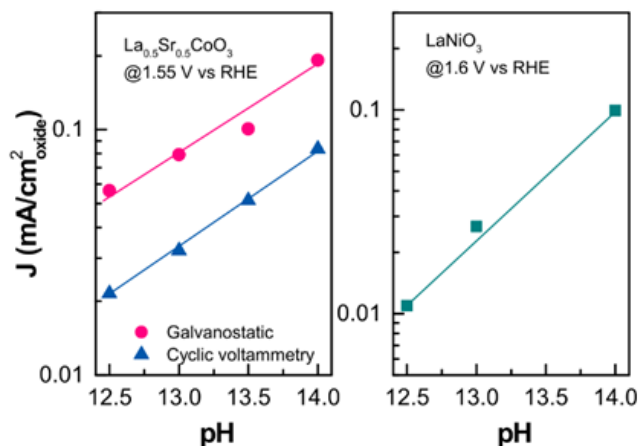
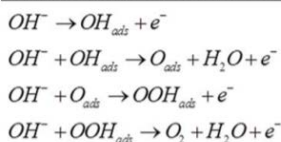


Figure 2.20 pH dependent OER activities of LSCO and LaNiO₃. . This figure is adapted from Ref 55.

For these materials showing either severe surface degradation with the redox activity of lattice oxygen or the formation of negatively charged surface sites⁵⁶, their activity can be influenced by the concentration of alkaline solution. A pH dependent OER activity has been found in LSCO⁴⁸ and LaNiO₃⁵⁵ (Figure 2.20). The pH-dependence suggests a non-concerted proton-electron transfer involved in the OER steps.⁵²

Concerted OH⁻/e⁻ transfer OER mechanism:



Decoupled OH⁻/e⁻ transfer OER mechanisms:

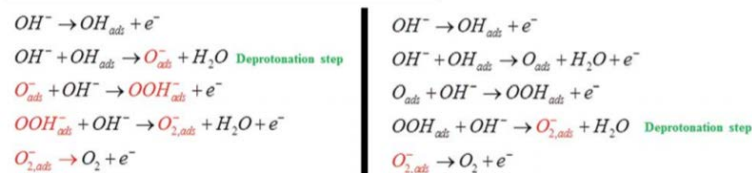


Figure 2.21 Comparison between the concerted proton-electron transfer OER mechanism and the non-concerted proton-electron transfer OER mechanism. These reactions are adapted from Ref 57.

For various catalysts varying from pH-independent and pH-dependent materials, their activation energies decrease with increased current density (Figure 2.22).⁵⁸ The reaction rate r for a reaction is related to reaction free energy:

$$r \propto A' \exp\left(\frac{-\Delta G^\ddagger}{RT}\right)$$

r is also related to the activation energy E_a as extrapolated by the Arrhenius equation⁵⁹:

$$r \propto A' \exp\left(\frac{-E_a}{RT}\right)$$

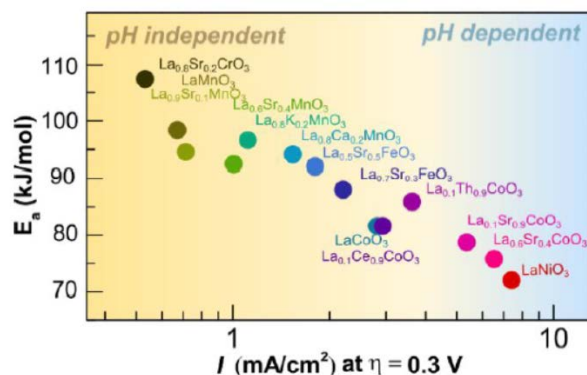


Figure 2.22 Activation energies as reported by Otagawa and Bockris for perovskites OER catalysts as a function of the OER current density measured at 300 mV overpotential. This figure is adapted from Ref 58.

2.4.3 Multi-metal transition metal oxides/hydroxides as OER catalyst

The viability of elemental substitution, doping or surface modifications for metal oxides/hydroxides offer design flexibility and potential for OER activity enhancement^{18,60–62} and stability improvement^{63–65}. Large variety of additional metals have been incorporated into metal oxides/hydroxides to regulate their electronic structure^{10–14}, conductivity^{66–70} and kinetics^{71–77} for the OER. Of those, iron incorporation has been proposed as a promising strategy to boost OER activities.^{2,71,74,76,78–86} Examples can be found in perovskite oxides $\text{Ba}_{1-x}\text{Sr}_x\text{Co}_{1-y}\text{Fe}_y\text{O}_3$ ^{2,80}, Fe substituted $\text{La}_{0.6}\text{Ca}_{0.4}\text{CoO}_3$ ⁷⁷, spinel oxides $\text{ZnCo}_{2-x}\text{Fe}_x\text{O}_4$ ⁷⁸, $\text{Ni}_{3-x}\text{Fe}_x\text{O}_4$ ^{25,87}, $\text{Co}_{3-x}\text{Fe}_x\text{O}_4$ ^{66,88}, rock-salt structure NiFeO_x ⁸⁹, layered structure $\text{LiCo}_{1-x}\text{Fe}_x\text{O}_2$ ⁷⁹, iron-doped (oxy)hydroxide^{84,90–92}, among others.

It should be noted that this metal incorporation approach is much more complex in the case of spinel oxides. Not only the cations in octahedral sites, but also the metal cations in tetrahedral sites can influence the OER.⁹³ The interaction between the tetrahedral site and octahedral site can also tune the electronic structure and the performance.^{41,94} Iron-doped nickel oxide/(oxy)hydroxide is regarded as the best OER catalysts, by some metrics matching or exceeding the performance of benchmarked IrO_2 .^{90,92,94–96} Trotochaud et al. Fe impurities in the electrolyte largely enhance the OER performance for NiOOH ⁹² and CoOOH ⁹¹. The theoretical study by Toroker et. al.⁶⁷ considered that Fe, with many oxidation states, act as a dopant into the

structure. Burke et al. found that FeOOH had the highest intrinsic activity among the transition metal oxyhydroxide⁹⁷. This was supported by studies which recognized octahedral site Fe³⁺ as active sites for NiFeOOH^{98,99}. However, this is not agreed by Swierk et al. who found that Fe substituted metal oxyhydroxide exhibited better activity than FeOOH itself.⁷⁶ The contribution for Fe substitution in transition metal oxides/hydroxides remain discussion. In the following sessions of the thesis, Fe substituted catalysts will be studied on their electronic structure and interaction with electrolyte environments.

2.4.4 Influence by electrolyte cation species

OER takes place at the electrode-electrolyte interfaces. The interaction on the catalysts by the water surrounding influence their OER activity and stability. Not only the concentration of the alkaline solution but also the alkali cation species in the solution modify the interaction between the catalyst and the solution.^{100,101} Garcia et. al. found that varying the alkali cations species in alkaline solution tuned the OER activity of Fe-containing NiOOH.¹⁰² The film exhibit the best activity in CsOH, followed by KOH and NaOH, while the activity is the worst in LiOH. By employing Raman spectroscopy, Michael et. al found that Ni-O length can be adjusted by changing the alkali cation species in iron contaminated NiOOH film.¹⁰³ It is also found out that bigger cations (Cs⁺) provide a better stabilization to the Ni-OO--M⁺ intermediate.¹⁰¹

2.4.4.1 Chaotropicity and kosmotropicity

As shown in Figure 2.23, based on the B coefficient which reflects the ability to structure or disorder the hydrogen bonding network, the cations and anions in the solutions can be divided into categories. Kosmotropic cations such as Li⁺ with B coefficient lager than 0 are more able to order the water structure. Chaotropic cations such as K⁺ and Cs⁺ with B coefficient smaller than 0 are more able to disorder the structure of water, which can impact its reactivity on the catalyst surface.¹⁰⁴

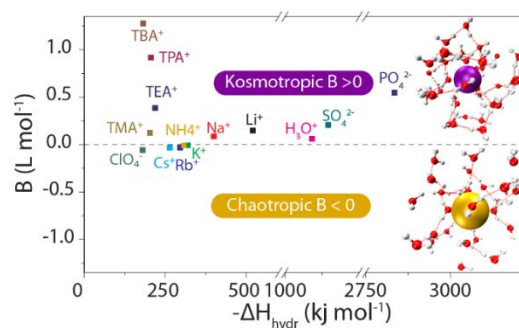


Figure 2.23 Two categories of cations and anions in the solutions. This figure is adapted from Ref 104.

2.5 Reference

- (1) Hong, W. T.; Risch, M.; Stoerzinger, K. A.; Grimaud, A.; Suntivich, J.; Shao-Horn, Y. Toward the Rational Design of Non-Precious Transition Metal Oxides for Oxygen Electrocatalysis. *Energy Environ. Sci.* **2015**, *8* (5), 1404–1427. <https://doi.org/10.1039/C4EE03869J>.
- (2) Suntivich, J.; May, K. J.; Gasteiger, H. A.; Goodenough, J. B.; Shao-Horn, Y. A Perovskite Oxide Optimized for Oxygen Evolution Catalysis from Molecular Orbital Principles. *Science* **2011**, *334* (6061), 1383–1385.
- (3) Hwang, J.; Rao, R. R.; Giordano, L.; Katayama, Y.; Yu, Y.; Shao-Horn, Y. Perovskites in Catalysis and Electrocatalysis. *Science* **2017**, *358* (6364), 751–756. <https://doi.org/10.1126/science.aam7092>.
- (4) Wei, C.; Rao, R. R.; Peng, J.; Huang, B.; Stephens, I. E. L.; Risch, M.; Xu, Z. J.; Shao-Horn, Y. Recommended Practices and Benchmark Activity for Hydrogen and Oxygen Electrocatalysis in Water Splitting and Fuel Cells. *Adv. Mater.* **2019**, *31* (31), 1806296. <https://doi.org/10.1002/adma.201806296>.
- (5) Maiyalagan, T.; Jarvis, K. A.; Therese, S.; Ferreira, P. J.; Manthiram, A. Spinel-Type Lithium Cobalt Oxide as a Bifunctional Electrocatalyst for the Oxygen Evolution and Oxygen Reduction Reactions. *Nat Commun* **2014**, *5* (1), 3949. <https://doi.org/10.1038/ncomms4949>.
- (6) Xie, X.; Li, Y.; Liu, Z.-Q.; Haruta, M.; Shen, W. Low-Temperature Oxidation of CO Catalysed by Co₃O₄ Nanorods. *Nature* **2009**, *458* (7239), 746–749. <https://doi.org/10.1038/nature07877>.
- (7) Xiao, J.; Kuang, Q.; Yang, S.; Xiao, F.; Wang, S.; Guo, L. Surface Structure Dependent Electrocatalytic Activity of Co₃O₄ Anchored on Graphene Sheets toward Oxygen Reduction Reaction. *Sci Rep* **2013**, *3* (1), 2300. <https://doi.org/10.1038/srep02300>.
- (8) Reshmi Varma, P. C. Low-Dimensional Perovskites. In *Perovskite Photovoltaics*; Elsevier, 2018; pp 197–229. <https://doi.org/10.1016/B978-0-12-812915-9.00007-1>.
- (9) Anderson, M.; Greenwood, K.; Taylor, G.; Poeppelmeier, K. B-Cation Arrangements in Double Perovskites. *Progress in Solid State Chemistry* **1993**, *22* (3), 197–233. [https://doi.org/10.1016/0079-6786\(93\)90004-B](https://doi.org/10.1016/0079-6786(93)90004-B).
- (10) Li, P.; Duan, X.; Kuang, Y.; Li, Y.; Zhang, G.; Liu, W.; Sun, X. Tuning Electronic Structure of NiFe Layered Double Hydroxides with Vanadium Doping toward High Efficient

Electrocatalytic Water Oxidation. *Adv. Energy Mater.* **2018**, 8 (15), 1703341. <https://doi.org/10.1002/aenm.201703341>.

(11) Yang, Y.; Dang, L.; Shearer, M. J.; Sheng, H.; Li, W.; Chen, J.; Xiao, P.; Zhang, Y.; Hamers, R. J.; Jin, S. Highly Active Trimetallic NiFeCr Layered Double Hydroxide Electrocatalysts for Oxygen Evolution Reaction. *Adv. Energy Mater.* **2018**, 8 (15), 1703189. <https://doi.org/10.1002/aenm.201703189>.

(12) Diaz-Morales, O.; Ledezma-Yanez, I.; Koper, M. T. M.; Calle-Vallejo, F. Guidelines for the Rational Design of Ni-Based Double Hydroxide Electrocatalysts for the Oxygen Evolution Reaction. *ACS Catal.* **2015**, 5 (9), 5380–5387. <https://doi.org/10.1021/acscatal.5b01638>.

(13) Ng, J. W. D.; García-Melchor, M.; Bajdich, M.; Chakthranont, P.; Kirk, C.; Vojvodic, A.; Jaramillo, T. F. Gold-Supported Cerium-Doped NiOx Catalysts for Water Oxidation. *Nat Energy* **2016**, 1 (5), 16053. <https://doi.org/10.1038/nenergy.2016.53>.

(14) Seh, Z. W.; Kibsgaard, J.; Dickens, C. F.; Chorkendorff, I.; Nørskov, J. K.; Jaramillo, T. F. Combining Theory and Experiment in Electrocatalysis: Insights into Materials Design. *Science* **2017**, 355 (6321), eaad4998. <https://doi.org/10.1126/science.aad4998>.

(15) Kour, R.; Arya, S.; Verma, S.; Gupta, J.; Bandhoria, P.; Bharti, V.; Datt, R.; Gupta, V. Potential Substitutes for Replacement of Lead in Perovskite Solar Cells: A Review. *Global Challenges* **2019**, 3 (11), 1900050. <https://doi.org/10.1002/gch2.201900050>.

(16) Buttner, R. H.; Maslen, E. N. Structural Parameters and Electron Difference Density in BaTiO₃. *Acta Crystallogr B Struct Sci* **1992**, 48 (6), 764–769. <https://doi.org/10.1107/S010876819200510X>.

(17) Issa, B.; Obaidat, I.; Albiss, B.; Haik, Y. Magnetic Nanoparticles: Surface Effects and Properties Related to Biomedicine Applications. *IJMS* **2013**, 14 (11), 21266–21305. <https://doi.org/10.3390/ijms141121266>.

(18) Kim, J. S.; Kim, B.; Kim, H.; Kang, K. Recent Progress on Multimetal Oxide Catalysts for the Oxygen Evolution Reaction. *Adv. Energy Mater.* **2018**, 8 (11), 1702774. <https://doi.org/10.1002/aenm.201702774>.

(19) Zasada, F.; Gryboś, J.; Indyka, P.; Piskorz, W.; Kaczmarczyk, J.; Sojka, Z. Surface Structure and Morphology of M[CoM']O₄ (M = Mg, Zn, Fe, Co and M' = Ni, Al, Mn, Co) Spinel Nanocrystals—DFT+U and TEM Screening Investigations. *J. Phys. Chem. C* **2014**, 118 (33), 19085–19097. <https://doi.org/10.1021/jp503737p>.

(20) Wei, C.; Feng, Z.; Baisariyev, M.; Yu, L.; Zeng, L.; Wu, T.; Zhao, H.; Huang, Y.; Bedzyk, M. J.; Sritharan, T.; Xu, Z. J. Valence Change Ability and Geometrical Occupation of Substitution Cations Determine the Pseudocapacitance of Spinel Ferrite XFe₂O₄ (X = Mn, Co, Ni, Fe). *Chem. Mater.* **2016**, 28 (12), 4129–4133. <https://doi.org/10.1021/acs.chemmater.6b00713>.

(21) Lenaz, D.; Skogby, H.; Princivalle, F.; Hellenius, U. Structural Changes and Valence States in the MgCr₂O₄/FeCr₂O₄ Solid Solution Series. *Phys Chem Minerals* **2004**, 31 (9), 633–642. <https://doi.org/10.1007/s00269-004-0420-0>.

(22) Lavina, B.; Salviulo, G.; Giusta, A. D. Cation Distribution and Structure Modelling of Spinel Solid Solutions. *Physics and Chemistry of Minerals* **2002**, 29 (1), 10–18. <https://doi.org/10.1007/s002690100198>.

(23) Benício, L. P. F.; Silva, R. A.; Lopes, J. A.; Eulálio, D.; Santos, R. M. M. dos; Aquino, L. A. de; Vergütz, L.; Novais, R. F.; Costa, L. M. da; Pinto, F. G.; Tronto, J. LAYERED DOUBLE HYDROXIDES: NANOMATERIALS FOR APPLICATIONS IN AGRICULTURE. *Rev. Bras. Ciênc. Solo* **2015**, 39 (1), 1–13. <https://doi.org/10.1590/01000683rbcs2015081>.

- (24) Evans, D. G.; Slade, R. C. T. *Structural Aspects of Layered Double Hydroxides*; Springer-Verlag: Berlin/Heidelberg, 2005. https://doi.org/10.1007/430_005.
- (25) Wei, C.; Feng, Z.; Scherer, G. G.; Barber, J.; Shao-Horn, Y.; Xu, Z. J. Cations in Octahedral Sites: A Descriptor for Oxygen Electrocatalysis on Transition-Metal Spinel. *Advanced Materials* **2017**, *29* (23), 1606800.
- (26) Yang, C.; Grimaud, A. Factors Controlling the Redox Activity of Oxygen in Perovskites: From Theory to Application for Catalytic Reactions. *Catalysts* **2017**, *7* (5), 149. <https://doi.org/10.3390/catal7050149>.
- (27) Zobel, C.; Kriener, M.; Bruns, D.; Baier, J.; Grüninger, M.; Lorenz, T.; Reutler, P.; Revcolevschi, A. Evidence for a Low-Spin to Intermediate-Spin State Transition in LaCoO₃. *Phys. Rev. B* **2002**, *66* (2), 020402. <https://doi.org/10.1103/PhysRevB.66.020402>.
- (28) Radaelli, P. G.; Cheong, S.-W. Structural Phenomena Associated with the Spin-State Transition in LaCoO₃. *Phys. Rev. B* **2002**, *66* (9), 094408. <https://doi.org/10.1103/PhysRevB.66.094408>.
- (29) Liu, S. T.; Wu, Y.; Jia, Y. Q. Spin and Valence State Equilibria of Cobalt and Magnetic Properties. *6*.
- (30) Rao, C. N. R.; Parkash, O. M.; Ganguly, P. Electronic and Magnetic Properties of LaNi_{1-x}CoxO₃, LaCo_{1-x}FexO₃ and LaNi_{1-x}FexO₃. *Journal of Solid State Chemistry* **1975**, *15* (2), 186–192. [https://doi.org/10.1016/0022-4596\(75\)90245-5](https://doi.org/10.1016/0022-4596(75)90245-5).
- (31) Zhou, S.; Miao, X.; Zhao, X.; Ma, C.; Qiu, Y.; Hu, Z.; Zhao, J.; Shi, L.; Zeng, J. Engineering Electrocatalytic Activity in Nanosized Perovskite Cobaltite through Surface Spin-State Transition. *Nat Commun* **2016**, *7* (1), 11510. <https://doi.org/10.1038/ncomms11510>.
- (32) Karpinsky, D. V.; Troyanchuk, I. O.; Bärner, K.; Szymczak, H.; Tovar, M. Crystal Structure and Magnetic Ordering of the LaCo_{1-x}Fe_xO₃ System. *J. Phys.: Condens. Matter* **2005**, *17* (46), 7219–7226. <https://doi.org/10.1088/0953-8984/17/46/006>.
- (33) Grimaud, A.; Diaz-Morales, O.; Han, B.; Hong, W. T.; Lee, Y.-L.; Giordano, L.; Stoerzinger, K. A.; Koper, M. T.; Shao-Horn, Y. Activating Lattice Oxygen Redox Reactions in Metal Oxides to Catalyse Oxygen Evolution. *Nature chemistry* **2017**, *9* (5), 457.
- (34) Song, J.; Wei, C.; Huang, Z.-F.; Liu, C.; Zeng, L.; Wang, X.; Xu, Z. J. A Review on Fundamentals for Designing Oxygen Evolution Electrocatalysts. *Chem. Soc. Rev.* **2020**, *49* (7), 2196–2214. <https://doi.org/10.1039/C9CS00607A>.
- (35) Dau, H.; Limberg, C.; Reier, T.; Risch, M.; Roggan, S.; Strasser, P. The Mechanism of Water Oxidation: From Electrolysis via Homogeneous to Biological Catalysis. *ChemCatChem* **2010**, *2* (7), 724–761. <https://doi.org/10.1002/cctc.201000126>.
- (36) Fabbri, E.; Haberer, A.; Waltar, K.; Kötz, R.; Schmidt, T. J. Developments and Perspectives of Oxide-Based Catalysts for the Oxygen Evolution Reaction. *Catal. Sci. Technol.* **2014**, *4* (11), 3800–3821. <https://doi.org/10.1039/C4CY00669K>.
- (37) Wang, Q.; Domen, K. Particulate Photocatalysts for Light-Driven Water Splitting: Mechanisms, Challenges, and Design Strategies. *Chem. Rev.* **2020**, *120* (2), 919–985. <https://doi.org/10.1021/acs.chemrev.9b00201>.
- (38) Lu, Z.; Wang, H.; Kong, D.; Yan, K.; Hsu, P.-C.; Zheng, G.; Yao, H.; Liang, Z.; Sun, X.; Cui, Y. Electrochemical Tuning of Layered Lithium Transition Metal Oxides for Improvement of Oxygen Evolution Reaction. *Nat Commun* **2014**, *5* (1), 4345. <https://doi.org/10.1038/ncomms5345>.
- (39) Vojvodic, A.; Nørskov, J. K. Optimizing Perovskites for the Water-Splitting Reaction. *Science* **2011**, *334* (6061), 1355–1356. <https://doi.org/10.1126/science.1215081>.

- (40) Park, J.-H.; Cheong, S.-W.; Chen, C. T. Double-Exchange Ferromagnetism in $\text{La}(\text{Mn}_{1-x}\text{Co}_x)\text{O}_3$. *Phys. Rev. B* **1997**, *55* (17), 11072–11075. <https://doi.org/10.1103/PhysRevB.55.11072>.
- (41) Zhou, Y.; Sun, S.; Xi, S.; Duan, Y.; Sritharan, T.; Du, Y.; Xu, Z. J. Superexchange Effects on Oxygen Reduction Activity of Edge-Sharing $[\text{Co}_x\text{Mn}_{1-x}\text{O}_6]$ Octahedra in Spinel Oxide. *Adv. Mater.* **2018**, *30* (11), 1705407. <https://doi.org/10.1002/adma.201705407>.
- (42) Kaufman, G. B. Inorganic Chemistry: Principles of Structure and Reactivity, 4th Ed. (Huheey, James E.; Keiter, Ellen A.; Keiter, Richard L.). *J. Chem. Educ.* **1993**, *70* (10), A279. <https://doi.org/10.1021/ed070pA279.1>.
- (43) Han, B.; Risch, M.; Lee, Y.-L.; Ling, C.; Jia, H.; Shao-Horn, Y. Activity and Stability Trends of Perovskite Oxides for Oxygen Evolution Catalysis at Neutral PH. *Phys. Chem. Chem. Phys.* **2015**, *17* (35), 22576–22580. <https://doi.org/10.1039/C5CP04248H>.
- (44) Lee, H. Y.; Goodenou, J. B. Sr- and Ni-Doped LaCoO_3 and LaFeO_3 Perovskites. 8.
- (45) Mefford, J. T.; Rong, X.; Abakumov, A. M.; Hardin, W. G.; Dai, S.; Kolpak, A. M.; Johnston, K. P.; Stevenson, K. J. Water Electrolysis on $\text{La}_{1-x}\text{Sr}_x\text{CoO}_{3-\delta}$ Perovskite Electrocatalysts. *Nature communications* **2016**, *7*, 11053.
- (46) Hong, W. T.; Risch, M.; Stoerzinger, K. A.; Grimaud, A.; Suntivich, J.; Shao-Horn, Y. Toward the Rational Design of Non-Precious Transition Metal Oxides for Oxygen Electrocatalysis. *Energy Environ. Sci.* **2015**, *8* (5), 1404–1427. <https://doi.org/10.1039/C4EE03869J>.
- (47) Cheng, X.; Fabbri, E.; Nachtegaal, M.; Castelli, I. E.; El Kazzi, M.; Haumont, R.; Marzari, N.; Schmidt, T. J. Oxygen Evolution Reaction on $\text{La}_{1-x}\text{Sr}_x\text{CoO}_3$ Perovskites: A Combined Experimental and Theoretical Study of Their Structural, Electronic, and Electrochemical Properties. *Chem. Mater.* **2015**, *27* (22), 7662–7672. <https://doi.org/10.1021/acs.chemmater.5b03138>.
- (48) Grimaud, A.; Diaz-Morales, O.; Han, B.; Hong, W. T.; Lee, Y.-L.; Giordano, L.; Stoerzinger, K. A.; Koper, M. T. M.; Shao-Horn, Y. Activating Lattice Oxygen Redox Reactions in Metal Oxides to Catalyse Oxygen Evolution. *Nature Chem* **2017**, *9* (5), 457–465. <https://doi.org/10.1038/nchem.2695>.
- (49) Grimaud, A.; Hong, W. T.; Shao-Horn, Y.; Tarascon, J.-M. Anionic Redox Processes for Electrochemical Devices. *Nature Mater* **2016**, *15* (2), 121–126. <https://doi.org/10.1038/nmat4551>.
- (50) Grimaud, A.; May, K. J.; Carlton, C. E.; Lee, Y.-L.; Risch, M.; Hong, W. T.; Zhou, J.; Shao-Horn, Y. Double Perovskites as a Family of Highly Active Catalysts for Oxygen Evolution in Alkaline Solution. *Nature communications* **2013**, *4*, 2439.
- (51) May, K. J.; Carlton, C. E.; Stoerzinger, K. A.; Risch, M.; Suntivich, J.; Lee, Y.-L.; Grimaud, A.; Shao-Horn, Y. Influence of Oxygen Evolution during Water Oxidation on the Surface of Perovskite Oxide Catalysts. *The journal of physical chemistry letters* **2012**, *3* (22), 3264–3270.
- (52) Fabbri, E.; Nachtegaal, M.; Binniger, T.; Cheng, X.; Kim, B.-J.; Durst, J.; Bozza, F.; Graule, T.; Schäublin, R.; Wiles, L. Dynamic Surface Self-Reconstruction Is the Key of Highly Active Perovskite Nano-Electrocatalysts for Water Splitting. *Nature materials* **2017**, *16* (9), 925.
- (53) Lee, Y.-L.; Kleis, J.; Rossmeisl, J.; Shao-Horn, Y.; Morgan, D. Prediction of Solid Oxide Fuel Cell Cathode Activity with First-Principles Descriptors. *Energy Environ. Sci.* **2011**, *4* (10), 3966. <https://doi.org/10.1039/c1ee02032c>.

- (54) Suntivich, J.; Gasteiger, H. A.; Yabuuchi, N.; Nakanishi, H.; Goodenough, J. B.; Shao-Horn, Y. Design Principles for Oxygen-Reduction Activity on Perovskite Oxide Catalysts for Fuel Cells and Metal–Air Batteries. *Nature Chem* **2011**, *3* (7), 546–550. <https://doi.org/10.1038/nchem.1069>.
- (55) Yang, C.; Batuk, M.; Jacquet, Q.; Rousse, G.; Yin, W.; Zhang, L.; Hadermann, J.; Abakumov, A. M.; Cibir, G.; Chadwick, A. Revealing PH-Dependent Activities and Surface Instabilities for Ni-Based Electrocatalysts during the Oxygen Evolution Reaction. *ACS Energy Letters* **2018**, *3* (12), 2884–2890.
- (56) Trześniewski, B. J.; Diaz-Morales, O.; Vermaas, D. A.; Longo, A.; Bras, W.; Koper, M. T. M.; Smith, W. A. In Situ Observation of Active Oxygen Species in Fe-Containing Ni-Based Oxygen Evolution Catalysts: The Effect of PH on Electrochemical Activity. *J. Am. Chem. Soc.* **2015**, *137* (48), 15112–15121. <https://doi.org/10.1021/jacs.5b06814>.
- (57) Diaz-Morales, O.; Ferrus-Suspedra, D.; Koper, M. T. M. The Importance of Nickel Oxyhydroxide Deprotonation on Its Activity towards Electrochemical Water Oxidation. *Chem. Sci.* **2016**, *7* (4), 2639–2645. <https://doi.org/10.1039/C5SC04486C>.
- (58) Bockris, J. O.; Otagawa, T. Mechanism of Oxygen Evolution on Perovskites. *The Journal of Physical Chemistry* **2002**, *87* (15), 2960–2971.
- (59) Shinagawa, T.; Takanabe, K. New Insight into the Hydrogen Evolution Reaction under Buffered Near-Neutral PH Conditions: Enthalpy and Entropy of Activation. *J. Phys. Chem. C* **2016**, *120* (42), 24187–24196. <https://doi.org/10.1021/acs.jpcc.6b07954>.
- (60) Royer, S.; Duprez, D.; Can, F.; Courtois, X.; Batiot-Dupeyrat, C.; Laassiri, S.; Alamdari, H. Perovskites as Substitutes of Noble Metals for Heterogeneous Catalysis: Dream or Reality. *Chem. Rev.* **2014**, *114* (20), 10292–10368. <https://doi.org/10.1021/cr500032a>.
- (61) Li, N.; Bediako, D. K.; Hadt, R. G.; Hayes, D.; Kempa, T. J.; von Cube, F.; Bell, D. C.; Chen, L. X.; Nocera, D. G. Influence of Iron Doping on Tetravalent Nickel Content in Catalytic Oxygen Evolving Films. *Proc Natl Acad Sci USA* **2017**, *114* (7), 1486–1491. <https://doi.org/10.1073/pnas.1620787114>.
- (62) Zhao, Q.; Yan, Z.; Chen, C.; Chen, J. Spinels: Controlled Preparation, Oxygen Reduction/Evolution Reaction Application, and Beyond. *Chem. Rev.* **2017**, *117* (15), 10121–10211. <https://doi.org/10.1021/acs.chemrev.7b00051>.
- (63) Katsounaros, I.; Cherevko, S.; Zeradjanin, A. R.; Mayrhofer, K. J. J. Oxygen Electrochemistry as a Cornerstone for Sustainable Energy Conversion. *Angew. Chem. Int. Ed.* **2014**, *53* (1), 102–121. <https://doi.org/10.1002/anie.201306588>.
- (64) Kötz, R.; Stucki, S. Stabilization of RuO₂ by IrO₂ for Anodic Oxygen Evolution in Acid Media. *Electrochimica Acta* **1986**, *31* (10), 1311–1316. [https://doi.org/10.1016/0013-4686\(86\)80153-0](https://doi.org/10.1016/0013-4686(86)80153-0).
- (65) Yang, F.; Sliozberg, K.; Sinev, I.; Antoni, H.; Bähr, A.; Ollegott, K.; Xia, W.; Masa, J.; Grünert, W.; Cuenya, B. R.; Schuhmann, W.; Muhler, M. Synergistic Effect of Cobalt and Iron in Layered Double Hydroxide Catalysts for the Oxygen Evolution Reaction. *ChemSusChem* **2017**, *10* (1), 156–165. <https://doi.org/10.1002/cssc.201601272>.
- (66) Xiao, C.; Lu, X.; Zhao, C. Unusual Synergistic Effects upon Incorporation of Fe and/or Ni into Mesoporous Co₃O₄ for Enhanced Oxygen Evolution. *Chem. Commun.* **2014**, *50* (70), 10122. <https://doi.org/10.1039/C4CC04922E>.
- (67) Fidelsky, V.; Toroker, M. C. The Secret behind the Success of Doping Nickel Oxyhydroxide with Iron. *Phys. Chem. Chem. Phys.* **2017**, *19* (11), 7491–7497. <https://doi.org/10.1039/C6CP08590C>.

- (68) Yuan, C.; Wu, H. B.; Xie, Y.; Lou, X. W. D. Mixed Transition-Metal Oxides: Design, Synthesis, and Energy-Related Applications. *Angew. Chem. Int. Ed.* **2014**, *53* (6), 1488–1504. <https://doi.org/10.1002/anie.201303971>.
- (69) Hamdani, M.; Singh, R. N.; Chartier, P. Co₃O₄ and Co- Based Spinel Oxides Bifunctional Oxygen Electrodes. *Int. J. Electrochem. Sci.* **2010**, *5*, 22.
- (70) Hu, L.; Wu, L.; Liao, M.; Hu, X.; Fang, X. Electrical Transport Properties of Large, Individual NiCo₂O₄ Nanoplates. *Adv. Funct. Mater.* **2012**, *22* (5), 998–1004. <https://doi.org/10.1002/adfm.201102155>.
- (71) Zhu, K.; Wu, T.; Zhu, Y.; Li, X.; Li, M.; Lu, R.; Wang, J.; Zhu, X.; Yang, W. Layered Fe-Substituted LiNiO₂ Electrocatalysts for High-Efficiency Oxygen Evolution Reaction. *ACS Energy Lett.* **2017**, *2* (7), 1654–1660. <https://doi.org/10.1021/acsenergylett.7b00434>.
- (72) Grewe, T.; Deng, X.; Tüysüz, H. Influence of Fe Doping on Structure and Water Oxidation Activity of Nanocast Co₃O₄. *Chem. Mater.* **2014**, *26* (10), 3162–3168. <https://doi.org/10.1021/cm5005888>.
- (73) Hardin, W. G.; Mefford, J. T.; Slanac, D. A.; Patel, B. B.; Wang, X.; Dai, S.; Zhao, X.; Ruoff, R. S.; Johnston, K. P.; Stevenson, K. J. Tuning the Electrocatalytic Activity of Perovskites through Active Site Variation and Support Interactions. *Chem. Mater.* **2014**, *26* (11), 3368–3376. <https://doi.org/10.1021/cm403785q>.
- (74) Görlin, M.; Chernev, P.; Ferreira de Araújo, J.; Reier, T.; Dresch, S.; Paul, B.; Krähnert, R.; Dau, H.; Strasser, P. Oxygen Evolution Reaction Dynamics, Faradaic Charge Efficiency, and the Active Metal Redox States of Ni–Fe Oxide Water Splitting Electrocatalysts. *J. Am. Chem. Soc.* **2016**, *138* (17), 5603–5614. <https://doi.org/10.1021/jacs.6b00332>.
- (75) Elbaz, Y.; Caspary Toroker, M. Dual Mechanisms: Hydrogen Transfer during Water Oxidation Catalysis of Pure and Fe-Doped Nickel Oxyhydroxide. *J. Phys. Chem. C* **2017**, *121* (31), 16819–16824. <https://doi.org/10.1021/acs.jpcc.7b04142>.
- (76) Swierk, J. R.; Klaus, S.; Trotochaud, L.; Bell, A. T.; Tilley, T. D. Electrochemical Study of the Energetics of the Oxygen Evolution Reaction at Nickel Iron (Oxy)Hydroxide Catalysts. *J. Phys. Chem. C* **2015**, *119* (33), 19022–19029. <https://doi.org/10.1021/acs.jpcc.5b05861>.
- (77) Abreu-Sepulveda, M. A.; Dhital, C.; Huq, A.; Li, L.; Bridges, C. A.; Paranthaman, M. P.; Narayanan, S. R.; Quesnel, D. J.; Tryk, D. A.; Manivannan, A. The Influence of Fe Substitution in Lanthanum Calcium Cobalt Oxide on the Oxygen Evolution Reaction in Alkaline Media. *J. Electrochem. Soc.* **2016**, *163* (9), F1124–F1132. <https://doi.org/10.1149/2.1311609jes>.
- (78) Zhou, Y.; Sun, S.; Song, J.; Xi, S.; Chen, B.; Du, Y.; Fisher, A. C.; Cheng, F.; Wang, X.; Zhang, H.; Xu, Z. J. Enlarged Co–O Covalency in Octahedral Sites Leading to Highly Efficient Spinel Oxides for Oxygen Evolution Reaction. *Adv. Mater.* **2018**, *30* (32), 1802912. <https://doi.org/10.1002/adma.201802912>.
- (79) Zhu, Y.; Zhou, W.; Chen, Y.; Yu, J.; Liu, M.; Shao, Z. A High-Performance Electrocatalyst for Oxygen Evolution Reaction: LiCo_{0.8}Fe_{0.2}O₂. *Adv. Mater.* **2015**, *27* (44), 7150–7155. <https://doi.org/10.1002/adma.201503532>.
- (80) Zhang, C.; Berlinguette, C. P.; Trudel, S. Water Oxidation Catalysis: An Amorphous Quaternary Ba-Sr-Co-Fe Oxide as a Promising Electrocatalyst for the Oxygen-Evolution Reaction. *Chem. Commun.* **2016**, *52* (7), 1513–1516. <https://doi.org/10.1039/C5CC09361A>.
- (81) Jin, H.; Mao, S.; Zhan, G.; Xu, F.; Bao, X.; Wang, Y. Fe Incorporated α -Co(OH)₂ Nanosheets with Remarkably Improved Activity towards the Oxygen Evolution Reaction. *J. Mater. Chem. A* **2017**, *5* (3), 1078–1084. <https://doi.org/10.1039/C6TA09959A>.

- (82) Butera, V.; Caspary Toroker, M. Electronic Properties of Pure and Fe-Doped β -Ni(OH)₂: New Insights Using Density Functional Theory with a Cluster Approach. *J. Phys. Chem. C* **2016**, *120* (23), 12344–12350. <https://doi.org/10.1021/acs.jpcc.6b01501>.
- (83) Zheng, X.; Zhang, B.; De Luna, P.; Liang, Y.; Comin, R.; Voznyy, O.; Han, L.; García de Arquer, F. P.; Liu, M.; Dinh, C. T.; Regier, T.; Dynes, J. J.; He, S.; Xin, H. L.; Peng, H.; Prendergast, D.; Du, X.; Sargent, E. H. Theory-Driven Design of High-Valence Metal Sites for Water Oxidation Confirmed Using in Situ Soft X-Ray Absorption. *Nature Chem* **2018**, *10* (2), 149–154. <https://doi.org/10.1038/nchem.2886>.
- (84) Görlin, M.; Ferreira de Araújo, J.; Schmies, H.; Bernsmeier, D.; Dresch, S.; Glied, M.; Jusys, Z.; Chernev, P.; Kraehnert, R.; Dau, H.; Strasser, P. Tracking Catalyst Redox States and Reaction Dynamics in Ni–Fe Oxyhydroxide Oxygen Evolution Reaction Electrocatalysts: The Role of Catalyst Support and Electrolyte pH. *J. Am. Chem. Soc.* **2017**, *139* (5), 2070–2082. <https://doi.org/10.1021/jacs.6b12250>.
- (85) Goldsmith, Z. K.; Harshan, A. K.; Gerken, J. B.; Vörös, M.; Galli, G.; Stahl, S. S.; Hammes-Schiffer, S. Characterization of NiFe Oxyhydroxide Electrocatalysts by Integrated Electronic Structure Calculations and Spectroelectrochemistry. *Proc Natl Acad Sci USA* **2017**, *114* (12), 3050–3055. <https://doi.org/10.1073/pnas.1702081114>.
- (86) Chen, J. Y. C.; Dang, L.; Liang, H.; Bi, W.; Gerken, J. B.; Jin, S.; Alp, E. E.; Stahl, S. S. Operando Analysis of NiFe and Fe Oxyhydroxide Electrocatalysts for Water Oxidation: Detection of Fe⁴⁺ by Mössbauer Spectroscopy. *J. Am. Chem. Soc.* **2015**, *137* (48), 15090–15093. <https://doi.org/10.1021/jacs.5b10699>.
- (87) Trotochaud, L.; Ranney, J. K.; Williams, K. N.; Boettcher, S. W. Solution-Cast Metal Oxide Thin Film Electrocatalysts for Oxygen Evolution. *J. Am. Chem. Soc.* **2012**, *134* (41), 17253–17261. <https://doi.org/10.1021/ja307507a>.
- (88) Gong, L.; Chng, X. Y. E.; Du, Y.; Xi, S.; Yeo, B. S. Enhanced Catalysis of the Electrochemical Oxygen Evolution Reaction by Iron(III) Ions Adsorbed on Amorphous Cobalt Oxide. *ACS Catal.* **2018**, *8* (2), 807–814. <https://doi.org/10.1021/acscatal.7b03509>.
- (89) Li, Y.-F.; Selloni, A. Mechanism and Activity of Water Oxidation on Selected Surfaces of Pure and Fe-Doped NiO_x. *ACS Catal.* **2014**, *4* (4), 1148–1153. <https://doi.org/10.1021/cs401245q>.
- (90) Landon, J.; Demeter, E.; İnoğlu, N.; Keturakis, C.; Wachs, I. E.; Vasić, R.; Frenkel, A. I.; Kitchin, J. R. Spectroscopic Characterization of Mixed Fe–Ni Oxide Electrocatalysts for the Oxygen Evolution Reaction in Alkaline Electrolytes. *ACS Catal.* **2012**, *2* (8), 1793–1801. <https://doi.org/10.1021/cs3002644>.
- (91) Burke, M. S.; Kast, M. G.; Trotochaud, L.; Smith, A. M.; Boettcher, S. W. Cobalt–Iron (Oxy)Hydroxide Oxygen Evolution Electrocatalysts: The Role of Structure and Composition on Activity, Stability, and Mechanism. *J. Am. Chem. Soc.* **2015**, *137* (10), 3638–3648. <https://doi.org/10.1021/jacs.5b00281>.
- (92) Trotochaud, L.; Young, S. L.; Ranney, J. K.; Boettcher, S. W. Nickel–Iron Oxyhydroxide Oxygen-Evolution Electrocatalysts: The Role of Intentional and Incidental Iron Incorporation. *J. Am. Chem. Soc.* **2014**, *136* (18), 6744–6753. <https://doi.org/10.1021/ja502379c>.
- (93) Wang, H.-Y.; Hung, S.-F.; Chen, H.-Y.; Chan, T.-S.; Chen, H. M.; Liu, B. In Operando Identification of Geometrical-Site-Dependent Water Oxidation Activity of Spinel Co₃O₄. *J. Am. Chem. Soc.* **2016**, *138* (1), 36–39. <https://doi.org/10.1021/jacs.5b10525>.

- (94) Szotek, Z.; Temmerman, W. M.; Ködderitzsch, D.; Svane, A.; Petit, L.; Winter, H. Electronic Structures of Normal and Inverse Spinel Ferrites from First Principles. *Phys. Rev. B* **2006**, *74* (17), 174431. <https://doi.org/10.1103/PhysRevB.74.174431>.
- (95) Corrigan, D. A. The Catalysis of the Oxygen Evolution Reaction by Iron Impurities in Thin Film Nickel Oxide Electrodes. *J. Electrochem. Soc.* **1987**, *134* (2), 377. <https://doi.org/10.1149/1.2100463>.
- (96) Potvin, E.; Brossard, L. Electrocatalytic Activity of Ni-Fe Anodes for Alkaline Water Electrolysis. *Materials Chemistry and Physics* **1992**, *31* (4), 311–318. [https://doi.org/10.1016/0254-0584\(92\)90192-B](https://doi.org/10.1016/0254-0584(92)90192-B).
- (97) Burke, M. S.; Zou, S.; Enman, L. J.; Kellon, J. E.; Gabor, C. A.; Pledger, E.; Boettcher, S. W. Revised Oxygen Evolution Reaction Activity Trends for First-Row Transition-Metal (Oxy)Hydroxides in Alkaline Media. *J. Phys. Chem. Lett.* **2015**, *6* (18), 3737–3742. <https://doi.org/10.1021/acs.jpcclett.5b01650>.
- (98) Friebel, D.; Louie, M. W.; Bajdich, M.; Sanwald, K. E.; Cai, Y.; Wise, A. M.; Cheng, M.-J.; Sokaras, D.; Weng, T.-C.; Alonso-Mori, R.; Davis, R. C.; Bargar, J. R.; Nørskov, J. K.; Nilsson, A.; Bell, A. T. Identification of Highly Active Fe Sites in (Ni,Fe)OOH for Electrocatalytic Water Splitting. *J. Am. Chem. Soc.* **2015**, *137* (3), 1305–1313. <https://doi.org/10.1021/ja511559d>.
- (99) Enman, L. J.; Burke, M. S.; Batchellor, A. S.; Boettcher, S. W. Effects of Intentionally Incorporated Metal Cations on the Oxygen Evolution Electrocatalytic Activity of Nickel (Oxy)Hydroxide in Alkaline Media. *ACS Catal.* **2016**, *6* (4), 2416–2423. <https://doi.org/10.1021/acscatal.5b02924>.
- (100) Kuo, D.-Y.; Kawasaki, J. K.; Nelson, J. N.; Kloppenburg, J.; Hautier, G.; Shen, K. M.; Schlom, D. G.; Suntivich, J. Influence of Surface Adsorption on the Oxygen Evolution Reaction on IrO₂ (110). *Journal of the American chemical society* **2017**, *139* (9), 3473–3479.
- (101) Garcia, A. C.; Touzalin, T.; Nieuwland, C.; Perini, N.; Koper, M. T. M. Enhancement of Oxygen Evolution Activity of Nickel Oxyhydroxide by Electrolyte Alkali Cations. *Angew. Chem. Int. Ed.* **2019**, *58*, 5.
- (102) Garcia, A. C.; Touzalin, T.; Nieuwland, C.; Perini, N.; Koper, M. T. M. Enhancement of Oxygen Evolution Activity of NiOOH by Electrolyte Alkali Cations. *Angew. Chem. Int. Ed.* **2019**. <https://doi.org/10.1002/anie.201905501>.
- (103) Michael, J. D.; Demeter, E. L.; Illes, S. M.; Fan, Q.; Boes, J. R.; Kitchin, J. R. Alkaline Electrolyte and Fe Impurity Effects on the Performance and Active-Phase Structure of NiOOH Thin Films for OER Catalysis Applications. *The Journal of Physical Chemistry C* **2015**, *119* (21), 11475–11481.
- (104) Zhang, R.; Pearce, P. E.; Duan, Y.; Dubouis, N.; Marchandier, T.; Grimaud, A. The Importance of Water Structure and Catalyst-Electrolyte Interface on the Design of Water Splitting Catalysts. *Chem. Mater.* **2019**, *31*, acs.chemmater.9b02318. <https://doi.org/10.1021/acs.chemmater.9b02318>.

Chapter 3

Experimental Methodology

In this chapter, the preparation methods for Co based transition metal oxides / hydroxides studied in this thesis as OER catalysts have been demonstrated. The working principles for the characterization techniques utilized in this thesis are explained and the reasons for their usage are stated. The setups for electrochemical studies have been illustrated. The data analysis techniques have been explained.

3.1 Material synthesis

3.1.1 Sol gel methods

A sol gel method has been adopted in Chapter 4 of the thesis for the synthesis of $\text{LaCo}_{1-x}\text{Fe}_x\text{O}_3$.

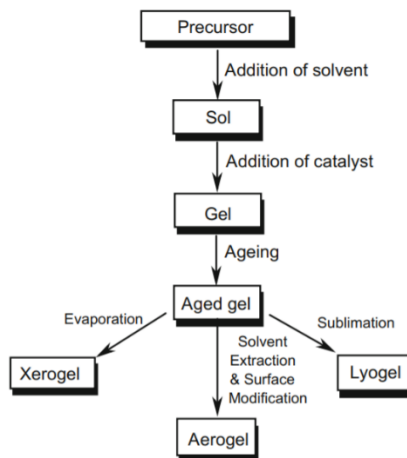


Figure 3.1 Sol-gel methods for synthesis. This figure is adapted from Ref 1.

In a sol-gel method, the inorganic metal salts and some organic compounds are dissolved for the preparation of a liquid “sol”. In this process, a hydrolysis process is included. Then, this “sol” is converted into a solid “gel” by heating. A condensation process takes place. Further sintering is needed for the crystallization of the powders.²

$\text{LaCo}_{1-x}\text{Fe}_x\text{O}_3$ powders were synthesized by a sol-gel method.² The LaCoO_3 precursors were produced by dissolving 3.75 mmol $\text{La}(\text{NO}_3)_3 \cdot 6\text{H}_2\text{O}$, 3.75 mmol $\text{Co}(\text{OAc})_2 \cdot 6\text{H}_2\text{O}$, 15 mmol urea, and 15 mmol citric acid in 30mL de-ionized (DI) water and 3 mL nitric acid. As for $\text{LaCo}_{1-x}\text{Fe}_x\text{O}_3$, $\text{Fe}(\text{NO}_3)_3 \cdot 9\text{H}_2\text{O}$ and $\text{Co}(\text{OAc})_2 \cdot 6\text{H}_2\text{O}$ were added stoichiometrically for Fe to partially substitute Co. LaFeO_3 precursor was prepared by using 3.75 mmol $\text{Fe}(\text{NO}_3)_3 \cdot 9\text{H}_2\text{O}$ instead of $\text{Co}(\text{OAc})_2 \cdot 6\text{H}_2\text{O}$. The solutions were then heated to 80 °C and stirred with a magnetic stirrer till a gel is generated. The gel was then dried at 170 °C for 12 h to remove the remaining water followed by calcination at 600 °C for 6 hours for crystallization.

3.1.2 Thermal decomposition methods

A thermal decomposition method has been employed for the synthesis of $\text{ZnCo}_{2-x}\text{Ni}_x\text{O}_4$ in Chapter 5 of the thesis.³ In a thermal decomposition process, a compound splits up into simpler substances under heat treatments.⁴

$\text{ZnCo}_{2-x}\text{Ni}_x\text{O}_4$ powders were synthesized by a thermal decomposition method.³ The ZnCo_2O_4 precursors were produced by dissolving 5 mmol $\text{Zn}(\text{OAc})_2 \cdot 2\text{H}_2\text{O}$ and 10 mmol $\text{Co}(\text{NO}_3)_2 \cdot 6\text{H}_2\text{O}$ in 30 mL de-ionized (DI) water and 3 mL nitric acid. As for $\text{ZnCo}_{2-x}\text{Ni}_x\text{O}_4$, $\text{Ni}(\text{NO}_3)_2 \cdot 6\text{H}_2\text{O}$ and $\text{Co}(\text{OAc})_2 \cdot 6\text{H}_2\text{O}$ were added stoichiometrically for Ni to substitute Co. The solutions were then heated and stirred with a magnetic stirrer to obtain a colorless solution. Then the solution was dried at 170 °C for 12 h to remove the remaining water followed by calcination at 300 °C for 6 hours for crystallization. The value of x was varied from 0, 0.2, 0.4, 0.6 to 0.8. When $\text{Ni}(\text{NO}_3)_2 \cdot 6\text{H}_2\text{O}$ and $\text{Co}(\text{OAc})_2 \cdot 6\text{H}_2\text{O}$ ($x=1$) were added in an equimolar fashion, a structure with a mixture of spinel phases, NiO and ZnO phases began to form. When no $\text{Co}(\text{OAc})_2 \cdot 6\text{H}_2\text{O}$ was used and only $\text{Ni}(\text{NO}_3)_2 \cdot 6\text{H}_2\text{O}$ was dissolved, a mixture of NiO and ZnO was formed instead of ZnNi_2O_4 , which was in accordance with the reports that ZnNi_2O_4 has yet to be synthesized.⁴

3.1.3 Solid state synthesis

LaCoO_3 , $\text{La}_{0.8}\text{Sr}_{0.2}\text{CoO}_3$, $\text{La}_{0.6}\text{Sr}_{0.4}\text{CoO}_3$ and $\text{La}_{0.5}\text{Sr}_{0.5}\text{CoO}_3$ were synthesized by a solid-state methods in the Chapter 6 of the thesis.⁵ The metal oxides with the needed element are mixed and grounded, then sintered at high temperature.

Perovskites LaCoO_3 , $\text{La}_{0.8}\text{Sr}_{0.2}\text{CoO}_3$, $\text{La}_{0.6}\text{Sr}_{0.4}\text{CoO}_3$ and $\text{La}_{0.5}\text{Sr}_{0.5}\text{CoO}_3$ were synthesized by conventional solid-state route. Stoichiometric amounts of La_2O_3 , SrCO_3 , Co_3O_4 previously dehydrated were thoroughly ground, pressed into pellets and annealed in air at 950 °C for 12 h. $\text{La}_{0.8}\text{Sr}_{0.2}\text{CoO}_3$, $\text{La}_{0.6}\text{Sr}_{0.4}\text{CoO}_3$ and $\text{La}_{0.5}\text{Sr}_{0.5}\text{CoO}_3$ were ground and annealed for a second time in air at 950 °C for another 12 h and slowly cooled down to room temperature.⁵

3.1.4 Electrodeposition methods

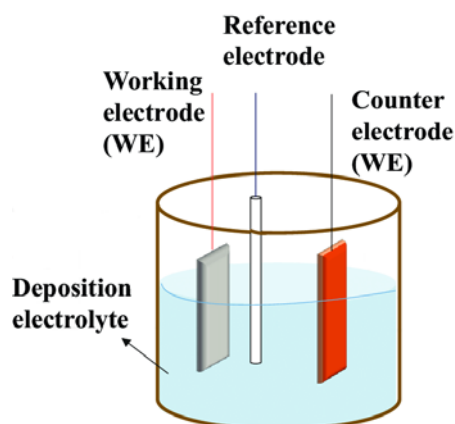


Figure 3.2 The electrochemical setup for electrodeposition.

For the cathodic electrodeposition of $\text{Co}(\text{OH})_2$ and $\text{Fe}_{0.5}\text{Co}_{0.5}(\text{OH})_2$ films in Chapter 6, glassy carbon electrode or graphite paper are used as working electrodes. Platinum plate is used as counter electrode. A saturated calomel electrode (SCE) is used as reference electrode. An illustration is shown in Figure 3.2.⁶

Prior to the film deposition, the glassy carbon inserts for the rotating disk electrodes were cleaned by cycling 10 times in alkaline solution within a potential range of 1.1-1.7 V vs. RHE. Prior to the electrochemical deposition, the electrodes were polished and ultrasonically washed with ethanol and $18.2 \text{ M}\Omega\cdot\text{cm}$ water. Films of $\text{Co}(\text{OH})_2$ were cathodically deposited in an argon saturated 10mM $\text{Co}(\text{NO}_3)_2$ solution at a current density of $50 \mu\text{A cm}^{-2}$ for 600 s. After deposition, films were rinsed by dipping in deionized water ($18.2 \text{ M}\Omega\cdot\text{cm}$). Prior to the OER measurements, the as-deposited electrodes were first cycled in “Fe-free” alkaline solution at 100 mV s^{-1} within a potential range of 1.1-1.7 V vs. RHE for 20 cycles for conditioning. Films of $\text{Fe}_{0.5}\text{Co}_{0.5}(\text{OH})_2$ were cathodically deposited in an argon saturated 6mM $\text{Co}(\text{NO}_3)_2$ + 4 mM FeCl_2 solution at a current density of $50 \mu\text{A cm}^{-2}$ for 600 s. After deposition, films were rinsed by dipping in deionized water ($18.2 \text{ M}\Omega\cdot\text{cm}$).⁶

3.2 Characterization

3.2.1 Electrochemical Characterization

3.2.1.1 Three electrode testing

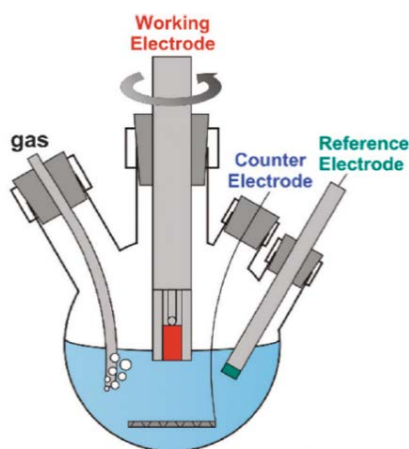


Figure 3.3 Experimental setup for the three-electrode cell. This figure is adapted from Ref 7.

The electrochemical tests were carried out by three-electrode method (Figure 3.3) with glassy carbon electrode as working electrode, SCE and Pt plate (1 cm × 3 cm) serving as reference and counter electrodes, respectively. 10 mg materials and 2 mg carbon black were dispersed in a 2mL mixed solution of Tetrahydrofuran (THF) and 65 μL Nafion perfluorinated 5% solution and DI water were added to prepare the catalyst ink. The mass ratio of material: carbon black was maintained at 4: 1. The mixture was sonicated for 40 mins to achieve homogenized dispersion of materials and carbon. 10 μL of the ink was dropped onto a newly polished rotating disk electrode (RDE). The catalysts decorated rotating disk electrode was characterized in a three-electrode one-compartment cell, in which the SCE and Pt wire were used as reference and counter electrode, respectively. All electrochemical potentials herein are reported against the reversible hydrogen electrode (RHE) in 1.0 M KOH. The conversion between potentials vs. SCE and vs. RHE was performed by the equation below.

$$E (\text{vs. RHE}) / \text{V} = E (\text{vs. SCE}) / \text{V} + E_{\text{SCE}} (\text{vs. SHE}) / \text{V} + 0.059 \times \text{pH} / \text{V}$$

$$(E_{\text{SCE}} (\text{reference}) / \text{V} = 0.2438 / \text{V vs. SHE at } 25^{\circ}\text{C})$$

For long term test in alkaline solution, a Hg/HgO reference electrode is employed.

$$E \text{ (vs. RHE)} / \text{V} = E \text{ (vs. Hg/HgO)} / \text{V} + E_{\text{Hg/HgO}} \text{ (vs. SHE)} / \text{V} + 0.059 \times \text{pH} / \text{V}$$

$$(E_{\text{Hg/HgO}} \text{ (vs. SHE)} / \text{V} = 0.098 / \text{V vs. SHE at } 25^\circ\text{C})$$

The oxygen evolution reaction was evaluated by cyclic voltammetry (CV) at a scan rate of 10 mV s⁻¹ at 1600 rpm.

3.2.1.2 Cyclic Voltammetry (CV)

During a CV measurement, the potential between the reference electrode and the working electrode is swept back and forth in between two potentials. The current at the working electrode is recorded.⁸ CV measurements have been employed in Chapter 4, 5 and 6 to study the activity of the catalysts. Tafel plot has been derived from the obtained CV curves for the understanding of the reaction path.

3.2.1.3 Electrochemically active surface area (ECSA)

The ECSA gives an estimation of the real surface area involved in electrochemical processes. It can be calculated by the follows⁹:

$$\text{ECSA} = C_{\text{DL}}/C_{\text{S}}$$

$$C_{\text{DL}} = i_{\text{DL}}/v$$

where i_{DL} indicates the capacitive current, v represents the scan rate, C_{DL} is the specific capacitance of the electrode double layer. C_{S} is the specific capacitance; it has a value of 60 $\mu\text{F cm}^{-2}$ for most oxides.

In Chapter 5, the ECSA of the $\text{ZnCo}_{1.2}\text{Ni}_{0.8}\text{O}_4$ were measured before, during and after stability tests to quantify the degradation properties of the catalysts.

3.2.1.4 Electrochemical impedance spectroscopy (EIS)

EIS is a method of impedimetric transduction involving the application of a sinusoidal electrochemical perturbation over a wide range of frequencies when measuring a sample.⁹ The

Ohmic drop has been determined from a Nyquist plot by EIS in this thesis. The Ohmic resistance is obtained as the real part of the impedance when the imaginary part is zero.

3.2.1.5 Chronoamperometry (CA)

During a CA measurement, the potential between the working electrode and the reference electrode is fixed and the current at the working electrode is measured over time. CA measurement has been used in Chapter 5 to measure the OER activity of the catalysts for the long term.

3.2.1.6 Chronopotentiometry (CP)

During a CP measurement, the current at the working electrode is fixed and the potential between the working electrode and the reference electrode is measured over time. CP measurement has been employed in Chapter 5 to measure the OER stability of the catalysts.

3.2.2 Structural Characterization

3.2.2.1 X-ray diffraction (XRD)

X-ray diffraction is employed to investigate the crystal structure of matter. The arrangement of atoms defines the crystal structure. Each crystalline solid has unique characteristic X-ray diffraction patterns. To understand how XRD instrument works, Bragg's Law needs to be introduced first.

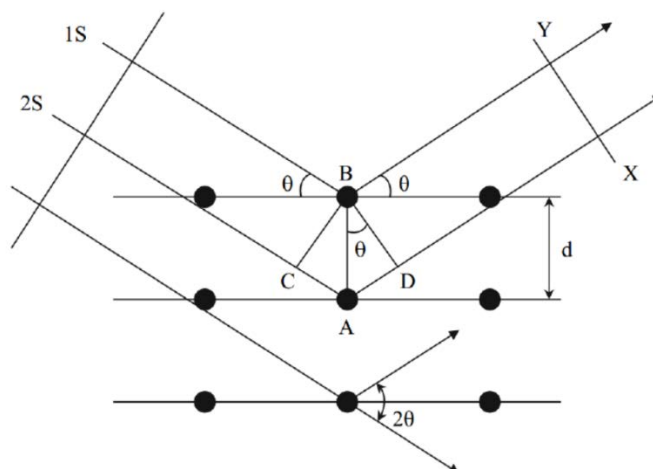


Figure 3.4 Scheme of X-ray Diffraction. This figure is adapted from Ref 10.

As a crystal is irradiated with X-rays of a fixed wavelength at certain incident angle, an intensified reflected X-rays can only be detected when the interference is a constructive one. Specifically, constructive interference means that the difference in phase between the parallel x-rays (two light orange lines in Figure 3.4) must be equal to integer multiples of the X-ray wavelength. The relation between the angle of incidence, wavelength of the incident X-rays as well as spacing distance between the crystal lattice planes fulfilling the constructive interference described is Bragg's Law can be expressed as an equation¹¹:

$$n\lambda = 2d\sin(\theta)$$

A powder X-ray diffractometer is designed to collecting the signals which happen to be oriented at the correct angle to fulfil the Bragg condition. The collection of "reflections" from all the crystal planes can be utilized to identify an unknown crystal uniquely. For that, a standard PDF card database can be used for matching the characteristic peaks in the obtained XRD pattern and obtain its crystal structure information. The crystal structures of the materials in this thesis were obtained by Bruker D8 Advance with Cu-K α radiation ($\lambda = 1.5418 \text{ \AA}$) in Facility for Analysis Characterization Testing and Simulation (FACTS) lab.

3.2.2.2 Brunauer-Emmett-Teller (BET) surface area

The particle surface area for the oxides synthesized in this thesis is calculated based on "Brunauer-Emmett-Teller" (BET) theory.¹² BET theory was developed to define the physical

adsorption of gas molecules on a solid surface and to get the surface area of the solid materials by calculating the amount of single layer gas molecular adsorbed on the surface. The amount of gas adsorbed predominantly depends on the exposed surface area of the solids and partially affected by temperature, gas pressure as well as interaction strength between the adsorbed gas and solid surface. Nitrogen is the most frequently used adsorbed gas due to its high purity and strong interaction with almost all kinds of solids. During nitrogen adsorption and desorption on a material surface, a pressure transducer precisely record the pressure changes caused by the adsorption process and the data collected presents the amount of gas adsorbed against the relative pressure, which is in the form of a BET isotherm. The BET specific surface areas of the materials in this thesis were obtained by ASAP Tristar II 3020.

3.2.2.3 X-ray Absorption Spectroscopy (XAS)

XAS measurements were carried out in this study to understand the electronic structure and the local environment of the catalysts.¹³

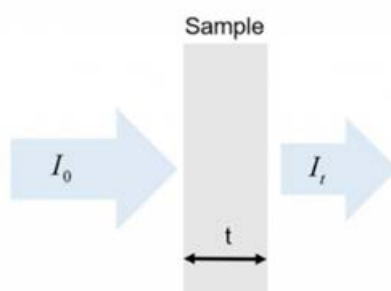


Figure 3.5 Scheme of transmission mode of XAS measurement. This figure is adapted from Ref 14.

A schematic illustration of how samples react to the beam when conducting XAS measurement in the transmission mode is shown in Figure 3.5. By passing through the sample (thickness x) with an incident beam (intensity I_0), transmitted beam with intensity I is detected. When the energy of incident beam is increased from low value to high value, the electron on the core state can be kicked off to unoccupied level (low energy X-ray Absorption Near-Edge Structure (XANES)), top of unoccupied level (XANES) and continuum (Extended X-ray Absorption Fine Structure (XAFS)), respectively. (Figure 3.6)¹⁵

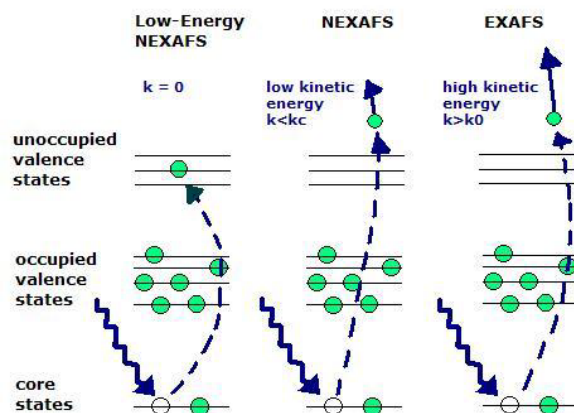


Figure 3.6 Three parts of XAS spectra depending on the energy of the incident photons. This figure is adapted from Ref ¹⁶.

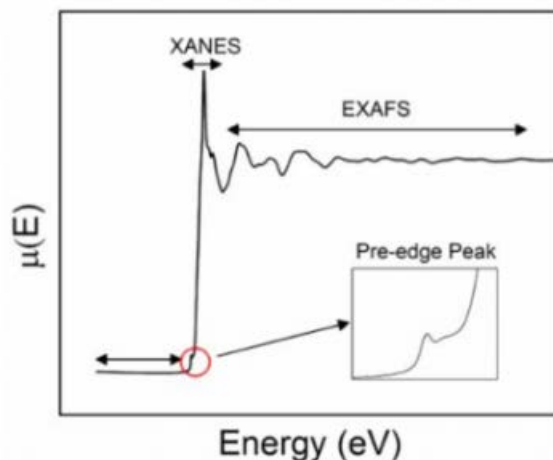


Figure 3.7 XAS spectrum. This figure is adapted from Ref 14.

In the XAS spectrum in Figure 3.7, the absorption coefficient (μ) is plotted versus incident photon energy (E). The different regions on the spectrum can be used for different analysis. The pre-edge peak in XANES provides information about the electronic structure and site symmetry. The XANES reflect the oxidation state of the elements. The sudden increase in the absorption coefficient is defined as absorption edge, where the incident photon energy begins to exceed the binding energy of the core electron K, L, and M etc. The core electron binding energy of each element can be found in the X-ray data booklet. ¹⁷

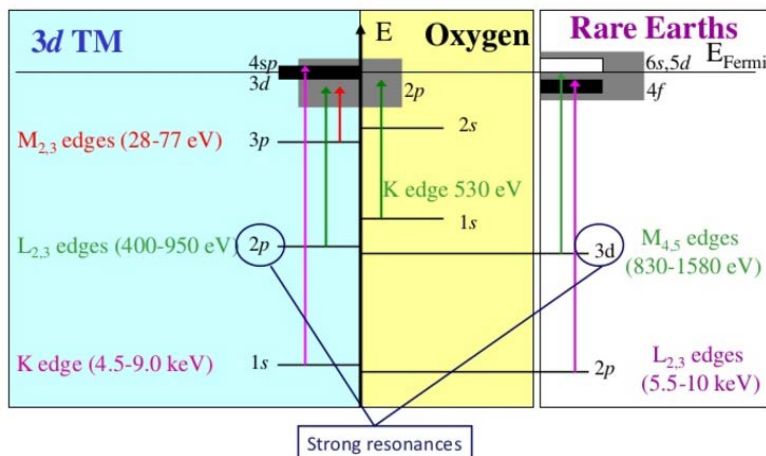


Figure 3.8 Resonance for different element in XAS. This figure is adapted from Ref ¹⁶.

In addition, the XAFS provides information on the coordination numbers and bond length between the absorb element and its neighbors. The ejected electron is photoelectron which behave like wave. When the outgoing wave comes across its neighbor atoms, they interact and oscillate, thus, the XAFS spectra presents itself in the form of oscillation.

X-ray absorption near edge structure (XANES) and extended X-ray absorption fine structure (EXAFS) characterizations in this thesis were carried out at XAFCA beamline of Singapore Synchrotron Light Source (SSLS) to obtain the structure information.

3.2.2.4 Fourier transform infrared spectroscopy (FT-IR)

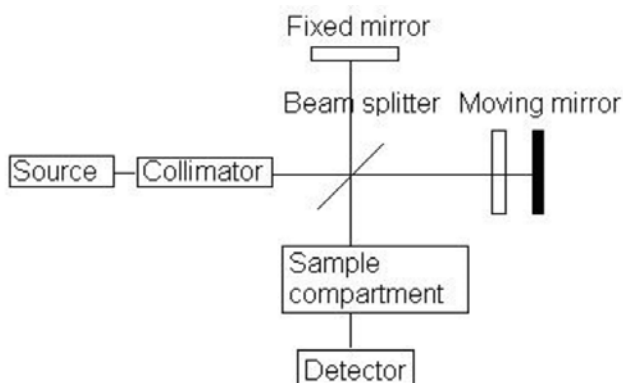


Figure 3.9 Operations Schematic of FTIR spectrometer. This figure is adapted from Ref 18.

As shown in Figure 3.9, the source of IR radiation passes through a half-silvered mirror. Half of the signal is reflected and hits the second moving mirror. After the reflection from the second mirror, the recombined IR signal is collected by the detector.

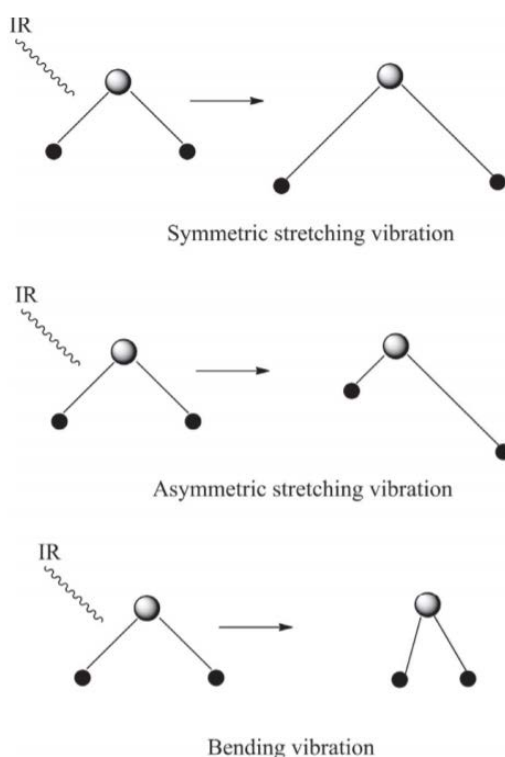


Figure 3.10 Stretching vibration and bending vibration of molecules after IR radiation. This figure is adapted from Ref 19.

When a molecule is exposed to radiations, it will either vibrate or rotate. The vibration energy can be divided into stretching vibration and bending vibration. Stretching vibration can be further divided into symmetric and asymmetric stretching vibration. (Figure 3.10) The energy for stretching a bond is higher than bending a bond. Based on Plank-Einstein Equation, $E=hf=hv/\lambda$, the stretching vibration happens at a higher wavenumber than bending vibrations. Similarly, asymmetric stretching vibrations occurs at higher wavelength than symmetric stretching vibrations. The FTIR data in Chapter 4 were recorded using FTIR Perkin Elmer Spectrum.

3.2.2.5 X-ray magnetic circular dichroism (XMCD)

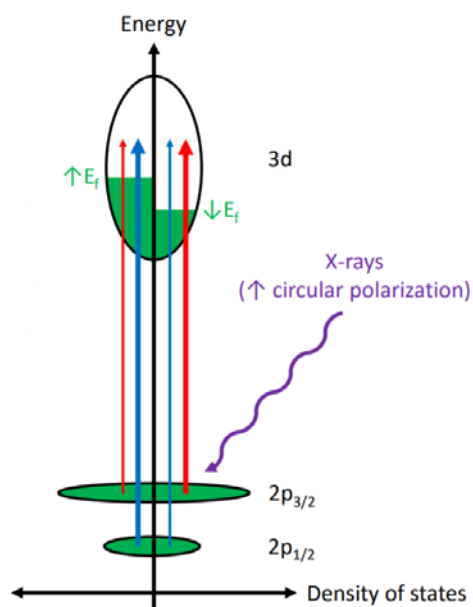


Figure 3.11 Diagram of XMCD. This figure is adapted from Ref 20.

XMCD is a technique allowing to obtain the magnetic properties of atoms.²¹ The absorption spectra for XMCD are usually measured at the L -edge for the transition metal cations. As shown in Figure 3.11, a magnetic field applied in the upward direction aligns valence electron in the upward direction, leaving hole states in the downward direction. For the $L3$ transition ($2p_{3/2} \rightarrow 3d$), X-rays with upward circular polarization are more likely to excite spin downward electrons into the hole states than spin upward electrons into the hole states. For the $L2$ transition ($2p_{1/2} \rightarrow 3d$), spin-orbit coupling is opposite ($l-s$ instead of $l+s$), so the excitation's spin sensitivity is opposite. In the Chapter 5 of this thesis, pairs of soft X-ray absorption spectra (μ^+/μ^-) are measured with circularly polarized x-rays with ± 1 T magnetic fields applying to the samples. The XMCD spectra arise from the difference between the μ^+ and μ^- spectra. Soft XAS and XMCD were obtained at SINS beamline of SSLs.

3.2.2.6 Transmission electron microscope (TEM)

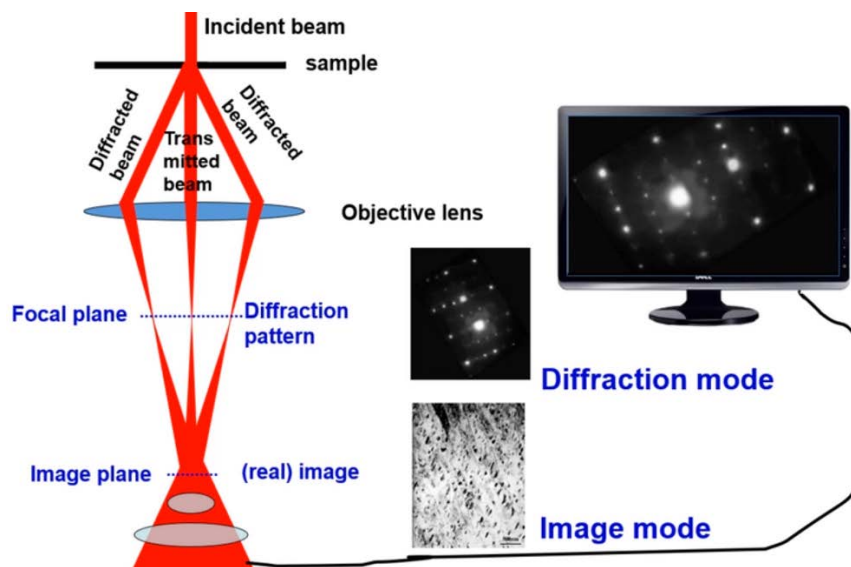


Figure 3.12 Working principles for TEM. This figure is adapted from Ref 22.

When the incidence beam passes through a sample, it can be divided into three beams, diffracted beams and transmitted beam. Each beam contains the microstructure information of the sample. These beams pass through an objective lens and gradually converge. On the focal plane of the objective lens, each beam gathers into a point. Different electrons converge at different positions of the focal plane to form the diffraction patterns, which can be regarded as the image of microstructure of the sample in the reciprocal space. After passing through the focal plane of the objective lens, the electron beams continuously deflect forward onto the image plane. High-resolution transmission electron microscopy (HRTEM) were adopted in the Chapter 5 of the thesis to image the surface of $\text{ZnCo}_{0.2}\text{Ni}_{0.8}\text{O}_4$ before and after OER.

3.2.2.7 Electron energy loss spectroscopy (EELS)

EELS are often coupled with TEM to provide structural and chemical information of the materials by detecting the energy loss for the elements inside the compound.²³

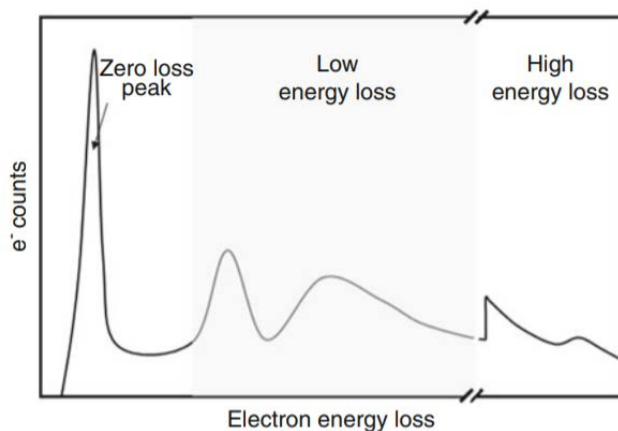


Figure 3.13 Schematic of electron energy loss spectrum. This figure is adapted from Ref 23.

Interactions between the incident electron beams and materials result in electron energy loss. A schematic diagram of electron energy loss has been shown in Figure 3.13. There are three types of energy losses: zero loss, low energy loss and high energy loss. Both HRTEM and EELS were adopted in the Chapter 5 of the thesis. The experiment was conducted in the Institute of Physics, Chinese Academy of Sciences using a JEOL 2100F transmission electron microscope at the operating voltage of 200 kV to investigate morphology and composition after OER cycling compared with that of the as-synthesized materials. Both the raw material and cycled material were prepared by suspending them in ethanol by ultrasonication. The suspensions were then dropped onto carbon film coated Cu TEM grids and dried at room temperature.

3.2.2.8 Scanning Electron Microscope (SEM)

SEM is an electron microscopy for surface morphology investigation. It can be coupled with Energy dispersive X-ray spectroscopy (EDX) detector for elemental composition studies. EDX measures the energies of the characteristic X-ray emitted from an atom after this atom is excited by an incident electron beam.²⁴ In the Chapter 4 of the thesis, Jeol FESEM 7600F was employed to observe the surface morphologies and elemental compositions of samples $\text{LaCo}_{1-x}\text{Fe}_x\text{O}_3$. In the Chapter 6 of the thesis, while the nominal stoichiometry of $\text{Co}_{0.6}\text{Fe}_{0.4}(\text{OH})_2$ was initially targeted owing to its enhanced OER activity as previously reported,²⁵ analysis by SEM-EDX

revealed a deviation from this nominal composition and the electrodeposition of a film with the composition $\text{Fe}_{0.5}\text{Co}_{0.5}(\text{OH})_2$.

3.2.2.9 Superconducting Quantum Design (SQUID)

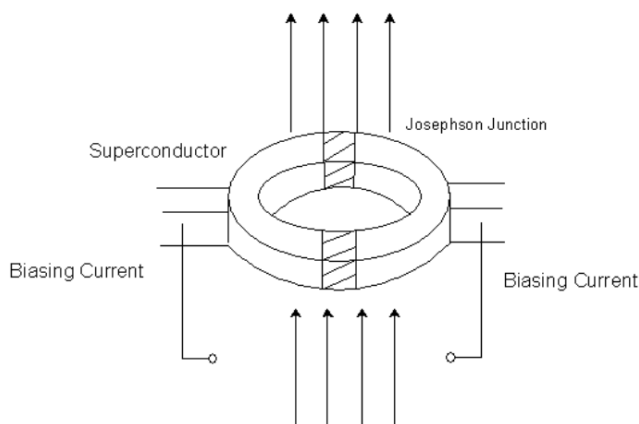


Figure 3.14 Working principle for the SQUID. This figure is adapted from Ref 26.

SQUID measures the magnetic moment induced by an applied external electric field in a sample.²⁷ In a SQUID magnetometer, the sample is moved through an external magnetic field. A pick-up coil links to a superconducting detector loop with parallel Josephson junctions. A magnetic flux from the moving sample interrupts the superconducting loop. An applied bias current re-establishes the superconducting loop and indicates the magnetism of the sample. DC magnetization measurements were performed on a SQUID magnetometer (MPMS-XL). Field-cooled (FC) DC magnetization measurements were carried out from room temperature to 5 K with a 100 Oe field.

3.2.2.10 X-ray photoelectron spectroscopy (XPS)

XPS uses a X-ray beam to irradiate a materials and measures the number and the kinetic energy of escaped electrons from the samples' surface.²⁸ It measures the surface species of the materials. XPS measurements in chapter 5 of the thesis were performed using a PHI-5400 with Al Ka beam source (250 W) and position-sensitive detector (PSD). The binding energy resolution is 0.8 eV,

angle resolution is 45° and the detection limit is 80 K CPS. Base pressure of the measurement chamber is 3.0×10^{-7} Pa. The Ar ion (voltage 12 kV, current 4.2 mA) sputtering speed is 0.28 nm/s over an area of $300 \times 300 \text{ um}^2$. Data from the measurements were calibrated using the adventitious carbon peak of the C 1s spectra (EB = 284.8 eV). The oxidation states of the elements are analyzed by peak deconvolution with XPSPEAK 4.1.

3.3 Reference

- (1) *Sol-Gel Materials for Energy, Environment and Electronic Applications*; Pillai, S. C., Hehir, S., Eds.; Advances in Sol-Gel Derived Materials and Technologies; Springer International Publishing: Cham, 2017. <https://doi.org/10.1007/978-3-319-50144-4>.
- (2) Yang, Z.; Huang, Y.; Dong, B.; Li, H.-L.; Shi, S.-Q. Sol-Gel Template Synthesis and Characterization of LaCoO₃ Nanowires. *Appl. Phys. A* **2006**, *84* (1–2), 117–122. <https://doi.org/10.1007/s00339-006-3591-3>.
- (3) Chi, B.; Li, J.; Yang, X.; Lin, H.; Wang, N. Electrophoretic Deposition of ZnCo₂O₄ Spinel and Its Electrocatalytic Properties for Oxygen Evolution Reaction. *Electrochimica Acta* **2005**, *50* (10), 2059–2064. <https://doi.org/10.1016/j.electacta.2004.09.014>.
- (4) Parida, P.; Kashikar, R.; Jena, A.; Nanda, B. R. K. Universality in the Electronic Structure of 3d Transition Metal Oxides. *Journal of Physics and Chemistry of Solids* **2018**, *123*, 133–149. <https://doi.org/10.1016/j.jpcs.2018.04.009>.
- (5) Yang, C.; Laberty-Robert, C.; Batuk, D.; Cibin, G.; Chadwick, A. V.; Pimenta, V.; Yin, W.; Zhang, L.; Tarascon, J.-M.; Grimaud, A. Phosphate Ion Functionalization of Perovskite Surfaces for Enhanced Oxygen Evolution Reaction. *J. Phys. Chem. Lett.* **2017**, *8* (15), 3466–3472. <https://doi.org/10.1021/acs.jpcclett.7b01504>.
- (6) Yang, C.; Fontaine, O.; Tarascon, J.-M.; Grimaud, A. Chemical Recognition of Active Oxygen Species on the Surface of Oxygen Evolution Reaction Electrocatalysts. *Angew. Chem. Int. Ed.* **2017**, *56* (30), 8652–8656. <https://doi.org/10.1002/anie.201701984>.
- (7) Hong, W. T.; Risch, M.; Stoerzinger, K. A.; Grimaud, A.; Suntivich, J.; Shao-Horn, Y. Toward the Rational Design of Non-Precious Transition Metal Oxides for Oxygen Electrocatalysis. *Energy Environ. Sci.* **2015**, *8* (5), 1404–1427. <https://doi.org/10.1039/C4EE03869J>.
- (8) Elgrishi, N.; Rountree, K. J.; McCarthy, B. D.; Rountree, E. S.; Eisenhart, T. T.; Dempsey, J. L. A Practical Beginner's Guide to Cyclic Voltammetry. *J. Chem. Educ.* **2018**, *95* (2), 197–206. <https://doi.org/10.1021/acs.jchemed.7b00361>.
- (9) Wei, C.; Rao, R. R.; Peng, J.; Huang, B.; Stephens, I. E. L.; Risch, M.; Xu, Z. J.; Shao-Horn, Y. Recommended Practices and Benchmark Activity for Hydrogen and Oxygen Electrocatalysis in Water Splitting and Fuel Cells. *Adv. Mater.* **2019**, *31* (31), 1806296. <https://doi.org/10.1002/adma.201806296>.
- (10) Waseda, Y.; Matsubara, E.; Shinoda, K. *X-Ray Diffraction Crystallography*; Springer Berlin Heidelberg: Berlin, Heidelberg, 2011. <https://doi.org/10.1007/978-3-642-16635-8>.
- (11) Ferrari, C.; Bocchi, C. Strain and Composition Determination in Semiconducting Heterostructures by High-Resolution X-Ray Diffraction. In *Characterization of Semiconductor*

Heterostructures and Nanostructures; Elsevier, 2008; pp 93–132. <https://doi.org/10.1016/B978-0-444-53099-8.00004-X>.

(12) Naderi, M. Surface Area. In *Progress in Filtration and Separation*; Elsevier, 2015; pp 585–608. <https://doi.org/10.1016/B978-0-12-384746-1.00014-8>.

(13) Du, Y.; Zhu, Y.; Xi, S.; Yang, P.; Moser, H. O.; Breese, M. B. H.; Borgna, A. XAFCA: A New XAFS Beamline for Catalysis Research. *J Synchrotron Rad* **2015**, *22* (3), 839–843. <https://doi.org/10.1107/S1600577515002854>.

(14) Wang, M.; Árnadóttir, L.; Xu, Z. J.; Feng, Z. In Situ X-Ray Absorption Spectroscopy Studies of Nanoscale Electrocatalysts. *Nano-Micro Lett.* **2019**, *11* (1), 47. <https://doi.org/10.1007/s40820-019-0277-x>.

(15) Haas, O.; Struis, R. P. W. J.; McBreen, J. M. Synchrotron X-Ray Absorption of LaCoO₃ Perovskite. *Journal of Solid State Chemistry* **2004**, *177* (3), 1000–1010. <https://doi.org/10.1016/j.jssc.2003.10.004>.

(16) <https://www.slideshare.net/Nirupam12/Xray-Absorption-Spectroscopy>.

(17) Thompson, A. C.; Attwood, D. T.; Howells, M. R.; Kortright, J. B.; Robinson, A. L.; Underwood, J. H.; Kim, K.-J.; Kirz, J.; Lindau, I.; Pianetta, P.; Winick, H.; Williams, G. P.; Scofield, J. H. X-Ray Data Booklet. 457.

(18) Macdonald, B. D. Augmenting 19th Century Thermoelectric Greenhouse Theory with 20th Century Quantum Mechanics Raman Spectroscopy: Towards a Coherent Radiation Theory of the Atmosphere. **2018**, 103.

(19) Sridharan, K. The Electromagnetic Spectrum. In *Spectral Methods in Transition Metal Complexes*; Elsevier, 2016; pp 1–12. <https://doi.org/10.1016/B978-0-12-809591-1.00001-3>.

(20) https://en.wikipedia.org/wiki/File:Diagram_of_X-Ray_magnetic_circular_dichroism.pdf.

(21) Schattschneider, P.; Rubino, S.; Hébert, C. Circular Dichroism in the Transmission Electron Microscope. In *Encyclopedia of Materials: Science and Technology*; Buschow, K. H. J., Cahn, R. W., Flemings, M. C., Ilschner, B., Kramer, E. J., Mahajan, S., Veyssi re, P., Eds.; Elsevier: Oxford, 2007; pp 1–11. <https://doi.org/10.1016/B978-0-08043152-9.02173-4>.

(22) Pennycook, S. J.; Lupini, A. R.; Varela, M.; Borisevich, A.; Peng, Y.; Oxley, M. P.; Van Benthem, K.; Chisholm, M. F. Scanning Transmission Electron Microscopy for Nanostructure Characterization. In *Scanning Microscopy for Nanotechnology*; Zhou, W., Wang, Z. L., Eds.; Springer New York: New York, NY, 2006; pp 152–191. https://doi.org/10.1007/978-0-387-39620-0_6.

(23) *Encyclopedia of Tribology*; Wang, Q. J., Chung, Y.-W., Eds.; Springer US: Boston, MA, 2013. <https://doi.org/10.1007/978-0-387-92897-5>.

(24) Abd Mutalib, M.; Rahman, M. A.; Othman, M. H. D.; Ismail, A. F.; Jaafar, J. Scanning Electron Microscopy (SEM) and Energy-Dispersive X-Ray (EDX) Spectroscopy. In *Membrane Characterization*; Elsevier, 2017; pp 161–179. <https://doi.org/10.1016/B978-0-444-63776-5.00009-7>.

(25) Burke, M. S.; Kast, M. G.; Trotochaud, L.; Smith, A. M.; Boettcher, S. W. Cobalt–Iron (Oxy)Hydroxide Oxygen Evolution Electrocatalysts: The Role of Structure and Composition on Activity, Stability, and Mechanism. *J. Am. Chem. Soc.* **2015**, *137* (10), 3638–3648. <https://doi.org/10.1021/jacs.5b00281>.

(26) Zhao, Z.; others, many. *Physical Methods in Chemistry and Nano Science*; 2012.

- (27) Borisov, P.; Hochstrat, A.; Shvartsman, V. V.; Kleemann, W. Superconducting Quantum Interference Device Setup for Magnetoelectric Measurements. *Review of Scientific Instruments* **2007**, 78 (10), 106105. <https://doi.org/10.1063/1.2793500>.
- (28) Hollander, J. M.; Jolly, W. L. X-Ray Photoelectron Spectroscopy. **1970**, 8.

Chapter 4

Tailoring the Co 3d-O 2p Covalency in LaCoO₃ by Fe Substitution to Promote Oxygen Evolution Reaction

LaCoO₃ is an active, stable catalyst in alkaline solution for oxygen evolution reaction (OER). However, room still remains for improving its activity according to recent understandings of OER on perovskite oxides. In this work, Fe substitution has been introduced in LaCoO₃ to boost its OER performance. Density function theory (DFT) calculation verified that the enhanced performance originates from the enhanced Co 3d-O 2p covalency with 10 at% Fe substitution in LaCoO₃. Both DFT calculations and Superconducting Quantum Design (SQUID) magnetometer (MPMS-XL) showed a Co³⁺ spin state transition from generally low spin state (LS: $t_{2g}^6 e_g^0$, $S = 0$) to a higher spin state with the effect of 10 at% Fe substitution. X-ray absorption near-edge structure (XANES) supports DFT calculations on an insulator to half-metal transition with 10 at% Fe substitution, induced by spin state transition. The half-metallic LaCo_{0.9}Fe_{0.1}O₃ possesses increased the overlap between Co 3d and O 2p states which results in enhanced covalency and promoted OER performance. This finding enlightens a new way of tuning the metal-oxygen covalency in oxide catalysts for OER.

*This section published substantially as Y. Duan, S. Sun, S. Xi, X. Ren, Y. Zhou, G. Zhang, H. Yang, Y. Du & Z. J. Xu, Tailoring the Co 3d-O 2p covalency in LaCoO₃ by Fe substitution to promote oxygen evolution reaction. *Chemistry of Materials*, 29(24), 10534-10541 (2017). DOI: 10.1021/acs.chemmater.7b04534.

4.1 Introduction

With a few decades of industrialization and urbanization, the overconsumption of fossil fuels has expedited energy depletion and environmental deterioration. Technologies to convert and store “green” energies therefore have been developed to mitigate these issues. Among these technologies, water electrolysis is a promising one, which generates hydrogen fuel for fuel cells to further generate electricity. Challenges towards water electrolysis lie in the difficulty in improving the energy efficiency of water splitting, attributable to high overpotential of OER on anodes.¹ A number of catalysts have been investigated to reduce OER overpotential, of which precious metal oxides like IrO₂ and RuO₂ stand out.¹ However, the high cost and scarcity have severely hampered their implementation in a large-scale. In contrast, transition metal oxides such as Ni, Fe, Co based oxides have emerged as promising alternatives due to their competitively lower overpotentials and lower cost.² Among these transition metal oxides, Co based oxide materials have attracted much research interest based on the superior OER activity of Co in octahedrally coordinated environments.³ Evidence can be found in the investigations on the OER performance of six-coordinated Co in different types of crystal structures, such as delafossite structure oxides (e.g. LiCoO₂), spinel structure oxides (e.g. ZnCo₂O₄), and perovskite (e.g. LaCoO₃). Typically, LiCoO₂ has a layered structure with edge-shared Co in single layer. Many recent studies are focused on lowering Li contents in Li_xCoO₂ to adjust the cobalt valence state, and hence to further boost the OER activity.⁴ ZnCo₂O₄ possesses a spinel structure with tetrahedrally-coordinated Zn and octahedrally-coordinated Co.⁵ By comparing the OER performance of ZnCo₂O₄ with that of Co₃O₄, it has been found that octahedrally-coordinated Co contribute to the OER activity dominantly.^{5,6} LaCoO₃ is a compacted oxide with corner-shared perovskite structure, where all Co atoms are accommodated in octahedral sites.⁷ As for its OER performance, LaCoO₃ has been recognized as a stable and active OER catalyst in alkaline solution.^{8,9} The OER activity of metal oxides can be correlated with their electronic structures. The location of oxygen 2*p* orbital centre (with the Fermi level (E_F) as reference) is a descriptor of OER activities for oxide catalysts.^{8,10,11} Alexis et al. found that the increase in metal-oxygen covalency lowered the required potential for the four steps in OER.¹² Thus, being less covalent than La_{0.5}Sr_{0.5}CoO_{3-δ} and SrCoO_{3-δ}, LaCoO₃ exhibits less activity.¹² However, LaCoO₃ was

found to be more stable in alkaline due to its optimal position of O p -band centre to Fermi level (E_F).⁸ Without the anionic redox reaction on surface, the conventional concerted proton-electron transfer mechanism works well on LaCoO_3 .¹³ In pure cationic redox reaction, electron occupancy is also a descriptor of OER activities for metal oxides. S. Trasatti et.al proposed that the M-O binding energy acted as a descriptor for OER activity attributable to all intermediates bonding with the surface through oxygen.⁴ Some reaction steps (formation of $^*\text{OH}$ and $^*\text{O}$) get easier with strong M-O bind energy, whereas other steps (formation of $^*\text{OOH}$) do not. Thus, there exists an optimal M-O binding energy. Nørskov et. al. found that decreasing occupancy of e_g orbital resulted in a stronger O binding energy through investigating the interplay between M-O binding energy and e_g .¹⁴ In 2011, Shao-Horn et al. raised an e_g theory to quantify the M-O binding energy in perovskites to guide the development of oxides for OER.¹⁵ The correlation between OER activity and the occupation of e_g orbital for different perovskite materials including LaCoO_3 was constructed and the conclusion pointed out that perovskites with $e_g \sim 1.2$ ameliorated OER activities.¹⁵ Based on the correlation between electronic structures and OER performance of metal oxides, several methods have been proposed to enhance the OER activity in Co based perovskites. For example, Zhou's group synthesized LaCoO_3 with different particle sizes at various annealing temperature to adjust the average spin state of Co.¹⁶ They found that high spin Co existed on the surface of LaCoO_3 , while low spin Co accommodated in the bulk of LaCoO_3 . As a result, LaCoO_3 with an average $e_g \sim 1.2$ gives a best OER activity.¹⁶ On the other hand, numerous investigations were given to tuning the cobalt valence state through the substitution of A site La by low valence state elements.¹⁰ For instance, Mefford et al. introduced divalent Sr into trivalent La lattice to increase the cobalt valence state as well as lift the O p orbital, accompanied by energy gap reduction between metal $3d$ and O p -band centre,^{12,17} and hence to promote the OER process.¹¹ Besides, the overlap between metal $3d$ and O $2p$ has been increased to a level that ligand holes are induced on the surface¹³ of $\text{La}_{1-x}\text{Sr}_x\text{CoO}_3$ and these oxygen vacancies take part in OER with a new mechanism, namely lattice oxygen mechanism (LOM). There are also studies on substituting B site Co by other transition metals like Mn, Ni, and Fe for tuning the OER activity. Among these transition metal substitutions, Fe substitution has been found to be a vital stimulator for OER. For example, it has been sufficiently exemplified by the improvement in electrocatalytic activity of Fe substituted $\text{La}_{0.6}\text{Ca}_{0.4}\text{CoO}_3$. Various oxidation states for Co cations are generated by the incorporation of Fe, which facilitates

the formation of cobalt-hydroxides and increases the electrical conductivity.¹⁸ In addition, Fe substitution has been also investigated in other oxide structures. Xiao et al. regarded the augment in OER activity after the incorporation of 10 wt% Fe into Co_3O_4 as a consequence of the increase in BET surface areas and electrical conductivity.¹⁹ Zhu et al. reported an enhancement of OER activity by modifying LiCoO_2 through 20 wt% Fe substitutions. It was proposed by authors that the Fe substitution might induce a synergistic effect with Co, resulting in favourable electronic structure of surface Co.²⁰ However, how the Fe substitution affects the electronic structures of the materials and how it subsequently results in OER activity improvement were not investigated.

In this work, the electronic structure change in Fe substituted LaCoO_3 was investigated and the Co 3d-O 2p covalency of LaCoO_3 was tuned towards an OER favourable one by the substitution. First, a series of $\text{LaCo}_{1-x}\text{Fe}_x\text{O}_3$ ($x=0.00, 0.10, 0.25, 0.50, 0.75, 1.00$) were synthesized for investigating their OER, of which LaCoO_3 with 10 at% Fe substitution ratio was found with the best OER activity. DFT calculations further revealed that the enhanced Co 3d-O 2p covalency in $\text{LaCo}_{0.9}\text{Fe}_{0.1}\text{O}_3$ compared to that of LaCoO_3 accounts for the improved performance. The augment in Co 3d-O 2p covalency of $\text{LaCo}_{0.9}\text{Fe}_{0.1}\text{O}_3$ is realised by the increased overlap between Co 3d and O 2p states as validated by both projected density of state (pDOS) and total density of states (TDOS). The strong Co(e_g)-O(p) hybridization originates from the half-metal $\text{LaCo}_{0.9}\text{Fe}_{0.1}\text{O}_3$, where the Co^{3+} has higher spin states compared to the ground state Co^{3+} in LaCoO_3 . XANES result agrees well with the half-metallic feature after 10 at% Fe substitution in LaCoO_3 by showing the delocalised feature of electrons on Fe p states. This insulator-to-half-metal transition with 10 at % additional Fe is induced by low spin state to higher spin state transition of Co^{3+} . Thus, the interplay between Co^{3+} spin configuration and Co 3d-O 2p covalency for LaCoO_3 and $\text{LaCo}_{0.9}\text{Fe}_{0.1}\text{O}_3$ has been established. The optimized spin state for Co^{3+} in $\text{LaCo}_{0.9}\text{Fe}_{0.1}\text{O}_3$ brings about maximized Co 3d-O 2p covalency. As a result, the optimal Fe substitution in LaCoO_3 promoted the OER performance.

4.2 Experimental Methods

4.2.1 Material synthesis

LaCo_{1-x}Fe_xO₃ powders were synthesized via a sol-gel method. Detailed method can be referred to Chapter 3.1.1.

4.2.2 Material Characterizations

The crystal structure was obtained by Bruker D8 Advance with Cu-K α radiation ($\lambda = 1.5418 \text{ \AA}$). JEOL JSM-7600F was employed to observe the surface morphologies of samples. The (Brunauer-Emitter-Teller) BET specific surface areas of the materials were obtained by ASAP Tristar II 3020. Fourier transform infrared spectroscopy (FT-IR) data were recorded using FTIR Perkin Elmer Spectrum. X-ray absorption near edge structure (XANES) and extended X-ray absorption fine structure (EXAFS) characterizations were carried out at XAFCA beamline of Singapore Synchrotron Light Source (SSLS) to obtain the structure information. DC magnetization measurements were performed on a Superconducting Quantum Design (SQUID) magnetometer (MPMS-XL). Field-cooled (FC) DC magnetization measurements were carried out from room temperature to 5 K with a 100 Oe field.

4.2.3 Electrochemical Tests

The electrochemical tests were carried out by three-electrode method with LaCo_{1-x}Fe_xO₃ as working electrode, saturated calomel electrode (SCE) and Pt wire severing as reference and counter electrodes, respectively. 16 mg perovskite material and 3.2 mg carbon black were dispersed in a mixed solution of 1.6 mL isopropanol (IPA), 6.4 mL DI water and 80 μL Nafion perfluorinated resin to prepare the ink of catalyst. The mixture was sonicated for 40 mins to achieve homogenized dispersion of perovskite and carbon. The perovskite material was dispersed in a diluted isopropanol solution containing 5% Nafion. The mass ratio of perovskite material: carbon black was maintained at 4: 1. The volume ratios of DI water: IPA: Nafion were maintained at 4: 1: 0.05. 15 μL of the ink was dropped onto a newly polished rotating disk electrode (RDE) (0.196 cm²). All electrochemical potentials here were against the reversible hydrogen electrode (RHE) under the condition with 1.0 M KOH. The conversion between potentials vs. SCE and vs. RHE was performed by the equation below.

$$E \text{ (vs. RHE)} = E \text{ (vs. SCE)} + E_{\text{SCE}} \text{ (vs. SHE)} + 0.059 \times \text{pH}$$

$$(E_{\text{SCE}} \text{ (vs. SHE)} = 0.2438 \text{ vs. SHE at } 25^\circ\text{C})$$

The oxygen evolution reaction was evaluated by cyclic voltammetry (CV) between 1.058 and 1.656 V (vs. RHE) at a scan rate of 10 mV s^{-1} at 1600 rpm).

4.2.4 DFT Calculations

The pDOSs for both LaCoO_3 and $\text{LaCo}_{0.9}\text{Fe}_{0.1}\text{O}_3$ were calculated using the QUANTUM-ESPRESSO package.³⁸ $\text{LaCo}_{0.9}\text{Fe}_{0.1}\text{O}_3$ supercell was created by replacing one of the Co atoms, with a Fe atom, in a $2 \times 2 \times 1$ LaCoO_3 supercell. The exchange-correlation interaction was treated with the Perdew-Burke-Ernzerhof (PBE) generalized gradient approximation.³⁹ The Vanderbilt-type ultrasoft pseudopotential was employed to approximate the potential between the ion core and valence.⁴⁰ The cutoff-energies of plane waves and charge densities were chosen as 64 and 640 Ry, respectively. Integration over the Brillouin zone was carried out using the Monkhorst-Pack scheme with an $8 \times 8 \times 8$ mesh of k-points for LaCoO_3 , and $4 \times 4 \times 8$ for $\text{LaCo}_{0.9}\text{Fe}_{0.1}\text{O}_3$. Structural optimization was performed using variable cell shape molecular dynamics.⁴¹ The relaxation was terminated when the interatomic forces are smaller than 10^{-4} Ry/a.u. Corrections that account for the strong correlation among the electrons at the Co and Fe sites were made by using a DFT+U approach with $U=8.33$.

4.3 Results and Discussions

4.3.1 Material characterizations

The X-ray Diffraction (XRD) patterns of $\text{LaCo}_{1-x}\text{Fe}_x\text{O}_3$ are shown in Figure 4.1. The pattern of LaCoO_3 powder corresponds to rhombohedral perovskite (Figure 4.2) structure ($a=b=c$ and $\alpha=\beta=\gamma \neq 90^\circ$) LaCoO_3 R-3m (166) (JCPDS: 25-1060) without peaks attributable to La_2O_3 , CoO , and Co_3O_4 , indicating the formation of pure phase LaCoO_3 . While introducing Fe substitution, the crystal system remains rhombohedral with the atomic ratio of Fe / (Co + Fe) of 0.10. As the Fe ratio increases to 0.25, a new phase appears, which is assigned to orthorhombic ($a \neq b \neq c$ and $\alpha=\beta=\gamma=90^\circ$). Thus, $\text{LaCo}_{0.75}\text{Fe}_{0.25}\text{O}_3$ and $\text{LaCo}_{0.50}\text{Fe}_{0.50}\text{O}_3$ exhibits the rhombohedral and

orthorhombic mixed structure. When the Fe ratios are 0.75 and 1.00, the crystal system changes to orthorhombic completely (JCPDS: 37-1493). Meanwhile, it can be found that with the increase of Fe, the diffraction peak shifts to lower angle direction, consistent with the fact that Fe^{3+} ion (LS 132 pm, HS 152 pm) has a larger covalent radius than Co^{3+} ion (LS 126 pm, HS 150 pm).¹⁹

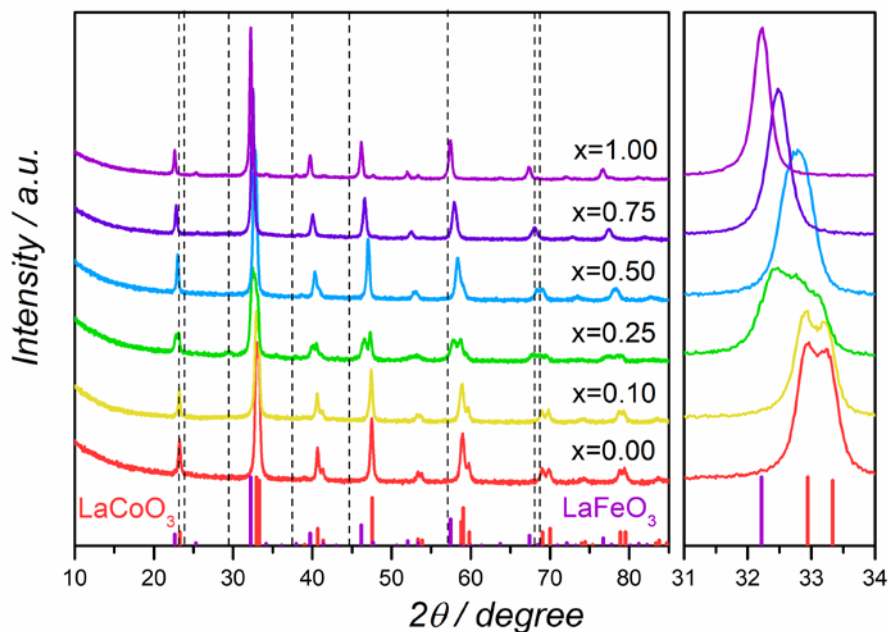


Figure 4.1 XRD patterns of $\text{LaCo}_{1-x}\text{Fe}_x\text{O}_3$ ($x=0.00, 0.10, 0.25, 0.50, 0.75, 1.00$).

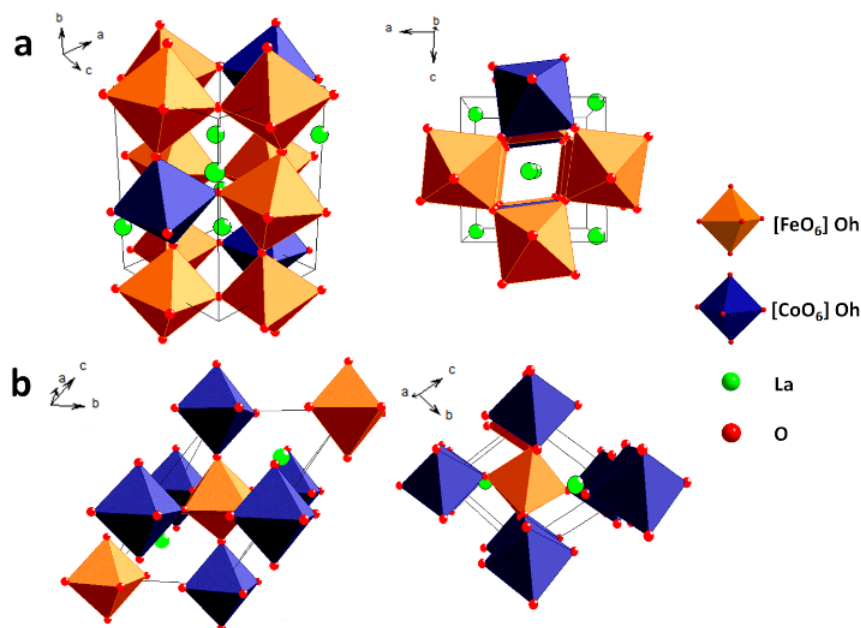


Figure 4.2 Perovskite structure (ABO₃) with rhombohedral distorted structure (a) and orthorhombic structure (b). A (La in green) represents the metal cation which accommodates at the corners of the unit cell. B (Co in blue and Fe in orange) represents the octahedrally coordinated transition metal cation which is at the centre of the unit cell. The negative oxygen ions occupy the face-centred positions.

The SEM images of the as-synthesized LaCo_{1-x}Fe_xO₃ (with $x = 0.00, 0.10, 0.25, 0.50, 0.75, 1.00$) are shown in Figure 4.3. The particles all adopt similar morphologies. The specific area, average pore size and average particle size of the series of samples were measured by Brunauer–Emmett–Teller (BET) technique. The adsorption and desorption isotherm curves for LaCo_{1-x}Fe_xO₃ are shown in Figure 4.4(a-f). The Type V isotherms are due to existence of mesoporous in the structures.²¹ From the BET surface area (Figure 4.4g), the average particle sizes are in the range of 400 ~ 500 nm for LaCo_{1-x}Fe_xO₃. The as-synthesized oxide powders with different Fe contents possess a specific surface area of 12 ~ 15 m² g⁻¹.

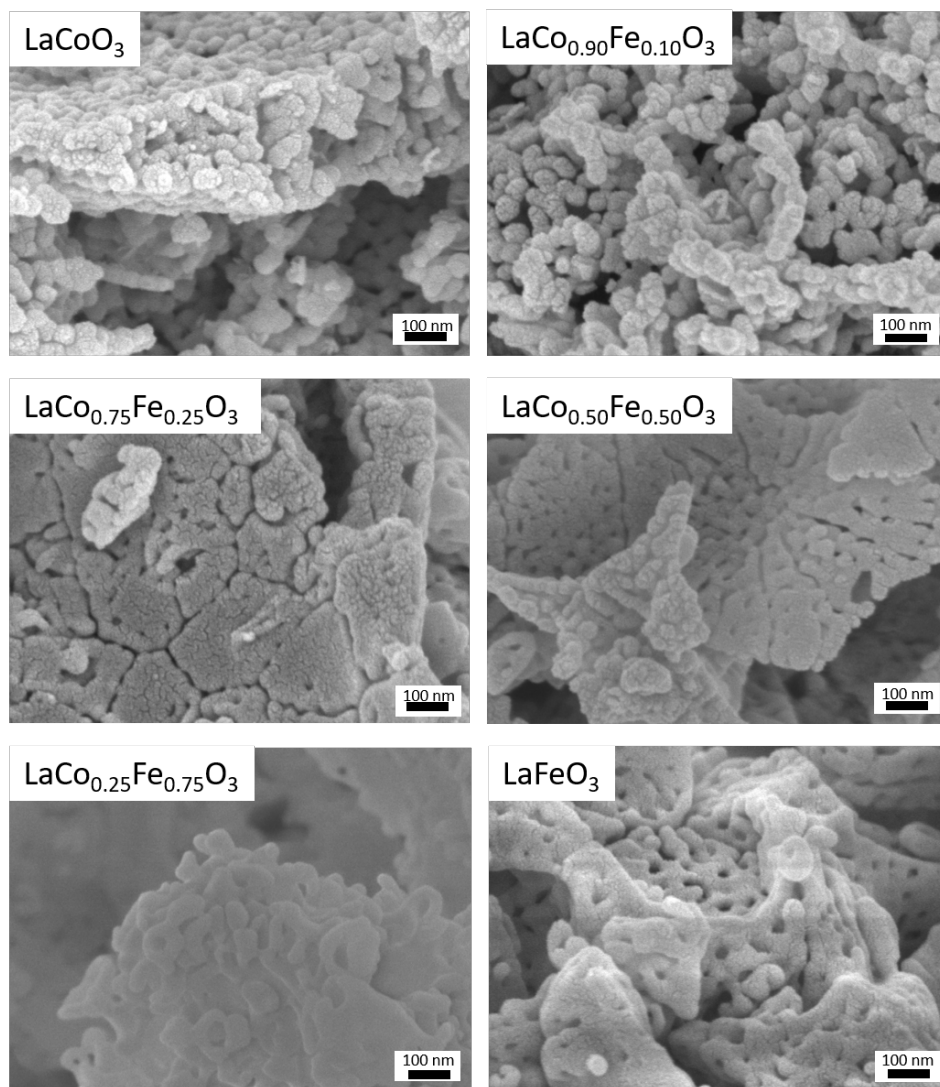


Figure 4.3 SEM images of LaCo_{1-x}Fe_xO₃ (x=0.00, 0.10, 0.25, 0.50, 0.75, 1.00).

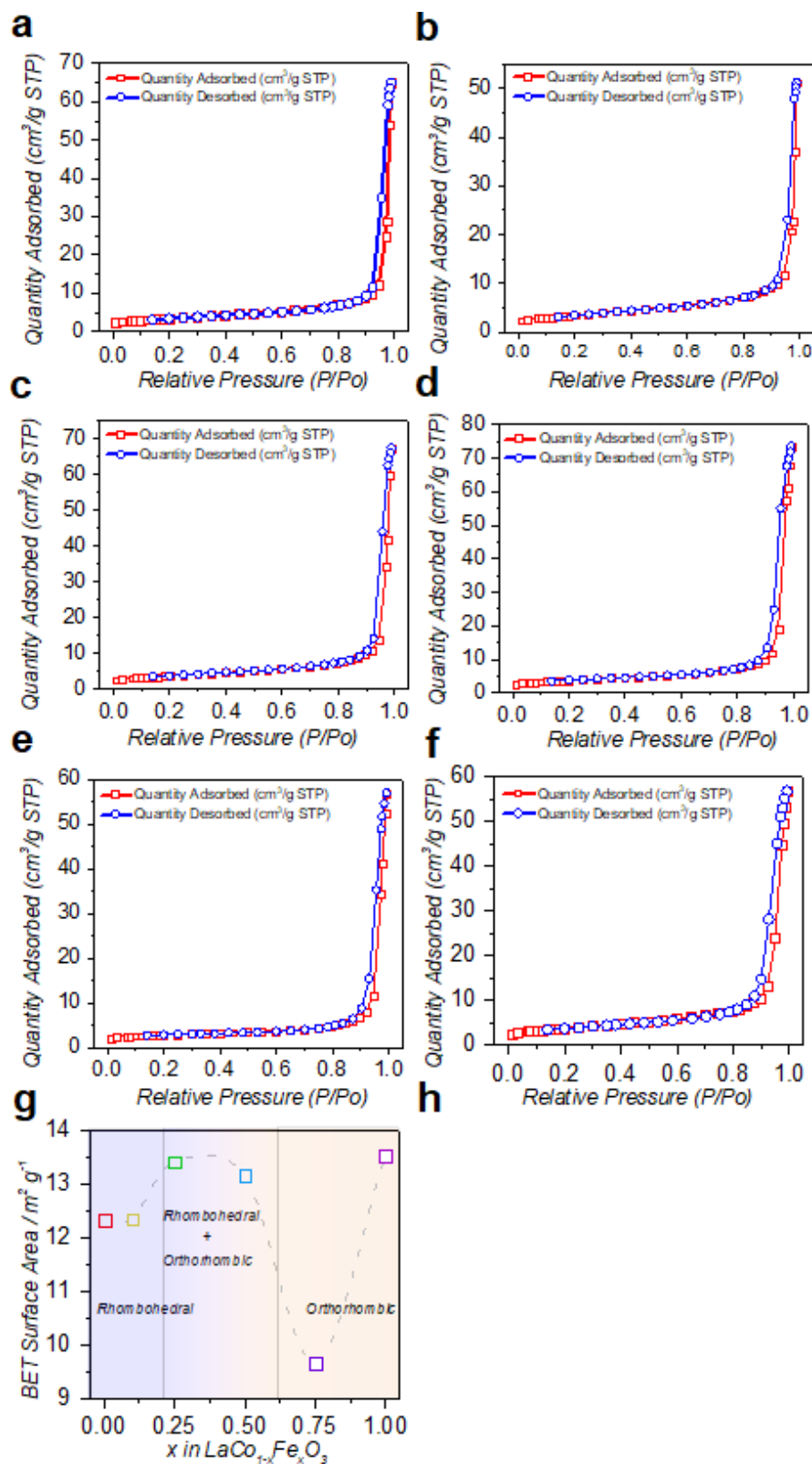


Figure 4.4 BET raw data of $\text{LaCo}_{1-x}\text{Fe}_x\text{O}_3$ ($x=0.00, 0.10, 0.25, 0.50, 0.75, 1.00$) and trend in specific surface area as Fe substitution increases.

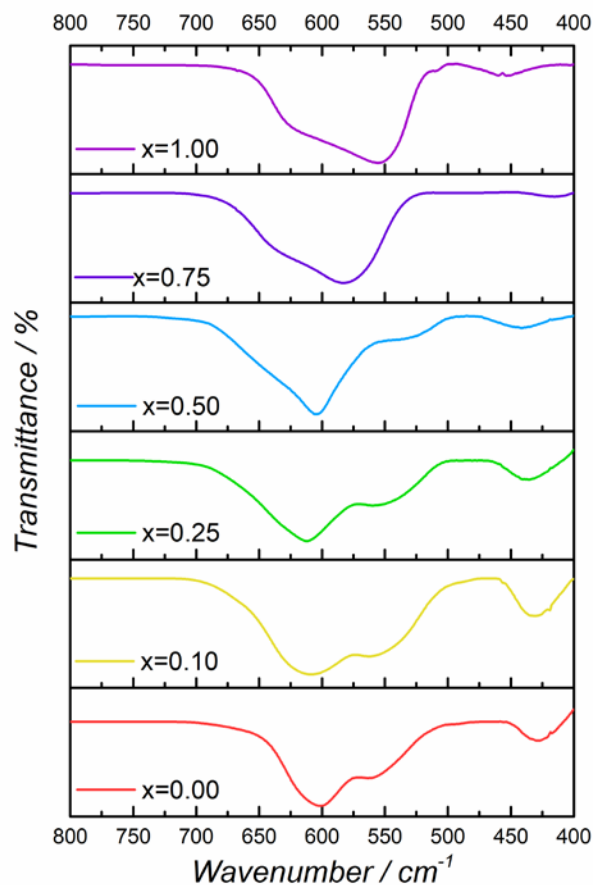


Figure 4.5 FT-IR spectra of $\text{LaCo}_{1-x}\text{Fe}_x\text{O}_3$ ($x=0.00, 0.10, 0.25, 0.50, 0.75, 1.00$).

The Fourier transform infrared spectroscopy (FT-IR spectra) of $\text{LaCo}_{1-x}\text{Fe}_x\text{O}_3$ is shown in Figure 4.5. For LaCoO_3 , a characteristic absorption band at 429 cm^{-1} is assigned to O-Co-O deformation modes in the CoO_6 octahedron and absorption bands at 600 cm^{-1} and 560 cm^{-1} are attributed to Co-O stretching vibration.²² While LaFeO_3 catalyst has two strong vibration bands at 555 cm^{-1} and 451 cm^{-1} , which could originate from the characteristic absorption bands of Fe-O stretching vibration and O-Fe-O bending vibration in FeO_6 octahedron, respectively.⁶ With the increase of Fe amount from 0 to 0.10, characteristic peaks for Co-O and O-Co-O maintain the same wavenumber, indicating an increase in Co-O and O-Co-O vibration energy due to the lattice distortion induced by Fe substitution. The Co-O bond length does not change from the evidence of extended X-ray absorption fine structure (EXAFS) (Figure 4.8), whereas the Fe-O bond length increases a bit with the Fe substitution ratio. In Figure 4.5, when the Fe substitution

ratio reaches 25 at% and 50 at%, these characteristic peaks at 429 cm^{-1} for O-Co-O deformation become less intense and the peaks at 600 cm^{-1} and 560 cm^{-1} for Co-O vibration change their shapes. These phenomena indicate a phase transition since 25 at% Fe incorporations, which agree well with XRD results. While the sample is modified with further addition of Fe ($x > 0.5$), Fe-O and O-Fe-O bonds vibration dominate. The corresponding peaks for Fe-O and O-Fe-O vibration are observed to shift to lower wavenumber direction with an increasing Fe ratio. It can be inferred that the vibration energy decreases. This is owing to that lattice distortion is induced by the coexistence of Co and Fe which may lead to higher B-O stretching vibration and O-B-O bending vibration energy. Thus, when small amount of Fe is substituted in LaCoO_3 , the small lattice distortion gives rise to small Co-O and O-Co-O vibration energy. When larger amount of Fe is introduced into LaCoO_3 , $\text{LaCo}_{0.5}\text{Fe}_{0.5}\text{O}_3$ exhibits the largest distortion due to large difference between Fe-O and Co-O bond lengths. This results in large B-O and O-B-O vibration energy. However, when the substituted Fe dominates the B site of $\text{LaCo}_{1-x}\text{Fe}_x\text{O}_3$, the lattice distortion is rather small, which is presented by smaller Fe-O and O-Fe-O vibration energy in $\text{LaCo}_{0.25}\text{Fe}_{0.75}\text{O}_3$ than in $\text{LaCo}_{0.5}\text{Fe}_{0.5}\text{O}_3$.

4.3.2 Electrochemical test

$\text{LaCo}_{1-x}\text{Fe}_x\text{O}_3$ were then tested for their OER performance under alkaline condition by employing three-electrode methods. $\text{LaCo}_{1-x}\text{Fe}_x\text{O}_3$ was mixed with acrylic black and coated on rotating disk electrode (RDE) to be used as working electrode. Cyclic voltammograms (CVs) were recorded by cycling the electrode between 1.058 and 1.656 V (vs. RHE) in O_2 -saturated 1.0 M KOH at a scan rate of 10 mV s^{-1} at 1600 rpm. The CV curves with current density versus potential (vs. RHE) are displayed in Figure 4.6a. The current densities of $\text{LaCo}_{1-x}\text{Fe}_x\text{O}_3$ were normalized to their BET surface areas.⁶ Besides, iR corrections were performed on the potentials. $\text{LaCo}_{0.9}\text{Fe}_{0.1}\text{O}_3$ emerges to have the best performance, whereas LaFeO_3 presents the least activity. The trend of current densities with the increase of Fe ratios is shown in Figure 4.6b. The data points and error bars were obtained by averaging the results of at least three independent measurements. Under an overpotential of 0.4 V, LaCoO_3 exhibits a current density of $0.183\text{ mA cm}^{-2}_{\text{oxide}}$. 10 at% Fe can increase the current density to $0.272\text{ mA cm}^{-2}_{\text{oxide}}$, which is almost twice that of LaCoO_3 . However, it is shown that higher amounts of Fe ($x \geq 0.25$) substitution

deteriorate the performance. Thus, when Fe ratio is 0.10, the materials exhibit better OER performance than LaCoO_3 . However, when Fe substitution ratio reaches 0.25 or higher, inferior OER performance is obtained. Analyzing the specific OER activity of $\text{LaCo}_{1-x}\text{Fe}_x\text{O}_3$ with their crystal structures, we can infer that the Co-rich rhombohedral system (LaCoO_3 and $\text{LaCo}_{0.90}\text{Fe}_{0.10}\text{O}_3$) has a superior OER activity compared with either a mixture of rhombohedral and orthorhombic structure ($\text{LaCo}_{0.75}\text{Fe}_{0.25}\text{O}_3$ and $\text{LaCo}_{0.50}\text{Fe}_{0.50}\text{O}_3$) or Fe-rich orthorhombic structure ($\text{LaCo}_{0.25}\text{Fe}_{0.75}\text{O}_3$ and LaFeO_3). $\text{LaCo}_{0.90}\text{Fe}_{0.10}\text{O}_3$ exhibits the largest OER performance improvement as compared to LaCoO_3 . The Tafel plot of $\text{LaCo}_{0.90}\text{Fe}_{0.10}\text{O}_3$ is presented in inset in Figure 4.6a for comparison with unsubstituted LaCoO_3 and benchmarked IrO_2 .²³ 10 at% Fe in LaCoO_3 has successfully raised the OER performance closer to IrO_2 . This shows the potential application of $\text{LaCo}_{0.90}\text{Fe}_{0.10}\text{O}_3$ as a catalyst in practical water electrolysis.

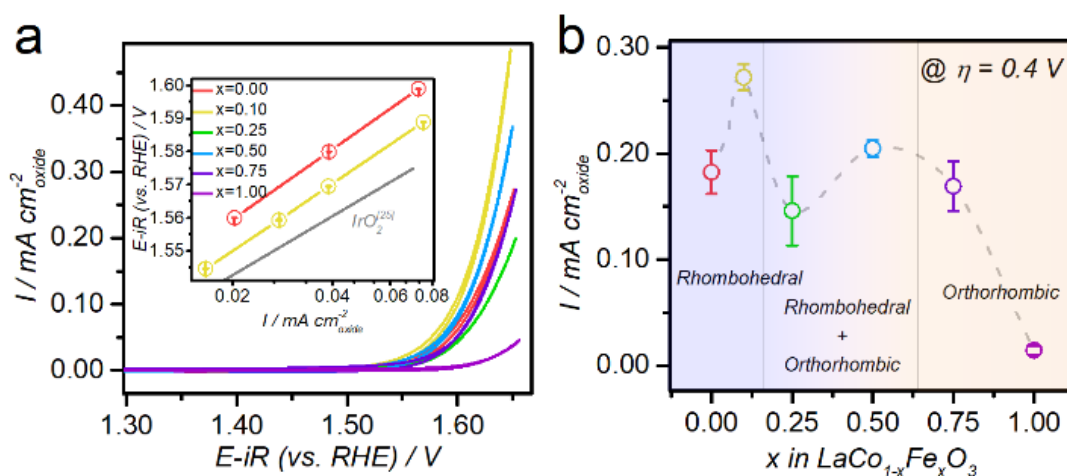


Figure 4.6 (a) The representative CV curves (the second cycle) of oxygen evolution reaction in 1.0 M KOH. The inset of (a) shows the Tafel plot of $\text{LaCo}_{0.90}\text{Fe}_{0.10}\text{O}_3$ (yellow line) for comparison with unsubstituted LaCoO_3 (red line) and benchmarked IrO_2 extracted from reference²⁴. (b) The specific current density for $\text{LaCo}_{1-x}\text{Fe}_x\text{O}_3$ at 1.63 V vs RHE.

4.3.3 X-ray absorption spectroscopy studies

X-ray absorption near-edge structure (XANES) spectra and extended X-ray absorption fine structure (EXAFS) spectra were carried out to explore the change in electronic structure and coordination environment of Co and Fe induced by the different amount of Fe substitution in the LaCoO_3 . Figure 4.7a shows the normalised Co K-edge XANES spectra of $\text{LaCo}_{1-x}\text{Fe}_x\text{O}_3$. The

E_{edge} defined by E ($\mu=0.5$) indicates substantial shift of E_{edge} with increasing Co formal valence.²⁵ As the substitution amounts of Fe increase, there is almost no energy shift of $\text{LaCo}_{1-x}\text{Fe}_x\text{O}_3$ relative to LiCoO_2 (Co^{3+}), indicating the valency of Co element in $\text{LaCo}_{1-x}\text{Fe}_x\text{O}_3$ remains almost the same (~ 3). The obvious main edge for $\text{LaCo}_{1-x}\text{Fe}_x\text{O}_3$ is attributed to $1s - 4p$ dipole transition, while the Co pre-edge for the samples are not obvious. Fe K-edge XANES spectra are shown in Figure 4.7b. Obvious pre-edge peaks (inset) can be observed at 7112.1 eV. Such pre-edge peaks are indicators for oxidation state and coordination geometry. The intensity of pre-edge for Fe K edge of $\text{LaCo}_{1-x}\text{Fe}_x\text{O}_3$ can be arranged in the following order: $\text{LaCo}_{0.9}\text{Fe}_{0.1}\text{O}_3 > \text{LaCo}_{0.5}\text{Fe}_{0.5}\text{O}_3 > \text{LaCo}_{0.75}\text{Fe}_{0.25}\text{O}_3 > \text{LaCo}_{0.25}\text{Fe}_{0.75}\text{O}_3 > \text{LaFeO}_3$. The prominent pre-edge features observed with 10 at% Fe substituted LaCoO_3 are mainly described by the nonlocal electric dipole transition of Fe from $1s$ to p states, where the empty p states of Fe atom are hybridized with the empty Co $3d$ states via O $2p$ empty states.²⁶ Other electronic transition also contributes to pre-edge, such as the local electric dipole transition of Fe atom from $1s$ to $4p$, where the empty p states of Fe are hybridized with Fe empty $3d$ states.²⁷ This $p-d$ hybridization is attributed to the non-centrosymmetric feature of the Fe site in the Fe substituted LaCoO_3 structure. Thus, the increasing intensity of pre-edge peak indicates the decrease in centrosymmetric and an increase in lattice distortion. When both Co and Fe atoms occupying the B site of perovskite $\text{LaCo}_{1-x}\text{Fe}_x\text{O}_3$, $\text{LaCo}_{0.5}\text{Fe}_{0.5}\text{O}_3$, $\text{LaCo}_{0.25}\text{Fe}_{0.75}\text{O}_3$, $\text{LaCo}_{0.75}\text{Fe}_{0.25}\text{O}_3$ and $\text{LaCo}_{0.9}\text{Fe}_{0.1}\text{O}_3$ exhibit larger degree of distortion than LaFeO_3 , which matches the FT-IR results. However, this factor is of small contribution to the pre-edge. The commensurate E_{edge} observed for Fe XANES K-edge of $\text{LaCo}_{1-x}\text{Fe}_x\text{O}_3$ with standard Fe_2O_3 (Fe^{3+}) indicates that the Fe valency maintains unchanged at ~ 3 when the Fe substitution ratio varies from 0.1 to 1.00 in $\text{LaCo}_{1-x}\text{Fe}_x\text{O}_3$.

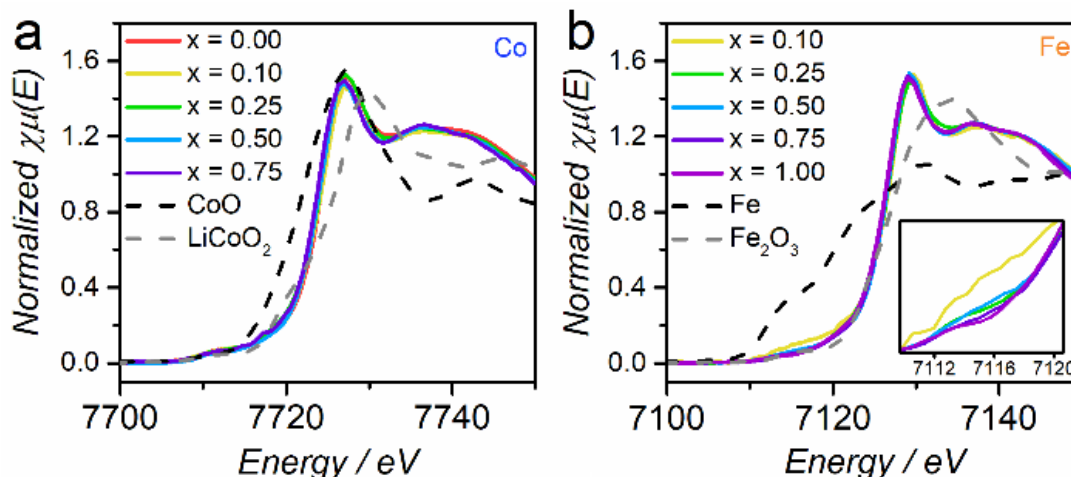


Figure 4.7 (a) Normalised Co K-edge XANES spectra of $\text{LaCo}_{1-x}\text{Fe}_x\text{O}_3$ ($x = 0.00, 0.10, 0.25, 0.50, 0.75, 1.00$) with CoO and LiCoO_2 (Sigma Aldrich) as reference. The inset exhibits the zoomed in Co K-edge XANES spectra for LaCoO_3 (red line) and $\text{LaCo}_{0.9}\text{Fe}_{0.1}\text{O}_3$ (yellow line) from 7709 to 7712 eV. (b) Normalised Fe K-edge XANES spectra of $\text{LaCo}_{1-x}\text{Fe}_x\text{O}_3$ ($x=0.00, 0.10, 0.25, 0.50, 0.75, 1.00$) with Fe foil and Fe_2O_3 (Sigma Aldrich) as reference. The inset shows the zoomed in Fe K-edge XANES spectra for $\text{LaCo}_{1-x}\text{Fe}_x\text{O}_3$ from 7110 to 7120 eV.

To subsequently study the local environment of metal cations in perovskite $\text{LaCo}_{1-x}\text{Fe}_x\text{O}_3$ ($x=0.00, 0.10, 0.25, 0.50, 0.75, 1.00$) oxides, EXAFs has been employed. The distances between the absorbing metal atoms and the backscattering atoms can be extracted from the Fourier transform (FT) EXAFs spectra. As shown in Figure 4.8a and Figure 4.8b, the first peaks in FT-EXAFS spectra located at $\sim 1.5 \text{ \AA}$ can be referred to the bond distances between the absorbing atoms and the oxygen atoms, representing by Co-O and Fe-O. The radial distance between Co and O atom in $\text{LaCo}_{1-x}\text{Fe}_x\text{O}_3$ maintain no change with increasing Fe substitution ratios (Figure 4.8a), indicating no effect of Fe substitution on Co-O bond lengths. From Figure 4.8b, the Fe-O bond lengths increase with the Fe substitution ratios in $\text{LaCo}_{1-x}\text{Fe}_x\text{O}_3$ ($x=0.10, 0.25, 0.50, 0.75, 1.00$), amongst which LaFeO_3 possesses the largest Fe-O bond length. Despite the observed increase in radial distance between Fe and O atom in $\text{LaCo}_{1-x}\text{Fe}_x\text{O}_3$, there is no significant difference between the Co-O and Fe-O bond length. Similar patterns between Co K-edge and Fe K-edge indicates similar coordination environment of Co and Fe atoms in $\text{LaCo}_{1-x}\text{Fe}_x\text{O}_3$. This, together with the unchanged Co and Fe valence state obtained by XANES studies, implies the successful substitution of Fe atom for Co atom on B site of $\text{LaCo}_{1-x}\text{Fe}_x\text{O}_3$. When Fe gradually takes the place of Co atom in LaCoO_3 , larger Fe-O bond length begins to induce lattice distortion in $\text{LaCo}_{1-x}\text{Fe}_x\text{O}_3$ ($x=0.10, 0.25, 0.50, 0.75$), which agrees with FT-IR results.

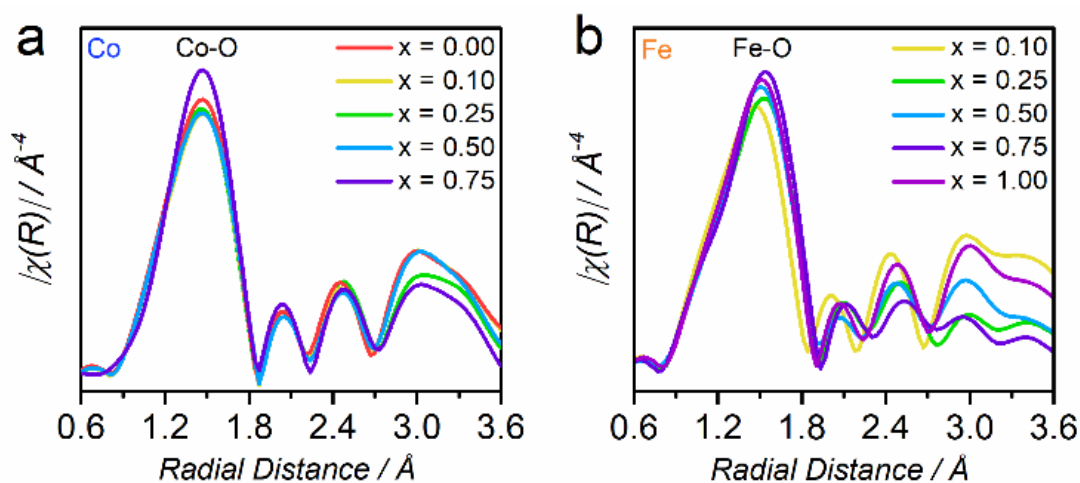


Figure 4.8 (a) EXAFS $k^3\chi(R)$ spectra of $\text{LaCo}_{1-x}\text{Fe}_x\text{O}_3$ ($x=0.00, 0.10, 0.25, 0.50, 0.75$) at Co K-edge. (b) EXAFS $k^3\chi(R)$ spectra of $\text{LaCo}_{1-x}\text{Fe}_x\text{O}_3$ ($x=0.10, 0.25, 0.50, 0.75, 1.00$) at Fe K-edge.

4.3.4 Magnetic studies

The temperature-dependent magnetizations were measured with a magnetic field (H) of 100 Oe under field-cooling procedures for all the samples $\text{LaCo}_{1-x}\text{Fe}_x\text{O}_3$ ($x=0.00, 0.10, 0.25, 0.50, 0.75, 1.00$) to reveal the spin structures of Co ions controlled by the Fe substitution ratios. In the high temperature area, the susceptibilities derived from the magnetizations ($\chi = M/H$) obey a paramagnetic Curie–Weiss law: $\chi = C/T - T_c$, where C is Curie constant (Figure 4.10b), and T_c is Curie–Weiss temperature. The field-cooled M - T curves of the $\text{LaCo}_{1-x}\text{Fe}_x\text{O}_3$ ($x=0.00, 0.10, 0.25, 0.50, 0.75, 1.00$) and the trend of Curie Temperature with the increase in Fe substitution are shown in Figure 4.9. By fitting the susceptibility versus T data in Figure 4.10a, an effective magnetic moment μ_{eff} can be obtained through $\mu_{\text{eff}} = \sqrt{8C} \mu_B$ (Table 4.1). Opinions diverge on the spin state of Co^{3+} ions in LaCoO_3 at room temperature. Some consider the spin state of Co^{3+} a mixture of high spin and intermediate spin. It springs from the fact that high-spin Co^{3+} state is preferred rather than low-spin Co^{3+} state when the Fe substitution ratios increase.²⁸ Many other recent theoretical and experimental studies revealed that the mixture of LS and HS states is more favorable.^{16,29} Here, we treated the spin state of Co^{3+} in LaCoO_3 as a mixture of high spin (HS: $t_{2g}^4 e_g^2$; $4.9 \mu_B$) (Figure 4.10a, inset) and low spin state (LS: $t_{2g}^6 e_g^0$; $0 \mu_B$) (Figure 4.10, inset).

Using the obtained values of μ_B , the volume fractions of Co ions in HS and LS states can be calculated from the following relationship:

$$\mu_{eff} = g\mu_B\sqrt{S_{HS}(S_{HS} + 1)V_{HS} + S_{LS}(S_{LS} + 1)V_{LS}}$$

where S_{HS} (= 2) and S_{LS} (= 0) are the S values, and V_{HS} and V_{LS} (= 1 - V_{HS}) are the volume fractions for Co^{3+} ions in HS and LS states, respectively. The ratios of Co^{3+} HS in $LaCo_{1-x}Fe_xO_3$ with $x=0.00, 0.10, 0.25, 0.50$ and 0.75 are exhibited in Figure 4.10c. When Fe is slightly substituted in $LaCoO_3$, from 0.00 to 0.10, the ratio of Co^{3+} HS increased from 4%, to 69.6%. When the Fe substitution ratio increases to 25 at%, the Co^{3+} HS ratio reaches more than that of $LaCo_{0.9}Fe_{0.1}O_3$, with a value of 70.8%. With more than 50 at% additional Fe, Co^{3+} HS ratio drops. We have found that, the $LaCo_{0.90}Fe_{0.10}O_3$, which has the best OER performance possesses an increased Co^{3+} HS ratio as compared to that of $LaCoO_3$. However, with higher Co^{3+} HS ratio, $LaCo_{0.75}Fe_{0.25}O_3$ has inferior performance compared to $LaCo_{0.90}Fe_{0.10}O_3$. This is mainly because a too high Co^{3+} HS ratio gives rise to increased e_g configuration, which results in a M-O binding energy larger smaller than optimal optimized one.¹⁴ Hence, the OER performance is not as good as $LaCo_{0.90}Fe_{0.10}O_3$. Besides, the phase transitions in the crystal structures of $LaCo_{1-x}Fe_xO_3$ also affect their OER activities. Despite being less critical as electronic structures, crystal structure has been reported to be a secondary descriptor for OER activity.³⁰ The structure transition when Fe substitution ratio is raised to more than 25 at% exerts an influence on the OER activity.

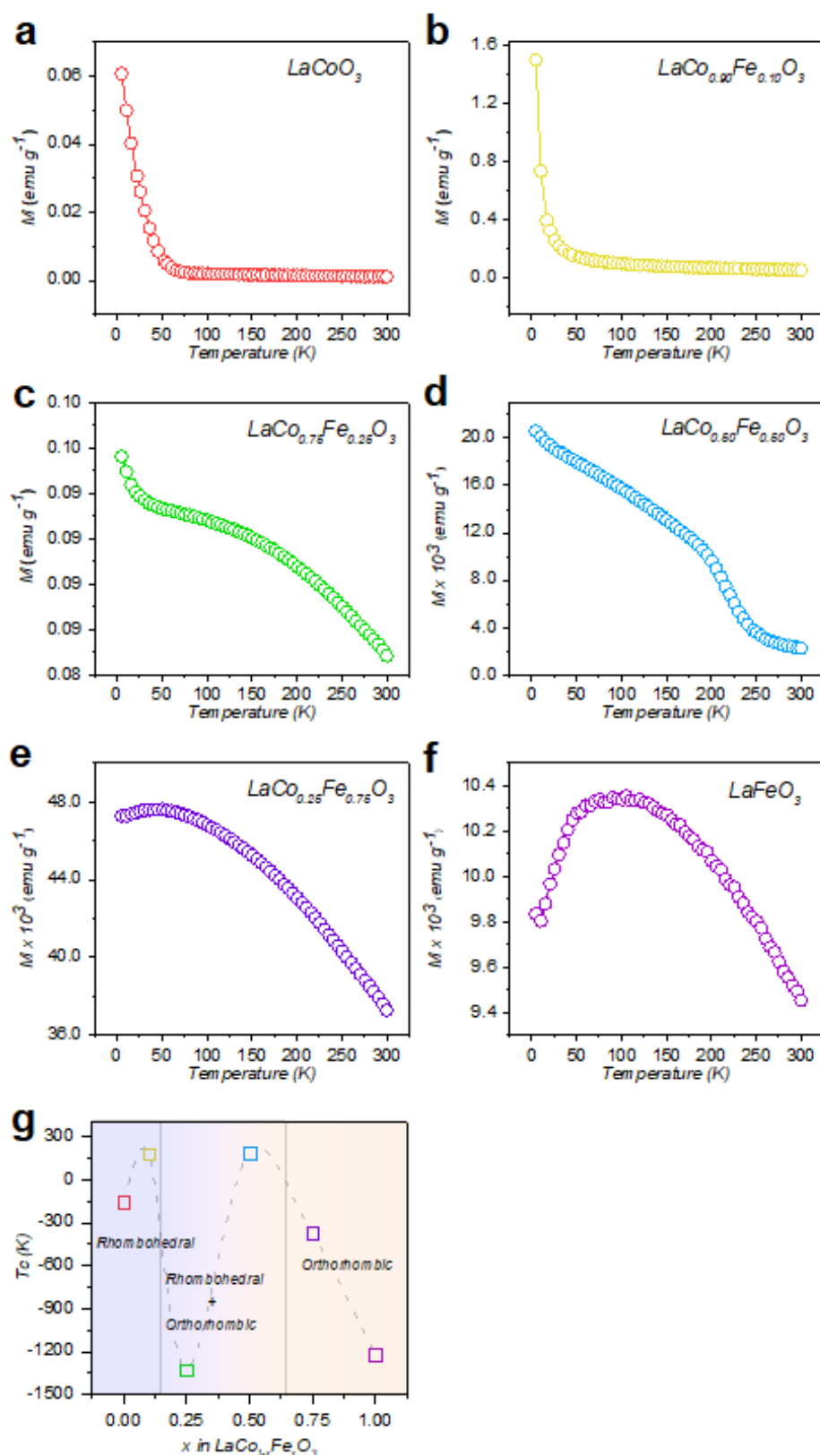


Figure 4.9 100Oe Field-cooled M-T curves of $\text{LaCo}_{1-x}\text{Fe}_x\text{O}_3$ ($x=0.00, 0.10, 0.25, 0.50, 0.75, 1.00$) and the trend of Curie Temperature with the increase in Fe substitution.

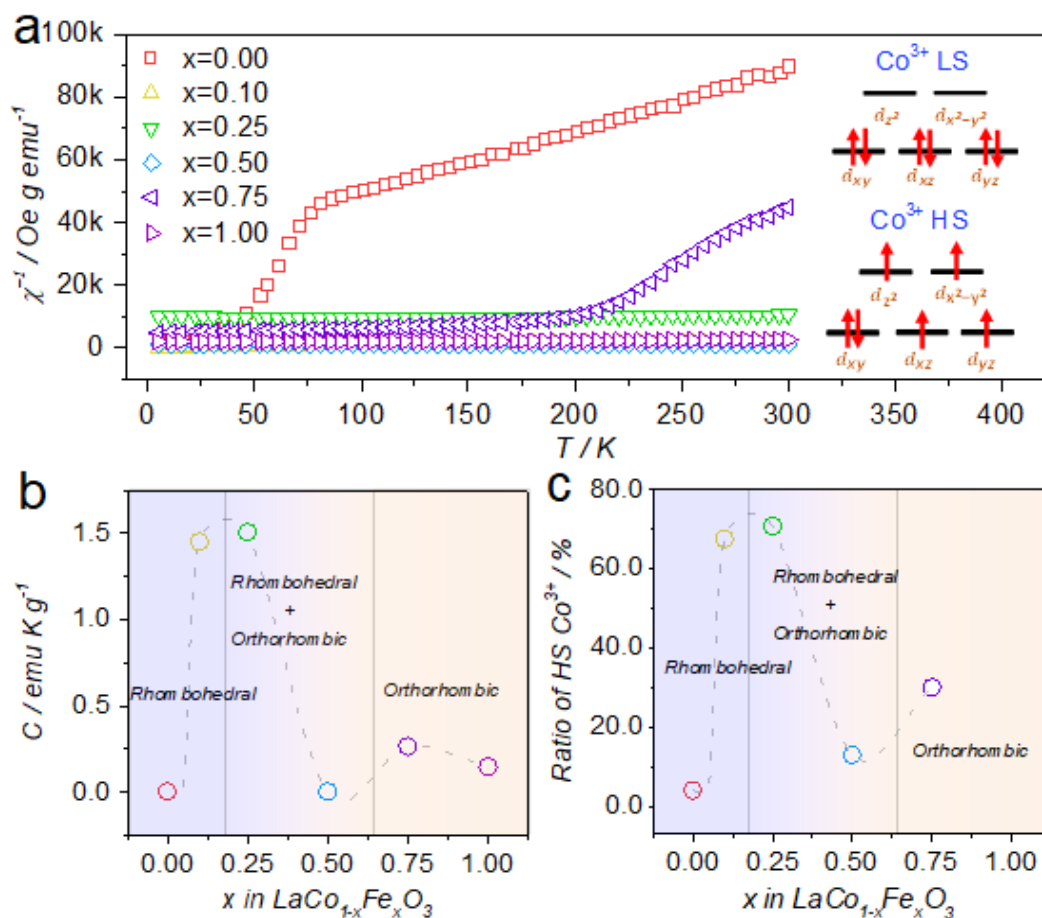


Figure 4.10 Spin structure analyses of $\text{LaCo}_{1-x}\text{Fe}_x\text{O}_3$. ($x=0.00, 0.10, 0.25, 0.50, 0.75, 1.00$) (a) The temperature-dependence inverse susceptibilities for $\text{LaCo}_{1-x}\text{Fe}_x\text{O}_3$ samples. The inset are the plots for Co^{3+} LS ($t_{2g}^6 e_g^0$, $S = 0$) and Co^{3+} HS ($t_{2g}^4 e_g^2$, $S = 2$) in the octahedral ligand-field. (b) Curie constant for $\text{LaCo}_{1-x}\text{Fe}_x\text{O}_3$. ($x=0.00, 0.10, 0.25, 0.50, 0.75, 1.00$). (c) The ratio of HS Co^{3+} in $\text{LaCo}_{1-x}\text{Fe}_x\text{O}_3$ with $x=0.00, 0.10, 0.25, 0.50, 0.75$.

Table 4.1 | Effective magnetic moment (μ_{eff}) for different spin states of Co^{3+} ions in $\text{LaCo}_{1-x}\text{Fe}_x\text{O}_3$ ($x=0.00, 0.10, 0.25, 0.50, 0.75$) (LS: low spin; HS: high spin).

Specimen			LaCoO_3	$\text{LaCo}_{0.9}\text{Fe}_{0.1}\text{O}_3$	$\text{LaCo}_{0.75}\text{Fe}_{0.25}\text{O}_3$	$\text{LaCo}_{0.5}\text{Fe}_{0.5}\text{O}_3$	$\text{LaCo}_{0.25}\text{Fe}_{0.75}\text{O}_3$
Curie Constant			0.0051	1.45	1.506	0.049	0.2656
Spin state	LS	HS	4%HS+96%LS	69.6%HS+30.4%LS	70.8%HS+29.2%LS	12.9%HS+87.1%LS	30%HS+70%LS
μ_{eff} (μ_B)	0	4.9	0.20	3.41	3.47	0.63	1.46

4.3.5 DFT calculations

The DFT calculations were carried out on LaCoO_3 and $\text{LaCo}_{0.9}\text{Fe}_{0.1}\text{O}_3$ by employing QUANTUM-ESPRESSO package. The detailed calculation methods and models can be found in experimental methods section. The computed TDOS (total density of states) for LaCoO_3 are shown in Figure 4.11a. Co (t_{2g}) and O (p) orbitals contribute to the peaks below E_F in the valence band. The peaks above E_F in the conduction band originate from both t_{2g} and e_g orbitals. All t_{2g} states below E_F are occupied and the density of states at the E_F are negligible (inset in Figure 4.11a). This indicates that Co^{3+} in LaCoO_3 stabilises in low spin state (LS: $t_{2g}^6e_g^0$)³¹ and LaCoO_3 exhibits an insulating nature.³² The spin state configuration is determined by the energy difference between crystal field splitting energy and Coulomb repulsion. The crystal field energy Δ_{cf} is only slightly larger than Hund exchange energy Δ_{ex} , thus, only small energy difference between LS and higher spin state exists.³² Co^{3+} is found to stabilises in a higher spin state in $\text{LaCo}_{0.9}\text{Fe}_{0.1}\text{O}_3$, the computed TDOS of which is shown in Figure 4.11b. A gap between minority spin t_{2g} states forms by the intersection of E_F (inset in Figure 4.11b), which indicates the half metallic feature of $\text{LaCo}_{0.9}\text{Fe}_{0.1}\text{O}_3$.³¹ Figure 4.11c and Figure 4.11d display the pDOS of Co d -band and p -band for ligand O in LaCoO_3 and $\text{LaCo}_{0.9}\text{Fe}_{0.1}\text{O}_3$, respectively. The pDOS for LaCoO_3 evidences the overlap between Co (t_{2g}) and O (p) states below Fermi level. The states on E_F for 10 at% Fe substituted LaCoO_3 are intermixed Co (e_g) – O(p) states³³. The strong hybridization between Co $3d$ states of e_g symmetry and oxygen $2p$ states leads to formation of broad σ^* bands, which cross over the E_F .³² This validates the half-metallic features of $\text{LaCo}_{0.9}\text{Fe}_{0.1}\text{O}_3$.³¹ The increased overlap of the Co and O in $\text{LaCo}_{0.9}\text{Fe}_{0.1}\text{O}_3$ indicates that Co $3d$ -O $2p$ covalency becomes stronger when 10 at% Fe is introduced in LaCoO_3 .^{11,34} Thus, Co^{3+} spin state transition from LS to higher spin state induced by 10 at% Fe substitution in LaCoO_3 gives rise to an insulator – half metal transition. The increase in the overlap between Co ($3d$) and O ($2p$) states lowers down the energy between occupied O $2p$ states and unoccupied Co $3d$ states. This ends up in enhanced Co $3d$ -O $2p$ covalency.¹³ The enhanced covalency enables $\text{LaCo}_{0.9}\text{Fe}_{0.1}\text{O}_3$ to be a more active catalyst than LaCoO_3 for OER.

Figure 4.11 Computed TDOS (total density of states) of LaCoO_3 with Co ions in low spin state (LS: $t_{2g}^6 e_g^0$) (a) and $\text{LaCo}_{0.9}\text{Fe}_{0.1}\text{O}_3$ with Co ions in higher spin state (b). Fermi level is denoted by vertical dashed line. Arrows correspond to spin-up and spin-down spin projection. Insets show the zoomed-in pDOS of LaCoO_3 and $\text{LaCo}_{0.9}\text{Fe}_{0.1}\text{O}_3$ from -1.5 eV to 1.5 eV relative to E_F . pDOS of the Co d states and O p states in LaCoO_3 (c) and $\text{LaCo}_{0.9}\text{Fe}_{0.1}\text{O}_3$ (d).

4.3.6 Interplay between Co^{3+} spin configuration and Co 3d-O 2p covalency

Figure 4.11e and Figure 4.11f show the schematic representation of O p -band and Co d -band (relative to E_F) derived from pDOS for LaCoO_3 and $\text{LaCo}_{0.9}\text{Fe}_{0.1}\text{O}_3$, respectively. As indicated by magnetic studies and TDOS calculations, majority of Co^{3+} in LaCoO_3 possesses low spin state. However, 10 at% of additional Fe in LaCoO_3 results in increased spin state of Co^{3+} . When Co^{3+} has low spin state, the Co 3d states hybridize with O p states via the occupied $\text{Co}(t_{2g})\text{-O}(p)$ just below E_F .³¹ A Co^{3+} with higher spin state presents strong hybridization between $\text{Co}(e_g)\text{-O}(p)$ states on E_F .³⁵ Thus, transitions from LS Co^{3+} to higher spin state Co^{3+} states result in enhanced hybridization between Co 3d states and O p states. Besides, higher spin state Co^{3+} leads to Co 3d states with narrower gap between e_g and t_{2g} , which indicates the insulator to half-metal transition

for 10 at% Fe substituted LaCoO_3 . This has been evidenced by the delocalised feature of electrons on the Fe p states in $\text{LaCo}_{0.9}\text{Fe}_{0.1}\text{O}_3$ in Fe K-edge XANES data. The better OER performance of $\text{LaCo}_{0.9}\text{Fe}_{0.1}\text{O}_3$ than LaCoO_3 is resulted from stronger Co $3d$ -O $2p$ covalency. It is originated from the Co^{3+} spin configuration transition from LS to higher spin state, which leads to insulator to half-metal transition and increases the electroconductivity. Hence, the increase in Co^{3+} spin state induces half-metal property of $\text{LaCo}_{0.9}\text{Fe}_{0.1}\text{O}_3$, which gives rise to enhanced Co $3d$ -O $2p$ covalency and promoted OER performance.

4.4 Summary

In summary, we have studied a substitution strategy to tune the electronic structure of LaCoO_3 in terms of Co $3d$ -O $2p$ covalency for enhancing the OER activity. The octahedral sites of rhombohedral distorted perovskite structure LaCoO_3 were substituted by Fe. $\text{LaCo}_{0.90}\text{Fe}_{0.10}\text{O}_3$ exhibited improved OER activity as compared to LaCoO_3 . The enlarged Co $3d$ -O $2p$ covalency computed by DFT calculations interpreted this activity enhancement after 10 at% Fe substitutions. Besides, magnetic studies and DFT calculation revealed that the increase in spin state of Co^{3+} ratio is due to 10 at% Fe substitutions. OER result shows that the onset potential for $\text{LaCo}_{0.90}\text{Fe}_{0.10}\text{O}_3$ is comparable to that of 80 nm LaCoO_3 with optimal e_g configuration¹⁶ and is close to that of benchmarked IrO_2 , indicating the effectiveness of 10 at% of Fe substitution on boosting OER activity of LaCoO_3 . This fine-tune strategy by Fe substitution enriches the existing methods to adjust electronic structure and it is promising to be extended to other oxide catalysts.

4.5 Reference

- (1) Trasatti, S. Electrocatalysis in the Anodic Evolution of Oxygen and Chlorine. *Electrochimica Acta* **1984**, 29 (11), 1503–1512. [https://doi.org/10.1016/0013-4686\(84\)85004-5](https://doi.org/10.1016/0013-4686(84)85004-5).
- (2) Fabbri, E.; Habereder, A.; Waltar, K.; Kötzer, R.; Schmidt, T. J. Developments and Perspectives of Oxide-Based Catalysts for the Oxygen Evolution Reaction. *Catal. Sci. Technol.* **2014**, 4 (11), 3800–3821. <https://doi.org/10.1039/C4CY00669K>.
- (3) 4.Pdf.
- (4) Lu, Z.; Wang, H.; Kong, D.; Yan, K.; Hsu, P.-C.; Zheng, G.; Yao, H.; Liang, Z.; Sun, X.; Cui, Y. Electrochemical Tuning of Layered Lithium Transition Metal Oxides for Improvement of Oxygen Evolution Reaction. *Nat Commun* **2014**, 5 (1), 4345. <https://doi.org/10.1038/ncomms5345>.

- (5) Kim, T. W.; Woo, M. A.; Regis, M.; Choi, K.-S. Electrochemical Synthesis of Spinel Type ZnCo_2O_4 Electrodes for Use as Oxygen Evolution Reaction Catalysts. *J. Phys. Chem. Lett.* **2014**, *5* (13), 2370–2374. <https://doi.org/10.1021/jz501077u>.
- (6) Wei, C.; Feng, Z.; Scherer, G. G.; Barber, J.; Shao-Horn, Y.; Xu, Z. J. Cations in Octahedral Sites: A Descriptor for Oxygen Electrocatalysis on Transition-Metal Spinel. *Adv. Mater.* **2017**, *29* (23), 1606800. <https://doi.org/10.1002/adma.201606800>.
- (7) Read, M. S. D.; Saiful Islam, M.; Watson, G. W.; King, F.; Hancock, F. E. Defect Chemistry and Surface Properties of LaCoO_3 . *J. Mater. Chem.* **2000**, *10* (10), 2298–2305. <https://doi.org/10.1039/b002168g>.
- (8) Han, B.; Risch, M.; Lee, Y.-L.; Ling, C.; Jia, H.; Shao-Horn, Y. Activity and Stability Trends of Perovskite Oxides for Oxygen Evolution Catalysis at Neutral PH. *Phys. Chem. Chem. Phys.* **2015**, *17* (35), 22576–22580. <https://doi.org/10.1039/C5CP04248H>.
- (9) Hong, W. T.; Risch, M.; Stoerzinger, K. A.; Grimaud, A.; Suntivich, J.; Shao-Horn, Y. Toward the Rational Design of Non-Precious Transition Metal Oxides for Oxygen Electrocatalysis. *Energy Environ. Sci.* **2015**, *8* (5), 1404–1427. <https://doi.org/10.1039/C4EE03869J>.
- (10) Lee, H. Y.; Goodenou, J. B. Sr- and Ni-Doped LaCoO_3 and LaFeO_3 Perovskites. 8.
- (11) Mefford, J. T.; Rong, X.; Abakumov, A. M.; Hardin, W. G.; Dai, S.; Kolpak, A. M.; Johnston, K. P.; Stevenson, K. J. Water Electrolysis on $\text{La}_{1-x}\text{Sr}_x\text{CoO}_{3-\delta}$ Perovskite Electrocatalysts. *Nature communications* **2016**, *7*, 11053.
- (12) Grimaud, A.; Diaz-Morales, O.; Han, B.; Hong, W. T.; Lee, Y.-L.; Giordano, L.; Stoerzinger, K. A.; Koper, M. T.; Shao-Horn, Y. Activating Lattice Oxygen Redox Reactions in Metal Oxides to Catalyze Oxygen Evolution. *Nature chemistry* **2017**, *9* (5), 457.
- (13) Yang, C.; Grimaud, A. Factors Controlling the Redox Activity of Oxygen in Perovskites: From Theory to Application for Catalytic Reactions. *Catalysts* **2017**, *7* (5), 149. <https://doi.org/10.3390/catal7050149>.
- (14) Vojvodic, A.; Norskov, J. K. Optimizing Perovskites for the Water-Splitting Reaction. *Science* **2011**, *334* (6061), 1355–1356. <https://doi.org/10.1126/science.1215081>.
- (15) Suntivich, J.; May, K. J.; Gasteiger, H. A.; Goodenough, J. B.; Shao-Horn, Y. A Perovskite Oxide Optimized for Oxygen Evolution Catalysis from Molecular Orbital Principles. *Science* **2011**, *334* (6061), 1383–1385.
- (16) Zhou, S.; Miao, X.; Zhao, X.; Ma, C.; Qiu, Y.; Hu, Z.; Zhao, J.; Shi, L.; Zeng, J. Engineering Electrocatalytic Activity in Nanosized Perovskite Cobaltite through Surface Spin-State Transition. *Nat Commun* **2016**, *7* (1), 11510. <https://doi.org/10.1038/ncomms11510>.
- (17) Cheng, X.; Fabbri, E.; Nachttegaal, M.; Castelli, I. E.; El Kazzi, M.; Haumont, R.; Marzari, N.; Schmidt, T. J. Oxygen Evolution Reaction on $\text{La}_{1-x}\text{Sr}_x\text{CoO}_3$ Perovskites: A Combined Experimental and Theoretical Study of Their Structural, Electronic, and Electrochemical Properties. *Chem. Mater.* **2015**, *27* (22), 7662–7672. <https://doi.org/10.1021/acs.chemmater.5b03138>.
- (18) Abreu-Sepulveda, M. A.; Dhital, C.; Huq, A.; Li, L.; Bridges, C. A.; Paranthaman, M. P.; Narayanan, S. R.; Quesnel, D. J.; Tryk, D. A.; Manivannan, A. The Influence of Fe Substitution in Lanthanum Calcium Cobalt Oxide on the Oxygen Evolution Reaction in Alkaline Media. *J. Electrochem. Soc.* **2016**, *163* (9), F1124–F1132. <https://doi.org/10.1149/2.1311609jes>.
- (19) Xiao, C.; Lu, X.; Zhao, C. Unusual Synergistic Effects upon Incorporation of Fe and/or Ni into Mesoporous Co_3O_4 for Enhanced Oxygen Evolution. *Chem. Commun.* **2014**, *50* (70), 10122. <https://doi.org/10.1039/C4CC04922E>.

- (20) Zhu, Y.; Zhou, W.; Chen, Y.; Yu, J.; Liu, M.; Shao, Z. A High-Performance Electrocatalyst for Oxygen Evolution Reaction: $\text{LiCo}_{0.8}\text{Fe}_{0.2}\text{O}_2$. *Adv. Mater.* **2015**, *27* (44), 7150–7155. <https://doi.org/10.1002/adma.201503532>.
- (21) Weidenthaler, C. Pitfalls in the Characterization of Nanoporous and Nanosized Materials. *Nanoscale* **2011**, *3* (3), 792. <https://doi.org/10.1039/c0nr00561d>.
- (22) Liang, H.; Hong, Y.; Zhu, C.; Li, S.; Chen, Y.; Liu, Z.; Ye, D. Influence of Partial Mn-Substitution on Surface Oxygen Species of LaCoO_3 Catalysts. *Catalysis Today* **2013**, *201*, 98–102. <https://doi.org/10.1016/j.cattod.2012.04.036>.
- (23) 24.Pdf.
- (24) Stoerzinger, K. A.; Qiao, L.; Biegalski, M. D.; Shao-Horn, Y. Orientation-Dependent Oxygen Evolution Activities of Rutile IrO_2 and RuO_2 . *J. Phys. Chem. Lett.* **2014**, *5* (10), 1636–1641. <https://doi.org/10.1021/jz500610u>.
- (25) Chang, J. Co K-Edge XANES and Spin-State Transition of RCoO_3 (R=La, Eu). *Physica B: Condensed Matter* **2003**, 329–333, 826–828. [https://doi.org/10.1016/S0921-4526\(02\)02595-4](https://doi.org/10.1016/S0921-4526(02)02595-4).
- (26) Cabaret, D.; Bordage, A.; Juhin, A.; Arfaoui, M.; Gaudry, E. First-Principles Calculations of X-Ray Absorption Spectra at the K-Edge of 3d Transition Metals: An Electronic Structure Analysis of the Pre-Edge. *Phys. Chem. Chem. Phys.* **2010**, *12* (21), 5619. <https://doi.org/10.1039/b926499j>.
- (27) 28.Pdf.
- (28) 29.Pdf.
- (29) Karpinsky, D. V.; Troyanchuk, I. O.; Bärner, K.; Szymczak, H.; Tovar, M. Crystal Structure and Magnetic Ordering of the $\text{LaCo}_{1-x}\text{Fe}_x\text{O}_3$ System. *J. Phys.: Condens. Matter* **2005**, *17* (46), 7219–7226. <https://doi.org/10.1088/0953-8984/17/46/006>.
- (30) Hong, W. T.; Welsch, R. E.; Shao-Horn, Y. Descriptors of Oxygen-Evolution Activity for Oxides: A Statistical Evaluation. *The Journal of Physical Chemistry C* **2015**, *120* (1), 78–86.
- (31) Knížek, K.; Novák, P.; Jiráček, Z. Spin State of LaCoO_3 : Dependence on CoO_6 Octahedra Geometry. *Phys. Rev. B* **2005**, *71* (5), 054420. <https://doi.org/10.1103/PhysRevB.71.054420>.
- (32) Korotin, M. A.; Ezhov, S. Yu.; Solovyev, I. V.; Anisimov, V. I.; Khomskii, D. I.; Sawatzky, G. A. Intermediate-Spin State and Properties of LaCoO_3 . *Phys. Rev. B* **1996**, *54* (8), 5309–5316. <https://doi.org/10.1103/PhysRevB.54.5309>.
- (33) 35.Pdf.
- (34) Rong, X.; Parolin, J.; Kolpak, A. M. A Fundamental Relationship between Reaction Mechanism and Stability in Metal Oxide Catalysts for Oxygen Evolution. *ACS Catal.* **2016**, *6* (2), 1153–1158. <https://doi.org/10.1021/acscatal.5b02432>.
- (35) Fuchs, D.; Merz, M.; Nagel, P.; Schneider, R.; Schuppler, S.; von Löhneysen, H. Double Exchange via t_{2g} Orbitals and the Jahn-Teller Effect in Ferromagnetic $\text{La}_{0.7}\text{Sr}_{0.3}\text{CoO}_3$ Probed by Epitaxial Strain. *Phys. Rev. Lett.* **2013**, *111* (25), 257203. <https://doi.org/10.1103/PhysRevLett.111.257203>.

Chapter 5

Mastering surface reconstruction of metastable spinel oxides for better water oxidation

A rational design of spinel catalysts can be guided by studying the structural/elemental properties which determine the reaction mechanism and activity. Here, OER performance and surface evolution for $\text{ZnCo}_{2-x}\text{Ni}_x\text{O}_4$ spinel oxides have been investigated. Stable $\text{ZnCo}_{2-x}\text{Ni}_x\text{O}_4$ ($x=0-0.4$) follows adsorbates evolving mechanism (AEM) under OER conditions. Lattice oxygen participate in the OER of metastable $\text{ZnCo}_{2-x}\text{Ni}_x\text{O}_4$ ($x=0.6, 0.8$) which gives rise to continuously formed oxyhydroxide as surface-active species and consequently enhanced OER activity. $\text{ZnCo}_{1.2}\text{Ni}_{0.8}\text{O}_4$ exhibits performance superior to the benchmarked IrO_2 . By using density functional theory (DFT) calculations, we find that the relative position of O p-band and M_{Oh} (Co and Ni in octahedron) d-band centre in $\text{ZnCo}_{2-x}\text{Ni}_x\text{O}_4$ ($x=0-2$) correlates with its stability as well as the possibility for lattice oxygen to participate in OER. Our work illuminates the design of highly active metastable spinel electrocatalysts through the prediction of the reaction mechanism and OER activity by determining the relative positions of the O p-band and M_{Oh} d-band centre.

*This section published substantially as Y. Duan, S. Sun, Y. Sun, S. Xi, , X. Chi, Q. Zhang, X. Ren, J. Wang, S. J. Ong, Y. Du, L. Gu, A. Grimaud, & Z. J. Xu, Mastering Surface Reconstruction of Metastable Spinel Oxides for Better Water Oxidation. *Advanced Materials*, **31**(12), 1807898 (2019). DOI: 10.1002/adma.201807898.

5.1 Introduction

The development of efficient electrocatalysts which lower the overpotential of oxygen evolution reaction (OER) is of fundamental importance in improving the overall efficiency of fuel production by water electrolysis.^{1,2} Among a plethora of catalysts being studied on, the precious metal oxides (i.e. IrO₂ and RuO₂) are commercially used ones.^{3,4} However, their elemental scarcity and high cost have aroused a search for cost-effective OER electrocatalyst such as transition metal oxides. To develop transition metal oxides as highly active catalysts, activity descriptors⁵ including electron occupancy⁶, covalency⁷, structure^{8,9} and exchange interaction¹⁰ have been established to correlate with M–O binding energy^{10,11}. However, recent studies have found plenty of unstable materials which undergo surface amorphization after OER cycles^{12,13}. It is almost impossible to predict activity of these materials as a function of the oxygen binding energy based on the ideal surfaces as a consequence of the constantly evolving surface during OER.^{14–18} The correlation of activity and stability of most catalysts, though, including metal oxides such as perovskite (e.g., LaMO₃^{19,20}, SrMO₃^{16,20}) and even non-oxide-based catalysts such as metal sulfides, selenides and phosphides²¹ (e.g., NiSe¹⁴, CoSe₂²², Ni₂P²³, Co₂P²⁴, etc.), have been found to come at the expense of each other^{16,20,25}. For example, highly stable catalysts such as LaCoO₃ normally do not have as high activity as Ba_{0.5}Sr_{0.5}Co_{0.8}Fe_{0.2}O_{3-δ} (BSCF)^{15,26} which yields at least an order of magnitude higher activity for OER than that of IrO₂ in alkaline conditions. The surface of the most active oxides such as BSCF, however, were observed to reconstruct into a structure with edge-shared MO₆ right after ball milling²⁵. Hence, stability is a critical parameter regarding to seeking highly active electrocatalysts.²⁵ Understanding the origin of the relation between stability and activity of oxides are crucial for rational design of high-performance catalysts.

Many descriptors have been developed for investigating the relationship between activity and stability of metal oxides such as monoxides and perovskite oxides. Surface density of defects is found to control the stability and activity of SrRuO₃ films.¹⁶ The defective surface is highly active, simultaneously, the residual polarity arises from the defects would increase the surface energy and results in unstable surfaces²⁷. Besides, simple parameters like the number of d electrons (Nd) have also been used to estimate the stability and activity of metal oxides including MO, LaBO₃ and SrBO₃^{28,29}. As the number of d electrons is increased through the *nd* series, more electrons are to accommodate into the bands. As more electrons fill into the antibonding e_g states, the bonding energy, so as the stability, decreases linearly with the number of d electrons.

Simultaneously, the activity of these metal oxides is found to increase along d series. However, Nd is not plausible in estimating the stability and activity for multimetal oxides. O p-band center (relative to E_F) which describes the surface oxygen exchange efficiency emerges as a descriptor to evaluate both stability and activity of perovskite^{30,31}. Surface amorphization along with increased current and electrochemical active surface area can be easily induced when the distance between O p-band center and E_F for a perovskite is closer than 2.2 eV²⁵, to which extent, the formation energy of oxygen vacancies drops³², and the structural relaxation is initiated. Tolerance factor also influences the activity/stability behavior. A tolerance factor higher than 1 strongly destabilizes the structure of the perovskites. For example, $\text{La}_{0.3}(\text{Ba}_{0.5}\text{Sr}_{0.5})_{0.7}\text{Co}_{0.8}\text{Fe}_{0.2}\text{O}_3$ (LBSCF), having La^{3+} with smaller cationic radius substituting Ba^{2+} and Sr^{2+} , gives rises to lower transition metal oxidation states. It is more stable whereas less active than BSCF in which large ionic radii of Ba^{2+} and Sr^{2+} couples with the small Co^{4+} and Fe^{4+} radii, giving a high tolerance factor.³³ Unstable perovskite oxides with high O p-band center (relative to E_F) and tolerance factor give rise to a non-concerted proton-electron transfer mechanism involving the participation of lattice oxygen for OER. This mechanism is in contrast to the conventional concerted proton-electron transfer mechanism works on stable materials such as LaCoO_3 , LaMnO_3 , and $\text{La}_{0.4}\text{Sr}_{0.6}\text{CoO}_3$ ²⁵ The intermediates species formed during OER process such as $^*\text{OH}$, $^*\text{O}$ and $^*\text{OOH}$ are all attached on the B sites atoms, the real active sites, of these electrocatalysts.³⁴ In this lattice oxygen participated mechanism, ineffective electron donation by the B-site cation results in favorable formation of the surface V_o intermediates, hence ends up in decreased catalyst stability. It applies for perovskite materials such as $\text{SrCoO}_{3-\delta}$ ³⁴ and LaNiO_3 ¹⁹, which are highly active but less stable under cycling.

The above-mentioned descriptors can well describe the activity/stability behaviour for monoxides and perovskite oxides. However, the relationship between activity and stability for spinel oxides are not yet been explored. Spinel oxides have been drawing growing attention to be promising catalysts as well.^{35,36} Interest in enhancing its activity generates investigations on underlying science such as catalytically active sites³⁷ and facets³⁸ due to complex spinel structure with two different sites, tetrahedral (Td) site and octahedral (Oh) site³⁹. Electron filling on e_g orbitals of octahedral site has been established as a descriptor for the OER activity of spinel oxides.⁴⁰ This enables metal cation substitutions and composition adjustments to boost the OER activity of spinel oxides. For example, the substitution of Co for Mn and Ni in $\text{Co}_3\text{O}_{4-\delta}$

optimises e_g filling and promotes OER.⁴⁰ However, the stability for $\text{Co}_3\text{O}_{4-\delta}$, $\text{MnCo}_2\text{O}_{4-\delta}$ and $\text{NiCo}_2\text{O}_{4-\delta}$ is very different from each other. $\text{Co}_3\text{O}_{4-\delta}$, $\text{MnCo}_2\text{O}_{4-\delta}$ are stable under OER conditions, whereas $\text{NiCo}_2\text{O}_{4-\delta}$ exhibits a similar behaviour as BSCF with growing current density and pseudocapacitive redox peaks upon cycling⁴¹. Studies have verified that the incorporation of Ni in spinel Co_3O_4 induces a surface modification with nickel/cobalt oxyhydroxide formed on the surface, which gives rise to increased activity¹². However, this is not sufficient in explaining the origin of the correlation between observed activity and stability of the oxides since it is undeniable that $\text{Co}_3\text{O}_{4-\delta}$ and $\text{NiCo}_2\text{O}_{4-\delta}$ are both liable to some extent of surface modification during OER process⁴¹, though in different respects. The elusiveness of OER mechanisms for stable and unstable spinel oxides hinders the understanding of their different surface modifications, hence the different behaviour regarding to OER activity and stability. Besides, insufficient studies are yet on the stability of spinel oxides and insights on the mechanism of surface reconstruction of spinel oxides under OER conditions have not been provided.

The metastable $\text{ZnCo}_{2-x}\text{Ni}_x\text{O}_4$ are found to exhibit continuously increased OER currents along with cyclic voltammetry (CV) cycles. Their activities triple at the thousands cycle and are superior to that of benchmarked IrO_2 . We have disclosed that the surface of these spinels deprotonate to (oxy)hydroxide via a non-concerted proton-electron transfer process under OER conditions. The lattice oxygen plays a key role during the surface reconstruction process in indorsing structure relaxation, which gives rise to continuously formed (oxy)hydroxide and enhanced OER activity. This has been supported by the modified relative position of O p-band center (relative to E_F) and M_{Oh} d-band center (relative to E_F), so as the potential lattice oxygen participated OER mechanism for metastable $\text{ZnCo}_{2-x}\text{Ni}_x\text{O}_4$ through density function theory (DFT) calculations. This work suggests tuning the relative position of O p-band center and M_{Oh} d-band center would trigger lattice oxygen participation in OER for spinel oxides and promote OER activities. The findings offer crucial insights in designing highly active metastable spinel oxide catalysts with lattice oxygen participated OER mechanisms.

5.2 Experimental Methods

5.2.1 Material synthesis

ZnCo_{2-x}Ni_xO₄ powders were synthesized by a thermal decomposition method. Detailed synthesis method can be referred to Chapter 3.1.2.

5.2.2 Material Characterizations

The crystal structure was obtained by Bruker D8 Advance with Cu-K_α radiation ($\lambda = 1.5418 \text{ \AA}$). The (Brunauer-Emitter-Teller) BET specific surface areas of the materials were obtained using an ASAP Tristar II 3020. XANES and extended EXAFS characterizations were carried out at the XAFCA beamline of the Singapore Synchrotron Light Source (SSLS) to obtain structural information⁴². Data reduction, data analysis, and EXAFS fitting were performed with the Athena and Artemis software packages⁴³. High-resolution transmission electron microscopy (HRTEM) and electron energy loss spectroscopy (EELS) were conducted in the Institute of Physics, Chinese Academy of Sciences by a JEOL 2100F transition electron microscope at the operating voltage of 200 kV to investigate morphology and composition after OER cycling compared with that of the as-synthesized materials. Both the raw material and cycled material were prepared by suspending them in ethanol by ultrasonication. The suspensions were then dropped onto carbon film coated Cu TEM grids and dried at room temperature. XPS measurements were conducted by a PHI-5400 with Al Ka beam source (250 W) and position-sensitive detector (PSD). The binding energy resolution is 0.8 eV, angle resolution is 45° and the detection limit is 80 K CPS. Base pressure of the measurement chamber is 3.0×10^{-7} Pa. The Ar ion (voltage 12 kV, current 4.2 mA) sputtering speed is 0.28 nm/s over an area of $300 \times 300 \text{ \mu m}^2$. Data from the measurements were calibrated using the adventitious carbon peak of the C 1s spectra (EB = 284.8 eV). Soft XAS and XMCD: Pairs of soft X-ray absorption spectra (μ_+/μ_-) are measured with circularly polarized x-rays with ± 1 T magnetic fields applying to the samples. The XMCD spectra arise from the difference between the μ_+ and μ_- spectra.⁴⁴ Soft XAS and XMCD were obtained at SINS beamline of SSLS⁴⁵.

5.2.3 Electrochemical Tests

The electrochemical tests were carried out by the three-electrode method in a plastic cell with $\text{ZnCo}_{2-x}\text{Ni}_x\text{O}_4$ as working electrode, and mercury-mercury oxide electrode (Hg/HgO) and Pt plate serving as reference and counter electrodes, respectively. 10 mg perovskite material and 2 mg carbon black were dispersed in a mixed solution of 0.4 mL isopropyl alcohol (IPA), 1.59 mL DI water and 10 μL Nafion perfluorinated resin to prepare the catalyst ink. The mixture was sonicated for 10 mins to achieve homogenized dispersion of spinel and carbon. The spinel material was dispersed in a diluted IPA containing 5% Nafion. The mass ratio of spinel material: carbon black was maintained at 4 : 1. The volume ratios of DI water: IPA: Nafion were maintained at 4 : 1 : 0.05. 10 μL of the ink was dropped onto a newly polished glassy carbon electrode (0.196 cm^2). All electrochemical potentials here were against the reversible hydrogen electrode (RHE) under the condition with 1.0 M KOH. The conversion between potentials vs. Hg/HgO and vs. RHE was performed by the equation below. The Ohmic drop has been determined by electrochemical impedance spectroscopy.

$$E (\text{vs. RHE}) / \text{V} = E (\text{vs. Hg/HgO}) / \text{V} + E_{\text{Hg/HgO}} (\text{vs. SHE}) / \text{V} + 0.059 \times \text{pH} / \text{V}$$

$$(E_{\text{Hg/HgO}} (\text{vs. SHE}) / \text{V} = 0.098 / \text{V vs. SHE at } 25^\circ\text{C})$$

The oxygen evolution reaction was evaluated by cyclic voltammetry (CV) between 0.904 and 1.624 V (vs. RHE) at a scan rate of 10 mV s^{-1} . The samples prepared for TEM, XAS, XMCD and XPS measurements were cycled using this program for 1000 cycles with the scan rate of 10 mVs^{-1} .

pH dependent experiments were conducted on pristine and cycled $\text{ZnCo}_{2-x}\text{Ni}_x\text{O}_4$ to study the reaction mechanism. The second cycle for each CV scan was extracted to analyze the pH dependence of pristine $\text{ZnCo}_{2-x}\text{Ni}_x\text{O}_4$ and the 1000th cycle of CV has been extracted to study the pH dependence of cycled $\text{ZnCo}_{2-x}\text{Ni}_x\text{O}_4$. CV measurements for each sample were carried out in 0.1M KOH (pH=13.12), 0.3162M (pH=13.54) and 1M (pH=13.98) with a scan rate of 10 mVs^{-1} using three working electrodes from 1.1 to 1.7 V (vs. RHE). 0.1M, 0.316M and 1M KOH solutions were prepared and the pH of these solutions were determined by pH meter. OER experiments were conducted to the same RHE scale to ensure that the OER overpotential with respect to the equilibrium $\text{O}_2/\text{H}_2\text{O}$ redox potential remained identical across different values of pH⁴⁶. Nernstian/non-Nernstian potential shift was obtained by CV measurements carried out in various pH at a scan rate of 200 mVs^{-1} to observe the shift to lower potential for the redox peak.

5.2.4 DFT Calculations

Researchers initially use metal *d*-band orbitals to describe the trend discovered in the adsorption energy of molecules on transition metals and metal alloys. They successfully correlated the *d*-band centre with electrocatalytic performance^{47–49}. Motivated by this, researchers established the occupancy of e_g electron for transition metal oxides as an activity descriptor, which correlates the surface adsorbate binding with the catalytic activity for transition metal oxides.¹⁰ Later, an ionic-covalent metal-oxygen bond is found to describe electronic structures of metal oxides more accurately³⁹, especially when oxygen redox reaction is considered in the electrochemical process³². To figure out the interaction between metal *d*-band and oxygen *p*-band orbitals for a better understanding of the electronic properties and electrocatalytic performances of substituted spinel oxides, we have carried out first-principles DFT+U calculations on the transition metal *d* states and oxygen *p* states for $\text{ZnCo}_{2-x}\text{Ni}_x\text{O}_4$. The DFT calculations have been done based on the assumption that ZnCo_2O_4 is a representative spinel oxide with Zn^{2+} occupying tetrahedral (Td) site and Co^{3+} staying in octahedral (Oh) site³⁹. When Ni is substituted into ZnCo_2O_4 , Ni atoms would take the place of Co atoms in octahedron. This is due to the preferential Td site occupancy of divalent Zn in spinel⁵⁰ and the large formation energy for antisite defects, $E_{\text{Zn-M}}$ (M denotes metal cations in octahedral sites)⁵¹. Besides, Ni and Co cations with a $3d^{6-8}$ electron configuration favor octahedral coordination (according to the crystal field stability energy).^{52–55} This has been verified by XAFS characterizations.

All density functional theory (DFT) calculations were carried out by the Vienna Ab-initio Simulation Package (VASP)⁷⁰, employing the projected augmented wave (PAW) model. The Perdew-Burke-Ernzerhof (PBE) functional, within the generalized gradient approximation (GGA) approach, was used to describe the exchange and correlation effect.⁵⁶ The GGA+U calculations were performed using the model proposed by Dudarev et al.,⁵⁷ with the U_{eff} ($U_{\text{eff}} = \text{Coulomb } U - \text{exchange } J$) values of 4.7 eV, 3.3 eV, and 6.4 eV for Zn, Co, and Ni, respectively. In all the cases, the cutoff energy was set to be 450 eV. The Monkhorst-Pack⁵⁸ k-point mesh was set to be $6 \times 6 \times 6$ and $9 \times 9 \times 9$ for bulk optimization and electronic structure calculations, respectively. Of all the calculations, the Brillouin zone was integrated using tetrahedron method

with Blöch corrections. The force and energy convergence tolerance were set to be $0.05 \text{ eV } \text{\AA}^{-1}$ and 10^{-5} eV , respectively.

The normal $\text{ZnCo}_{2-x}\text{Ni}_x\text{O}_4$ spinels were constructed with Zn^{2+} located at the tetrahedral sites and Co^{3+} and Ni^{3+} at the octahedral sites. The value of x was controlled by substituting Co atoms by Ni in spinel ZnCo_2O_4 . Both the O p -band centre and M_{Oh} d -band centre were computed by taking the weighted mean energy of the projected density of states of O- p and M_{Oh} d -states (both occupied and unoccupied states) relative to the Fermi level.

5.3 Results and Discussions

5.3.1 Material characterizations

Pure $\text{ZnCo}_{2-x}\text{Ni}_x\text{O}_4$ ($x=0.0, 0.2, 0.4, 0.6, 0.8$) phases were synthesized by thermal decomposition methods. Figure 5.1 exhibits the XRD patterns of the as-synthesized $\text{ZnCo}_{2-x}\text{Ni}_x\text{O}_4$ ($x=0.0, 0.2, 0.4, 0.6, 0.8$) oxides. With the increased amount of Ni replacing Co, a continuous peak shift towards smaller angle is observed, consistent with the increased lattice parameter for $\text{ZnCo}_{2-x}\text{Ni}_x\text{O}_4$ ($x=0.0, 0.2, 0.4, 0.6, 0.8$) from $8.124(7) \text{ \AA}$ to $8.180(7) \text{ \AA}$ (Table 5.1). This increase in lattice parameter corresponds to the simultaneous increase of Ni-O (Figure 5.1c), Co-O (Figure 5.1c) and Zn-O bond lengths (Figure 5.2), and an expanded unit cell as well as a decreased thermodynamic stability.

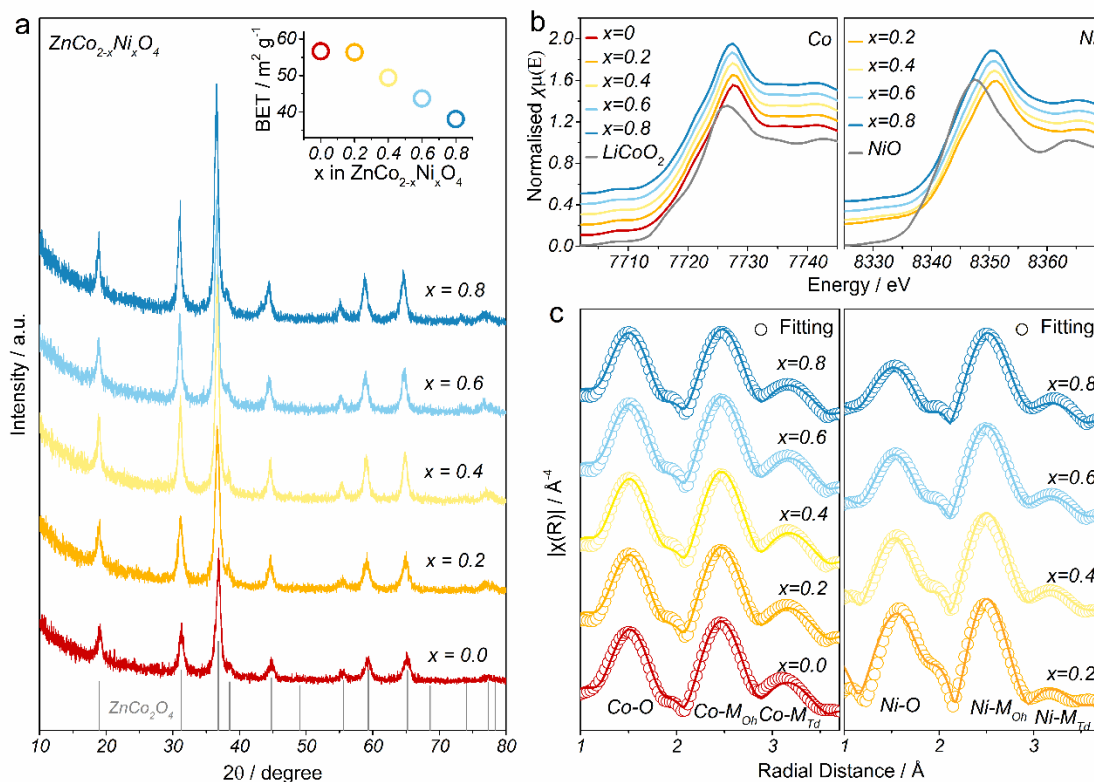


Figure 5.1 (a) XRD patterns of ZnCo_{2-x}Ni_xO₄ (x=0.0, 0.2, 0.4, 0.6, 0.8); BET surface area of ZnCo_{2-x}Ni_xO₄ (inset). (b) Electronic structural characterization of ZnCo_{2-x}Ni_xO₄ (x=0.0, 0.2, 0.4, 0.6, 0.8) by XANES. Normalized Co K-edge XANES spectra (left panel) and Normalized Ni K-edge XANES spectra (right panel). (c) Geometric information characterization by Fourier transform of the EXAFS (FT-EXAFS). FT-EXAFS spectra and fitting for Co K-edge (left panel) and Ni K-edge (right panel).

Table 5.1 Summary of lattice parameter of ZnCo_{2-x}Ni_xO₄ (x=0, 0.2, 0.4, 0.6, 0.8).

Sample	Rwp	Lattice parameter a (Å)	Zero-point error	Sample displacement
ZnCo ₂ O ₄	1.01%	8.124(7)	0.096	-0.03
ZnCo _{1.8} Ni _{0.2} O ₄	1.02%	8.14(1)	0.00014	0.01
ZnCo _{1.6} Ni _{0.4} O ₄	1.004%	8.149(5)	0.068	-0.02
ZnCo _{1.4} Ni _{0.6} O ₄	1.1%	8.165(5)	0.0029	-0.006
ZnCo _{1.2} Ni _{0.8} O ₄	1.2%	8.180(7)	0.0075	-0.01

The valency and site occupation of Zn, Co and Ni in $\text{ZnCo}_{2-x}\text{Ni}_x\text{O}_4$ ($x=0.0, 0.2, 0.4, 0.6, 0.8$) oxides have been determined by XANES spectroscopies (see Figure 5.1 and Figure 5.2) and X-ray absorption fine structure (EXAFS) (Figure 5.1 and Figure 5.2). They confirm $\text{ZnCo}_{2-x}\text{Ni}_x\text{O}_4$ ($x=0.0, 0.2, 0.4, 0.6, 0.8$) to have a normal spinel structure with Zn^{2+} accommodating the centre of tetrahedrons, Co^{3+} and Ni^{3+} staying in octahedral sites. However, when Ni substitution ratio is too high, to the extent where the O p -band centre is much higher in energy relative compared to M_{Oh} d -band centre, the structure becomes unstable and phase separation into rock-salt structure and wurtzite structure is observed by XRD where NiO and ZnO secondary phases coexist for $\text{ZnCo}_{0.8}\text{Ni}_{1.2}\text{O}_4$ and ZnNi_2O_4 (Figure 5.3). This is further confirmed by the X-ray absorption near edge structure (XANES) data for $\text{ZnCo}_{2-x}\text{Ni}_x\text{O}_4$ ($x=1.2, 1.6, 2.0$) (left panel of Figure 5.4), where the increase of F1 feature and the decrease of F2 in the white line of Zn K-edge in $\text{ZnCo}_{2-x}\text{Ni}_x\text{O}_4$ ($x=1.2, 1.6, 2.0$) indicate the appearance of ZnO wurtzite phase⁵⁹. The position of Ni K-edge in $\text{ZnCo}_{2-x}\text{Ni}_x\text{O}_4$ ($x=1.2, 1.6, 2.0$) (right panel of Figure 5.4) progressively shifts towards lower energies, closer to that of NiO, indicating the dropped valence state of Ni cations and supporting the existence of NiO in $\text{ZnCo}_{2-x}\text{Ni}_x\text{O}_4$ ($x=1.2, 1.6, 2.0$).

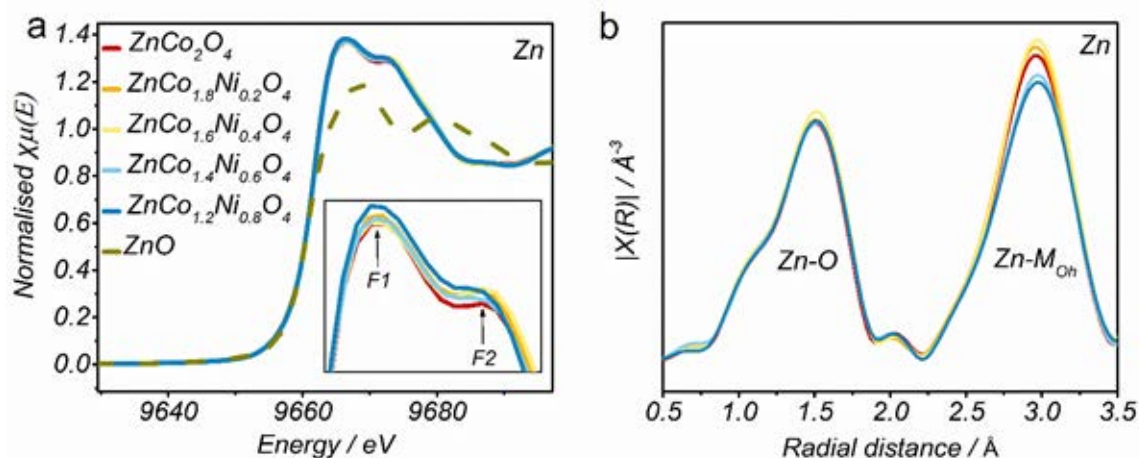


Figure 5.2 (a) Normalized Zn K-edge XANES spectra of $\text{ZnCo}_{2-x}\text{Ni}_x\text{O}_4$ ($x=0.0, 0.2, 0.4, 0.6, 0.8, 1.2, 1.6, 2.0$). The inset shows the white lines of $\text{ZnCo}_{2-x}\text{Ni}_x\text{O}_4$ ($x=0.0, 0.2, 0.4, 0.6, 0.8$) oxides. An increase in the intensity of F1 and decrease in F2 indicates the decreased degree of disorder in spinel structure. (b) FT-EXAFS $k^3\chi(R)$ spectra of $\text{ZnCo}_{2-x}\text{Ni}_x\text{O}_4$ ($x=0, 0.2, 0.4, 0.6, 0.8$) at Zn K edge.

Figure 5.3 XRD patterns of ZnCo_2O_4 , $\text{ZnCo}_{0.8}\text{Ni}_{1.2}\text{O}_4$ and ZnNi_2O_4 . Peaks denoted by ‘*’ correspond to ZnO wurtzite structure and peaks indicated with ‘#’ refers to NiO rock-salt structure.

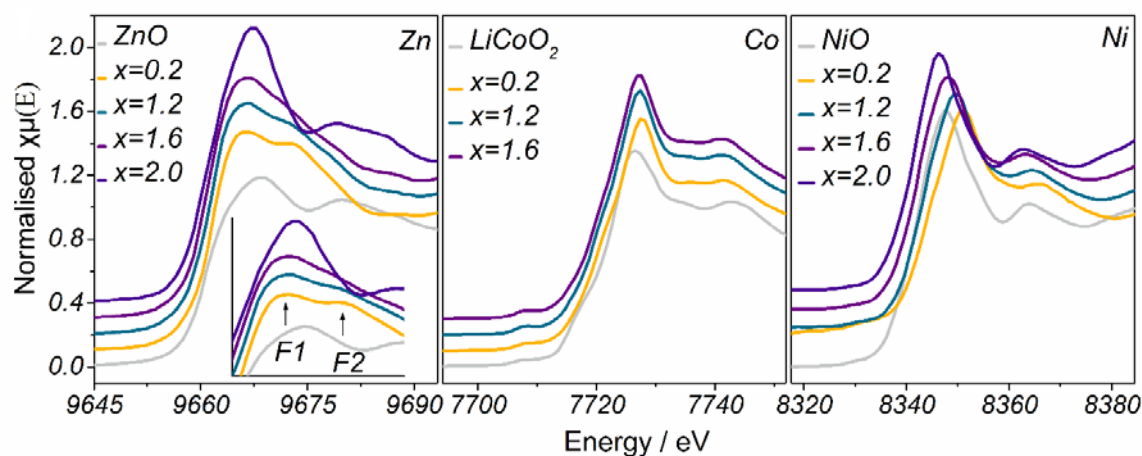


Figure 5.4 Normalized Zn K-edge XANES spectra of $\text{ZnCo}_{2-x}\text{Ni}_x\text{O}_4$ ($x=0.0, 0.2, 0.4, 0.6, 0.8, 1.2, 1.6, 2.0$) (left panel). The inset shows the white lines of $\text{ZnCo}_{2-x}\text{Ni}_x\text{O}_4$ ($x=0.0, 0.2, 0.4, 0.6, 0.8$) oxides. An increase in the intensity of F1 and decrease in F2 indicates the increased degree of disorder in spinel structure. Normalized Co K-edge XANES spectra of $\text{ZnCo}_{2-x}\text{Ni}_x\text{O}_4$ ($x=0.0, 0.2, 0.4, 0.6, 0.8, 1.2, 1.6$) (middle panel). Normalized Ni K-edge XANES spectra of $\text{ZnCo}_{2-x}\text{Ni}_x\text{O}_4$ ($x=0.2, 0.4, 0.6, 0.8, 1.2, 1.6, 2.0$) (right panel).

5.3.2 Electrochemical studies

Electrochemical measurements were then performed on pure $\text{ZnCo}_{2-x}\text{Ni}_x\text{O}_4$ ($x=0.0, 0.2, 0.4, 0.6, 0.8$) spinel phases. Cyclic voltammetry (CV) curves for $\text{ZnCo}_{2-x}\text{Ni}_x\text{O}_4$ at the 2nd and 1000th cycle are shown in Figure 5.5a. $\text{ZnCo}_{2-x}\text{Ni}_x\text{O}_4$ oxides exhibit for every Ni substitution level comparable activities at the 2nd cycle when normalized by BET surface area. After one thousand scans, the current density triples for $\text{ZnCo}_{1.4}\text{Ni}_{0.6}\text{O}_4$ and that of $\text{ZnCo}_{1.2}\text{Ni}_{0.8}\text{O}_4$ septuples to become superior to that of the state-of-the-art Co^{3+} -based perovskite LaCoO_3 ⁶⁰, Ni^{3+} -based perovskite LaNiO_3 ⁶⁰, as well as to the benchmarked IrO_2 ⁶¹ and comparable to that of the best-ever reported IrO_2 nanoparticles⁶² (inset of Figure 5.5a). The overpotential measured for $\text{ZnCo}_{1.4}\text{Ni}_{0.6}\text{O}_4$ and $\text{ZnCo}_{1.2}\text{Ni}_{0.8}\text{O}_4$ at $25 \mu\text{A cm}^{-2}_{\text{oxide}}$ are found decreased from 0.389 and 0.391 to 0.336 V and 0.311 V, respectively, after one thousand cycles (Figure 5.5b). These observations contrast with those for ZnCo_2O_4 , $\text{ZnCo}_{1.8}\text{Ni}_{0.2}\text{O}_4$ and $\text{ZnCo}_{1.6}\text{Ni}_{0.4}\text{O}_4$, for which the OER activity remains stable during repeated scans. This finding is also confirmed by chronoamperometry (CA) studies after cycling (Figure 5.6). When looking into the subsequent CV curves for the stable ZnCo_2O_4 (Figure 5.7a) and the metastable $\text{ZnCo}_{1.2}\text{Ni}_{0.8}\text{O}_4$ (Figure 5.5c), $\text{ZnCo}_{1.2}\text{Ni}_{0.8}\text{O}_4$ yields continuously increased OER current along with cycles (decrease of the potential at $25 \mu\text{A cm}^{-2}_{\text{oxide}}$ from 1.621 V to 1.543 V). In contrast, ZnCo_2O_4 presents negligible change in activity during cycling. This result confirms the role of Ni substitution in controlling both stability and activity for ZnCo_2O_4 . To further understand the different activity/stability behaviour of ZnCo_2O_4 and $\text{ZnCo}_{1.2}\text{Ni}_{0.8}\text{O}_4$, the evolution of the pseudocapacitive charge was tracked over thousands of cycles (Figure 5.7b and Figure 5.5d). Neither significant change in capacitive current nor evolution of pseudocapacitive curve along with OER activity is observed for ZnCo_2O_4 . In contrast, the pseudocapacitive charge is correlated with the OER activity for $\text{ZnCo}_{1.2}\text{Ni}_{0.8}\text{O}_4$ (Figure 5.5c inset and Figure 5.5d), which indicates that the major increase in the OER activity for $\text{ZnCo}_{1.2}\text{Ni}_{0.8}\text{O}_4$ is well-explained by the reconstruction of a new surface. The Tafel slope for $\text{ZnCo}_{1.2}\text{Ni}_{0.8}\text{O}_4$ increases to $\sim 60 \text{ mV dec}^{-1}$ after cycling (inset of Figure 5.5a), similar to what is found for pure NiOOH , hence suggesting the formation of NiOOH on the surface of $\text{ZnCo}_{1.2}\text{Ni}_{0.8}\text{O}_4$ ⁶³. This is different from earlier studies in which mixed nickel/cobalt oxyhydroxide formed on the surface of Co-Ni oxides^{12,64}

was found to exhibit a Tafel slope of $\sim 40\text{-}60\text{ mV dec}^{-1}$. Therefore, this calls for a careful study of the chemical and structural properties of the reconstructed surface of these spinel materials.

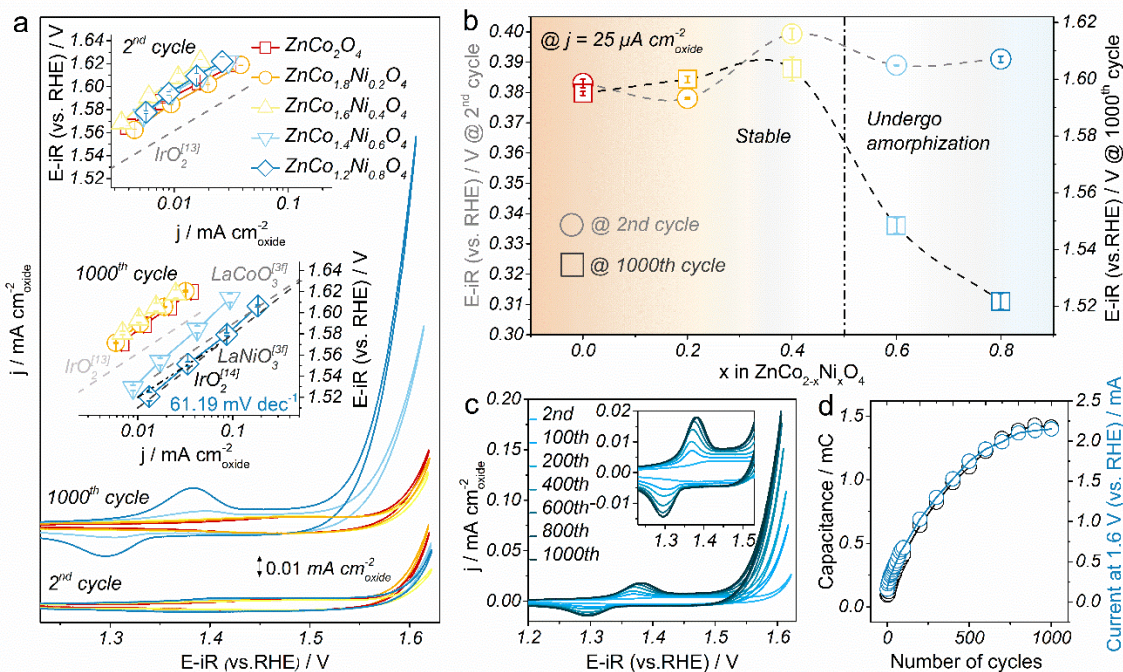


Figure 5.5 Electrochemical characterization on OER performance of ZnCo_{2-x}Ni_xO₄ (x=0.0, 0.2, 0.4, 0.6, 0.8). All data points and error bars were obtained by averaging the results of at least three independent measurements. (a) CV curves of the 1000th cycle comparing to the 2nd cycle of ZnCo_{2-x}Ni_xO₄ (x=0.0, 0.2, 0.4, 0.6, 0.8). The insets present the Tafel plot for surface-area-normalized ZnCo_{2-x}Ni_xO₄ (x=0.0, 0.2, 0.4, 0.6, 0.8) at the 2nd cycle (top) and 1000th cycle (bottom) compared with LaCoO₃⁶⁰, LaNiO₃⁶⁰, IrO₂ (100) extracted from IrO₂⁶¹ and IrO₂⁶². (b) iR corrected potential (in RHE scale) of the 1000th cycle comparing to the 2nd cycle of ZnCo_{2-x}Ni_xO₄ (x=0.0, 0.2, 0.4, 0.6, 0.8) at $25\ \mu\text{A cm}^{-2}$ oxide. (c) Evolutive CV curves for representative ZnCo_{1.2}Ni_{0.8}O₄ from 2nd to 1000th cycle in 1M KOH at 10 mV s^{-1} in between 0.904 and 1.624 V (vs. RHE). The insets show the redox peaks from 1.23 V to 1.5 V. (d) Evolution of the pseudocapacitive charge during cycling (0.904-1.624 V versus RHE) in 1M KOH (left axis) and the OER activity at 1.6V versus RHE (right axis) for ZnCo_{1.2}Ni_{0.8}O₄.

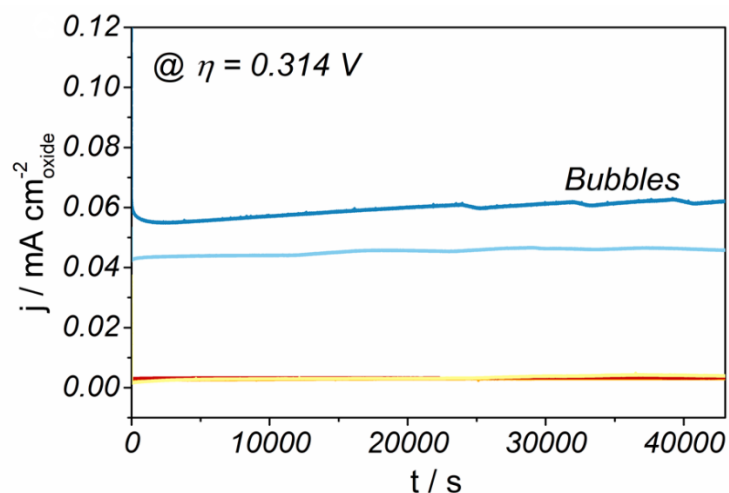


Figure 5.6 Chronoamperometry of $\text{ZnCo}_{2-x}\text{Ni}_x\text{O}_4$ ($x=0.0, 0.2, 0.4, 0.6, 0.8$) after 100th CV at an overpotential of 0.314 V (vs. RHE).

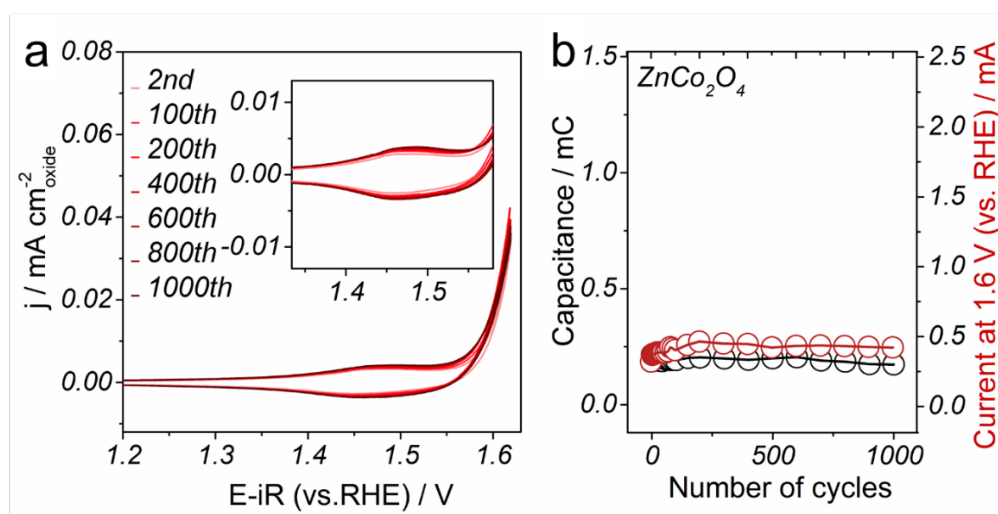


Figure 5.7 a) Evolutive CV curves for representative ZnCo_2O_4 from 2nd to 1000th cycle in 1M KOH at 10 mV s^{-1} in between 0.904 and 1.624 V (vs. RHE). The insets show the redox peaks from 1.33 V to 1.59 V. b) Evolution of the pseudocapacitive charge during cycling (0.904-1.624 V versus RHE) in 1M KOH (left axis) and the OER activity at 1.6V versus RHE (right axis) for ZnCo_2O_4 .

5.3.3 Characterization after electrochemical study

A new phase is observed by high-resolution transmission electron microscopy (HRTEM) on the surface of $\text{ZnCo}_{1.2}\text{Ni}_{0.8}\text{O}_4$ after cycling (Figure 5.8). To reveal the elemental composition of the

new surface phase, scanning transmission electron microscopy-energy-dispersive X-ray spectroscopy (STEM-EDS) and line-scan were conducted. The surface is found rich in Ni, while deficient in Zn and Co (Figure 5.8, Figure 5.9), suggesting that surface Zn and Co atoms are leached out during the OER process, while Ni segregates on the surface to reconstruct into a layer-type NiOOH. As observed by Electron energy loss spectroscopy (EELS), the disappearance of the feature B (Figure 5.10a) at 532 eV in the O K-edge indicates the decreased hybridization between oxygen and the antibonding minority spin M 3d states after cycling, suggesting an increase in oxygen vacancies and structural relaxation^{65–67} due to structural oscillations⁶⁸. From the ratios of L3/L2 (Figure 5.10b and Figure 5.10c) calculated by Hartree–Slater cross section method^{69–71}, surface Ni cations possess higher valence state after cycling, which is confirmed by XPS spectra. Indeed, peaks referring to Ni²⁺ at about 873 eV and 854 eV⁷² disappear, while remaining peaks at 971 eV and 855.5eV⁷³ can be ascribed to Ni³⁺ after OER (Figure 5.11). This is consistent with the presence of Ni^{III} (oxy) hydroxide on the surface of this catalyst. Finally, a remarkable increase in the satellite structure of Ni edges at 861eV and 881eV is observed after OER cycling (Figure 5.12).

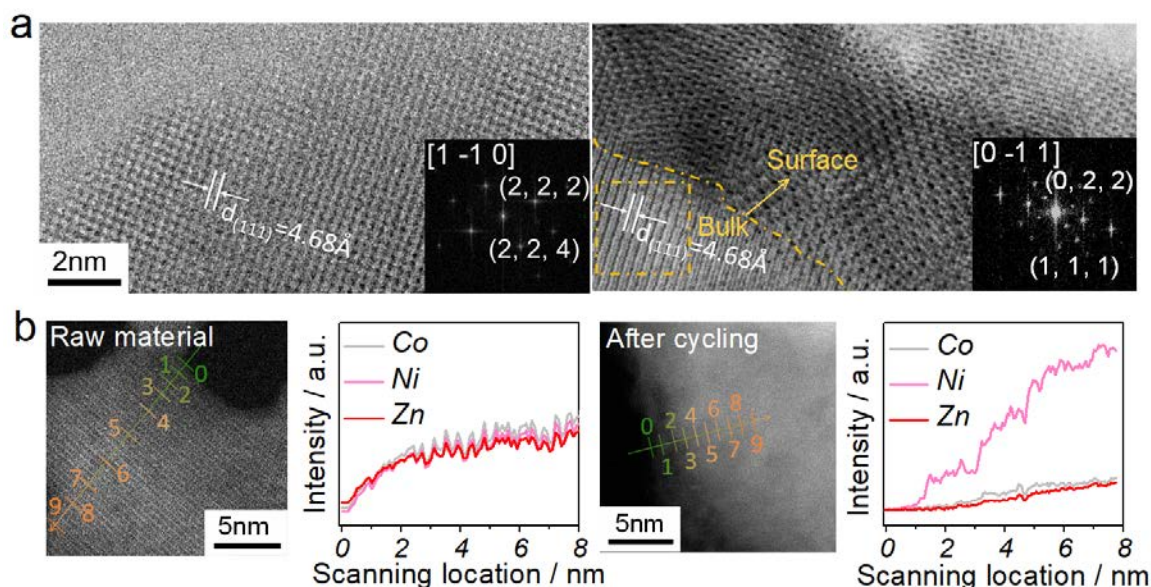


Figure 5.8 Structural and compositional characterization of $\text{ZnCo}_{0.2}\text{Ni}_{0.8}\text{O}_4$ before and after OER cycling. (a) ABF image of pristine $\text{ZnCo}_{0.2}\text{Ni}_{0.8}\text{O}_4$ (left) and $\text{ZnCo}_{0.2}\text{Ni}_{0.8}\text{O}_4$ after thousand cycles of OER in 1M KOH at 10 mV/s between 0.904 and 1.624 V (vs. RHE) (right). The inset at the bottom right is the FFT pattern for the bulk which can be referred to Fd3m space group. (b) STEM-EDS image and analysis of pristine (left) and cycled (right) $\text{ZnCo}_{0.2}\text{Ni}_{0.8}\text{O}_4$.

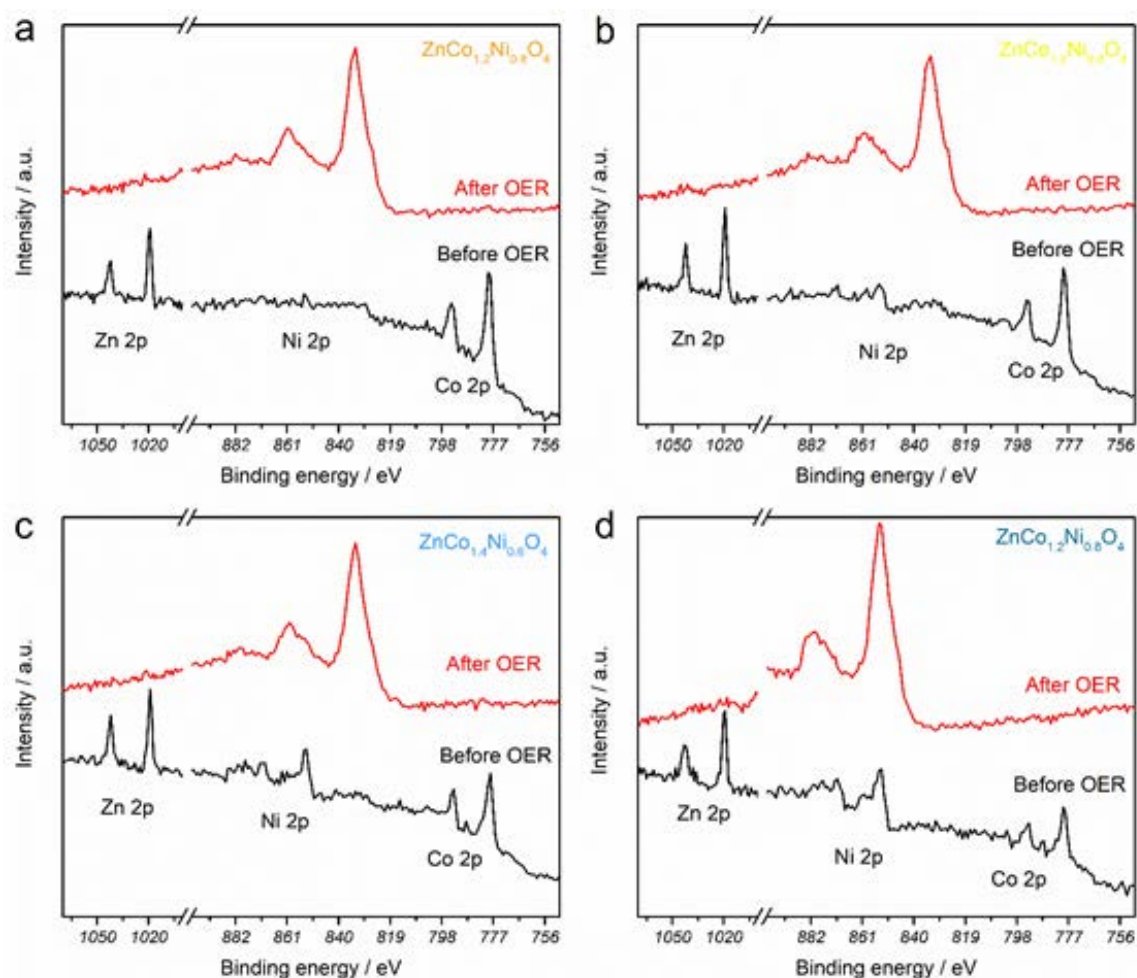


Figure 5.9 X-ray photoelectron spectra (XPS) survey of Zn, Co and Ni 2p regions for $\text{ZnCo}_{1.8}\text{Ni}_{0.2}\text{O}_4$ (a), $\text{ZnCo}_{1.6}\text{Ni}_{0.4}\text{O}_4$ (b), $\text{ZnCo}_{1.4}\text{Ni}_{0.6}\text{O}_4$ (c) and $\text{ZnCo}_{1.2}\text{Ni}_{0.8}\text{O}_4$ (d) surface before OER testing (black line) and after thousand cycles of OER (after OER) in 1M KOH at 10 mVs^{-1} between 0.904 and 1.624 V (vs. RHE).

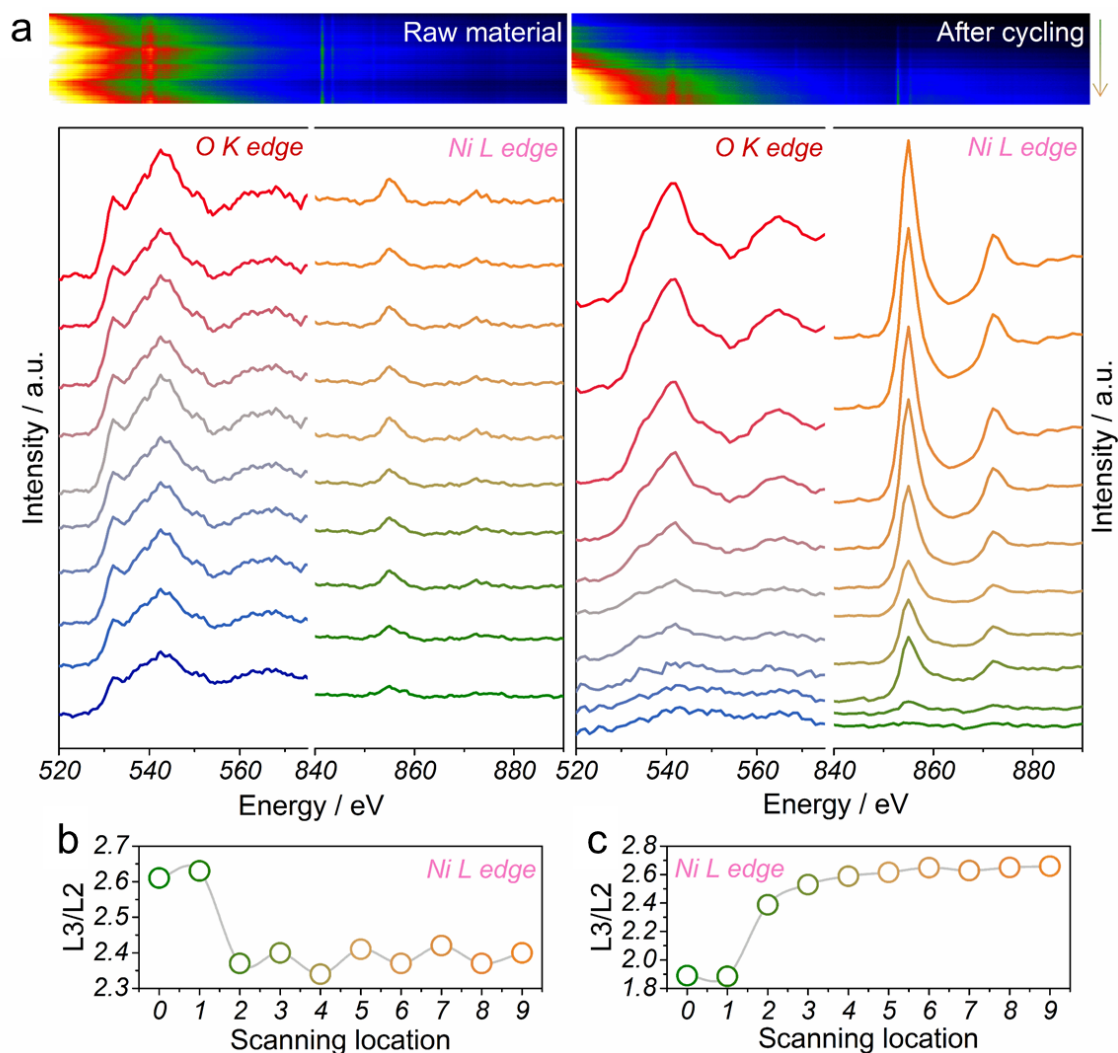


Figure 5.10 (a) EELS spectra of O K-edge and Ni L-edge along the scanning pathway are to detect the change in O electronic structures and charge distributions of metal cations. L3/L2 ratios of Ni edge calculated from Ni L-edge EELS spectra for pristine ZnCo_{0.2}Ni_{0.8}O₄ (b) and cycled ZnCo_{0.2}Ni_{0.8}O₄ (c). The ratios of L3/L2 for Ni edge before and after cycling have been determined by a Hartree–Slater cross section method⁷⁴. Lower L3/L2 corresponds to higher chemical states of the Ni cations. This indicates that there is surface Ni²⁺ before OER, and these surface Ni cations acquire higher valence state after cycling.

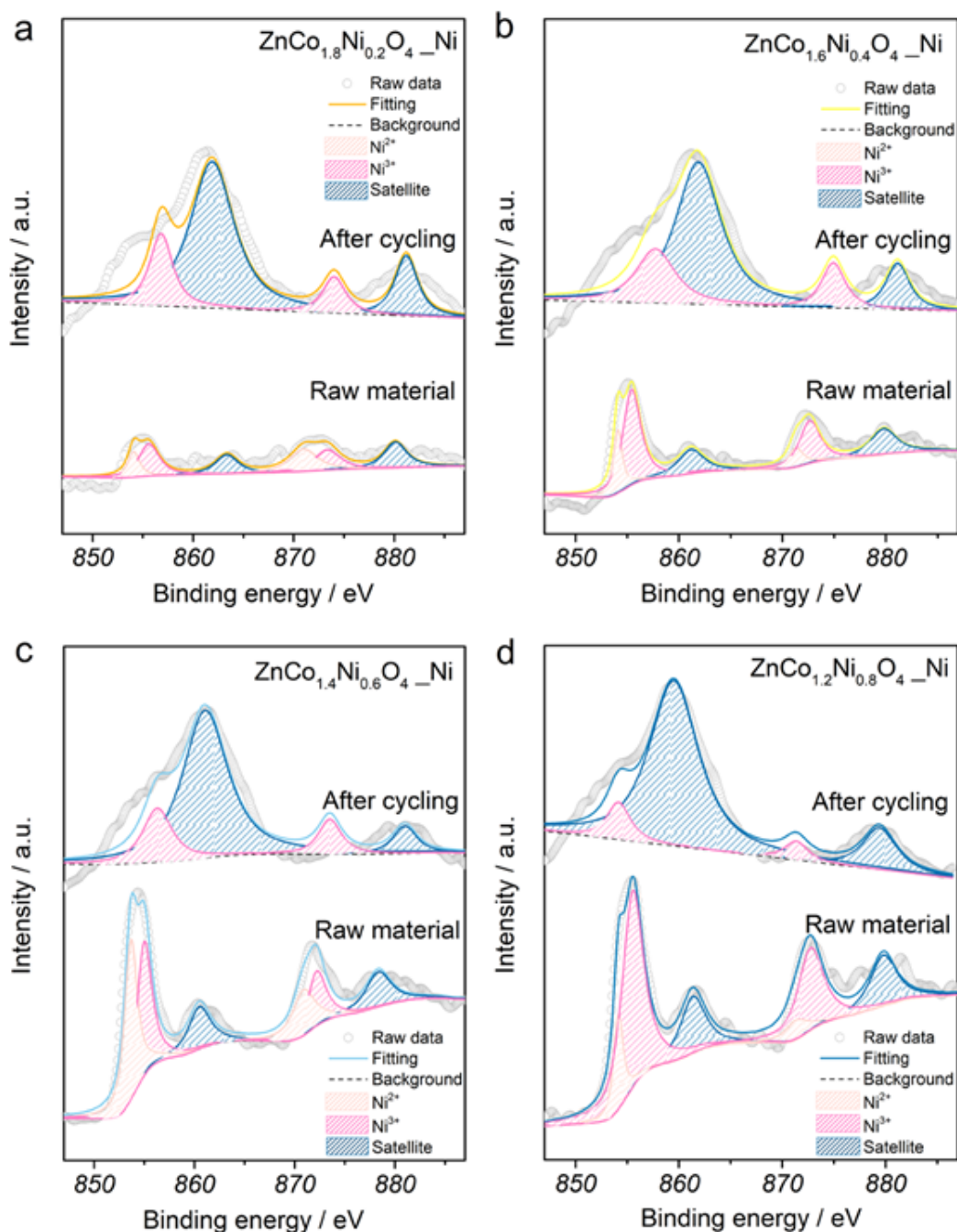


Figure 5.11 X-ray photoelectron spectra (XPS) of Ni 2p regions for ZnCo_{2-x}Ni_xO₄ surface before OER testing and after thousand cycles of OER in 1M KOH at 10 mVs⁻¹ between 0.904 and 1.624 V (vs. RHE). Fittings of experimental spectra obtained for ZnCo_{2-x}Ni_xO₄ are shown in coloured curves. Fittings of satellites are shown in dark blue colour.

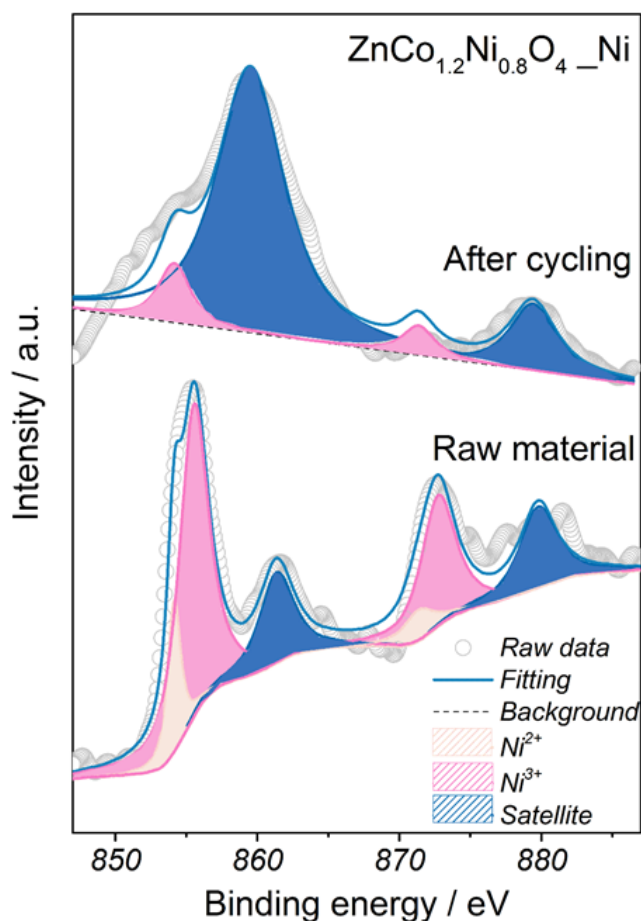


Figure 5.12 XPS of Ni 2p regions for $\text{ZnCo}_{1.2}\text{Ni}_{0.8}\text{O}_4$ surface before OER testing and after thousand cycles of OER in 1M KOH at 10 mVs^{-1} between 0.904 and 1.624 V (vs. RHE). Fittings of experimental spectra obtained for $\text{ZnCo}_{1.2}\text{Ni}_{0.8}\text{O}_4$ are shown in coloured curves. Fittings of satellites are shown in dark blue colour. Shadowed area demonstrates the fitting of satellites. The satellite structure at 881eV is associated with a $2p^5 3d^7$ final state transformed from a $2p^6 3d^7$ state in the photoemission process, and the structure at 861eV is attributed to the $2p^5 3d^8 L$ final state from $2p^6 3d^8$.^{69,70} Thus, the relatively strong satellite structure at the lower binding strength compared to that at higher binding strength is the result of increased Ni^{3+} which gives rise to removal of electrons from valence levels to which charge transfer from the ligand is facilitated⁷⁵⁻⁷⁷. The broadening of main peaks for the Ni edge indicates the presence of delocalised electrons on 3d-2p states after OER.¹⁰²

Soft XAS and X-ray magnetic circular dichroism (XMCD) have then been employed to unveil the change in surface electronic structure of $\text{ZnCo}_{1.2}\text{Ni}_{0.8}\text{O}_4$ before and after OER cycling. The average $L_{2,3}$ absorption centroids for the Ni XAS of $\text{ZnCo}_{1.2}\text{Ni}_{0.8}\text{O}_4$ is shifted to higher energy, which agrees well with the increased Ni valence state⁷⁸ after OER as detected by XPS.(Figure

5.11, Figure 5.12) The Ni $L_{2,3}$ edge spectrum of cycled $\text{ZnCo}_{1.2}\text{Ni}_{0.8}\text{O}_4$ after subtraction of the non-cycled one is illustrated by a pink line in Figure 5.13, which coincide with that of NiOOH ⁷⁴. From the XMCD spectra (Figure 5.14), the net magnetic moment of surface Ni for $\text{ZnCo}_{1.2}\text{Ni}_{0.8}\text{O}_4$ disappears after OER cycling. The disappeared magnetic moment arises from the newly formed NiOOH on the surface of $\text{ZnCo}_{1.2}\text{Ni}_{0.8}\text{O}_4$ owing to the fact that NiOOH has no magnetic moment⁷⁹. From the surface characterizations conducted before and after OER, we confirm that the leaching of Zn gives rise to surface reconstruction and a larger concentration of near-surface Ni^{3+} active species. The Ni^{3+} rich surface induces a strong surface hydroxylation of $\text{ZnCo}_{1.2}\text{Ni}_{0.8}\text{O}_4$ and leads in alkaline conditions to the formation of NiOOH , which is the main active phase for OER and leads to the promotion of the OER performances. However, at that stage of our study, understanding the exact reconstruction mechanism from spinel $\text{ZnCo}_{2-x}\text{Ni}_x\text{O}_4$ to oxyhydroxide and how the stability correlates with the reconstruction mechanism requires further elaboration.

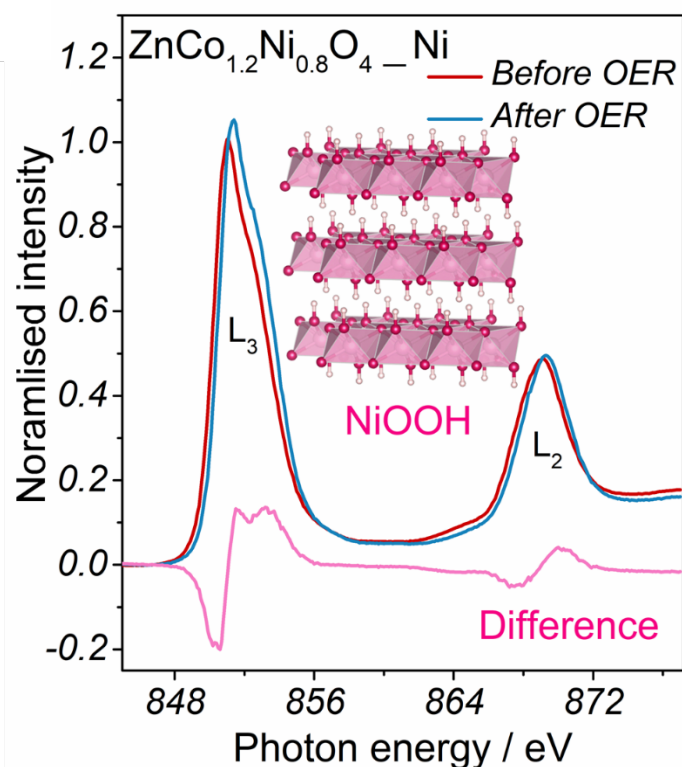


Figure 5.13 Soft XAS spectra at the Ni $L_{2,3}$ -edge for $\text{ZnCo}_{1.2}\text{Ni}_{0.8}\text{O}_4$ before (red line) and after OER cycling (blue line).

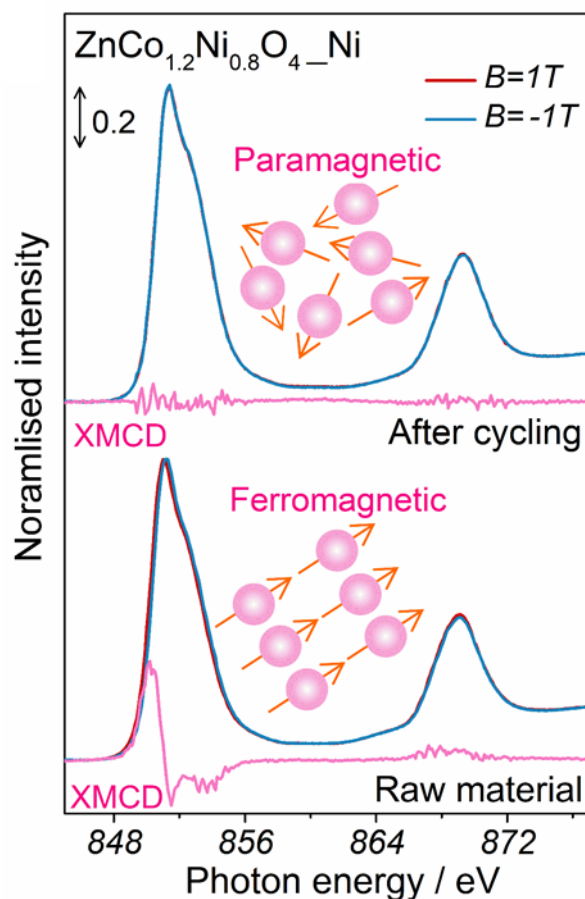


Figure 5.14 XMCD spectra raised from the difference between the μ^+ and μ^- soft XAS spectra at the Ni L_{2,3}-edge for ZnCo_{1.2}Ni_{0.8}O₄ before (bottom) and after OER cycling (top).

5.3.4 Reaction mechanism

To aid the understanding of the OER reaction mechanism for ZnCo_{2-x}Ni_xO₄, pH dependent experiments were conducted on both pristine and cycled ZnCo_{2-x}Ni_xO₄. An increase in current density along with pH is observed for the whole series of ZnCo_{2-x}Ni_xO₄ at the second cycle (Figure 5.15). A decreased Tafel slope along with increased pH is also observed, suggesting a change in rate limiting step or reaction pathways when increasing the KOH concentration.⁸⁰ To further understand this observation, the Nernstian/non-Nernstian potential shift was studied (Figure 5.16). The Pourbaix slopes ($\Delta E_{\text{peak,SHE}}/\Delta\text{pH}$) reach values lower than -120 mV/pH for both ZnCo₂O₄ (-146.34 mV/pH) and ZnCo_{1.2}Ni_{0.8}O₄ (-129.27 mV/pH), indicative of a super-

Nernstian effect with two protons exchanging for a single electron^{81,82}. The decomposition of spinel oxides $\text{ZnCo}_{2-x}\text{Ni}_x\text{O}_4$ to CoOOH ($x=0$) or NiOOH ($x=0.8$) were further studied by sweeping one electrode in each KOH electrolyte from low to high concentration (Figure 5.17, Figure 5.18) and the other electrode from high to low concentration (Figure 5.18, Figure 5.19, Figure 5.20, Figure 5.21). The activity of ZnCo_2O_4 in $\text{pH}=13$ does not return to its initial value after three cycles at $\text{pH}=14$ and $\text{pH}=13.5$ (Figure 5.18a), and a similar observation is made for $\text{pH}=13.5$ (Figure 5.18b). At high pH of 14, stable performances are obtained independently of the pH used for the activation process (Figure 5.18c). These results suggest that the kinetics of decomposition from pristine ZnCo_2O_4 to CoOOH is more significant at higher pH . When sweeping from high to low pH , the activity does not change, (Figure 5.20a) indicating that a stable CoOOH layer quickly forms and its OER is not pH dependent. Similarly, the kinetics for the transition from $\text{ZnCo}_{1.2}\text{Ni}_{0.8}\text{O}_4$ to NiOOH layer are faster at higher pH values (Figure 5.18m to o). However, unlike that of ZnCo_2O_4 (Figure 5.20a), when sweeping from high to low pH , activity of $\text{ZnCo}_{1.2}\text{Ni}_{0.8}\text{O}_4$ at pH 13.5 is greater than at pH 14 (Figure 5.20b). This is attributed to the unstable nature of $\text{ZnCo}_{1.2}\text{Ni}_{0.8}\text{O}_4$ for which more cycles are needed to reach a stable surface. In other words, $\text{ZnCo}_{1.2}\text{Ni}_{0.8}\text{O}_4$ easily decomposes to form a thicker NiOOH layer at high pH value. pH dependent experiments for cycled $\text{ZnCo}_{2-x}\text{Ni}_x\text{O}_4$ were then conducted. The cycled ZnCo_2O_4 shows no pH dependence after the 1000th OER cycles (Figure 5.22, Figure 5.23), indicating that the CoOOH layer formed on the surface is highly stable and undergoes a classical concerted proton electron transfer. For cycled $\text{ZnCo}_{1.2}\text{Ni}_{0.8}\text{O}_4$, whether sweeping from low to high or high to low pH , identical performances are obtained for a given pH value (Figure 5.24), indicating the formation of a stable NiOOH layer after the 1000th cycle.

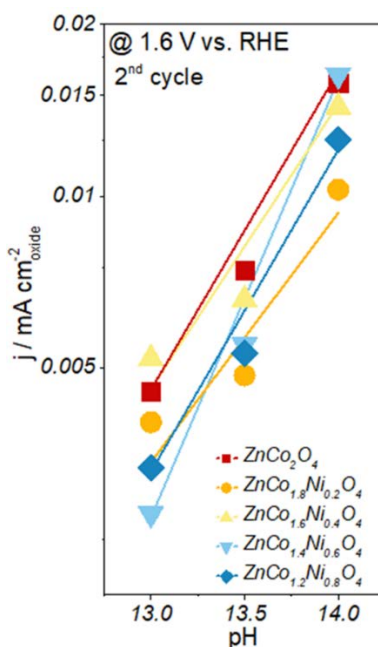


Figure 5.15 OER activity (current normalized by surface area of oxide) of pristine $\text{ZnCo}_{2-x}\text{Ni}_x\text{O}_4$ at 1.6 V (versus RHE) after iR correction as a function of pH.

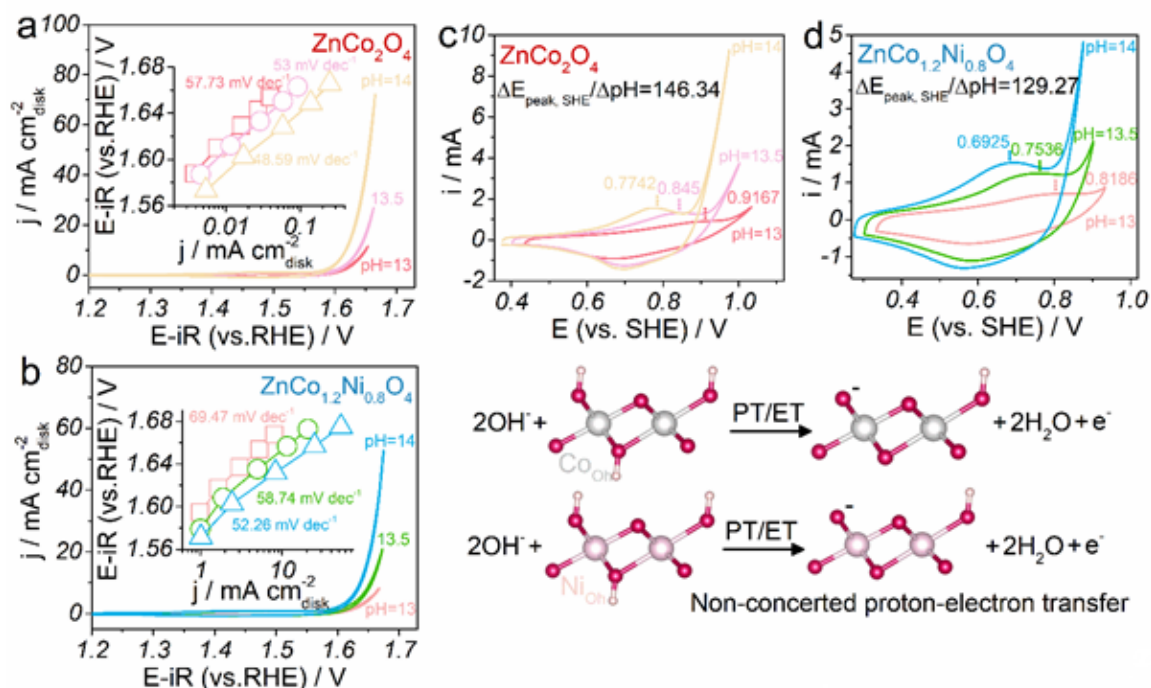


Figure 5.16 pH-dependent OER activity for pristine $\text{ZnCo}_{2-x}\text{Ni}_x\text{O}_4$. CV measurements for pristine ZnCo_2O_4 (a) and $\text{ZnCo}_{1.2}\text{Ni}_{0.8}\text{O}_4$ (b) from 0.1 M KOH (pH 13) to 1 M KOH (pH 14)

recorded at 10 mV s^{-1} on the RHE scales after iR correction. Insets are the Tafel plots in different pH. Increasing the pH value from 13 to 14 leads to seven times greater intrinsic OER activity (OER activity normalised by the surface area of working electrode) for pristine ZnCo_2O_4 . The decreased Tafel slope along with increased pH, from $57.73 \text{ mV dec}^{-1}$ to $48.59 \text{ mV dec}^{-1}$, indicates a change in reaction pathways when using KOH with different concentrations. [25] All other samples exhibit similar performance. CV measurements for pristine ZnCo_2O_4 (c) and $\text{ZnCo}_{1.2}\text{Ni}_{0.8}\text{O}_4$ (d) from 0.1 M KOH (pH 13) to 1 M KOH (pH 14) recorded at 200 mV s^{-1} on the SHE scales. Bottom panel shows the schematic for non-concerted proton-electron transfer of surface deprotonation of pristine ZnCo_2O_4 and $\text{ZnCo}_{1.2}\text{Ni}_{0.8}\text{O}_4$. The Pourbaix slopes obtained for these materials are quite different from $\text{Ni}(\text{OH})_2$ (-90 mV/pH) which also reconstructs to NiOOH under OER conditions, meaning that this deprotonation behaviour is very dependent on the oxide which is used to form the hydroxide.

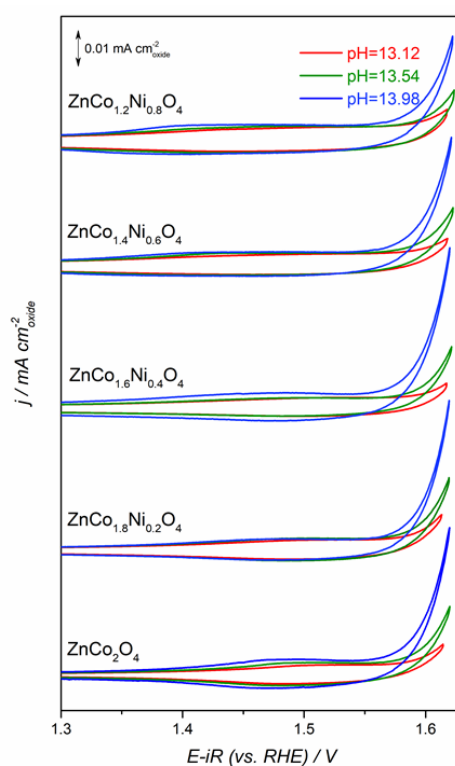


Figure 5.17 OER activity swept from low pH to high pH for pristine $\text{ZnCo}_{2-x}\text{Ni}_x\text{O}_4$.

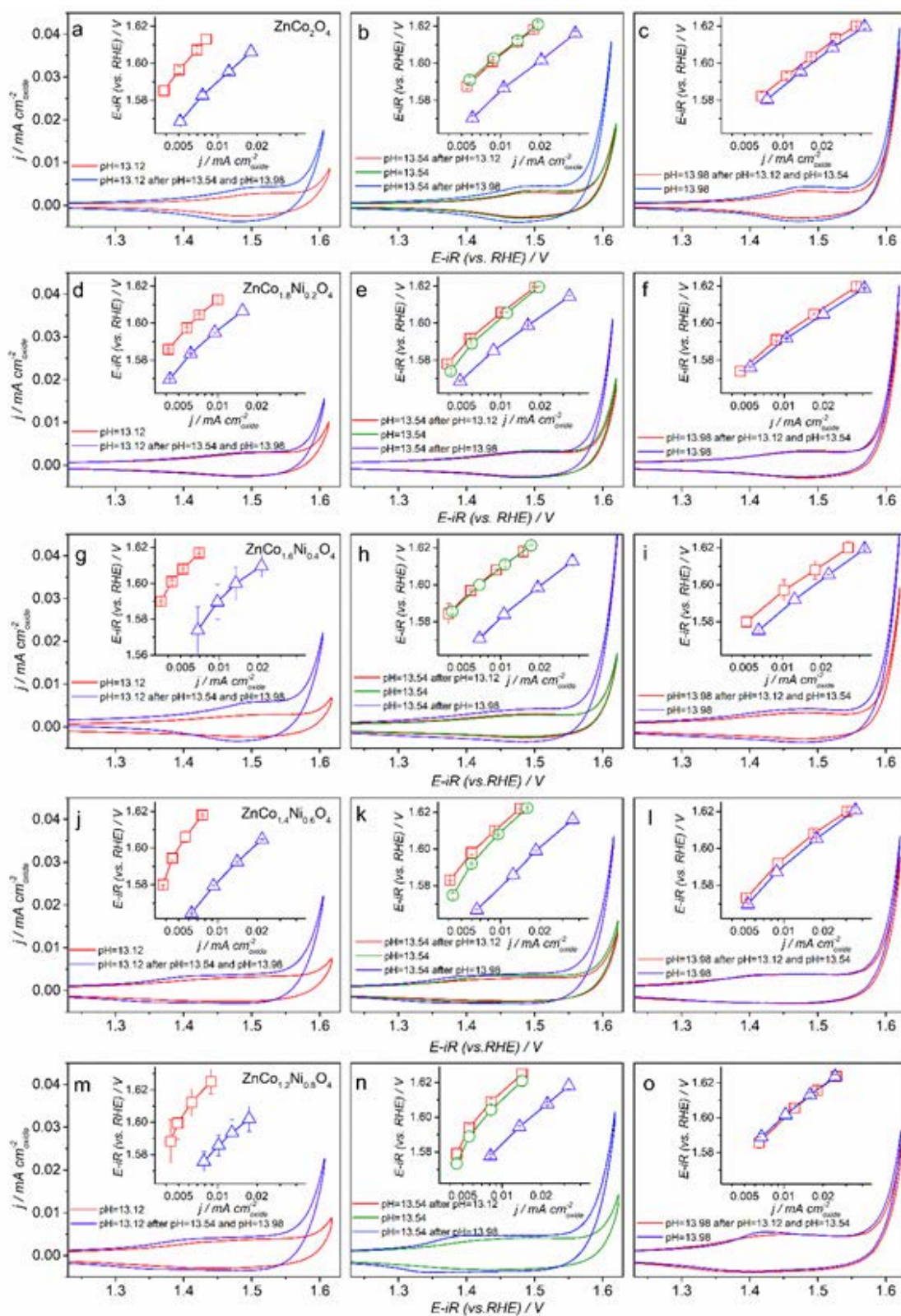


Figure 5.18 OER activity swept from low pH to high pH comparing with activity swept from high pH to low pH in pH=13, pH =13.5 and pH=14 for pristine $\text{ZnCo}_{2-x}\text{Ni}_x\text{O}_4$.

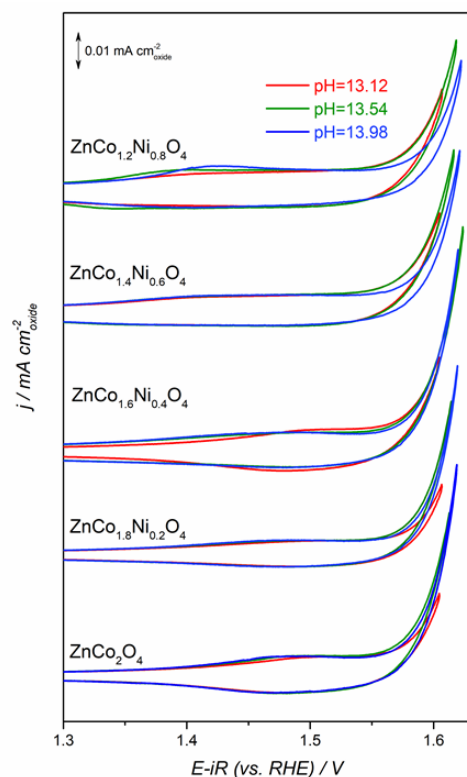


Figure 5.19 OER activity swept from high pH to low pH for pristine $\text{ZnCo}_{2-x}\text{Ni}_x\text{O}_4$.

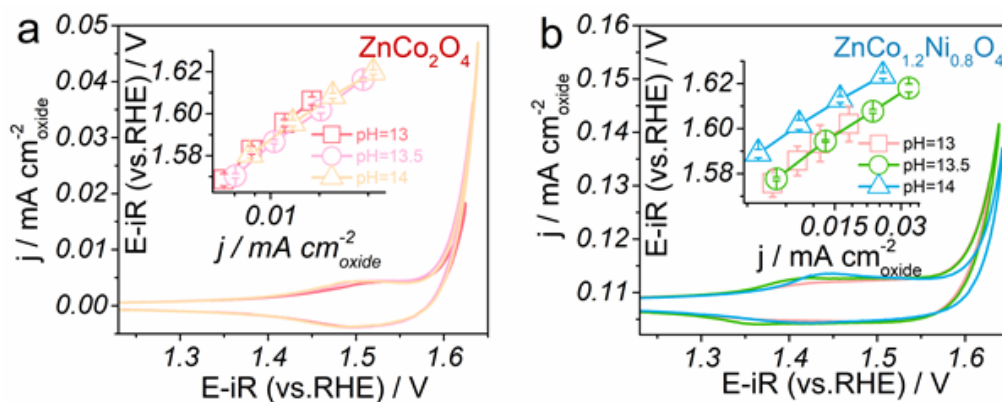


Figure 5.20 OER activity swept from high pH to low pH for pristine ZnCo_2O_4 (a) and $\text{ZnCo}_{1.2}\text{Ni}_{0.8}\text{O}_4$ (b). Tafel plots are shown in the insets.

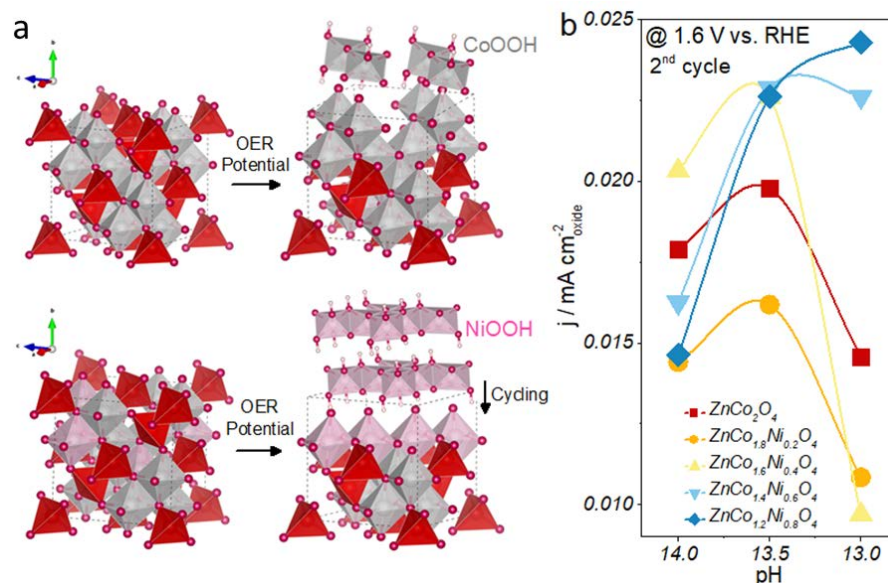


Figure 5.21 a) The schematic for the transition from pristine ZnCo₂O₄/ZnCo_{1.2}Ni_{0.8}O₄ to CoOOH/NiOOH. b) OER activity swept from high pH to low pH (current normalized by surface area of oxide) of pristine ZnCo_{2-x}Ni_xO₄ at 1.6 V (versus RHE) after iR correction as a function of pH.

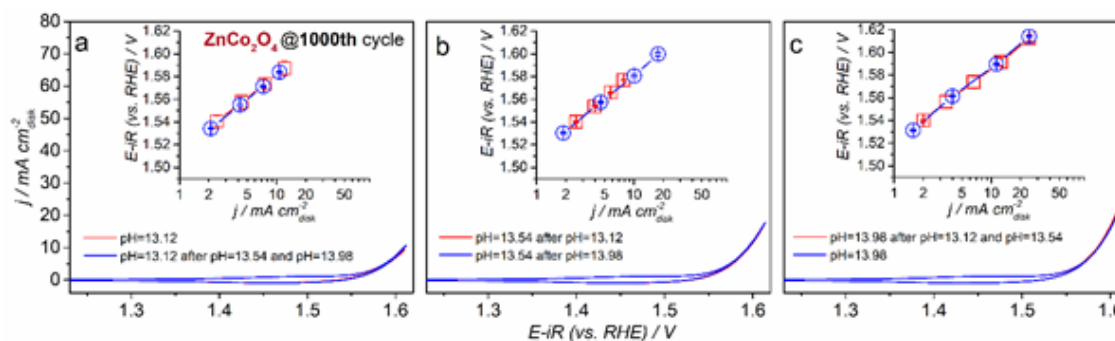


Figure 5.22 OER activity swept from low pH to high pH comparing with activity swept from high pH to low pH in pH=13 (a), pH =13.5 (b) and pH=14 (c) for ZnCo₂O₄ after 1000th OER cycles.

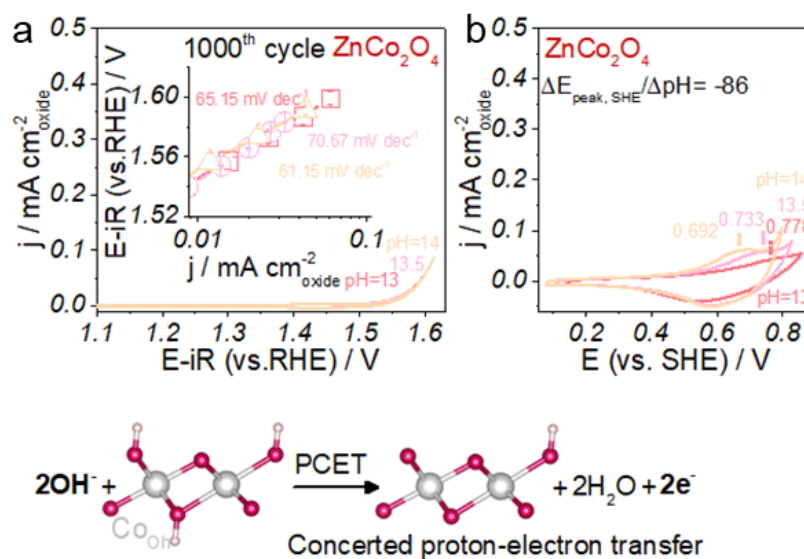


Figure 5.23 (a) CV measurements for cycled ZnCo_2O_4 from 0.1 M KOH (pH 13.12) to 1 M KOH (pH 13.98) recorded at 10 mV s^{-1} on the RHE scales after iR correction. Insets are the Tafel plots in different pH. (b) CV measurements for cycled ZnCo_2O_4 from 0.1 M KOH (pH 13.12) to 1 M KOH (pH 13.98) recorded at 200 mV s^{-1} on the SHE scales. Bottom panels show the schematic for concerted proton-electron transfer of surface deprotonation of cycled ZnCo_2O_4 .

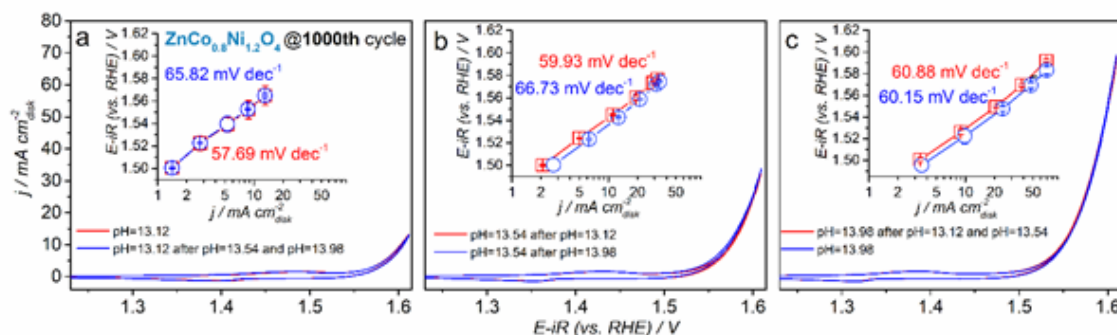


Figure 5.24 OER activity swept from low pH to high pH comparing with activity swept from high pH to low pH in pH=13, pH =13.5 and pH=14 for $\text{ZnCo}_{1.2}\text{Ni}_{0.8}\text{O}_4$ after 1000th OER cycles.

However, unlike for cycled ZnCo_2O_4 , the OER performance of $\text{ZnCo}_{1.2}\text{Ni}_{0.8}\text{O}_4$ is found pH dependent (Figure 5.25a), which can tentively be explained by the different stability for both phases. Stable materials such as ZnCo_2O_4 , $\text{ZnCo}_{1.8}\text{Ni}_{0.2}\text{O}_4$ and $\text{ZnCo}_{1.6}\text{Ni}_{0.4}\text{O}_4$ quickly form a thin layer of CoOOH (formed by ZnCo_2O_4) or NiOOH (formed by $\text{ZnCo}_{1.8}\text{Ni}_{0.2}\text{O}_4$ and $\text{ZnCo}_{1.6}\text{Ni}_{0.4}\text{O}_4$) on the surface. $\text{ZnCo}_{1.4}\text{Ni}_{0.6}\text{O}_4$ and $\text{ZnCo}_{1.2}\text{Ni}_{0.8}\text{O}_4$, however, are unstable under OER conditions, and so their surface continuously reconstruct and NiOOH is formed, which results in more durable improved activity upon cycling (Figure 5.25b). Because this

thicker amorphous layer participates in the OER, it might selectively impede the proton or electron transport within the whole thickness (Figure 5.25c), which is not the case for thin surface made of CoOOH. Hence, the stability of oxides is critical in determining the depth of CoOOH or NiOOH formation from the surface and thus the OER mechanism, which affects the activity of surface-active species.

A representative unit for spinel oxide has been selected to study the ability of lattice oxygen to participate in the OER. In this cluster, one tetrahedron and three octahedrons are connected by an oxygen atom. Zn occupies the tetrahedral site, while Co and Ni are accommodated in octahedral sites. The lowest unoccupied molecular orbital (LUMO) of the cluster has been calculated while varying the number of Ni in octahedral sites from 0 to 2. The LUMO, which controls the energy required to remove an electron from the cluster and which is found to be of oxygen character mostly (inset in Figure 5.25d), dictates for these clusters the potential at which lattice oxygen becomes redox active. Thus, the lower the LUMO for the material, the easier the lattice oxygen evolution reaction. In Figure 5.25, when the number of Ni in octahedral sites is increased from 0 to 2, LUMO first decreases before to increase. It indicates the increased ability for the material with a Ni substitution around 33% to undergo lattice oxidation under OER conditions. From the charge density of the materials, decreased oxygen bonding is observed for the 33% Ni substituted model, indicating that the lattice oxygen can be easily activated in this case. Hence, activating the redox for lattice oxygen in $\text{ZnCo}_{1.4}\text{Ni}_{0.6}\text{O}_4$ and $\text{ZnCo}_{1.2}\text{Ni}_{0.8}\text{O}_4$ would increase the participation of lattice oxygen in the OER, creating oxygen vacancies on the surface and continuously destabilizing the structure of the spinel, as we observed upon cycling. This results in the formation of a thick Ni oxyhydroxide surface layer and the continuous improvement of the OER activity.

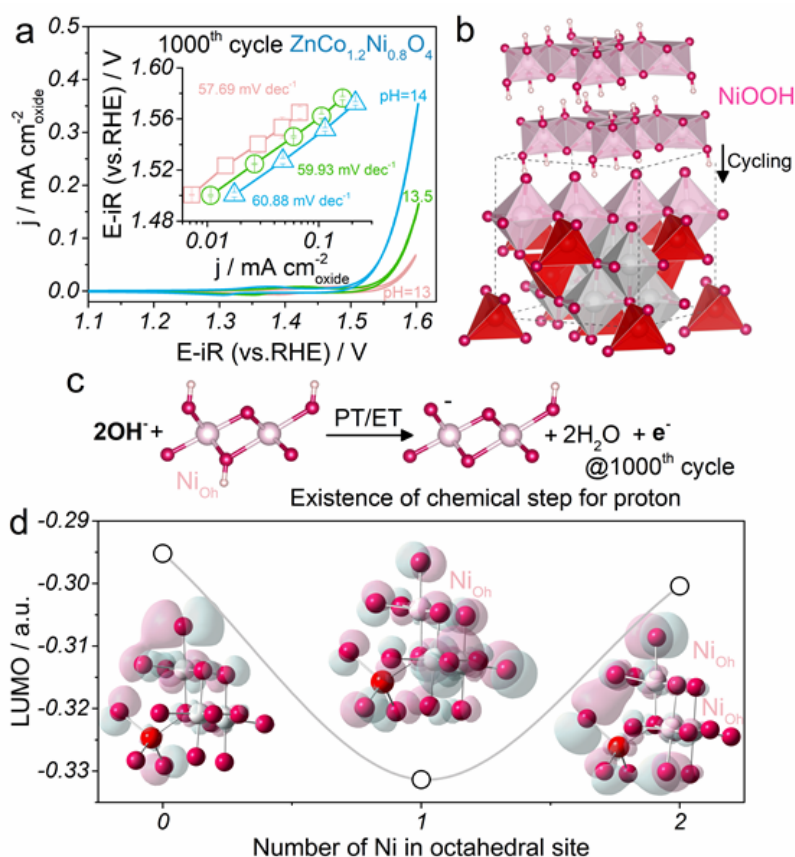


Figure 5.25 (a) pH-dependent OER activity for cycled ZnCo_{1.2}Ni_{0.8}O₄. (b) The schematic for the transition from pristine ZnCo₂O₄/ZnCo_{1.2}Ni_{0.8}O₄ to CoOOH/NiOOH. (c) The schematic for nonconcerted proton-electron transfer (2 H⁺:1e⁻ ratio is shown as an example) of surface deprotonation of cycled ZnCo_{1.2}Ni_{0.8}O₄. (d) Energy of lowest unoccupied molecular orbital (LUMO) versus number of Ni in octahedral site. Insets are the schematic plots of models with one Zn atom in tetrahedral site, three Co or Ni atoms in octahedral site.

5.3.5 DFT Calculation

ZnCo₂O₄ is a representative spinel oxide with Zn²⁺ occupying tetrahedral (Td) site and Co³⁺ staying in octahedral (Oh) site³⁹. With more electronegative Ni metal cations partially substituting Co³⁺, electrons would be drawn away from the remaining Co³⁺ and the energy of antibonding states would be lowered down,⁸³ initiating a redistribution of electronic density between metal cations and oxygen⁸⁴ and thus altering the electrocatalytic performances. To figure out the interaction between metal *d*-band and oxygen *p*-band orbitals, we have carried out first-principles DFT+U calculations on the transition metal *d* states and oxygen *p* states for

$\text{ZnCo}_{2-x}\text{Ni}_x\text{O}_4$. Detailed calculation methods are shown in the supporting information. M_{Oh} d -band centre (relative to E_{F}) is initially 0.705 eV higher than O p -band centre (relative to E_{F}) in ZnCo_2O_4 and decreases to 0.455 eV for $\text{ZnCo}_{1.8}\text{Ni}_{0.2}\text{O}_4$ (Figure 5.26). When $x \geq 0.4$, O p -band centre becomes higher than M_{Oh} d -band centre and the energy difference between them grows larger with further increased Ni substitution ratios. The relative position of O p -band and M_{Oh} d -band should, to some extent, explain and predict the structural stability of spinel $\text{ZnCo}_{2-x}\text{Ni}_x\text{O}_4$. In spinel with the ratio $x=0$ and 0.2, the energy of O states is lower than that of M_{Oh} , suggesting that lattice oxygen is redox inactive under oxidative conditions and that oxygen would binds strongly to the cations. When x is continuously increased to 0.4, the energy of O states becomes higher than that of M_{Oh} and thus oxygen ions become redox active. Nevertheless, since their energy are still relatively close, the whole lattice structure is still stable. However, when x is further increased to 0.6 and above, the energy of O states becomes greater than the energy of M_{Oh} states. According to previous work on perovskites, this finding suggest higher activity for lattice oxygen in the materials and thus the destabilization of the oxide.³⁴ To verify whether $\text{ZnCo}_{2-x}\text{Ni}_x\text{O}_4$ ($x=0-2$) oxides are thermodynamically stable in these spinel phases, we have calculated their formation energies (Figure 5.26). The formation enthalpy of ZnCo_2O_4 is weaker than that of $\text{ZnCo}_{2-x}\text{Ni}_x\text{O}_4$. Hence, with increasing Ni substitution into ZnCo_2O_4 , the structure becomes more unstable. In order to assess the effect of the continuous shift of the spinel electronic structure, pure $\text{ZnCo}_{2-x}\text{Ni}_x\text{O}_4$ ($x=0.0, 0.2, 0.4, 0.6, 0.8$) phases were synthesized by thermal decomposition methods.

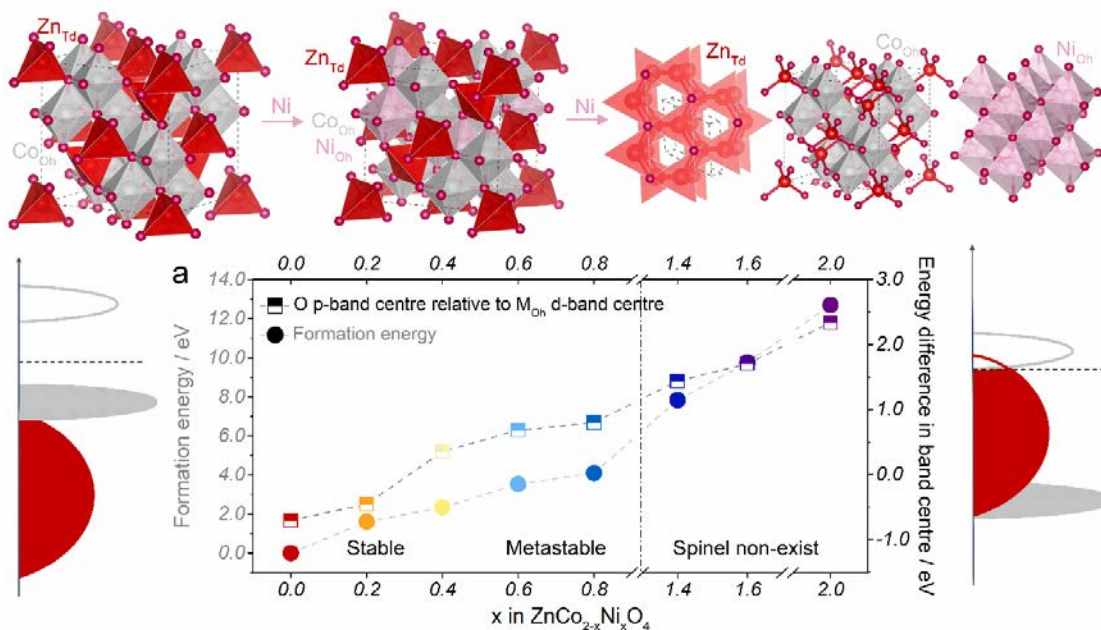


Figure 5.26 Top panel shows the crystal structures of Ni substituted ZnCo_2O_4 . $\text{ZnCo}_{2-x}\text{Ni}_x\text{O}_4$ ($x \leq 0.8$) possesses a spinel structure with Zn accommodating tetrahedron (red), Co (grey) and Ni (pink) occupying an octahedron. $\text{ZnCo}_{2-x}\text{Ni}_x\text{O}_4$ ($x > 0.8$) has phase separation into wurtzite, spinel and rock-salt structures. Bottom left panel shows the schematic representation of M_{Oh} d-band and O p-band for $\text{ZnCo}_{2-x}\text{Ni}_x\text{O}_4$ ($x=0, 0.2$) with M_{Oh} d-band centre higher than O p-band centre. Bottom right panel is the schematic representation of M_{Oh} d-band and O p-band for $\text{ZnCo}_{2-x}\text{Ni}_x\text{O}_4$ ($x=0.4, 0.6, 0.8$) with O p-band centre higher than M_{Oh} d-band centre. (a) Formation energy of $\text{ZnCo}_{2-x}\text{Ni}_x\text{O}_4$ ($x=0, 0.2, 0.4, 0.6, 0.8, 1.4, 1.6, 2.0$) relative to ZnCo_2O_4 and O p-band centre relative to M_{Oh} d-band centre of $\text{ZnCo}_{2-x}\text{Ni}_x\text{O}_4$ ($x=0, 0.2, 0.4, 0.6, 0.8, 1.4, 1.6, 2.0$). Three regions are distinguished with the increased amount of x ratio: stable region for $\text{ZnCo}_{2-x}\text{Ni}_x\text{O}_4$ ($x=0, 0.2$ and 0.4); unstable region for $\text{ZnCo}_{2-x}\text{Ni}_x\text{O}_4$ ($x=0.6$ and 0.8) which undergoes significant surface reconstruction during OER cycles; for $\text{ZnCo}_{2-x}\text{Ni}_x\text{O}_4$ with $x > 0.8$, too high the formation energy or O p-band centre relative to M_{Oh} d-band centre results in a very unstable phase and non-existent spinel structure.

The PDOS for pure-phase ZnCo_2O_4 , $\text{ZnCo}_{1.6}\text{Ni}_{0.4}\text{O}_4$ and $\text{ZnCo}_{1.2}\text{Ni}_{0.8}\text{O}_4$ spinel oxides are shown in Figure 5.27. Non-bonded oxygen *p* states can be observed for $\text{ZnCo}_{1.2}\text{Ni}_{0.8}\text{O}_4$, but not for ZnCo_2O_4 and $\text{ZnCo}_{1.6}\text{Ni}_{0.4}\text{O}_4$, which can be oxidized and form electrophilic oxygen species as active sites⁸⁵. With increased substitution level, oxygen becomes much more electropositive than the metal cations in octahedron especially when *x* is larger than 0.4. Electrons from the O *p*-band are poured into the *d*-band for $\text{ZnCo}_{2-x}\text{Ni}_x\text{O}_4$ ($x=0.6, 0.8$), which initiates the dropped in formation energy of oxygen vacancies⁸⁶ and structural relaxations. Overall, those two findings

(presence of non-bonding oxygen states and oxygen states at the Fermi level) suggest that lattice oxygen are more prone to participate to the OER reaction on the surface of $\text{ZnCo}_{2-x}\text{Ni}_x\text{O}_4$ ($x=0.6, 0.8$). (Figure 5.28)

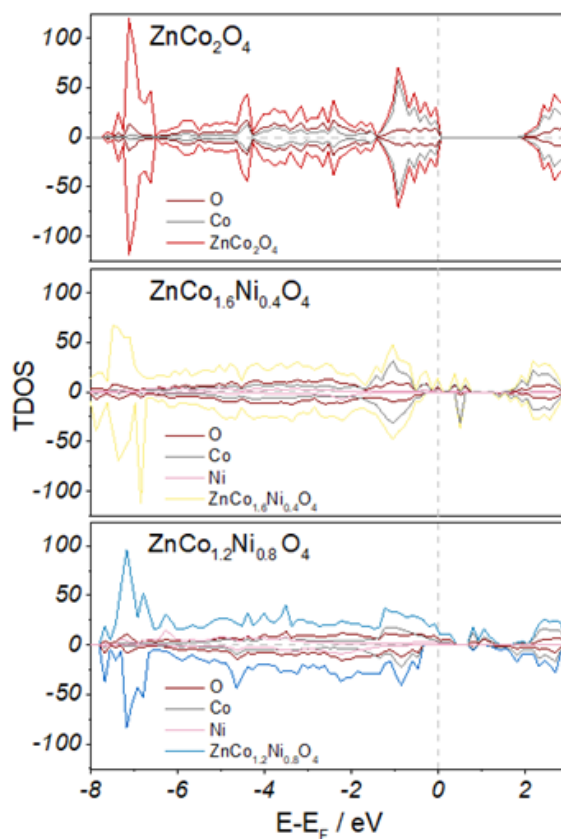


Figure 5.27 Electronic density of states (DOS) of ZnCo_2O_4 (top panel), $\text{ZnCo}_{1.6}\text{Ni}_{0.4}\text{O}_4$ (middle panel) and $\text{ZnCo}_{1.2}\text{Ni}_{0.8}\text{O}_4$ (bottom panel).

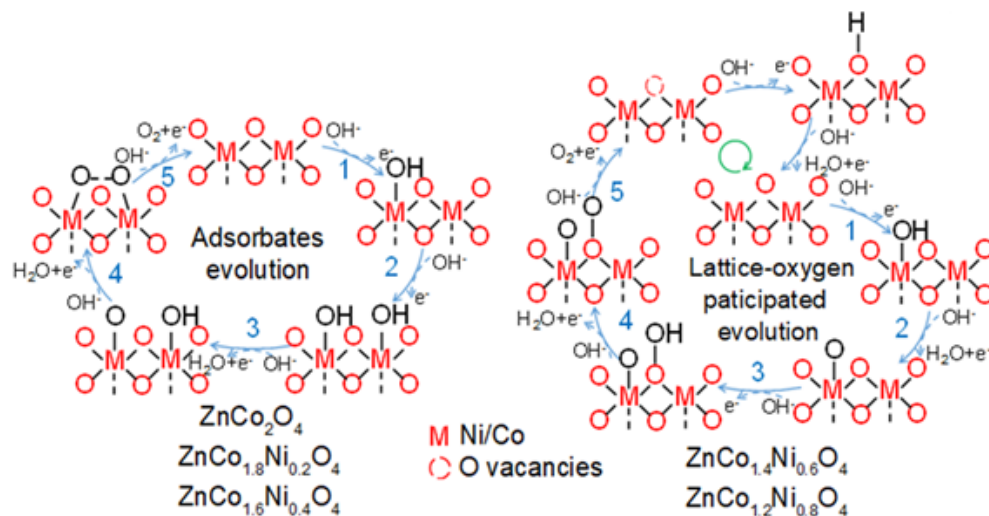


Figure 5.28 The schematics in the bottom middle show the adsorbates evolution mechanism (AEM) for $\text{ZnCo}_{2-x}\text{Ni}_x\text{O}_4$ ($x=0, 0.2$ and 0.4) and the lattice-oxygen participated evolution mechanism (LOM) for $\text{ZnCo}_{2-x}\text{Ni}_x\text{O}_4$ ($x=0.6$ and 0.8). Red and black atoms are from the lattice and the solvent, respectively.

5.4 Summary

This reveals the mechanism of activity/stability behaviour for spinel oxides through investigating Ni-substitution mediated OER activity and stability of ZnCo_2O_4 . $\text{ZnCo}_{2-x}\text{Ni}_x\text{O}_4$ has been synthesized by thermal decomposition methods and a Ni substitution larger than 40% does not give pure phased spinel oxides. The lattice parameter as well as M-O bond length of $\text{ZnCo}_{2-x}\text{Ni}_x\text{O}_4$ ($x=0, 0.2, 0.4, 0.6, 0.8$) increases with Ni substitution ratio, in accordance with the decreased stability of $\text{ZnCo}_{2-x}\text{Ni}_x\text{O}_4$ as predicted by DFT. The OER performance of $\text{ZnCo}_{2-x}\text{Ni}_x\text{O}_4$ ($x=0, 0.2, 0.4, 0.6, 0.8$) has been studied by cyclic voltammetry (CV) at 10mV s^{-1} for thousand cycles. With small amount of Ni addition ($x=0.2, 0.4$), $\text{ZnCo}_{2-x}\text{Ni}_x\text{O}_4$ exhibit similar activity and maintain commensurate stability as ZnCo_2O_4 . With more Ni substitution ($x=0.6, 0.8$), $\text{ZnCo}_{2-x}\text{Ni}_x\text{O}_4$ exhibit continuously increased OER currents after cycling, and they possess triple activity at thousands cycle and superior to that of IrO_2 . The electrons on O p-bands of $\text{ZnCo}_{1.2}\text{Ni}_{0.8}\text{O}_4$ can be easily provided, which results in decreased stability and amorphized surface. $\text{ZnCo}_{2-x}\text{Ni}_x\text{O}_4$ has been synthesized by thermal decomposition methods. The OER performance of $\text{ZnCo}_{2-x}\text{Ni}_x\text{O}_4$ ($x=0, 0.2, 0.4, 0.6, 0.8$) Transmission electron microscopy (TEM), X-ray photoelectron spectroscopy (XPS), X-ray absorption spectroscopy (XAS) and X-ray

magnetic circular dichroism (XMCD) techniques aid the investigation on the surface-active forms of representative $\text{ZnCo}_{0.2}\text{Ni}_{0.8}\text{O}_4$ under OER conditions. The surface of $\text{ZnCo}_{0.2}\text{Ni}_{0.8}\text{O}_4$ undergoes reconstruction, Ni^{3+} segregates on the surface of the catalysts, giving NiOOH as the real active species for $\text{ZnCo}_{0.2}\text{Ni}_{0.8}\text{O}_4$. This transition from spinel oxide $\text{ZnCo}_{0.2}\text{Ni}_{0.8}\text{O}_4$ to layered (oxy)hydroxide has been studied by pH dependent experiments, finding that a pH-dependent deprotonation process occurs in the surface reconstruction. A non-concerted OER mechanism is proposed for $\text{ZnCo}_{0.2}\text{Ni}_{0.8}\text{O}_4$. On the contrary, stable ZnCo_2O_4 is also verified to deprotonate during OER. However, this decomposition process for the transition from ZnCo_2O_4 to a very thin layer of CoOOH is stabilized quickly. This work indicates that the OER activity and stability can be tuned by the amount of Ni substitution in spinel oxides ZnCo_2O_4 . Variation in stability of $\text{ZnCo}_{2-x}\text{Ni}_x\text{O}_4$ impacts on the reconstruction process occurring under OER condition in alkaline medium. Besides, the real active species for $\text{ZnCo}_{2-x}\text{Ni}_x\text{O}_4$ have been revealed. The findings of this work provide insights for studying the surface evolution of spinel oxides under OER conditions and understanding the activity/stability behavior for spinel oxides. Density function theory (DFT) is applied in the disclosure of decreased stability, in the term of formation energy, of $\text{ZnCo}_{2-x}\text{Ni}_x\text{O}_4$ with increased amount of Ni substitution. Besides, O p-band center (relative to E_F) of $\text{ZnCo}_{2-x}\text{Ni}_x\text{O}_4$ is predicted to uplift as compared to that of ZnCo_2O_4 , which indicates a lattice oxygen participated OER mechanism for metastable $\text{ZnCo}_{2-x}\text{Ni}_x\text{O}_4$. Simultaneously, the M_{Oh} d-band center goes down with increased Ni amount. When M_{Oh} d-band center is much lower than O p-band center, the compounds are unstable in pure-phase spinel structure.

5.5 Reference

- (1) Lewis, N. S. Toward Cost-Effective Solar Energy Use. *Science* **2007**, *315* (5813), 798–801. <https://doi.org/10.1126/science.1137014>.
- (2) McCrory, C. C.; Jung, S.; Peters, J. C.; Jaramillo, T. F. Benchmarking Heterogeneous Electrocatalysts for the Oxygen Evolution Reaction. *Journal of the American Chemical Society* **2013**, *135* (45), 16977–16987.
- (3) Song, S.; Zhang, H.; Ma, X.; Shao, Z.; Baker, R. T.; Yi, B. Electrochemical Investigation of Electrocatalysts for the Oxygen Evolution Reaction in PEM Water Electrolyzers. *International Journal of Hydrogen Energy* **2008**, *33* (19), 4955–4961. <https://doi.org/10.1016/j.ijhydene.2008.06.039>.
- (4) Trasatti, S. Electrocatalysis by Oxides—Attempt at a Unifying Approach. *Journal of Electroanalytical Chemistry and Interfacial Electrochemistry* **1980**, *111* (1), 125–131.

- (5) Hong, W. T.; Welsch, R. E.; Shao-Horn, Y. Descriptors of Oxygen-Evolution Activity for Oxides: A Statistical Evaluation. *The Journal of Physical Chemistry C* **2015**, *120* (1), 78–86.
- (6) Bockris, J. O. The Electrocatalysis of Oxygen Evolution on Perovskites. *J. Electrochem. Soc.* **1984**, *131* (2), 290. <https://doi.org/10.1149/1.2115565>.
- (7) Suntivich, J.; Hong, W. T.; Lee, Y.-L.; Rondinelli, J. M.; Yang, W.; Goodenough, J. B.; Dabrowski, B.; Freeland, J. W.; Shao-Horn, Y. Estimating Hybridization of Transition Metal and Oxygen States in Perovskites from O *K* -Edge X-Ray Absorption Spectroscopy. *J. Phys. Chem. C* **2014**, *118* (4), 1856–1863. <https://doi.org/10.1021/jp410644j>.
- (8) Zhou, W.; Sunarso, J. Enhancing Bi-Functional Electrocatalytic Activity of Perovskite by Temperature Shock: A Case Study of LaNiO_{3-δ}. *J. Phys. Chem. Lett.* **2013**, *4* (17), 2982–2988. <https://doi.org/10.1021/jz401169n>.
- (9) Ezbiri, M.; Allen, K. M.; Gàlvez, M. E.; Michalsky, R.; Steinfeld, A. Design Principles of Perovskites for Thermochemical Oxygen Separation. *ChemSusChem* **2015**, *8* (11), 1966–1971. <https://doi.org/10.1002/cssc.201500239>.
- (10) Suntivich, J.; May, K. J.; Gasteiger, H. A.; Goodenough, J. B.; Shao-Horn, Y. A Perovskite Oxide Optimized for Oxygen Evolution Catalysis from Molecular Orbital Principles. *Science* **2011**, *334* (6061), 1383–1385. <https://doi.org/10.1126/science.1212858>.
- (11) Vojvodic, A.; Nørskov, J. K. Optimizing Perovskites for the Water-Splitting Reaction. *Science* **2011**, *334* (6061), 1355–1356. <https://doi.org/10.1126/science.1215081>.
- (12) Abidat, I.; Morais, C.; Comminges, C.; Canaff, C.; Rousseau, J.; Guignard, N.; Napporn, T. W.; Habrioux, A.; Kokoh, K. B. Three Dimensionally Ordered Mesoporous Hydroxylated Ni_xCo_{3-x}O₄ Spinels for the Oxygen Evolution Reaction: On the Hydroxyl-Induced Surface Restructuring Effect. *J. Mater. Chem. A* **2017**, *5* (15), 7173–7183. <https://doi.org/10.1039/C7TA00185A>.
- (13) Abidat, I.; Bouchenafa-Saib, N.; Habrioux, A.; Comminges, C.; Canaff, C.; Rousseau, J.; Napporn, T. W.; Dambournet, D.; Borkiewicz, O.; Kokoh, K. B. Electrochemically Induced Surface Modifications of Mesoporous Spinels (Co₃O_{4-δ}, MnCo₂O_{4-δ}, NiCo₂O_{4-δ}) as the Origin of the OER Activity and Stability in Alkaline Medium. *J. Mater. Chem. A* **2015**, *3* (33), 17433–17444. <https://doi.org/10.1039/C5TA04437E>.
- (14) Tang, C.; Cheng, N.; Pu, Z.; Xing, W.; Sun, X. NiSe Nanowire Film Supported on Nickel Foam: An Efficient and Stable 3D Bifunctional Electrode for Full Water Splitting. *Angew. Chem. Int. Ed.* **2015**, *54* (32), 9351–9355. <https://doi.org/10.1002/anie.201503407>.
- (15) Grimaud, A.; May, K. J.; Carlton, C. E.; Lee, Y.-L.; Risch, M.; Hong, W. T.; Zhou, J.; Shao-Horn, Y. Double Perovskites as a Family of Highly Active Catalysts for Oxygen Evolution in Alkaline Solution. *Nature communications* **2013**, *4*, 2439.
- (16) Chang, S. H.; Danilovic, N.; Chang, K.-C.; Subbaraman, R.; Paulikas, A. P.; Fong, D. D.; Highland, M. J.; Baldo, P. M.; Stamenkovic, V. R.; Freeland, J. W. Functional Links between Stability and Reactivity of Strontium Ruthenate Single Crystals during Oxygen Evolution. *Nature communications* **2014**, *5*, 4191.
- (17) Diaz-Morales, O.; Ferrus-Suspedra, D.; Koper, M. T. M. The Importance of Nickel Oxyhydroxide Deprotonation on Its Activity towards Electrochemical Water Oxidation. *Chem. Sci.* **2016**, *7* (4), 2639–2645. <https://doi.org/10.1039/C5SC04486C>.
- (18) Danilovic, N.; Subbaraman, R.; Chang, K.-C.; Chang, S. H.; Kang, Y. J.; Snyder, J.; Paulikas, A. P.; Strmcnik, D.; Kim, Y.-T.; Myers, D.; Stamenkovic, V. R.; Markovic, N. M. Activity–Stability Trends for the Oxygen Evolution Reaction on Monometallic Oxides in Acidic Environments. *J. Phys. Chem. Lett.* **2014**, *5* (14), 2474–2478. <https://doi.org/10.1021/jz501061n>.

- (19) Rong, X.; Parolin, J.; Kolpak, A. M. A Fundamental Relationship between Reaction Mechanism and Stability in Metal Oxide Catalysts for Oxygen Evolution. *ACS Catal.* **2016**, *6* (2), 1153–1158. <https://doi.org/10.1021/acscatal.5b02432>.
- (20) Calle-Vallejo, F.; Díaz-Morales, O. A.; Kolb, M. J.; Koper, M. T. M. Why Is Bulk Thermochemistry a Good Descriptor for the Electrocatalytic Activity of Transition Metal Oxides? *ACS Catal.* **2015**, *5* (2), 869–873. <https://doi.org/10.1021/cs5016657>.
- (21) Xu, X.; Song, F.; Hu, X. A Nickel Iron Diselenide-Derived Efficient Oxygen-Evolution Catalyst. *Nature communications* **2016**, *7*, 12324.
- (22) Kwak, I. H.; Im, H. S.; Jang, D. M.; Kim, Y. W.; Park, K.; Lim, Y. R.; Cha, E. H.; Park, J. CoSe₂ and NiSe₂ Nanocrystals as Superior Bifunctional Catalysts for Electrochemical and Photoelectrochemical Water Splitting. *ACS Appl. Mater. Interfaces* **2016**, *8* (8), 5327–5334. <https://doi.org/10.1021/acsami.5b12093>.
- (23) Stern, L.-A.; Feng, L.; Song, F.; Hu, X. Ni₂P as a Janus Catalyst for Water Splitting: The Oxygen Evolution Activity of Ni₂P Nanoparticles. *Energy Environ. Sci.* **2015**, *8* (8), 2347–2351. <https://doi.org/10.1039/C5EE01155H>.
- (24) Wang, P.; Song, F.; Amal, R.; Ng, Y. H.; Hu, X. Efficient Water Splitting Catalyzed by Cobalt Phosphide-Based Nanoneedle Arrays Supported on Carbon Cloth. *ChemSusChem* **2016**, *9* (5), 472–477. <https://doi.org/10.1002/cssc.201501599>.
- (25) May, K. J.; Carlton, C. E.; Stoerzinger, K. A.; Risch, M.; Suntivich, J.; Lee, Y.-L.; Grimaud, A.; Shao-Horn, Y. Influence of Oxygen Evolution during Water Oxidation on the Surface of Perovskite Oxide Catalysts. *The journal of physical chemistry letters* **2012**, *3* (22), 3264–3270.
- (26) Suntivich, J.; May, K. J.; Gasteiger, H. A.; Goodenough, J. B.; Shao-Horn, Y. A Perovskite Oxide Optimized for Oxygen Evolution Catalysis from Molecular Orbital Principles. *Science* **2011**, *334* (6061), 1383–1385.
- (27) Goniakowski, J.; Finocchi, F.; Noguera, C. Polarity of Oxide Surfaces and Nanostructures. *Rep. Prog. Phys.* **2008**, *71* (1), 016501. <https://doi.org/10.1088/0034-4885/71/1/016501>.
- (28) Pankajavalli, R.; Sreedharan, O. M. Thermodynamic Stabilities of LaVO₃ and LaVO₄ by e.m.f. Methods. *Materials Letters* **1995**, *24* (4), 247–251. [https://doi.org/10.1016/0167-577X\(95\)00096-8](https://doi.org/10.1016/0167-577X(95)00096-8).
- (29) Calle-Vallejo, F.; Martínez, J. I.; García-Lastra, J. M.; Mogensen, M.; Rossmeisl, J. Trends in Stability of Perovskite Oxides. *Angewandte Chemie International Edition* **2010**, *49* (42), 7699–7701. <https://doi.org/10.1002/anie.201002301>.
- (30) Hong, W. T.; Risch, M.; Stoerzinger, K. A.; Grimaud, A.; Suntivich, J.; Shao-Horn, Y. Toward the Rational Design of Non-Precious Transition Metal Oxides for Oxygen Electrocatalysis. *Energy Environ. Sci.* **2015**, *8* (5), 1404–1427. <https://doi.org/10.1039/C4EE03869J>.
- (31) Lee, Y.-L.; Kleis, J.; Rossmeisl, J.; Shao-Horn, Y.; Morgan, D. Prediction of Solid Oxide Fuel Cell Cathode Activity with First-Principles Descriptors. *Energy Environ. Sci.* **2011**, *4* (10), 3966. <https://doi.org/10.1039/c1ee02032c>.
- (32) Yang, C.; Grimaud, A. Factors Controlling the Redox Activity of Oxygen in Perovskites: From Theory to Application for Catalytic Reactions. *Catalysts* **2017**, *7* (5), 149. <https://doi.org/10.3390/catal7050149>.

- (33) Jung, J.-I.; Jeong, H. Y.; Lee, J.-S.; Kim, M. G.; Cho, J. A Bifunctional Perovskite Catalyst for Oxygen Reduction and Evolution. *Angew. Chem.* **2014**, *126* (18), 4670–4674. <https://doi.org/10.1002/ange.201311223>.
- (34) Grimaud, A.; Diaz-Morales, O.; Han, B.; Hong, W. T.; Lee, Y.-L.; Giordano, L.; Stoerzinger, K. A.; Koper, M. T.; Shao-Horn, Y. Activating Lattice Oxygen Redox Reactions in Metal Oxides to Catalyse Oxygen Evolution. *Nature chemistry* **2017**, *9* (5), 457.
- (35) Kovtunenkov, P. V. Defect Formation in Spinels in Oxygen Nonstoichiometry (a Review). *Glass and Ceramics* **1997**, *54* (5), 143–148. <https://doi.org/10.1007/BF02767937>.
- (36) Bao, J.; Zhang, X.; Fan, B.; Zhang, J.; Zhou, M.; Yang, W.; Hu, X.; Wang, H.; Pan, B.; Xie, Y. Ultrathin Spinel-Structured Nanosheets Rich in Oxygen Deficiencies for Enhanced Electrocatalytic Water Oxidation. *Angew. Chem.* **2015**, *127* (25), 7507–7512. <https://doi.org/10.1002/ange.201502226>.
- (37) Wang, H.-Y.; Hung, S.-F.; Chen, H.-Y.; Chan, T.-S.; Chen, H. M.; Liu, B. In Operando Identification of Geometrical-Site-Dependent Water Oxidation Activity of Spinel Co_3O_4 . *J. Am. Chem. Soc.* **2016**, *138* (1), 36–39. <https://doi.org/10.1021/jacs.5b10525>.
- (38) Jacobs, J. P.; Maltha, A.; Reintjes, J. G. H.; Drimal, J.; Ponc, V.; Brongersma, H. H. The Surface of Catalytically Active Spinels. *Journal of Catalysis* **1994**, *147* (1), 294–300. <https://doi.org/10.1006/jcat.1994.1140>.
- (39) Parida, P.; Kashikar, R.; Jena, A.; Nanda, B. R. K. Universality in the Electronic Structure of 3d Transition Metal Oxides. *Journal of Physics and Chemistry of Solids* **2018**, *123*, 133–149. <https://doi.org/10.1016/j.jpcs.2018.04.009>.
- (40) Wei, C.; Feng, Z.; Scherer, G. G.; Barber, J.; Shao-Horn, Y.; Xu, Z. J. Cations in Octahedral Sites: A Descriptor for Oxygen Electrocatalysis on Transition-Metal Spinels. *Advanced Materials* **2017**, *29* (23), 1606800.
- (41) Abidat, I.; Bouchenafa-Saib, N.; Habrioux, A.; Comminges, C.; Canaff, C.; Rousseau, J.; Napporn, T. W.; Dambournet, D.; Borkiewicz, O.; Kokoh, K. B. Electrochemically Induced Surface Modifications of Mesoporous Spinels ($\text{Co}_3\text{O}_{4-\delta}$, $\text{MnCo}_2\text{O}_{4-\delta}$, $\text{NiCo}_2\text{O}_{4-\delta}$) as the Origin of the OER Activity and Stability in Alkaline Medium. *J. Mater. Chem. A* **2015**, *3* (33), 17433–17444. <https://doi.org/10.1039/C5TA04437E>.
- (42) Du, Y.; Zhu, Y.; Xi, S.; Yang, P.; Moser, H. O.; Breese, M. B. H.; Borgna, A. XAFCA: A New XAFS Beamline for Catalysis Research. *J Synchrotron Rad* **2015**, *22* (3), 839–843. <https://doi.org/10.1107/S1600577515002854>.
- (43) Ravel, B.; Newville, M. *ATHENA*, *ARTEMIS*, *HEPHAESTUS*: Data Analysis for X-Ray Absorption Spectroscopy Using *IFEFFIT*. *J Synchrotron Rad* **2005**, *12* (4), 537–541. <https://doi.org/10.1107/S0909049505012719>.
- (44) Sanz-Ortiz, M. N.; Rodríguez, F.; Rodríguez, J.; Demazeau, G. Optical and Magnetic Characterisation of Co^{3+} and Ni^{3+} in LaAlO_3 : Interplay between the Spin State and Jahn–Teller Effect. *J. Phys.: Condens. Matter* **2011**, *23* (41), 415501. <https://doi.org/10.1088/0953-8984/23/41/415501>.
- (45) Yu, X.; Wilhelmi, O.; Moser, H. O.; Vidyardaj, S. V.; Gao, X.; Wee, A. T. S.; Nyunt, T.; Qian, H.; Zheng, H. New Soft X-Ray Facility SINS for Surface and Nanoscale Science at SSSL. *Journal of Electron Spectroscopy and Related Phenomena* **2005**, *144–147*, 1031–1034. <https://doi.org/10.1016/j.elspec.2005.01.256>.
- (46) Giordano, L.; Han, B.; Risch, M.; Hong, W. T.; Rao, R. R.; Stoerzinger, K. A.; Shao-Horn, Y. pH Dependence of OER Activity of Oxides: Current and Future Perspectives. *Catalysis Today* **2016**, *262*, 2–10.

- (47) Hammer, B.; Norskov, J. K. Why Gold Is the Noblest of All the Metals. *Nature* **1995**, *376* (6537), 238–240. <https://doi.org/10.1038/376238a0>.
- (48) Stamenkovic, V. R.; Fowler, B.; Mun, B. S.; Wang, G.; Ross, P. N.; Lucas, C. A.; Markovic, N. M. Improved Oxygen Reduction Activity on Pt₃Ni(111) via Increased Surface Site Availability. *Science* **2007**, *315* (5811), 493–497. <https://doi.org/10.1126/science.1135941>.
- (49) Hammer, B.; Nørskov, J. K. Theoretical Surface Science and Catalysis—Calculations and Concepts. In *Advances in Catalysis*; Elsevier, 2000; Vol. 45, pp 71–129. [https://doi.org/10.1016/S0360-0564\(02\)45013-4](https://doi.org/10.1016/S0360-0564(02)45013-4).
- (50) Goodenough, J. B.; Loeb, A. L. Theory of Ionic Ordering, Crystal Distortion, and Magnetic Exchange Due to Covalent Forces in Spinels. *Phys. Rev.* **1955**, *98* (2), 391–408. <https://doi.org/10.1103/PhysRev.98.391>.
- (51) Amini, M. N.; Dixit, H.; Saniz, R.; Lamoen, D.; Partoens, B. The Origin of P-Type Conductivity in ZnM₂O₄ (M = Co, Rh, Ir) Spinels. *Phys. Chem. Chem. Phys.* **2014**, *16* (6), 2588. <https://doi.org/10.1039/c3cp53926a>.
- (52) Haenen, J.; Visscher, W.; Barendrecht, E. Characterization of NiCo₂O₄ Electrodes for O₂ Evolution. *Journal of Electroanalytical Chemistry and Interfacial Electrochemistry* **1986**, *208* (2), 323–341. [https://doi.org/10.1016/0022-0728\(86\)80541-1](https://doi.org/10.1016/0022-0728(86)80541-1).
- (53) Shi, X.; Bernasek, S. L.; Selloni, A. Formation, Electronic Structure, and Defects of Ni Substituted Spinel Cobalt Oxide: A DFT+U Study. *J. Phys. Chem. C* **2016**, *120* (27), 14892–14898. <https://doi.org/10.1021/acs.jpcc.6b03096>.
- (54) Navrotsky, A.; Kleppa, O. J. The Thermodynamics of Cation Distributions in Simple Spinels. *Journal of Inorganic and Nuclear Chemistry* **1967**, *29* (11), 2701–2714. [https://doi.org/10.1016/0022-1902\(67\)80008-3](https://doi.org/10.1016/0022-1902(67)80008-3).
- (55) Kresse, G.; Furthmüller, J. Efficient Iterative Schemes for *Ab Initio* Total-Energy Calculations Using a Plane-Wave Basis Set. *Phys. Rev. B* **1996**, *54* (16), 11169–11186. <https://doi.org/10.1103/PhysRevB.54.11169>.
- (56) Perdew, J. P.; Burke, K.; Ernzerhof, M. Generalized Gradient Approximation Made Simple. *Phys. Rev. Lett.* **1996**, *77* (18), 3865–3868. <https://doi.org/10.1103/PhysRevLett.77.3865>.
- (57) Dudarev, S. L.; Botton, G. A.; Savrasov, S. Y.; Humphreys, C. J.; Sutton, A. P. Electron-Energy-Loss Spectra and the Structural Stability of Nickel Oxide: An LSDA+U Study. *Phys. Rev. B* **1998**, *57* (3), 1505–1509. <https://doi.org/10.1103/PhysRevB.57.1505>.
- (58) Monkhorst, H. J.; Pack, J. D. Special Points for Brillouin-Zone Integrations. *Phys. Rev. B* **1976**, *13* (12), 5188–5192. <https://doi.org/10.1103/PhysRevB.13.5188>.
- (59) Henne, B.; Ney, V.; Ollefs, K.; Wilhelm, F.; Rogalev, A.; Ney, A. Magnetic Interactions in the Zn-Co-O System: Tuning Local Structure, Valence and Carrier Type from Extremely Co Doped ZnO to ZnCo₂O₄. *Sci Rep* **2015**, *5* (1), 16863. <https://doi.org/10.1038/srep16863>.
- (60) Suntivich, J.; May, K. J.; Gasteiger, H. A.; Goodenough, J. B.; Shao-Horn, Y. A Perovskite Oxide Optimized for Oxygen Evolution Catalysis from Molecular Orbital Principles. *Science* **2011**, *334* (6061), 1383–1385. <https://doi.org/10.1126/science.1212858>.
- (61) Nguyen, T. D.; Scherer, G. G.; Xu, Z. J. A Facile Synthesis of Size-Controllable IrO₂ and RuO₂ Nanoparticles for the Oxygen Evolution Reaction. *Electrocatalysis* **2016**, *7* (5), 420–427. <https://doi.org/10.1007/s12678-016-0321-2>.
- (62) Lee, Y.; Suntivich, J.; May, K. J.; Perry, E. E.; Shao-Horn, Y. Synthesis and Activities of Rutile IrO₂ and RuO₂ Nanoparticles for Oxygen Evolution in Acid and Alkaline Solutions. *J. Phys. Chem. Lett.* **2012**, *3* (3), 399–404. <https://doi.org/10.1021/jz2016507>.

- (63) Yang, C.; Fontaine, O.; Tarascon, J.-M.; Grimaud, A. Chemical Recognition of Active Oxygen Species on the Surface of Oxygen Evolution Reaction Electrocatalysts. *Angewandte Chemie* **2017**, *129* (30), 8778–8782.
- (64) Trotochaud, L.; Ranney, J. K.; Williams, K. N.; Boettcher, S. W. Solution-Cast Metal Oxide Thin Film Electrocatalysts for Oxygen Evolution. *J. Am. Chem. Soc.* **2012**, *134* (41), 17253–17261. <https://doi.org/10.1021/ja307507a>.
- (65) Mildner, S.; Beleggia, M.; Mierwaldt, D.; Hansen, T. W.; Wagner, J. B.; Yazdi, S.; Kasama, T.; Ciston, J.; Zhu, Y.; Jooss, C. Environmental TEM Study of Electron Beam Induced Electrochemistry of Pr_{0.64}Ca_{0.36}MnO₃ Catalysts for Oxygen Evolution. *J. Phys. Chem. C* **2015**, *119* (10), 5301–5310. <https://doi.org/10.1021/jp511628c>.
- (66) Muller, D. A.; Nakagawa, N.; Ohtomo, A.; Grazul, J. L.; Hwang, H. Y. Atomic-Scale Imaging of Nanoengineered Oxygen Vacancy Profiles in SrTiO₃. *Nature* **2004**, *430* (7000), 657–661. <https://doi.org/10.1038/nature02756>.
- (67) Atiya, G.; Mikhelashvili, V.; Eisenstein, G.; Kaplan, W. D. Solid-State Dewetting of Pt on (100) SrTiO₃. *J. Mater. Sci.* **2014**, *49* (11), 3863–3874. <https://doi.org/10.1007/s10853-013-7966-5>.
- (68) Han, B.; Stoerzinger, K. A.; Tileli, V.; Gamalski, A. D.; Stach, E. A.; Shao-Horn, Y. Nanoscale Structural Oscillations in Perovskite Oxides Induced by Oxygen Evolution. *Nature materials* **2017**, *16* (1), 121.
- (69) Wang, Z. L.; Yin, J. S.; Jiang, Y. D. EELS Analysis of Cation Valence States and Oxygen Vacancies in Magnetic Oxides. *Micron* **2000**, *31* (5), 571–580. [https://doi.org/10.1016/S0968-4328\(99\)00139-0](https://doi.org/10.1016/S0968-4328(99)00139-0).
- (70) Tan, H.; Verbeeck, J.; Abakumov, A.; Van Tendeloo, G. Oxidation State and Chemical Shift Investigation in Transition Metal Oxides by EELS. *Ultramicroscopy* **2012**, *116*, 24–33. <https://doi.org/10.1016/j.ultramic.2012.03.002>.
- (71) Graetz, J.; Ahn, C. C.; Ouyang, H.; Rez, P.; Fultz, B. White Lines and 3d-Occupancy for the 3d Transition-Metal Oxides. *Phys. Rev. B* **2004**, *69* (23), 235103. <https://doi.org/10.1103/PhysRevB.69.235103>.
- (72) Shen, Z.-X.; Shih, C. K.; Jepsen, O.; Spicer, W. E.; Lindau, I.; Allen, J. W. Aspects of the Correlation Effects, Antiferromagnetic Order, and Translational Symmetry of the Electronic Structure of NiO and CoO. *Phys. Rev. Lett.* **1990**, *64* (20), 2442–2445. <https://doi.org/10.1103/PhysRevLett.64.2442>.
- (73) Ng, K. T.; Hercules, D. M. Studies of Nickel-Tungsten-Alumina Catalysts by x-Ray Photoelectron Spectroscopy. *J. Phys. Chem.* **1976**, *80* (19), 2094–2102. <https://doi.org/10.1021/j100560a009>.
- (74) Deng, J.; Lv, X.; Zhang, H.; Zhao, B.; Sun, X.; Zhong, J. Loading the FeNiOOH Cocatalyst on Pt-Modified Hematite Nanostructures for Efficient Solar Water Oxidation. *Phys. Chem. Chem. Phys.* **2016**, *18* (15), 10453–10458. <https://doi.org/10.1039/C6CP01482H>.
- (75) Veal, B. W.; Paulikas, A. P. Final-State Screening and Chemical Shifts in Photoelectron Spectroscopy. *Phys. Rev. B* **1985**, *31* (8), 5399–5416. <https://doi.org/10.1103/PhysRevB.31.5399>.
- (76) Ghijsen, J.; Tjeng, L. H.; van Elp, J.; Eskes, H.; Westerink, J.; Sawatzky, G. A.; Czyzyk, M. T. Electronic Structure of Cu₂O and CuO. *Phys. Rev. B* **1988**, *38* (16), 11322–11330. <https://doi.org/10.1103/PhysRevB.38.11322>.

- (77) Vaz, C. A. F.; Prabhakaran, D.; Altman, E. I.; Henrich, V. E. Experimental Study of the Interfacial Cobalt Oxide in $\text{Co}_3\text{O}_4/\alpha\text{-Al}_2\text{O}_3$ (0001) Epitaxial Films. *Phys. Rev. B* **2009**, *80* (15), 155457. <https://doi.org/10.1103/PhysRevB.80.155457>.
- (78) Wang, H.; Ralston, C. Y.; Patil, D. S.; Jones, R. M.; Gu, W.; Verhagen, M.; Adams, M.; Ge, P.; Riordan, C.; Marganian, C. A.; Mascharak, P.; Kovacs, J.; Miller, C. G.; Collins, T. J.; Brooker, S.; Croucher, P. D.; Wang, K.; Stiefel, E. I.; Cramer, S. P. Nickel L-Edge Soft X-Ray Spectroscopy of Nickel–Iron Hydrogenases and Model Compounds Evidence for High-Spin Nickel(II) in the Active Enzyme. *J. Am. Chem. Soc.* **2000**, *122* (43), 10544–10552. <https://doi.org/10.1021/ja000945g>.
- (79) Tkalych, A. J.; Yu, K.; Carter, E. A. Structural and Electronic Features of $\beta\text{-Ni}(\text{OH})_2$ and $\beta\text{-NiOOH}$ from First Principles. *J. Phys. Chem. C* **2015**, *119* (43), 24315–24322. <https://doi.org/10.1021/acs.jpcc.5b08481>.
- (80) Hong, W. T.; Stoerzinger, K. A.; Lee, Y.-L.; Giordano, L.; Grimaud, A.; Johnson, A. M.; Hwang, J.; Crumlin, E. J.; Yang, W.; Shao-Horn, Y. Charge-Transfer-Energy-Dependent Oxygen Evolution Reaction Mechanisms for Perovskite Oxides. *Energy & Environmental Science* **2017**, *10* (10), 2190–2200.
- (81) Kuo, D.-Y.; Kawasaki, J. K.; Nelson, J. N.; Kloppenburg, J.; Hautier, G.; Shen, K. M.; Schlom, D. G.; Suntivich, J. Influence of Surface Adsorption on the Oxygen Evolution Reaction on IrO_2 (110). *Journal of the American chemical society* **2017**, *139* (9), 3473–3479.
- (82) Görlin, M.; Ferreira de Araújo, J.; Schmies, H.; Bernsmeier, D.; Dresch, S.; Gliech, M.; Jusys, Z.; Chernev, P.; Kraehnert, R.; Dau, H.; Strasser, P. Tracking Catalyst Redox States and Reaction Dynamics in Ni–Fe Oxyhydroxide Oxygen Evolution Reaction Electrocatalysts: The Role of Catalyst Support and Electrolyte pH. *J. Am. Chem. Soc.* **2017**, *139* (5), 2070–2082. <https://doi.org/10.1021/jacs.6b12250>.
- (83) Kuznetsov, D. A.; Han, B.; Yu, Y.; Rao, R. R.; Hwang, J.; Román-Leshkov, Y.; Shao-Horn, Y. Tuning Redox Transitions via Inductive Effect in Metal Oxides and Complexes, and Implications in Oxygen Electrocatalysis. *Joule* **2018**, *2* (2), 225–244. <https://doi.org/10.1016/j.joule.2017.11.014>.
- (84) Krewald, V.; Neese, F.; Pantazis, D. A. Redox Potential Tuning by Redox-Inactive Cations in Nature’s Water Oxidizing Catalyst and Synthetic Analogues. *Phys. Chem. Chem. Phys.* **2016**, *18* (16), 10739–10750. <https://doi.org/10.1039/C5CP07213A>.
- (85) Grimaud, A.; Demortière, A.; Saubanere, M.; Dachraoui, W.; Duchamp, M.; Doublet, M.-L.; Tarascon, J.-M. Activation of Surface Oxygen Sites on an Iridium-Based Model Catalyst for the Oxygen Evolution Reaction. *Nature Energy* **2017**, *2* (1), 16189.
- (86) Grimaud, A.; Hong, W. T.; Shao-Horn, Y.; Tarascon, J.-M. Anionic Redox Processes for Electrochemical Devices. *Nature Mater* **2016**, *15* (2), 121–126. <https://doi.org/10.1038/nmat4551>.

Chapter 6

Revealing the impact of electrolyte composition for Co-based water oxidation catalysts by the study of reaction kinetics parameters

Recent studies have revealed the critical role played by the electrolyte composition on the oxygen evolution reaction (OER) kinetics on the surface of highly active catalysts. While numerous works were devoted to understand the effect of the electrolyte composition on the physical properties of catalysts' surface, very little is known yet about its exact impact on the OER kinetics parameters. In this work, we reveal that the origin for the electrolyte-dependent OER activity for Co-based catalysts originates from two different effects. Increasing the alkaline electrolyte concentration for $La_{1-x}Sr_xCoO_{3-\square}$ perovskites with $x > 0$ and for amorphous CoOOH increases the pre-exponential factor, which can be explained either by an increase of the concentration of active sites or by a change in the entropy of activation. However, changing the alkali cation results in a decrease of the apparent activation enthalpy for Fe-containing amorphous films, traducing a change in intermediates binding energies.

*This section is published substantially as Y. Duan, N. Dubouis, J. Huang, D. Alves Dalla Corte, V. Pimenta, Z. J. Xu & A. Grimaud, Revealing the impact of electrolyte composition for Co-based water oxidation catalysts by the study of reaction kinetics parameters. ACS Catal, 10(7), 4160 (2020). DOI: 10.1021/acscatal.0c00490.

6.1 Introduction

Water electrolysis has long been envisioned as critical for the penetration of renewable energies in the energy mix and into the chemical industry by storing electricity in the form of a chemical

fuel: hydrogen. Nevertheless, water electrolysis suffers from the slow kinetics associated with its two half reactions, namely the hydrogen evolution reaction (HER) and the oxygen evolution reaction (OER). This is especially true for the OER which shows slower kinetics when compared to the HER, as well as drastic instabilities associated with the harsh oxidative and corrosive conditions employed.¹⁻⁴ While early reports in the design of new OER catalysts were often focusing on the tuning of the physical properties of the electrocatalysts surface in order to improve the OER kinetics,^{1,2,5,6} recent findings pointed towards the OER being highly dependent on the electrolyte composition for a wide variety of catalysts, including Co- and Ni-based compounds.⁶⁻¹³ Indeed, for crystalline Co-based catalysts such as the perovskites $\text{La}_{1-x}\text{Sr}_x\text{CoO}_{3-\delta}$ (with $x \geq 0.2$),^{6,14,15} and LaNiO_3 ,¹¹ the Ruddlesden-Popper phase $\text{La}_2\text{Li}_{0.5}\text{Ni}_{0.5}\text{O}_4$ ¹¹ or spinel based catalysts ($\text{ZnCo}_{0.12}\text{Ni}_{0.8}\text{O}_4$ ⁷, $\text{Zn}_{0.2}\text{Co}_{0.8}\text{OOH}$ ⁸, $\text{ZnFe}_{0.4}\text{Co}_{1.6}\text{O}_4$ ⁹ and $\text{CoFe}_{0.25}\text{Al}_{1.75}\text{O}_4$ ¹⁰), the OER kinetics was found to be dependent on the concentration of alkaline solution MOH. Nevertheless, confronting this concentration dependence with results from an online electrochemical mass spectrometry (OEMS) analysis using isotopic labelling, it could be observed for the $\text{La}_{1-x}\text{Sr}_x\text{CoO}_{3-\delta}$ series that it is correlated with the evolution of oxygen originating from the transition metal oxide lattice.¹⁵ The conclusion was thus made that triggering the formation of electrophilic oxygen species “ O^n ” by decreasing the Fermi level energy into oxygen bands with increasing Sr^{2+} -substitution level would induce a change in mechanism with the proton transfer being determining. Eventually, this limitation thus gives rise to the OER to be dependent on the electrolyte concentration. Hence, for LaCoO_3 the OER activity was found independent on the KOH concentration, unlike for $x \geq 0.2$. This proton transfer limitation could later be alleviated by the surface decoration of $\text{La}_{0.5}\text{Sr}_{0.5}\text{CoO}_{3-\delta}$ by phosphates moieties serving as proton relay, therefore increasing the OER kinetics¹⁶.

Moreover, the OER dependence on the electrolyte composition is not limited to crystalline catalysts and was observed for amorphous electrodeposited oxyhydroxides catalysts such as CoOOH which have long been described as being greatly affected by the presence of impurities in the alkaline electrolyte, especially iron impurities¹⁷⁻²⁰. For this class of amorphous catalysts, not only the alkaline electrolyte concentration controls the OER kinetics, but also changing the alkali cation from Li^+ to Cs^+ was found to affect the electrocatalytic properties of such films. Furthermore, as experimentally observed by different groups, the impact of the alkali cation is

more predominant for Fe-containing amorphous films and is thus dependent on the catalysts composition, alike for crystalline compounds.^{12,21,22,23,24} The reason for this change resides in both the change in the structure of the oxyhydroxides with a greater interlayer distance^{12,21} which favors the insertion of large alkali cation inside the catalyst,^{22,23} as well as the formation of different oxygen active species following the substitution of Ni or Co by Fe, as previously discussed for crystalline catalysts.²³⁻²⁵

Hence, assessing and controlling the impact of the electrolyte composition on the OER kinetics was recently at the heart of the development of better OER electrocatalysts. Toward gaining deeper understanding of these complex effects, several operando analytical techniques as well as computation works were carried out to study the impact of the cations and/or electrolyte concentration on the physical properties of catalysts and/or the modification of surface intermediates.^{19,25-30} However, very little is known yet about the exact correlation existing between these interfacial properties and the OER kinetics parameters, hampering further improvement of efficient electrocatalysts. Hence, in order to decipher the origin for the modification of the OER activity as a function of the electrolyte nature, we embarked into a systematic temperature dependence study.

Indeed, as for any catalytic reaction, the catalytic current is given by the product of the rate of the reaction by the concentration of active sites:

$$j \propto \theta_o * k \quad (1)$$

with j the current density, θ_o the concentration of active species, k the rate constant for the reaction. Following the transition state theory, the rate constant of the reaction is given by the following equation:

$$k = \kappa \frac{k_B T}{h} \exp\left(\frac{-\Delta G^*}{RT}\right) \quad (2)$$

with κ the transmission coefficient, k_B the Boltzmann's constant, T absolute temperature, h the Plank constant and ΔG^* the activation Gibb's free energy. However, while the rate constant is thus given by the product of the activation Gibb's free energy of the reaction and the transmission coefficient for electron transfer, experimentally assessing the activation Gibb's free energy is rather challenging. Instead, reaction rates are often compared by assessing the activation energy E_a as given by the Arrhenius equation:

$$E_a = RT^2 \left(\frac{d \ln k}{dT} \right), \quad (3a)$$

Leading after integration to:

$$k = A \exp \left(\frac{-E_a}{RT} \right) \quad (3b)$$

with E_a the activation energy, R gas constant and A the pre-exponential factor. Thus, identifying the experimental Arrhenius equation with the transition state theory leads to:

$$A \propto \exp \left(\frac{-\Delta S^*}{R} \right) \quad (4)$$

with ΔS^* the activation entropy (full derivation is given in the Supplementary Information). Furthermore, following the Bronsted-Evans-Polanyi relation, the energy of formation of the surface intermediates involved into the OER scales linearly with the activation energy. Therefore, when comparing the activation energies with the rate of the reaction, a linear trend should be obtained if the rate is only controlled by the energy of formation of the intermediates. Any deviation of this colinearity could be explained by two factors. First, the concentration of active sites must be accurately determined for each catalyst and must not be modified under operating conditions. Second, the pre-exponential factor is dependent on the conditions (electrolyte, operating potential, etc.).

Therefore, when screening a wide array of catalysts with fixed operating conditions, we expect to measure a linearity between the activation energy and the rate of the reaction (normalized current density). However, when studying the impact of the electrolyte on the rate of an electrocatalytic process, this linearity may not hold since the pre-exponential factor might be modified. In this study, we therefore compare changes in experimentally assessed activation energies and pre-exponential factors for a series of Co-based catalysts in different alkaline electrolytes. Doing so, we aim at revealing if the modification of the OER kinetics as a function of the electrolyte originates from a change in the energy of surface intermediates or rather in a change in the pre-exponential factor that we discuss in light of the structure of water at the interface.

6.2 Experimental methods

Materials. Cobalt (II) nitrate hexahydrate ($\text{Co}(\text{NO}_3)_2$, reagent grade, 98%, Sigma-Aldrich), Iron (II) chloride (FeCl_2 , anhydrous, 99.5%, Alfa Aesar), Lanthanum (III) oxide (La_2O_3 , Reacton®)

99.9%, Alfa Aesar), Strontium carbonate (SrCO_3 , $\geq 99.9\%$ trace metals basis, Sigma-Aldrich), Cobalt (II, III) oxide (Co_3O_4 , 99.7% metals basis, Alfa Aesar), Nickel(II) hydroxide, ($\text{Ni}(\text{OH})_2$, Ni 61%, Alfa Aesar), Lithium hydroxide (LiOH , anhydrous, 99.995%, Alfa Aesar), Sodium hydroxide pellets (NaOH , Sigma-Aldrich), Potassium hydroxide (KOH , 99.99% purity, Sigma-Aldrich), Cesium hydroxide hydrate (CsOH , 99.9% (metals basis) Alfa Aesar) and Tetramethylammonium hydroxide solution (TMAOH, ACS reagent Sigma-Aldrich) were purchased from commercial suppliers. Milli-Q water of $18.2 \text{ M}\Omega\cdot\text{cm}$ was used in all experiments.

Synthesis of $\text{La}_{1-x}\text{Sr}_x\text{CoO}_3$. Perovskites LaCoO_3 , $\text{La}_{0.8}\text{Sr}_{0.2}\text{CoO}_3$, $\text{La}_{0.6}\text{Sr}_{0.4}\text{CoO}_3$ and $\text{La}_{0.5}\text{Sr}_{0.5}\text{CoO}_3$ were synthesized by conventional solid-state route. Detailed synthesis method can be referred to Chapter 3.1.3.

Film deposition of $\text{Co}(\text{OH})_2$ and $\text{Fe}_{0.5}\text{Co}_{0.5}(\text{OH})_2$. $\text{Co}(\text{OH})_2$ and $\text{Fe}_{0.5}\text{Co}_{0.5}(\text{OH})_2$ were cathodically deposited. Detailed synthesis method can be referred to Chapter 3.1.4.

Electrochemistry measurement. Electrodes were prepared for the perovskites series by drop-casting an ink containing the oxide catalyst powder on a glassy carbon electrode. $10 \mu\text{L}$ of ink with a mass ratio of 5:1:1 of oxide catalyst to acetylene black carbon to Nafion® were loaded on the polished glassy carbon electrode surface (0.196 cm^2). Oxygen evolution reaction (OER) measurements were performed on a biologic VSP potentiostat with a rotating disk electrode setup (PINE Inc, US.). A three-electrode configuration was adopted using glassy carbon electrode as working electrode, an Ag/AgCl saturated reference electrode and a Pt wire as counter electrode. The Ag/AgCl reference electrode was calibrated using a reversible hydrogen electrode (RHE) (HydroFlex, Gaskatel, Germany) before and after each experiment. A jacked cell connected with a chiller was used for temperature adjustment.

For the measurements of CoOOH and perovskites LaCoO_3 , $\text{La}_{0.8}\text{Sr}_{0.2}\text{CoO}_3$, $\text{La}_{0.6}\text{Sr}_{0.4}\text{CoO}_3$ and $\text{La}_{0.5}\text{Sr}_{0.5}\text{CoO}_3$ in alkaline solutions, all the alkaline solutions including LiOH , NaOH , KOH ,

CsOH, and TMAOH were purified by $\text{Ni}(\text{OH})_2$ to remove Fe impurities. Prior to the temperature dependence study, a preconditioning step was applied during 20 scans at a scan rate of 100 mV/s in the potential range 1.1-1.7 V vs RHE. For the OER measurements, a scan rate of 10 mV/s was used for cyclic voltammetry (CV) measurements and the rotation speed was set to 1600 rpm. For this study, CV measurements were used instead of galvanostatic or potentiostatic measurements. Indeed, during potentiostatic or galvanostatic holdings, oxygen bubbles are generated on the electrode which surface is eventually partially blocked with time, as observed in Figure 6.1. This surface blocking is relatively limited during much shorter CV scans performed at 10 mV/s. For the temperature dependence measurements, the temperature was increased from 10 to 60 °C with an increment of 10 °C and electrochemical tests were performed afterwards at room temperature to ensure that the electrode suffered no drastic degradation or modifications.

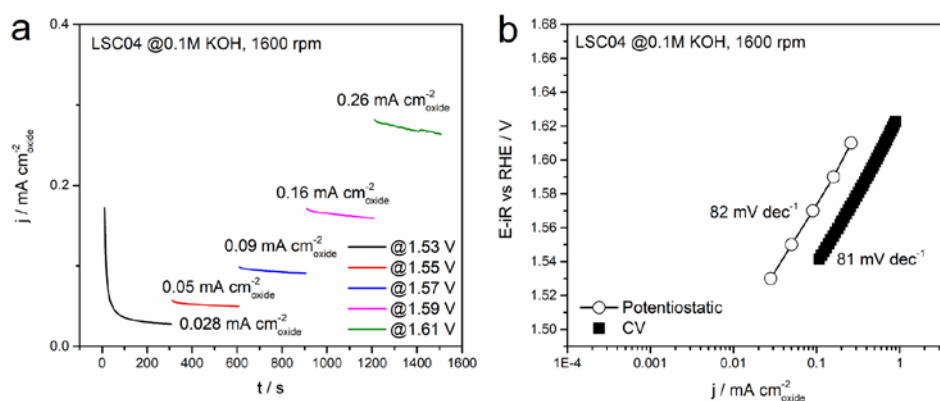


Figure 6.1 (a) Potentiostatic measurements performed for $\text{La}_{0.6}\text{Sr}_{0.4}\text{CoO}_3$ at 25 °C in 0.1 M KOH with a rotation rate of 1600 rpm and (b) Tafel slopes obtained by potentiostatic measurements compared to the one obtained for the same electrode using CV scan performed at 10 mV/s.

All electrochemical potentials here are reported against the reversible hydrogen electrode (RHE). The conversion between potentials versus Ag/AgCl and versus RHE was performed by the equation below:

$$E \text{ (vs RHE)} = E \text{ (vs Ag/AgCl)} + E_{\text{Ag/AgCl}} \text{ (vs RHE)}$$

and $E_{\text{Ag/AgCl}}$ was calibrated at the different temperatures in the different solutions prior to the measurements using the RHE electrode (see above). Furthermore, the reversible potentials for the OER have been corrected as a function of the temperature³¹.

From the CV scans obtained at the different temperatures, Tafel curves were plotted for the OER currents which were obtained from the average between the forward and the backward scans in order to remove the capacitive current contribution, before to be corrected with the ohmic losses. The ohmic drops were corrected by subtracting the ohmic voltage drop from the measured potential, using an electrolyte resistance determined by high-frequency AC impedance, where iR -corrected potentials are denoted as $E - iR$ (i as the current and R as the electrolyte resistance). Activation energy and pre-exponential factors for the perovskites and films in electrolyte with different pH and cations were extrapolated from the slope and the intercept of the $\ln(j)$ vs. $1000/T$ curves. Error bars represent standard deviation from at least 3 independent measurements.

Below, with LaCoO_3 in 0.1M KOH as an example, we show the activation energy and pre-exponential factor calculation:

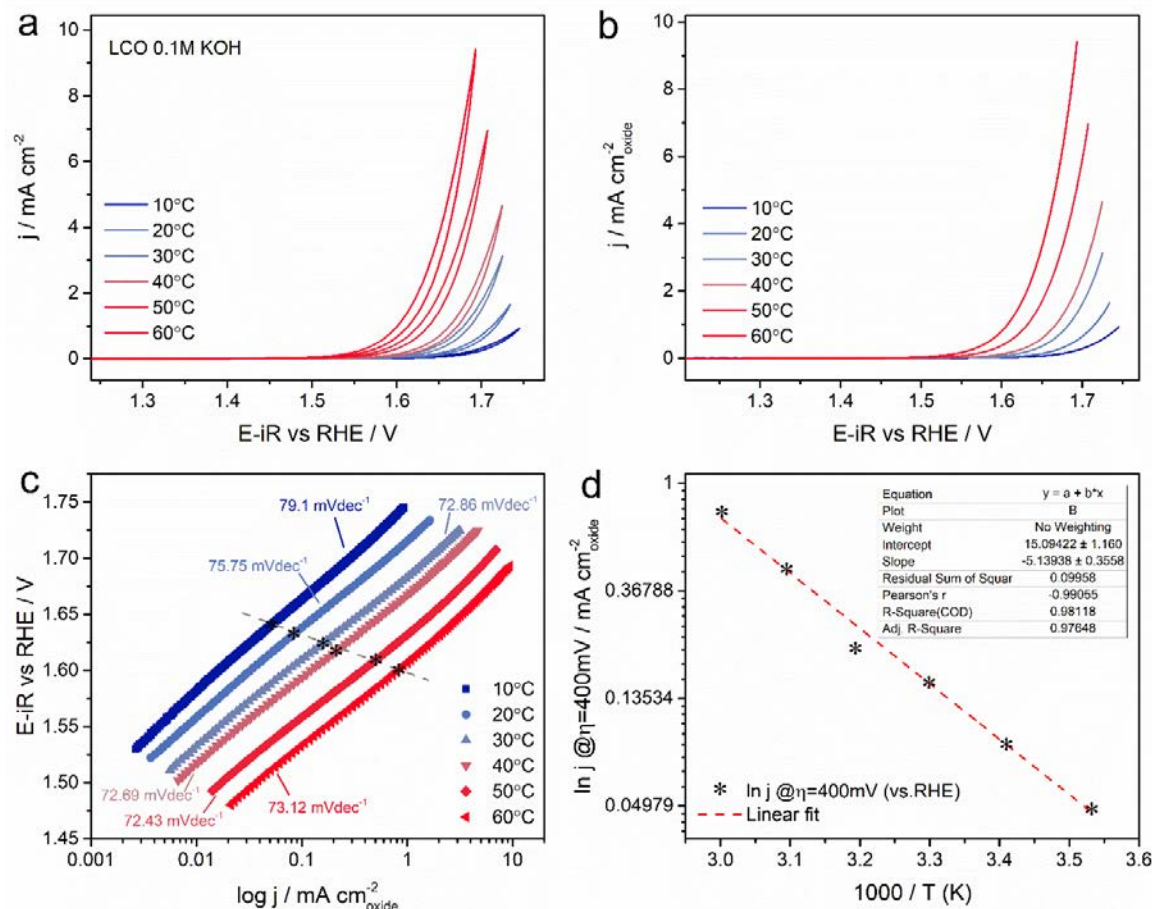


Figure 6.2 a) CV Measurements of LaCoO₃ from 10 to 60°C with an increment of 10°C. b) Averaged CV curves obtained from taking the average OER kinetic currents between forward and backward scans in order to remove the capacitive current contribution. c) Averaged Tafel plots by taking the average OER kinetic currents between forward and backward scans. Tafel slopes (~75mVdec⁻¹) are labelled. d) Extrapolation of activation energy and pre-exponential factor from lnj vs 1000/T curve.

Identification between the Arrhenius equation and TST theory: The activation energy is calculated from the slope of the Arrhenius plot of lnj @ η = 400mV vs. 1000/T curve:^{32,33}

$$\frac{\partial \ln(j)}{\partial (1/T)} = -\frac{E_a}{2.303 \cdot R}$$

The pre-exponential factor is calculated from the intercept of the curve lnj @ η=400mV vs. 1000/T curve:

By Arrhenius equation, the activation energy has the following relationship with the rate constant:

$$E_a = RT^2 \left(\frac{d \ln k}{dT} \right)$$

where E_a is the activation energy, T is absolute temperature, R is gas constant, k is the rate constant for the reaction.

By the transition state theory, the standard free energy ΔG^* , can be written in terms of the equilibrium constant:

$$k = \kappa \frac{k_B T}{h} \exp\left(\frac{-\Delta G^*}{RT}\right)$$

$$\Delta G^* = \Delta H - T \Delta S$$

$$k = \kappa \frac{k_B T}{h} \exp\left(\frac{\Delta S^*}{R}\right) \exp\left(\frac{-\Delta H^*}{RT}\right)$$

$$\ln k = \ln \kappa \frac{k_B T}{h} + \frac{\Delta S^*}{R} - \frac{\Delta H^*}{RT}$$

$$\frac{d \ln k}{dT} = \frac{1}{T} + \frac{\Delta H^*}{RT^2}$$

$$E_a = RT^2 \left(\frac{1}{T} + \frac{\Delta H^*}{RT^2} \right)$$

$$\frac{E_a}{RT} = 1 + \frac{\Delta H^*}{RT}$$

$$k = \kappa \frac{k_B T}{h} e \exp\left(\frac{-\Delta S^*}{R}\right) \exp\left(\frac{-E_a}{RT}\right)$$

$$k \propto \exp\left(\frac{-\Delta S^*}{R}\right) \exp\left(\frac{-E_a}{RT}\right)$$

For LaCoO₃ in 0.1M KOH, the slope of $\ln j$ @ $\eta = 400\text{mV}$ vs. $1000/T$ curve is -5.14, activation energy is:

$$E_a = -2.303 \cdot R \frac{\partial \ln(j)}{\partial (1/T)}$$

$$E_a = 98.29 \text{ kJ mol}^{-1}$$

The pre-exponential factor for LaCoO_3 in 0.1M KOH is 15.09, as obtained from the intercept.

The activation energy and pre-exponential factors are potential dependent.³² The values obtained are different when extrapolate at different potentials, and the activation energies and the pre-exponential factors could also be extrapolated at $\eta = 0\text{mV}$, as done previously.³³ By doing so, the trend of activation energies and pre-exponential factors for $\text{La}_{1-x}\text{Sr}_x\text{CoO}_3$ are shown in Figure 6.3 below. The trend remains the same as the one found when extrapolated at $\eta = 400\text{mV}$.

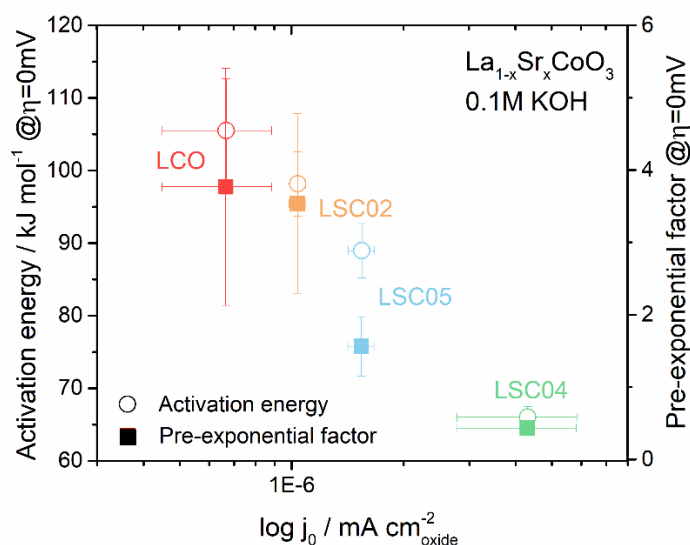


Figure 6.3 Activation energy and pre-exponential factor at $\eta=0\text{mV}$ for $\text{La}_{1-x}\text{Sr}_x\text{CoO}_3$ vs OER exchange current density in 0.1M KOH at 20°C.

Influence of the Mass-Transport. In order to assess the kinetic parameters from the measured current density, we must first make sure that all the mass-transport limitations are discarded so that the activity of the reactant at the electrode-electrolyte interface (a_R) can be considered as

constant. The effect of the mass-transport can be quantified by considering the Koutecký-Levich equation when a RDE setup is employed:³⁴

$$\frac{1}{j_{measured}} = \frac{1}{j_k} + \left(\frac{1}{0.62nFD^{\frac{2}{3}}\nu^{-\frac{1}{6}}C_{bulk}} \right) \omega^{-\frac{1}{2}}$$

where j_k is the kinetic current, n is the number of electrons transferred, F the Faraday constant, D the diffusion coefficient for the reactant, ν the scan rate in the experiment and ω the rotation speed of the electrode. In the absence of mass transport limitation, the second term of the Koutecký-Levich equation should be null and the measured current density is the true kinetic current density. In the case of the alkaline OER, we first demonstrated the absence of influence of the rotation speed for the OER activity measured for different electrodes/compositions (both for dropped-casted perovskites as well as for electrodeposited materials, Figure 6.4). These measurements undoubtedly demonstrate that there is no mass transport limitation and that the measured current density truly reflects the OER kinetics. This is to no surprise, since the soluble reactive species involved in the OER rate determining steps are probably OH^- anions ($\text{O}^* + \text{OH}^- = \text{OOH}^* + e^-$) (or maybe H_2O molecules) for which the activity is large in the pH conditions explored ($\text{pH} > 13$).

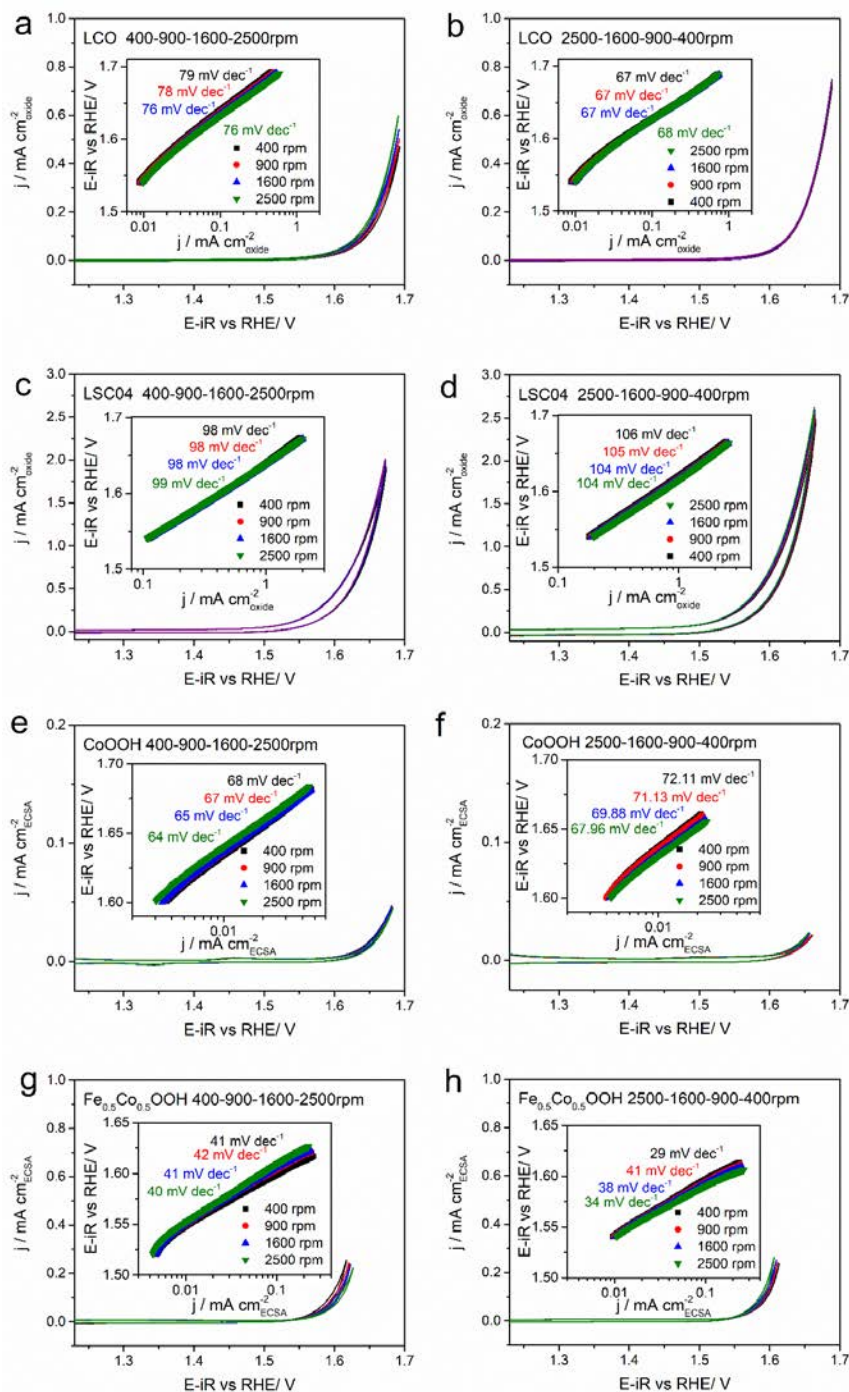


Figure 6.4. CV measurements for LaCoO_3 (a), $\text{La}_{0.6}\text{Sr}_{0.4}\text{CoO}_3$ (c), CoOOH (e) and $\text{Co}_{0.5}\text{Fe}_{0.5}\text{OOH}$ (g) at 20°C with a rotation speed gradually increased from 400 rpm, to 900, 1600 and 2500 rpm. CV measurements for LaCoO_3 (b), $\text{La}_{0.6}\text{Sr}_{0.4}\text{CoO}_3$ (d), CoOOH (f) and $\text{Co}_{0.5}\text{Fe}_{0.5}\text{OOH}$ (h) at 20°C with a rotation speed gradually decreased from 1500 rpm to 1600, 900 and 400 rpm. Tafel plots and Tafel slopes are shown in insets. These measurements demonstrate that no mass transport limitations are measured for these electrodes under these conditions, making valid the assumption that the measured current is the kinetics one.

Characterization. X-ray powder diffraction (XRD) measurements were performed using a BRUKER D8 Advance diffractometer with Cu K α radiation ($\lambda K\alpha_1 = 1.54056 \text{ \AA}$, $\lambda K\alpha_2 = 1.54439 \text{ \AA}$). Data were collected using the X'Celerator detector in the 10-85° window in the 2 θ range.

The specific surface area for LaCoO₃, La_{0.8}Sr_{0.2}CoO₃, La_{0.6}Sr_{0.4}CoO₃, La_{0.5}Sr_{0.5}CoO₃ perovskites were determined through Brunauer, Emmet and Teller (BET) analysis. Nitrogen porosimetry measurements were performed on a Micromeritics Triflex instrument at 77 K, after 7 h outgassing at 150 °C.

The electrochemically active surface area (ECSA) of CoOOH and Fe_{0.5}Co_{0.5}OOH were quantified based on the following equation: ECSA = C_{DL} / C_S where C_{DL} is the non-faradaic double layer capacitance, C_S is the specific capacitance and $i = \nu C_{DL}$ where i is the current, ν is the CV scan rate. C_{DL} is the slope of the i vs ν curve.

6.3 Results and Discussions

6.3.1 La_{1-x}Sr_xCoO_{3- δ} perovskite series

Toward understanding the impact of the electrolyte on the OER kinetics on the surface of transition metal oxides, we first reinvestigated the La_{1-x}Sr_xCoO_{3- δ} perovskite series previously reported by several groups to show enhanced OER kinetics with the Sr²⁺ content.^{6,16,35,36} The OER kinetics for La_{1-x}Sr_xCoO_{3- δ} catalysts with $x = 0, 0.2, 0.4$ and 0.5 were first investigated in 0.1 M KOH by the means of cyclic voltammetry in the 283-333 K range (Figure 6.5a). In this temperature range, no significant modification of the Tafel slope which is measured in the range of 72-79 mV dec⁻¹ is observed (Figure 6.2 and Inset in Figure 6.5a), values which deviate from the ones predicted by microkinetics analysis.^{37,38 32,39} Under such conditions, it becomes rather complex to correctly extrapolate the exchange current densities from the Tafel analysis. Similar observation was previously made for other complex electrocatalytic processes such as the HER on the surface of Pt-based catalysts and, in order to tackle this issue, analysis of the HER kinetics

was then done in the so-called micropolarization region.^{37,38} However, owing to the irreversible nature of the oxygen reactions (OER/ORR), this approach cannot be used for OER electrocatalysts. Therefore, in this work, the apparent activation energies were extracted from the current density at a fixed overpotential of $\eta = 400$ mV rather than by using the extrapolated exchange current densities (inset in Figure 6.5a and Figure 6.5b), while the apparent pre-exponential factors were extrapolated following the method described in the Supplementary Information. Nevertheless, the activation energies and the apparent pre-exponential factors should theoretically be dependent on the overpotential,³² values may differ from previously reported values.³⁹ However, this does not hamper comparing the results obtained for the different catalysts and/or electrolyte compositions. In fact, similar trends were obtained at $\eta = 400$ mV when compared to those extrapolated using the temperature dependence of the exchange current density as extrapolated from the Tafel slopes (Figure 6.3). Therefore, conclusions on the physical origin for the OER dependence on the electrolyte and/or on the catalyst composition can be drawn from this experimental methodology. However, when comparing the values estimated at $\eta = 400$ mV with those extrapolated using the temperature dependence of the exchange current density as extrapolated from the Tafel slopes (Figure 6.3), they are relatively similar. Such observation is rather surprising as, with 400 mV overpotential, one would expect the activation barrier to be lowered by 400 meV (~ 40 kJ mol⁻¹). This emphasizes that no direct microkinetics analysis can be made for the OER in these conditions, and that both the concentration of active sites as well as change in the exposed oxide surface can occur, as recently pointed out.⁴⁰ Therefore, we believe than adopting a more phenomenological approach by extracting the activation energies and the pre-exponential factors at given values for the overpotential is a more adapted methodology.

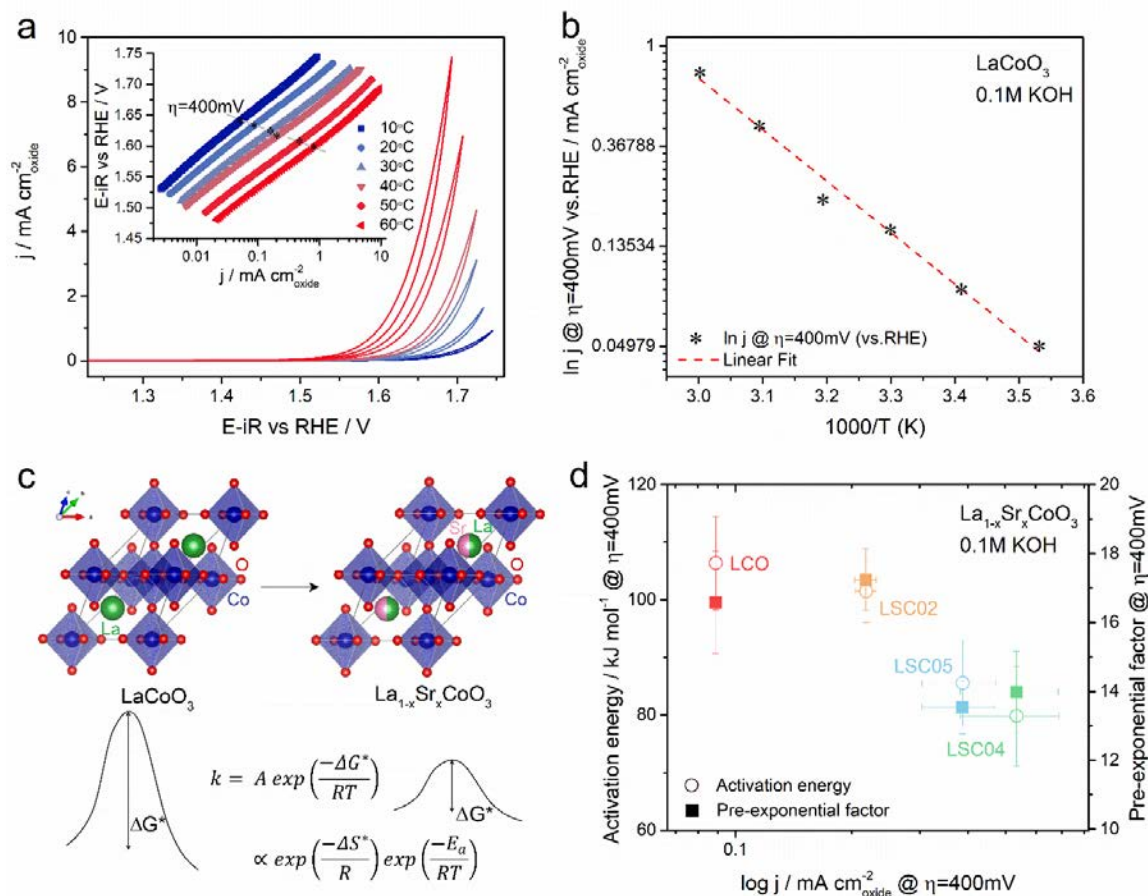


Figure 6.5 (a) Cyclic voltammetry (CV) measurements for LaCoO₃ electrode measured at 10 mV/s in 0.1 M KOH from 10 to 60°C with an increment of 10°C. (b) Extrapolation of the apparent activation energy and the pre-exponential factor from the Arrhenius plot $\ln(j)$ vs $1000/T$. (c) Schematic illustration for the effect of Sr²⁺ substitution into LaCoO₃ on the activation barrier for the OER. (d) Apparent activation energies and pre-exponential factors extrapolated at $\eta = 400$ mV vs. RHE for the La_{1-x}Sr_xCoO₃ series as a function of the OER activity at $\eta = 400$ mV vs. RHE measured in 0.1 M KOH at 20°C.

The OER current density for the different Co-based perovskites was then normalized by the BET surface area to estimate the rate of the reaction (equation 1) and the apparent activation energies experimentally obtained were plotted as a function of the OER current density at $\eta = 400$ mV in 0.1 M KOH. Doing so, it appears that when the rate of the reaction is increasing, i.e. when the normalized current density is increasing, a decrease of the experimentally determined apparent activation energies is found (Figure 6.5 c-d). Thus, one can confirm that this methodology can accurately capture the previously reported trend in which the partial substitution of La³⁺ by Sr²⁺

leads to an enhancement of the OER activity (note that, similarly to previous reports⁶, the OER activity in the $0.4 \leq x \leq 0.6$ range for $\text{La}_{1-x}\text{Sr}_x\text{CoO}_{3-\delta}$ is only marginally impacted by the substitution level). This observation is in agreement with a previous report by Bockris and Otagawa who found a linear trend between the OER activity and the activation energies measured for a wide variety of perovskites, as we recently discussed.^{39,41}

Now turning to the evolution of the pre-exponential factor as a function of the OER activity, it is found to decrease concomitantly to the decrease of the activation energies. While the decrease of the pre-exponential factor should result in a decrease of the OER activity (equation 3b), the effect associated with the decrease of the activation energy is predominant on the OER kinetics for these perovskites. As previously discussed in the introduction, a modification of the pre-exponential factor should either indicate that the rate of the reaction is incorrectly normalized, i.e. that the concentration of active sites is changing during the reaction, or that the entropy of activation is changed. However, observations that the activation energies and the pre-exponential factors evolve in a competing fashion was previously made with for instance Pt-based ORR catalysts. This effect is often referred to as a compensation effect.^{33,42,43} The physical origin for such effect is beyond the scope of this manuscript, however, when plotting the pre-exponential factor as a function of the activation energies that were obtained for the $\text{La}_{1-x}\text{Sr}_x\text{CoO}_{3-\delta}$ series, a linear correlation is obtained (Figure 6.6). Similar linear trends were previously obtained in other fields (biology, chemistry, solid-state conductors) and were explained by a multi-excitation effect.^{33,42,43} From this first study, we can however conclude, and to no surprise, that the enhancement of the OER activity within the $\text{La}_{1-x}\text{Sr}_x\text{CoO}_{3-\delta}$ series arises from a modification of the enthalpy of formation of the intermediates on the surface of these perovskites which lowers the activation energy.

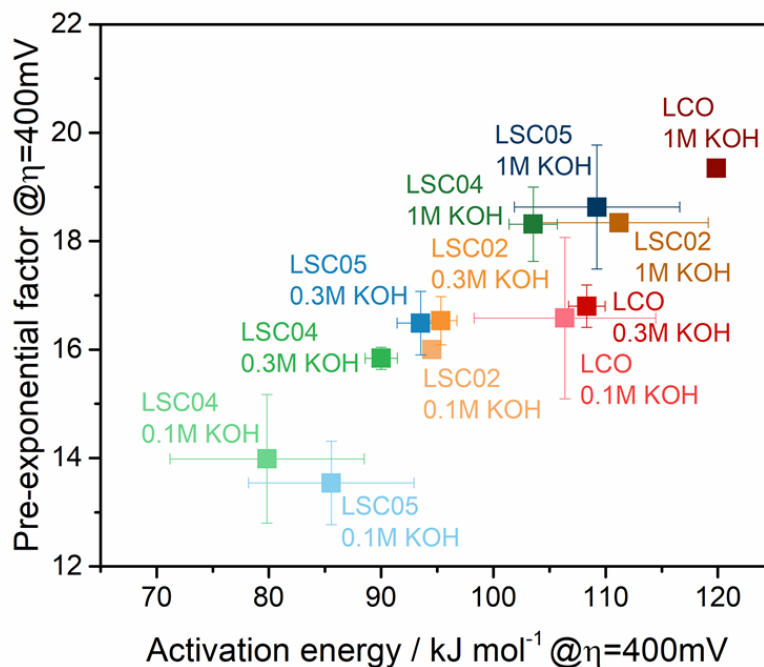


Figure 6.6 Pre-exponential factors plotted as a function of the apparent activation energies extrapolated at $\eta = 400\text{mV}$ for the $\text{La}_{1-x}\text{Sr}_x\text{CoO}_3$ series in 0.1, 0.3 and 1M KOH from Figure 6.5d and Figure 6.7a.

Having confirmed that modifying the electronic properties of OER catalysts has a direct impact on the activation energy and therefore on the energy of the surface intermediates, our attention then turned to the effect of the electrolyte concentration on the OER kinetics measured for Co-based catalysts. First, as previously observed,^{16,35} the OER activity for LaCoO_3 is found independent on the concentration of KOH while it increases for $\text{La}_{1-x}\text{Sr}_x\text{CoO}_{3-\delta}$ catalysts with $x > 0$ (Figure 6.7a). More importantly, the enhanced OER activity for $\text{La}_{1-x}\text{Sr}_x\text{CoO}_{3-\delta}$ catalysts with $x > 0$ is found to arise from an increase of the pre-exponential factor (Figure 6.7b). Instead, following the aforementioned compensation effect⁴³, the activation energy is found to increase but not sufficiently for its effect to be predominant on the OER kinetics. Similar observation was made for Pt-based oxygen reduction reaction (ORR) alloy catalysts for which the activation energy was found invariant on the composition.⁴⁴ Thus, two effects can explain the so-called pH dependence OER activity previously observed for perovskites. First, it can originate from an invalid normalization of the current density as the result of an increase of the concentration of active sites on the surface of the catalysts (equation 1). This change in concentration of active sites would suggest that a chemical deprotonation to form $\ast\text{O}$ can precede the hydroxyl

adsorption on the surface of the catalyst. Second, the pH-dependence OER kinetics can also arise from an increase of the entropy of activation ΔS^* ,⁴⁴ which results in a greater apparent pre-exponential factor.⁴⁵ This would traduce a change in ions reorganization, certainly protons and hydroxyls, at the interface as a function of the electrolyte concentration.^{41,46,47} Finally, similar observation is made independently on the alkali-cation where the increase of the OER activity as a function of LiOH concentration is explained, alike for KOH, by an increase of the pre-exponential factor rather than by a decrease of the apparent activation energy (Figure 6.7b). Overall, while the concentration has a great influence on the OER kinetics, the nature of the alkali-cation has a rather limited impact on the OER kinetics for these Co-based perovskites (Figure 6.7c and Figure 6.8-Figure 6.9). This is especially true when compared to the effect reported for amorphous Co-based electrodeposited films⁴⁸ which will be discussed below.

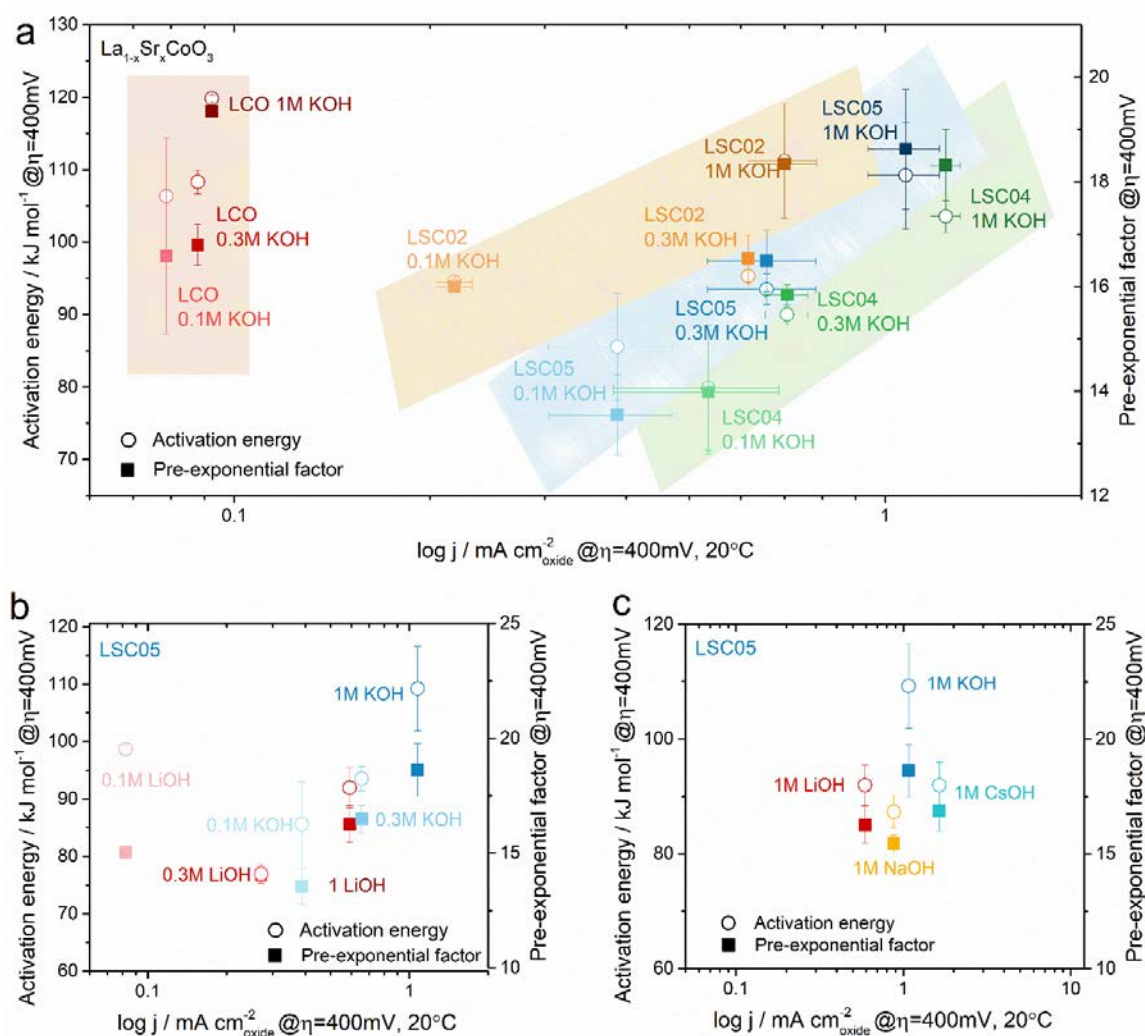


Figure 6.7 Apparent activation energies and pre-exponential factors as a function of the OER activity measured at 20°C at $\eta = 400\text{mV}$ (a) in 0.1, 0.3 and 1 M KOH for the $\text{La}_{1-x}\text{Sr}_x\text{CoO}_3$ series, (b) measured for $\text{La}_{0.5}\text{Sr}_{0.5}\text{CoO}_{3-\delta}$ (LSC05) 0.1, 0.3 and 1 M KOH and LiOH and (c) measured for $\text{La}_{0.5}\text{Sr}_{0.5}\text{CoO}_{3-\delta}$ (LSC05) in 1 M LiOH, NaOH, KOH and CsOH.

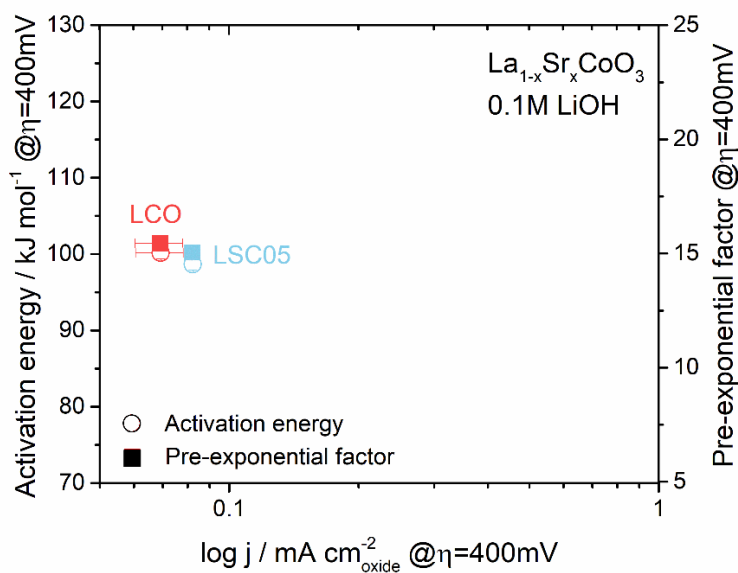


Figure 6.8 Activation energy and pre-exponential factor at $\eta = 400\text{mV}$ for $\text{La}_{1-x}\text{Sr}_x\text{CoO}_3$ vs activity at $\eta = 400\text{mV}$ in 0.1M LiOH and KOH at 20°C.

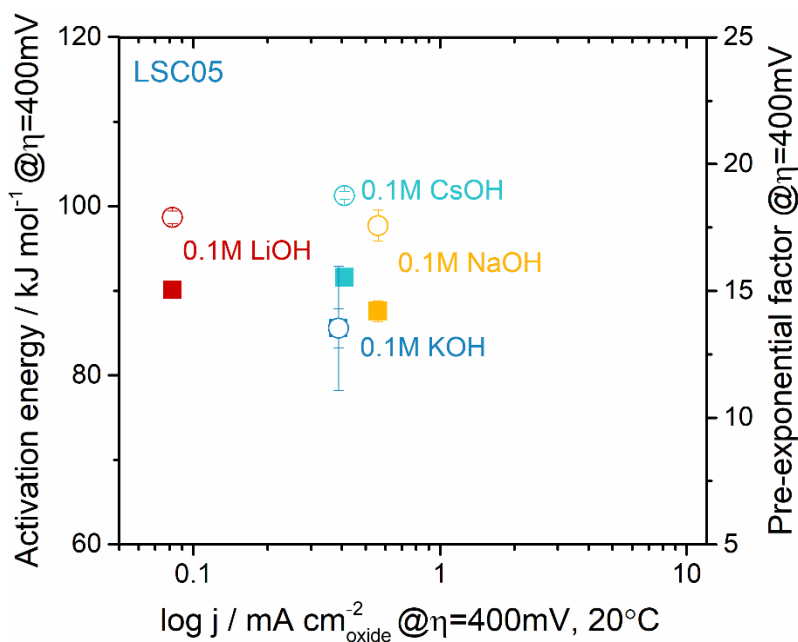


Figure 6.9 Cation dependence studies of $\text{La}_{0.5}\text{Sr}_{0.5}\text{CoO}_3$ in 0.1M LiOH, NaOH, KOH and CsOH. Activation energy and pre-exponential factor at $\eta = 400\text{mV}$ for $\text{La}_{0.5}\text{Sr}_{0.5}\text{CoO}_3$ vs activity at $\eta = 400\text{mV}$ in 0.1M LiOH, NaOH, KOH and CsOH at 20°C .

6.3.2 Cobalt oxyhydroxide films

To assess if such behavior is ubiquitous to every Co-based catalysts, we then investigated the behavior of electrodeposited amorphous cobalt oxyhydroxide films in different electrolytes. First, we should recall that the electrocatalytic activity of such amorphous catalysts is greatly affected by the presence of Fe-impurities in the alkaline electrolytes,^{12,20,21,23,49–53} and that the origin for such effects is still under intensive debate. For Fe-free electrolytes and films, the OER activity for CoOOH is found to be dependent on the concentration of KOH (Figure 6.10a). Alike for Co-based perovskites, this enhanced OER activity is explained by an increase of the pre-exponential factor rather than by a decrease of the apparent activation energy (Figure 6.10b). Nevertheless, unlike for perovskites, this concentration effect depends on the nature of the alkali-cation. Hence, no concentration dependence was observed with LiOH (Figure 6.10a) for which even though the pre-exponential factor is found to increase with the concentration of LiOH, this effect is counter-balanced by the decrease of the activation energy (Figure 6.10b) following the previously discussed compensation effect. Overall, the OER activity for amorphous CoOOH films is sensitive to the nature of the alkali-cation with $\text{Cs}^+ > \text{Na}^+ \approx \text{K}^+ > \text{Li}^+$ (Figure 6.10c), alike what was recently reported for Fe-free NiOOH films by Koper and coworkers.⁴⁸ Additionally, this dependence is only mild for K^+ , Na^+ and Cs^+ with only a factor of 2-3 in enhancement for the OER activity, while Li^+ shows an order of magnitude in decrease when compared to K^+ , similarly to our previous observations.²⁴ Furthermore, a decrease of the activation energy could explain this increase in OER activity (Figure 6.10d). Nevertheless, the trend is not as conclusive as for Fe-containing CoOOH films, as discussed below.

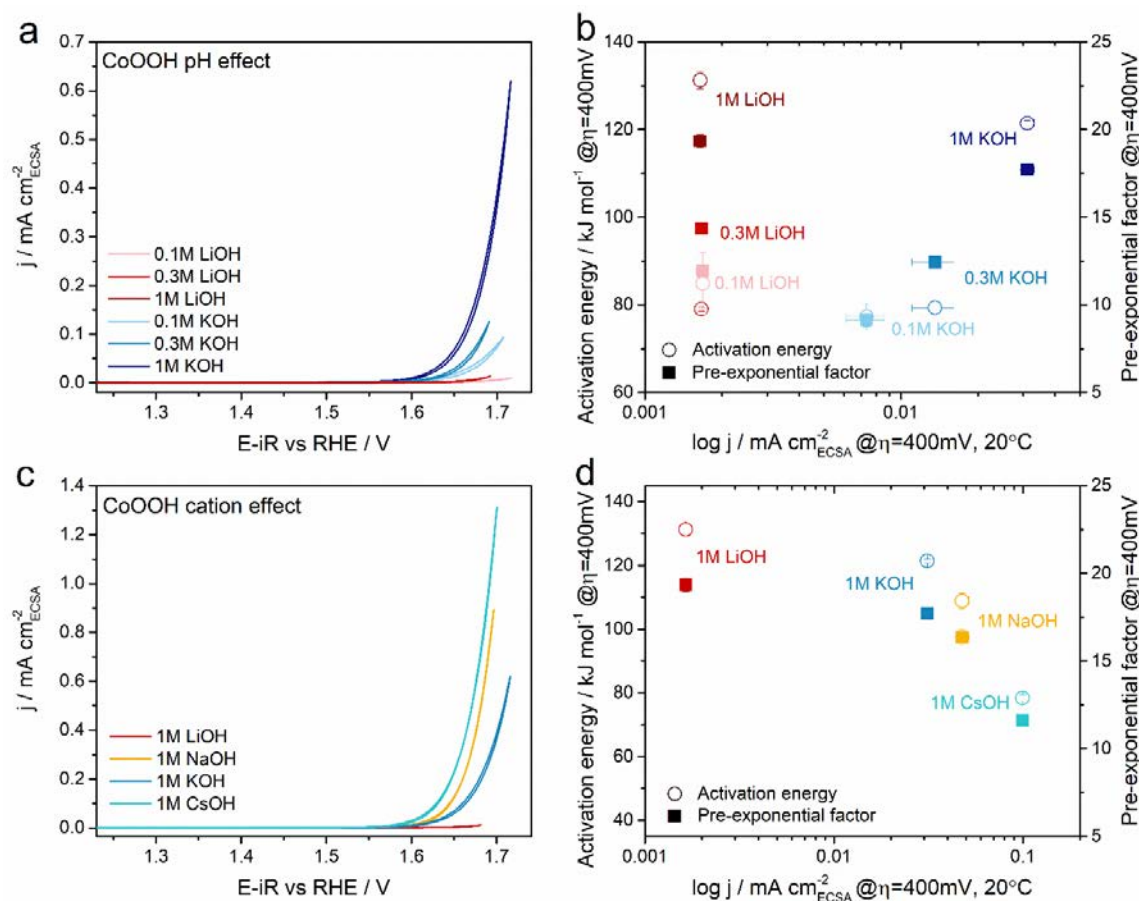


Figure 6.10 (a) CV curves for CoOOH measured at 20°C and (b) corresponding apparent activation energies and pre-exponential factors as a function of the OER activity at 20°C and $\eta = 400\text{mV}$ in 0.1, 0.3 and 1 M LiOH and KOH. (c) CV curves for CoOOH measured at 20°C and (b) corresponding apparent activation energies and pre-exponential factors as a function of the OER activity at 20°C and $\eta = 400\text{mV}$ in 1 M LiOH, NaOH, KOH and CsOH.

6.3.3 Fe-containing cobalt oxyhydroxide films

Unlike for Fe-free CoOOH, the OER activity for $\text{Co}_{0.5}\text{Fe}_{0.5}\text{OOH}$ films shows no dependence on the concentration of alkali salts with either LiOH or KOH (Figure 6.11a). This observation is in line with our previous measurements for Ni-oxyhydroxide Fe-containing films for which almost no concentration dependence was observed.²⁴ Once again, this concentration-independent OER kinetics is found to be accompanied with an almost perfect compensation of the increase of the activation energy by an increase of the pre-exponential factor (Figure 6.11b). More interestingly, the OER kinetics for the $\text{Co}_{0.5}\text{Fe}_{0.5}\text{OOH}$ films are found to be greatly dependent on the alkali-

cation with $\text{Cs}^+ > \text{K}^+ > \text{Na}^+ > \text{Li}^+$ (Figure 6.11c and d) following the decrease of the activation energy from $\approx 138 \text{ kJ/mol}$ (± 2) in 1M LiOH to $\approx 47 \text{ kJ/mol}$ (± 2) in 1M CsOH (Figure 6.11d).

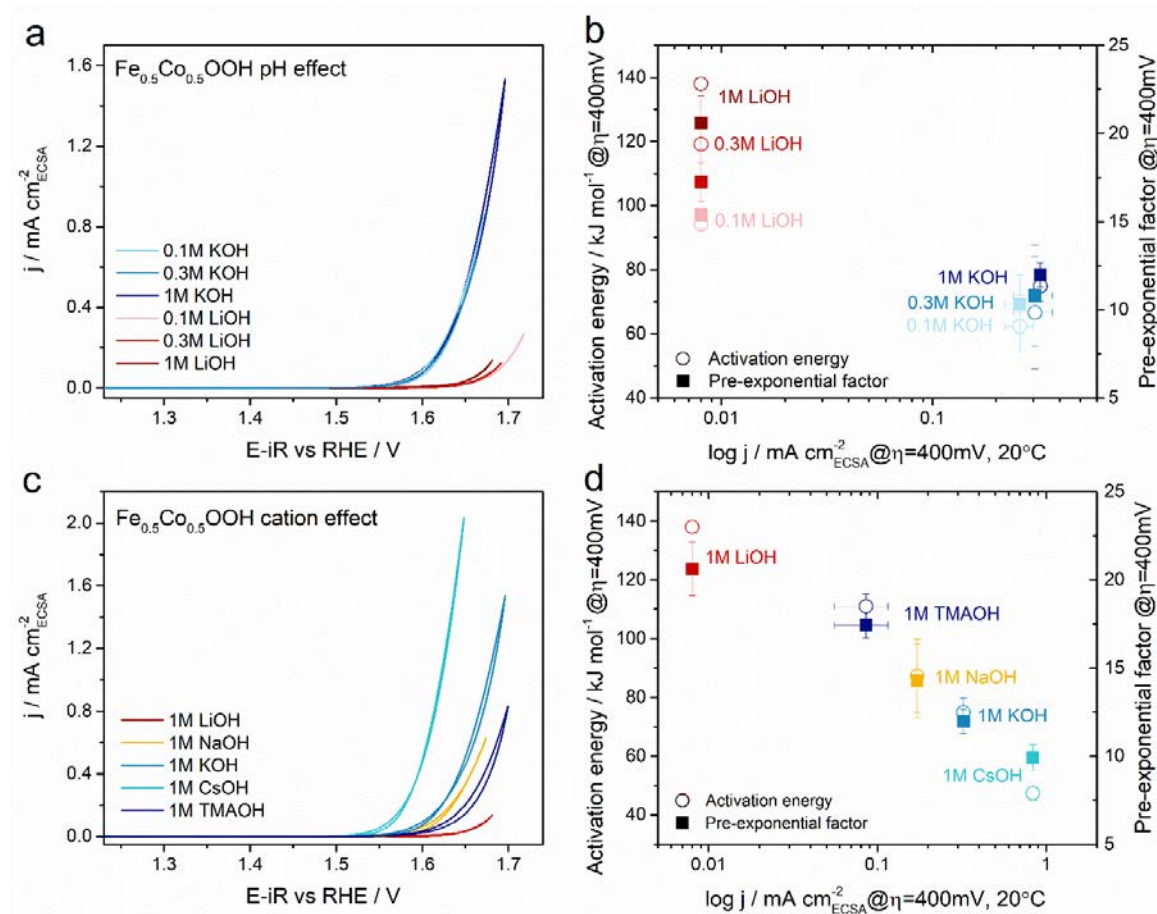


Figure 6.11(a) CV curves for $\text{Fe}_{0.5}\text{Co}_{0.5}\text{OOH}$ measured at 20°C and (b) corresponding apparent activation energies and pre-exponential factors as a function of the OER activity at 20°C and $\eta = 400 \text{ mV}$ in 0.1, 0.3 and 1 M LiOH and KOH. (c) CV curves for $\text{Fe}_{0.5}\text{Co}_{0.5}\text{OOH}$ measured at 20°C and (b) corresponding apparent activation energies and pre-exponential factors as a function of the OER activity at 20°C and $\eta = 400 \text{ mV}$ in 1 M LiOH, NaOH, KOH and CsOH.

Having demonstrated the effect of alkali-cation for Fe-containing films, one can then try to rationalize these observations. Indeed, our results suggest that the physical origin for both the concentration dependence observed for Fe-free films (as well as for perovskites) and the cation dependence measured and Fe-containing films (and to a lesser extent Fe-free films) is different. For Fe-free films, the concentration dependence in KOH arises from an increase of the pre-exponential factor (Figure 6.10b). This increase can be explained by a greater concentration of

active sites (*O) following a partial deprotonation of the hydroxide sites at greater hydroxyls activity (i.e. greater concentration). Additionally, this increase can also arise from a change in the entropy of activation S^* reflecting a modification of the electrolyte structure surrounding the active sites and a perturbation of the ions reorganization at the water/catalyst interface. In fact, as previously discussed for the HER, when transferring protons across the electrochemical interface from the inner to the outer Helmholtz plane, protons undergo a change in configurational entropy,^{33,54,55} this change being dependent on the strength of the electrical field. Therefore, strengthening the electrical field stiffens the water structure in the double layer⁵⁶ and therefore increases the work necessary to transfer protons or ions through the interface. Rather, for Fe-containing films, the apparent activation energies are modified by changing the nature of the alkali-cation (Figure 6.11d), which suggests a strong interaction of the whole film thickness with the electrolyte. This modification can be ascribed to the so-called self-insertion of cations in the film upon operation which modifies the chemical composition and the physical properties of the films and therefore the binding energies of intermediates.

In order to better understand the major factor influencing this change in intermediates binding energies, the OER kinetics previously measured for $\text{Co}_{0.5}\text{Fe}_{0.5}\text{OOH}$ with MOH solutions, M being an alkali-cation, were compared with the one measured for a large hydrophobic cation, namely tetramethylammonium TMA^+ (Figure 6.11c and d). Doing so, we found that the subsequent modification of the OER kinetics when using TMA^+ is related to a change in the apparent activation energy (Figure 6.11d). Plotting the OER activity for MOH solutions, a correlation is found with the size of the alkali-cations (Li^+ , Na^+ , K^+ and Cs^+) and therefore with their hydration enthalpy (Figure 6.12a). This could reflect that, unlike for the HER for which the use of Li^+ was found to enhance the kinetics for Pt-based catalysts in alkaline solution owing to the stabilization of $\text{Li}^+\text{-OH}^-$ adduct,^{46,47} stabilizing OH^- which is the reactant and not the product for the OER leads to decreased kinetics by modifying the enthalpy of formation of the intermediates.

Nevertheless, this trend does not hold for TMA^+ which possesses a smaller hydration enthalpy when compared to Cs^+ and for which the kinetics was found slower than for Cs^+ . Instead, it could be related to a modification of the hydrogen bonds formed between the alkaline electrolyte and the active sites of the amorphous films. Indeed, as shown for RuO_2 catalyst, interactions

with neighboring OH groups can modify the energy of the *OO intermediate and therefore impact the OER kinetics⁵⁷. In order to tentatively capture such modification of the hydrogen bonding network as induced by cations self-inserted in the amorphous films, the OER activity for $\text{Co}_{0.5}\text{Fe}_{0.5}\text{OOH}$ was thus plotted as a function of the so-called B coefficient of the Jones-Dole equation for these five different cations (Figure 6.12b). Indeed, this coefficient empirically reflects the ability for cations to structure or disorder the hydrogen bonding network around themselves, as largely discussed in the field of liquid-liquid extraction.⁵⁸⁻⁶¹ Hence, while cations that structure the hydrogen bonding network around themselves (Li^+ , TMA^+ and Na^+) - the so-called kosmotropic cations which possess a positive B coefficients – tend to decrease the OER kinetics, introducing cations that disorder hydrogen bonds around themselves (chaotropic cations with negative B coefficients) enhances the OER activity of Fe-containing films. The physical origin for such trend remains at that stage largely unknown and further work is certainly needed to understand and control such effect. Nevertheless, one could tentatively propose that the stiffening of the water structure when using kosmotropic cations (Li^+ , TMA^+ and Na^+) can hamper the hydrogen bonding at the water/catalyst interface and affect the enthalpy of formation of *OO intermediate. These two effects (hydration enthalpy and stiffening of the water structure at the interface) are certainly simultaneously at play, nevertheless the strategy consisting in modifying the water structure by the wise selection of cations appears as promising in order to improve the OER kinetics of amorphous films. It could also be extended to anions that are known to greatly affect the OER kinetics of those films when intercalated.^{2,62}

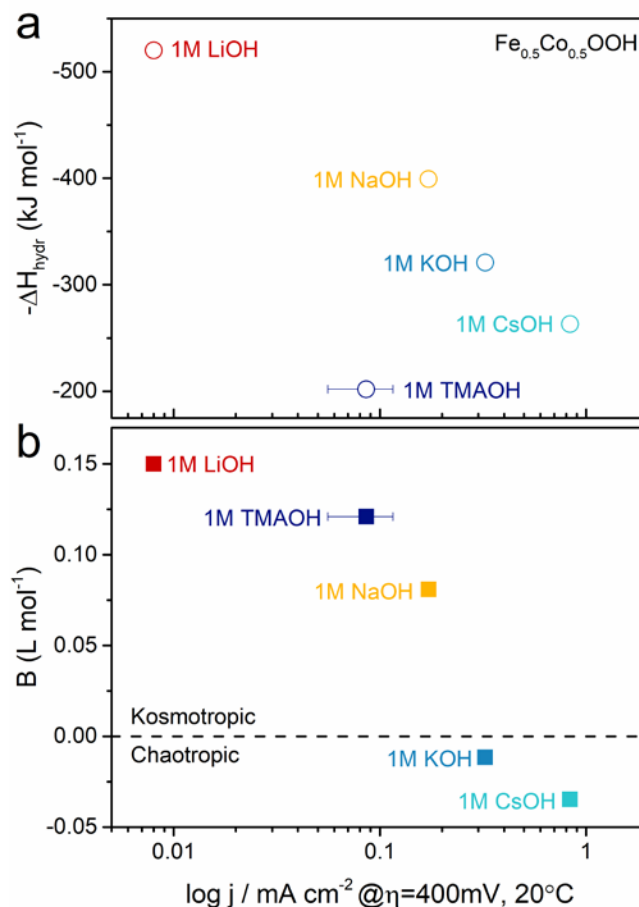


Figure 6.12 OER activity at $\eta=400\text{mV}$ vs. RHE for $\text{Fe}_{0.5}\text{Co}_{0.5}\text{OOH}$ measured in 1 M LiOH, NaOH, KOH, CsOH and TMAOH as a function of (a) the cation hydration enthalpy obtained from ref³⁰ and (b) the B coefficients from the Jones-Dole equation for the different cations as obtained from ref³⁰.

6.4 Summary

In conclusion, through a systematic temperature dependence study we could establish the physical origin for the concentration- and cation-dependence of the OER kinetics for a series of Co-based catalysts. First, we discussed how challenging the obtention of reliable experimental kinetic parameters for the OER catalysts is. Especially, we emphasize that the proper determination of exchange current densities for OER catalysts from a simple Tafel analysis may not be an adequate approach. Indeed, the modification of the surface coverage³⁷ or of the catalyst nature⁴⁰ with the applied potential result in Tafel slopes that do not match simple microkinetic

models, thus preventing the extraction of meaningful exchange current densities. In this work, we overcame this issue by comparing the kinetics of different materials at a given overpotential. Applying this methodology, we confirmed that when modifying the physical properties of perovskites based OER catalysts through a substitution strategy, the apparent activation energies are modified, reflecting a modification of the enthalpy of formation for the intermediates of the reaction. Furthermore, we could demonstrate for the first time for the OER that similarly to other fields such as biology, the experimentally determined apparent pre-exponential factors linearly trend with the apparent activation energies, following a so-called compensation effect. Having established the validity of the methodology, we then turned our attention to the study of the effect of the electrolyte composition on amorphous cobalt oxyhydroxides films. Doing so, we confirmed that Fe incorporation into these amorphous films greatly affects their OER activity. Comparing the apparent activation energies and the pre-exponential factors extracted from the temperature dependence study, we demonstrate that the concentration dependence observed for Fe-free films (as well as for the $\text{La}_{1-x}\text{Sr}_x\text{CoO}_{3-\delta}$ series) originates from an increase in the pre-exponential factor as a result of either an increase of active sites or a change in the entropy of activation. These effects, which can hardly be captured by either operando measurements or by classical computational methods, are nicely captured by our experimental methodology which reinforces its significance to the field. Instead, for Fe-containing films, no concentration dependence was found but a large cation dependence is observed. This cation dependence arises from a change in the apparent activation energies, which reflect a change in the enthalpy of formation of the intermediates, certainly as a result of cation self-insertion into the film. Eventually, more remains to be done to fully uncover the concentration and cation dependence of the OER activity for these catalysts, especially from a theoretical point of view. However, we believe that such findings open up new avenues to intrinsically tune the electrocatalytic activity of OER catalysts by controlling the water/catalysts interactions in the vicinity of the active sites. Finally, we believe that this experimental methodology can be applied to understand complex electrolyte effects previously reported for other complex reactions such as the ORR or CO_2 reduction.

6.5 Reference

- (1) Hong, W. T.; Risch, M.; Stoerzinger, K. A.; Grimaud, A.; Suntivich, J.; Shao-Horn, Y. Toward the Rational Design of Non-Precious Transition Metal Oxides for Oxygen

Electrocatalysis. *Energy Environ. Sci.* **2015**, *8* (5), 1404–1427. <https://doi.org/10.1039/C4EE03869J>.

(2) Fabbri, E.; Haberer, A.; Walz, K.; Kötter, R.; Schmidt, T. J. Developments and Perspectives of Oxide-Based Catalysts for the Oxygen Evolution Reaction. *Catal. Sci. Technol.* **2014**, *4* (11), 3800–3821. <https://doi.org/10.1039/C4CY00669K>.

(3) Shen, P. K.; Wang, C.-Y.; Jiang, S. P.; Sun, X.; Zhang, J. Electrochemical Energy. 619.

(4) Lee, J.; Kim, I.; Park, S. Boosting Stability and Activity of Oxygen Evolution Catalyst in Acidic Medium: Bimetallic Ir–Fe Oxides on Reduced Graphene Oxide Prepared through Ultrasonic Spray Pyrolysis. *ChemCatChem* **2019**, *11* (11), 2615–2623. <https://doi.org/10.1002/cctc.201900287>.

(5) Hong, W. T.; Welsch, R. E.; Shao-Horn, Y. Descriptors of Oxygen-Evolution Activity for Oxides: A Statistical Evaluation. *J. Phys. Chem. C* **2016**, *120* (1), 78–86. <https://doi.org/10.1021/acs.jpcc.5b10071>.

(6) Mefford, J. T.; Rong, X.; Abakumov, A. M.; Hardin, W. G.; Dai, S.; Kolpak, A. M.; Johnston, K. P.; Stevenson, K. J. Water Electrolysis on La_{1-x}Sr_xCoO_{3-δ} Perovskite Electrocatalysts. *Nature communications* **2016**, *7*, 11053.

(7) Duan, Y.; Sun, S.; Sun, Y.; Xi, S.; Chi, X.; Zhang, Q.; Ren, X.; Wang, J.; Ong, S. J. H.; Du, Y. Mastering Surface Reconstruction of Metastable Spinel Oxides for Better Water Oxidation. *Advanced Materials* **2019**, *31* (12), 1807898.

(8) Huang, Z.-F.; Song, J.; Du, Y.; Xi, S.; Dou, S.; Nsanzimana, J. M. V.; Wang, C.; Xu, Z. J.; Wang, X. Chemical and Structural Origin of Lattice Oxygen Oxidation in Co–Zn Oxyhydroxide Oxygen Evolution Electrocatalysts. *Nat Energy* **2019**, *4* (4), 329–338. <https://doi.org/10.1038/s41560-019-0355-9>.

(9) Zhou, Y.; Sun, S.; Song, J.; Xi, S.; Chen, B.; Du, Y.; Fisher, A. C.; Cheng, F.; Wang, X.; Zhang, H.; Xu, Z. J. Enlarged Co–O Covalency in Octahedral Sites Leading to Highly Efficient Spinel Oxides for Oxygen Evolution Reaction. *Adv. Mater.* **2018**, *30* (32), 1802912. <https://doi.org/10.1002/adma.201802912>.

(10) Wu, T.; Sun, S.; Song, J.; Xi, S.; Du, Y.; Chen, B.; Sasangka, W. A.; Liao, H.; Gan, C. L.; Scherer, G. G.; Zeng, L.; Wang, H.; Li, H.; Grimaud, A.; Xu, Z. J. Iron-Facilitated Dynamic Active-Site Generation on Spinel CoAl₂O₄ with Self-Termination of Surface Reconstruction for Water Oxidation. *Nat Catal* **2019**. <https://doi.org/10.1038/s41929-019-0325-4>.

(11) Yang, C.; Batuk, M.; Jacquet, Q.; Rouse, G.; Yin, W.; Zhang, L.; Hadermann, J.; Abakumov, A. M.; Cibir, G.; Chadwick, A. Revealing PH-Dependent Activities and Surface Instabilities for Ni-Based Electrocatalysts during the Oxygen Evolution Reaction. *ACS Energy Letters* **2018**, *3* (12), 2884–2890.

(12) Trotochaud, L.; Young, S. L.; Ranney, J. K.; Boettcher, S. W. Nickel–Iron Oxyhydroxide Oxygen-Evolution Electrocatalysts: The Role of Intentional and Incidental Iron Incorporation. *J. Am. Chem. Soc.* **2014**, *136* (18), 6744–6753. <https://doi.org/10.1021/ja502379c>.

(13) Abidat, I.; Bouchenafa-Saib, N.; Habrioux, A.; Comminges, C.; Canaff, C.; Rousseau, J.; Napporn, T. W.; Dambournet, D.; Borkiewicz, O.; Kokoh, K. B. Electrochemically Induced Surface Modifications of Mesoporous Spinels (Co₃O_{4-δ}, MnCo₂O_{4-δ}, NiCo₂O_{4-δ}) as the Origin of the OER Activity and Stability in Alkaline Medium. *J. Mater. Chem. A* **2015**, *3* (33), 17433–17444. <https://doi.org/10.1039/C5TA04437E>.

(14) Man, I. C.; Su, H.-Y.; Calle-Vallejo, F.; Hansen, H. A.; Martínez, J. I.; Inoglu, N. G.; Kitchin, J.; Jaramillo, T. F.; Nørskov, J. K.; Rossmeisl, J. Universality in Oxygen Evolution Electrocatalysis on Oxide Surfaces. *ChemCatChem* **2011**, *3* (7), 1159–1165.

- (15) Grimaud, A.; Diaz-Morales, O.; Han, B.; Hong, W. T.; Lee, Y.-L.; Giordano, L.; Stoerzinger, K. A.; Koper, M. T. M.; Shao-Horn, Y. Activating Lattice Oxygen Redox Reactions in Metal Oxides to Catalyze Oxygen Evolution. *Nature Chem* **2017**, *9* (5), 457–465. <https://doi.org/10.1038/nchem.2695>.
- (16) Yang, C.; Laberty-Robert, C.; Batuk, D.; Cibir, G.; Chadwick, A. V.; Pimenta, V.; Yin, W.; Zhang, L.; Tarascon, J.-M.; Grimaud, A. Phosphate Ion Functionalization of Perovskite Surfaces for Enhanced Oxygen Evolution Reaction. *The journal of physical chemistry letters* **2017**, *8* (15), 3466–3472.
- (17) Burke, M. S.; Kast, M. G.; Trotochaud, L.; Smith, A. M.; Boettcher, S. W. Cobalt–Iron (Oxy)Hydroxide Oxygen Evolution Electrocatalysts: The Role of Structure and Composition on Activity, Stability, and Mechanism. *J. Am. Chem. Soc.* **2015**, *137* (10), 3638–3648. <https://doi.org/10.1021/jacs.5b00281>.
- (18) Burke, M. S.; Enman, L. J.; Batchellor, A. S.; Zou, S.; Boettcher, S. W. Oxygen Evolution Reaction Electrocatalysis on Transition Metal Oxides and (Oxy)Hydroxides: Activity Trends and Design Principles. *Chem. Mater.* **2015**, *27* (22), 7549–7558. <https://doi.org/10.1021/acs.chemmater.5b03148>.
- (19) Enman, L. J.; Stevens, M. B.; Dahan, M. H.; Nellist, M. R.; Toroker, M. C.; Boettcher, S. W. Operando X-Ray Absorption Spectroscopy Shows Iron Oxidation Is Concurrent with Oxygen Evolution in Cobalt-Iron (Oxy)Hydroxide Electrocatalysts. *Angew. Chem. Int. Ed.* **2018**, *57* (39), 12840–12844. <https://doi.org/10.1002/anie.201808818>.
- (20) Zhang, T.; Nellist, M. R.; Enman, L. J.; Xiang, J.; Boettcher, S. W. Modes of Fe Incorporation in Co–Fe (Oxy)Hydroxide Oxygen Evolution Electrocatalysts. *ChemSusChem* **2019**, *12* (9), 2015–2021. <https://doi.org/10.1002/cssc.201801975>.
- (21) Michael, J. D.; Demeter, E. L.; Illes, S. M.; Fan, Q.; Boes, J. R.; Kitchin, J. R. Alkaline Electrolyte and Fe Impurity Effects on the Performance and Active-Phase Structure of NiOOH Thin Films for OER Catalysis Applications. *The Journal of Physical Chemistry C* **2015**, *119* (21), 11475–11481.
- (22) Zaffran, J.; Stevens, M. B.; Trang, C. D. M.; Nagli, M.; Shehadeh, M.; Boettcher, S. W.; Caspary Toroker, M. Influence of Electrolyte Cations on Ni(Fe)OOH Catalyzed Oxygen Evolution Reaction. *Chem. Mater.* **2017**, *29* (11), 4761–4767. <https://doi.org/10.1021/acs.chemmater.7b00517>.
- (23) Trzeźniewski, B. J.; Diaz-Morales, O.; Vermaas, D. A.; Longo, A.; Bras, W.; Koper, M. T. M.; Smith, W. A. In Situ Observation of Active Oxygen Species in Fe-Containing Ni-Based Oxygen Evolution Catalysts: The Effect of PH on Electrochemical Activity. *J. Am. Chem. Soc.* **2015**, *137* (48), 15112–15121. <https://doi.org/10.1021/jacs.5b06814>.
- (24) Yang, C.; Fontaine, O.; Tarascon, J.-M.; Grimaud, A. Chemical Recognition of Active Oxygen Species on the Surface of Oxygen Evolution Reaction Electrocatalysts. *Angewandte Chemie* **2017**, *129* (30), 8778–8782.
- (25) Merrill, M.; Worsley, M.; Wittstock, A.; Biener, J.; Stadermann, M. Determination of the “NiOOH” Charge and Discharge Mechanisms at Ideal Activity. *Journal of Electroanalytical Chemistry* **2014**, *717–718*, 177–188. <https://doi.org/10.1016/j.jelechem.2014.01.022>.
- (26) Ali-Löyty, H.; Louie, M. W.; Singh, M. R.; Li, L.; Sanchez Casalongue, H. G.; Ogasawara, H.; Crumlin, E. J.; Liu, Z.; Bell, A. T.; Nilsson, A.; Friebel, D. Ambient-Pressure XPS Study of a Ni–Fe Electrocatalyst for the Oxygen Evolution Reaction. *J. Phys. Chem. C* **2016**, *120* (4), 2247–2253. <https://doi.org/10.1021/acs.jpcc.5b10931>.

- (27) Zhu, K.; Zhu, X.; Yang, W. Application of In Situ Techniques for the Characterization of NiFe-Based Oxygen Evolution Reaction (OER) Electrocatalysts. *Angewandte Chemie International Edition* **2019**, *58* (5), 1252–1265. <https://doi.org/10.1002/anie.201802923>.
- (28) Yeo, B. S.; Bell, A. T. In Situ Raman Study of Nickel Oxide and Gold-Supported Nickel Oxide Catalysts for the Electrochemical Evolution of Oxygen. *J. Phys. Chem. C* **2012**, *116* (15), 8394–8400. <https://doi.org/10.1021/jp3007415>.
- (29) Tkalych, A. J.; Zhuang, H. L.; Carter, E. A. A Density Functional + U Assessment of Oxygen Evolution Reaction Mechanisms on β -NiOOH. *ACS Catal.* **2017**, *7* (8), 5329–5339. <https://doi.org/10.1021/acscatal.7b00999>.
- (30) Huang, B.; Mui, S.; Feng, S.; Katayama, Y.; Lu, Y.-C.; Chen, G.; Shao-Horn, Y. Non-Covalent Interactions in Electrochemical Reactions and Implications in Clean Energy Applications. *Physical Chemistry Chemical Physics* **2018**, *20* (23), 15680–15686.
- (31) Lide, D. R.; Baysinger, G.; Chemistry, S.; Berger, L. I.; Goldberg, R. N.; Kehiaian, H. V. CRC Handbook of Chemistry and Physics. 2661.
- (32) Matsumoto, Y.; Manabe, H.; Sato, E. Oxygen Evolution on Lal_ Sr CoO Electrodes in Alkaline Solutions. 4.
- (33) Shinagawa, T.; Takanabe, K. New Insight into the Hydrogen Evolution Reaction under Buffered Near-Neutral PH Conditions: Enthalpy and Entropy of Activation. *J. Phys. Chem. C* **2016**, *120* (42), 24187–24196. <https://doi.org/10.1021/acs.jpcc.6b07954>.
- (34) Bard, A. J.; Faulkner, L. R. *Electrochemical Methods: Fundamentals and Applications*, 2. ed.; Wiley: Hoboken, NJ, 2001.
- (35) Grimaud, A.; Diaz-Morales, O.; Han, B.; Hong, W. T.; Lee, Y.-L.; Giordano, L.; Stoerzinger, K. A.; Koper, M. T.; Shao-Horn, Y. Activating Lattice Oxygen Redox Reactions in Metal Oxides to Catalyze Oxygen Evolution. *Nature chemistry* **2017**, *9* (5), 457.
- (36) Grimaud, A.; May, K. J.; Carlton, C. E.; Lee, Y.-L.; Risch, M.; Hong, W. T.; Zhou, J.; Shao-Horn, Y. Double Perovskites as a Family of Highly Active Catalysts for Oxygen Evolution in Alkaline Solution. *Nature communications* **2013**, *4*, 2439.
- (37) Shinagawa, T.; Garcia-Esparza, A. T.; Takanabe, K. Insight on Tafel Slopes from a Microkinetic Analysis of Aqueous Electrocatalysis for Energy Conversion. *Sci Rep* **2015**, *5* (1), 13801. <https://doi.org/10.1038/srep13801>.
- (38) Conway, B. E.; Bockris, J. O.; Linton, H. Proton Conductance and the Existence of the H_3O^+ Ion. *The Journal of Chemical Physics* **1956**, *24* (4), 834–850. <https://doi.org/10.1063/1.1742619>.
- (39) Bockris, J. O.; Otagawa, T. Mechanism of Oxygen Evolution on Perovskites. *J. Phys. Chem.* **1983**, *87* (15), 2960–2971. <https://doi.org/10.1021/j100238a048>.
- (40) Mefford, J. T. Interpreting Tafel Behavior of Consecutive Electrochemical Reactions through Combined Thermodynamic and Steady State Microkinetic Approaches. *Environmental Science* **2020**, 13.
- (41) Zhang, R.; Pearce, P. E.; Duan, Y.; Dubouis, N.; Marchandier, T.; Grimaud, A. The Importance of Water Structure and Catalyst-Electrolyte Interface on the Design of Water Splitting Catalysts. *Chem. Mater.* **2019**, *acs.chemmater.9b02318*. <https://doi.org/10.1021/acs.chemmater.9b02318>.
- (42) Conner, Wm. C. A General Explanation for the Compensation Effect: The Relationship between ΔS^\ddagger and Activation Energy. *Journal of Catalysis* **1982**, *78* (1), 238–246. [https://doi.org/10.1016/0021-9517\(82\)90303-7](https://doi.org/10.1016/0021-9517(82)90303-7).

- (43) Yelon, A.; Movaghar, B.; Crandall, R. S. Multi-Excitation Entropy: Its Role in Thermodynamics and Kinetics. *Rep. Prog. Phys.* **2006**, *69* (4), 1145–1194. <https://doi.org/10.1088/0034-4885/69/4/R04>.
- (44) Anderson, A. B.; Roques, J.; Mukerjee, S.; Murthi, V. S.; Markovic, N. M.; Stamenkovic, V. Activation Energies for Oxygen Reduction on Platinum Alloys: Theory and Experiment. *The Journal of Physical Chemistry B* **2005**, *109* (3), 1198–1203.
- (45) Zeradjanin, A. R. Is a Major Breakthrough in the Oxygen Electrocatalysis Possible? *Current Opinion in Electrochemistry* **2018**, *9*, 214–223. <https://doi.org/10.1016/j.coelec.2018.04.006>.
- (46) Kuo, D.-Y.; Paik, H.; Kloppenburg, J.; Faeth, B.; Shen, K. M.; Schlom, D. G.; Hautier, G.; Suntivich, J. Measurements of Oxygen Electroadsorption Energies and Oxygen Evolution Reaction on RuO₂ (110): A Discussion of the Sabatier Principle and Its Role in Electrocatalysis. *Journal of the American Chemical Society* **2018**, *140* (50), 17597–17605.
- (47) Kuo, D.-Y.; Kawasaki, J. K.; Nelson, J. N.; Kloppenburg, J.; Hautier, G.; Shen, K. M.; Schlom, D. G.; Suntivich, J. Influence of Surface Adsorption on the Oxygen Evolution Reaction on IrO₂ (110). *Journal of the American chemical society* **2017**, *139* (9), 3473–3479.
- (48) Garcia, A. C.; Touzalin, T.; Nieuwland, C.; Perini, N.; Koper, M. T. M. Enhancement of Oxygen Evolution Activity of NiOOH by Electrolyte Alkali Cations. *Angew. Chem. Int. Ed.* **2019**. <https://doi.org/10.1002/anie.201905501>.
- (49) Gong, L.; Ren, D.; Deng, Y.; Yeo, B. S. Efficient and Stable Evolution of Oxygen Using Pulse-Electrodeposited Ir/Ni Oxide Catalyst in Fe-Spiked KOH Electrolyte. *ACS Appl. Mater. Interfaces* **2016**, *8* (25), 15985–15990. <https://doi.org/10.1021/acsami.6b01888>.
- (50) Gong, L.; Chng, X. Y. E.; Du, Y.; Xi, S.; Yeo, B. S. Enhanced Catalysis of the Electrochemical Oxygen Evolution Reaction by Iron(III) Ions Adsorbed on Amorphous Cobalt Oxide. *ACS Catal.* **2018**, *8* (2), 807–814. <https://doi.org/10.1021/acscatal.7b03509>.
- (51) Klaus, S.; Trotochaud, L.; Cheng, M.-J.; Head-Gordon, M.; Bell, A. T. Experimental and Computational Evidence of Highly Active Fe Impurity Sites on the Surface of Oxidized Au for the Electrocatalytic Oxidation of Water in Basic Media. *ChemElectroChem* **2016**, *3* (1), 66–73. <https://doi.org/10.1002/celec.201500364>.
- (52) Li, N.; Bediako, D. K.; Hadt, R. G.; Hayes, D.; Kempa, T. J.; von Cube, F.; Bell, D. C.; Chen, L. X.; Nocera, D. G. Influence of Iron Doping on Tetravalent Nickel Content in Catalytic Oxygen Evolving Films. *Proc Natl Acad Sci USA* **2017**, *114* (7), 1486–1491. <https://doi.org/10.1073/pnas.1620787114>.
- (53) Corrigan, D. A. The Catalysis of the Oxygen Evolution Reaction by Iron Impurities in Thin Film Nickel Oxide Electrodes. *J. Electrochem. Soc.* **1987**, *134* (2), 377. <https://doi.org/10.1149/1.2100463>.
- (54) Rossmeisl, J.; Chan, K.; Skúlason, E.; Björketun, M. E.; Tripkovic, V. On the PH Dependence of Electrochemical Proton Transfer Barriers. *Catalysis Today* **2016**, *262*, 36–40. <https://doi.org/10.1016/j.cattod.2015.08.016>.
- (55) Zeradjanin, A. R.; Vimalanandan, A.; Polymeros, G.; Topalov, A. A.; Mayrhofer, K. J.; Rohwerder, M. Balanced Work Function as a Driver for Facile Hydrogen Evolution Reaction—Comprehension and Experimental Assessment of Interfacial Catalytic Descriptor. *Physical Chemistry Chemical Physics* **2017**, *19* (26), 17019–17027.
- (56) Ledezma-Yanez, I.; Wallace, W. D. Z.; Sebastián-Pascual, P.; Climent, V.; Feliu, J. M.; Koper, M. T. M. Interfacial Water Reorganization as a PH-Dependent Descriptor of the

Hydrogen Evolution Rate on Platinum Electrodes. *Nat Energy* **2017**, *2* (4), 17031. <https://doi.org/10.1038/nenergy.2017.31>.

(57) Rao, R. R.; Kolb, M. J.; Halck, N. B.; Pedersen, A. F.; Mehta, A.; You, H.; Stoerzinger, K. A.; Feng, Z.; Hansen, H. A.; Zhou, H.; Giordano, L.; Rossmeisl, J.; Vegge, T.; Chorkendorff, I.; Stephens, I. E. L.; Shao-Horn, Y. Towards Identifying the Active Sites on RuO₂ (110) in Catalyzing Oxygen Evolution. *Energy Environ. Sci.* **2017**, *10* (12), 2626–2637. <https://doi.org/10.1039/C7EE02307C>.

(58) Dubouis, N.; Park, C.; Deschamps, M.; Abdelghani-Idrissi, S.; Kanduč, M.; Colin, A.; Salanne, M.; Dzubiella, J.; Grimaud, A.; Rotenberg, B. Chasing Aqueous Biphasic Systems from Simple Salts by Exploring the LiTFSI/LiCl/H₂O Phase Diagram. *ACS Cent. Sci.* **2019**, *5* (4), 640–643. <https://doi.org/10.1021/acscentsci.8b00955>.

(59) Gutowski, K. E.; Broker, G. A.; Willauer, H. D.; Huddleston, J. G.; Swatloski, R. P.; Holbrey, J. D.; Rogers, R. D. Controlling the Aqueous Miscibility of Ionic Liquids: Aqueous Biphasic Systems of Water-Miscible Ionic Liquids and Water-Structuring Salts for Recycle, Metathesis, and Separations. *J. Am. Chem. Soc.* **2003**, *125* (22), 6632–6633. <https://doi.org/10.1021/ja0351802>.

(60) Marcus, Y. Effect of Ions on the Structure of Water: Structure Making and Breaking. *Chem. Rev.* **2009**, *109* (3), 1346–1370. <https://doi.org/10.1021/cr8003828>.

(61) Bridges, N. J.; Gutowski, K. E.; Rogers, R. D. Investigation of Aqueous Biphasic Systems Formed from Solutions of Chaotropic Salts with Kosmotropic Salts (Salt–Salt ABS). *Green Chem.* **2007**, *9* (2), 177–183. <https://doi.org/10.1039/B611628K>.

(62) Hunter, B. M.; Hieringer, W.; Winkler, J. R.; Gray, H. B.; Müller, A. M. Effect of Interlayer Anions on [NiFe]-LDH Nanosheet Water Oxidation Activity. *Energy Environ. Sci.* **2016**, *9* (5), 1734–1743. <https://doi.org/10.1039/C6EE00377J>.

Chapter 7

Implications/Impact/Outstanding Questions

Chapter 7 draws together the threads of the thesis. The hypotheses are tested, and the goals are met. This thesis presents investigations on Co-based transition metal oxides/hydroxides as OER catalysts in alkaline solutions. It demonstrates how the intrinsic properties, surface properties and interfacial properties tune the mechanism and the kinetics of the OER. The understandings from these studies shine light on future catalysts improvements and design. Future research directions that can help to gain more insights on the understandings of surface electrochemistry are proposed. In the future, the gap existing in our understanding between the starting catalysts and the surface for the reconstructed materials will be bridged. The surface of the catalysts under exposure to different electrolytes environments will be explored. Extrinsic stimulations that can tune the intrinsic, surface and interfacial properties will be investigated.

7.1 Implications

The hypotheses in the thesis are tested by experiments, characterizations, modeling and kinetic parameter extrapolations. How the goals are met will be explained in this section. This thesis regards the revealing of the OER mechanism by establishing the correlation between the material properties and the electrocatalytic properties. In the Chapter 4, the example of perovskite transition metal oxides $\text{LaCo}_{0.9}\text{Fe}_{0.1}\text{O}_3$ demonstrates how electronic structure can be modified such that the OER activity is tailored. Characterizations providing structural insights such as XRD, SEM, FTIR, SEM and SQUID aid the understanding of the bulk properties of the materials. DFT modeling facilitates the comprehension of the intrinsic electronic structure of $\text{LaCo}_{0.9}\text{Fe}_{0.1}\text{O}_3$. A link is built between the electrochemical performance of the material and its covalency of metal *d* band and O *p* band. In Chapter 5, both the electronic properties and the surface reconstructed properties have been probed by characterization techniques and DFT calculations. The novel OER mechanism involving surface reorganization is correlated with the intrinsic properties. In details, electrochemical studies, XAS, XRD, XPS, TEM-EDS, EELS and XMCD analyze the Ni agglomeration and the reconstruction with the participation of surface oxygen. This observed electrocatalytic performance is due to the more active O *p*-band compared with M *d*-band. In the Chapter 6, perovskite transition metal oxide LSCO and transition metal hydroxides $\text{CoOOH}/\text{Co}_{0.5}\text{Fe}_{0.5}\text{OOH}$ are found to exhibit different behaviors when tuning the electrolyte compositions, which include the concentration of the OH^- and the alkali cation species in the electrolyte. Different from that in Chapter 5 which employs electrochemical studies on the study of interfacial properties, here, kinetic parameters are extrapolated by the use of temperature dependent experiments. The pH dependence of LSCO and CoOOH originates from the increase in pre-exponential factors as a result of increased concentration of active sites and/or a change in the entropy of activation of the reaction. Instead, the cation dependence observed for $\text{Co}_{0.5}\text{Fe}_{0.5}\text{OOH}$ is attributed to the change in activation energy as a result of the modified formation enthalpies of the intermediates. From the listed studies in the thesis, we have reached out from the bulk of the catalysts, to the surface of the catalysts, finally to the interface between the catalysts and the electrolyte. The catalytic activity is well correlated with their intrinsic, surface and interfacial properties. The findings are not only meaningful for the understanding of OER for Co-based transition metal oxides/hydroxides, they are helpful for future design of highly active electrocatalysts.

7.2 Recommended Future Work 1

From the previous studies in the thesis, some very active catalysts such as $\text{ZnCo}_{1.2}\text{Ni}_{0.8}\text{O}_4$ and LSC were found to undergo surface reconstruction, their surfaces forming an oxyhydroxide outermost layer under OER conditions, while others catalysts were found quite stable and presenting a poor activity during OER, examples including LCO and ZnCo_2O_4 . We suspect that the surface of these stable materials would form oxyhydroxide on the surface as well, but a rather thin layer. Though in both cases, oxyhydroxide is formed, the activities vary. This difference in activity does not come from the thickness of the oxyhydroxide layer itself, because the activity for pure oxyhydroxide is very low. Rather, the starting catalyst onto which the oxyhydroxide forms is important. However, how does the structure of the starting catalyst influence the resulted oxyhydroxide surface, which give rise to different overall activity, remains unexplored. We believe that by establishing the relationship between the starting catalyst and the surface, we would have better design principles for catalysts.

Furthermore, spin-state conservation has been found in transition metal oxides with metal cations of d^4 – d^7 configurations during redox reaction.¹ We propose that after OER, the newly formed oxyhydroxide would remain in the spin state of the starting catalyst. To test this hypothesis, two Co-based materials would be used as a comparison to study their electronic structure before and after OER. One is CoO with Co(II) HS, the other is CoS_2 with Co(II) LS. We would hold the OER potential for a long time for the surface oxyhydroxide to form for both materials. Then, soft XAS with TEY mode would be employed to study the spin state of Co after OER to see whether Co atoms in the surface oxyhydroxide would remain in the same spin state as the starting material.

7.2.1 Experimental details

Commercial cobalt (II) oxide CoO (99.99% trace metals basis) and commercial cobalt sulfide CoS_2 (99.98% trace metals basis) were purchased from Sigma-Aldrich.

Their crystal structures and purity were assessed by Bruker D8 Advance with Cu-K α radiation ($\lambda = 1.5418 \text{ \AA}$). The (Brunauer-Emitter-Teller) BET specific surface areas of the materials were obtained by ASAP Tristar II 3020. CoO shows a BET surface area of $16.95 \text{ m}^2\text{g}^{-1}$ and CoS_2 exhibits a surface area of $6.56 \text{ m}^2\text{g}^{-1}$.

Electrochemical studies were conducted using a three-electrode method in 0.1M KOH. 10 mg materials and 2 mg carbon black were dispersed in a mixed solution of 0.4 mL isopropyl alcohol (IPA), 1.59 mL DI water and 10 μ L Nafion perfluorinated resin to prepare the catalyst ink. The mixture was sonicated for 10 mins to achieve homogenized dispersion of the materials and carbon. The oxides were dispersed in a diluted IPA containing 5% Nafion. The mass ratio of material: carbon black was maintained at 4 : 1. The volume ratios of DI water: IPA: Nafion were maintained at 4: 1: 0.05. 10 μ L of the ink was drop casted onto a freshly polished glassy carbon electrode (0.196 cm²). All electrochemical potentials here are reported against the reversible hydrogen electrode (RHE) using a 1.0 M KOH solution. The conversion between potentials vs. Hg/HgO and vs. RHE was performed by the equation below. The Ohmic drop has been determined by electrochemical impedance spectroscopy.

$$E \text{ (vs. RHE)} / \text{V} = E \text{ (vs. Hg/HgO)} / \text{V} + E_{\text{Hg/HgO}} \text{ (vs. SHE)} / \text{V} + 0.059 \times \text{pH} / \text{V}$$
$$(E_{\text{Hg/HgO}} \text{ (vs. SHE)} / \text{V} = 0.098 / \text{V vs. SHE at } 25^{\circ}\text{C})$$

The oxygen evolution reaction was evaluated by cyclic voltammetry (CV) between 1.1 and 1.7 V (vs. RHE) at a scan rate of 10 mV s⁻¹. CV scans were found for CoO to slightly decrease before to quickly stabilize. The CV curves for CoS₂ stabilized after 25 cycles. The activities for CoO and CoS₂ were compared after stabilization.

Soft X-ray absorption were carried out at XAFCA beamline of SSLS to obtain the surface structure information of CoO and CoS₂ before and after OER.

7.2.2 Preliminary results

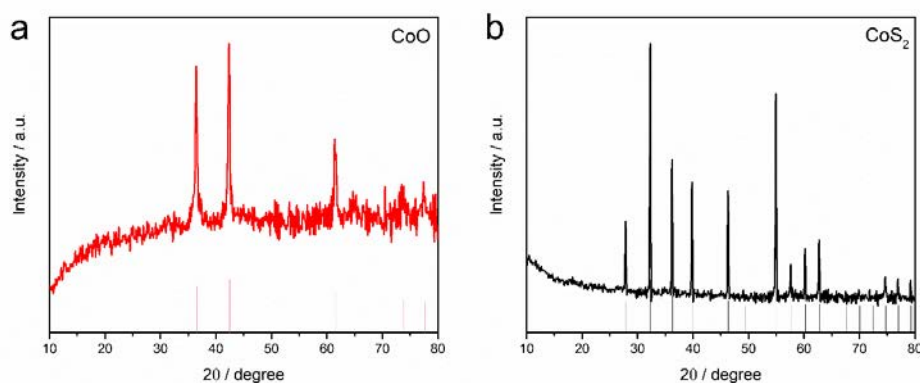


Figure 7.1 XRD patterns for CoO and CoS₂.

The crystal structures of CoO and CoS₂ were characterized by powder X-ray diffraction (XRD). As displayed in Figure 7.1, the diffraction peaks of the as-prepared CoO match with

that of the standard rock-salt (Fm-3m) structure with Co in octahedral sites. CoS_2 exhibits a typical pyrite (Pa-3) structure with Co in a 6-coordinate environment.

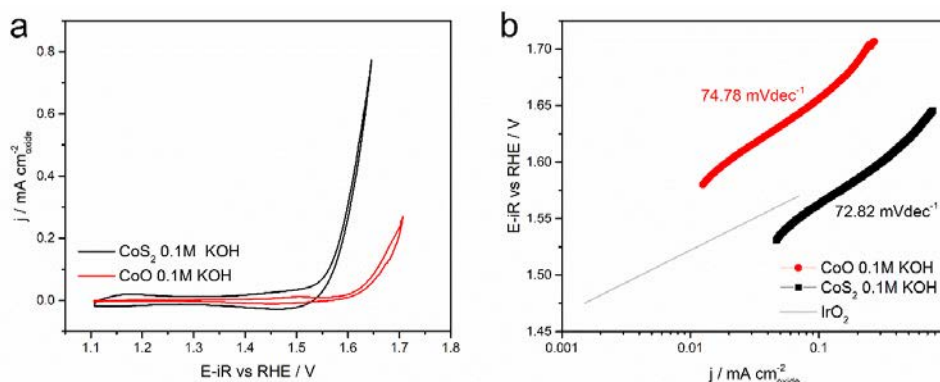


Figure 7.2 Electrochemical studies of CoO and CoS_2 in 0.1M KOH.

Cyclic Voltammometry measurements were performed on CoO and CoS_2 in 0.1M KOH with a scan rate of 10 mVs^{-1} . CoO is very stable in the electrolyte. However, CoS_2 is stabilized after 25 cycles activation in KOH. Activities normalized by the BET surface area are presented in Figure 7.2. The OER current density for CoS_2 is 4 times higher than CoO.

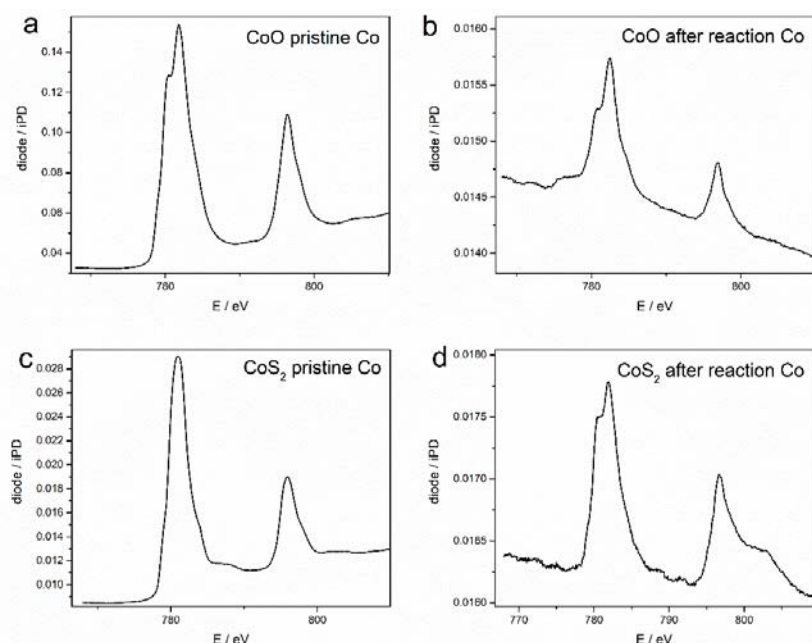


Figure 7.3 Co L-edge for CoO and CoS_2 before and after OER.

The Co L-edge XAS spectra recorded for CoO and CoS_2 before and after OER have been shown in Figure 7.3. Based on theoretical calculated spectra for high spin Co^{2+} and low spin

Co²⁺ reference^{2,3}, the Co²⁺ in pristine CoO exhibits a high spin configuration⁴, whereas Co²⁺ in pristine CoS₂ possesses a low spin configuration.⁵ (Figure 7.4) The main peak for both pristine CoO and CoS₂ lies at around 781 eV (Figure 7.3a and b). Normally, low-spin fragments possess shorter metal-ligand bond lengths than their high-spin counterparts.⁹ However, CoO with Co²⁺ at higher spin state possesses shorter Co-O length compared to Co-S in CoS₂. Based on ligand field theory, S-S in CoS₂ is a strong σ bond, which has a strong ligand field. Thus, this ligand field splitting energy is larger than the exchange energy and Co²⁺ in CoS₂ is in the low spin state.⁶ CoO is considered as an ionic compound, which has low ligand field energy. This results in high spin state of Co²⁺ in CoO.⁷ The bond length is not only influenced by the spin state, but also by the type of ligands as well. Though Co²⁺ in CoS₂ has low spin state ($t_{2g}^6 e_g^1$), it does not exhibit a Jahn-Teller (J-T) distortion. This is manifested in the cubic structure of CoS₂ and 90° bond angle of Co-S-Co (Figure 7.4d). With valence state of S⁻¹, there is an electronic hole on the 3p state of S, which results in a FM spin conductive band. Hence, a half metallic feature of CoS₂ is observed from DOS calculation. As shown in Figure 7.5, CoO possesses a band gap energy of ~2eV which indicates an insulating feature. The majority spin state and minority spin state fully coincident with each other, indicating nonmagnetic feature of CoO. (Figure 7.5c) ⁴ Unlike for LCO, ZnCo₂O₄ and CoO materials, CoS₂ shows a half metallic feature (Figure 7.5d). This agrees well with previous reports as well⁵. Besides, the eg state of Co²⁺ in CoS₂ partially degenerates, which weakens the J-T distortion of CoS₂.⁸

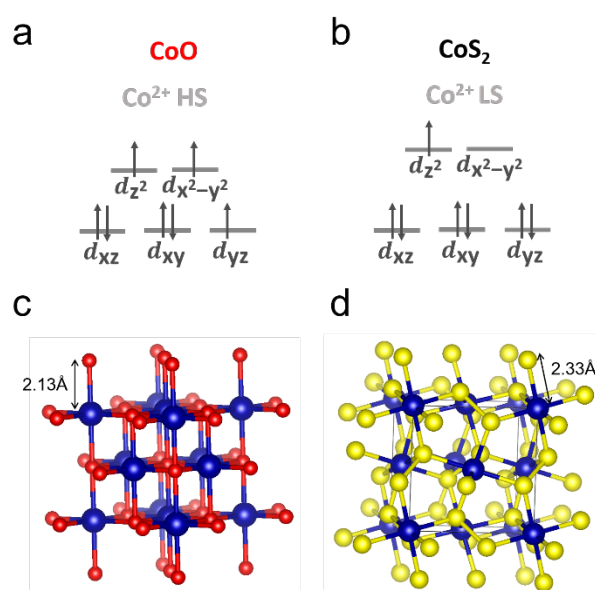


Figure 7.4 Spin state and electron configuration for pristine CoO (a) and CoS₂ (b). Crystal structures for CoO (Co-O bond length=2.13 Å) (c) and CoS₂ (Co-S bond length=2.33 Å) (d).

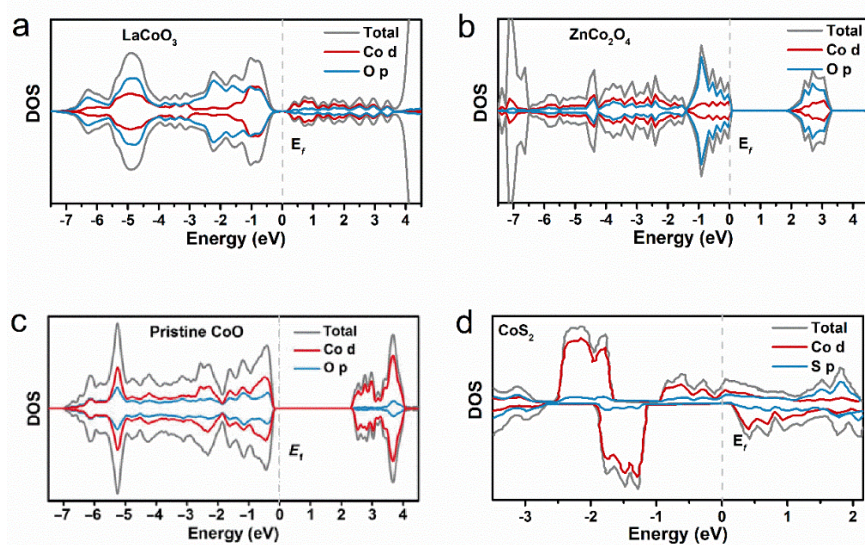


Figure 7.5 DOS of LaCoO_3 , ZnCo_2O_4 , CoO and CoS_2 .

After reaction, the main energy peak for both CoO and CoS_2 (Figure 7.3c and d) becomes 1 eV higher than for the pristine materials.⁹ This is explained by the generally accepted notion that the increase in the valence state results in the shift of the $L_{2,3}$ XAS spectra to higher energies by 1 eV or more.¹⁰ Furthermore, a small shoulder is present before the main peaks, indicating the partial existence of Co^{2+} on the surface of CoO and CoS_2 after OER. The reacted CoS_2 has a rather sharp main peak at 795 eV with a high-energy shoulder, while the CoO spectrum shows a weak main peak.¹¹ Besides, the Co spectrum for CoO after OER shows a larger $I(L_3)/I(L_2)$ branching ratio as compared with the CoS_2 after OER. This indicates that Co in CoS_2 maintains its low spin state after reaction and Co in CoO maintains its high spin state (Figure 7.6).¹¹

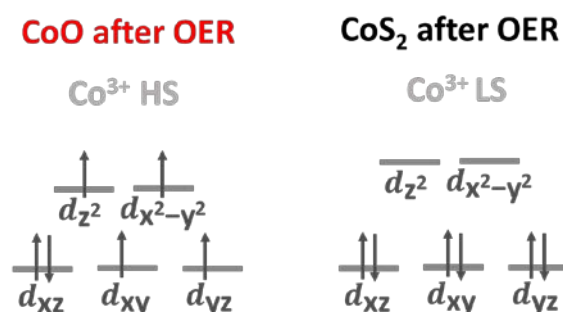


Figure 7.6 Spin state and electron configuration for CoO and CoS_2 after OER.

Figure 7.7 O K-edge for CoO and CoS₂ before and after OER.

The XAS O K-edge spectra for pristine CoO and CoS₂ are shown in Figure 7.7a and c, respectively. The pre-edge peak for CoO with the energy lower than 535 eV can be assigned to the transitions from O 1s orbital to the hybridized states between O 2p orbital and Co 3d orbital.¹² The peaks above 535 eV are indexed to the transition from O 1s to the hybridized states between O 2p and Co 4sp orbitals.¹³ The O signals detected for pristine CoS₂ are from the absorption of oxygen from the atmosphere (Figure 7.7c). After OER, the oxygen states on the surface of CoO and CoS₂ are quite similar, which is the result of the formation of an (oxy)hydroxide surface layer after oxidation (Figure 7.7b and d). Both CoO and CoS₂ change their oxidation states from Co²⁺ to Co³⁺ after cycled in KOH. Co cations in CoO retain high spin state and those in CoS₂ remains low spin states after OER. With similar oxidation states but different spin states, the OER activities for CoO and CoS₂ are very different. This observation hints towards the effect of spin state on the OER activity that will need to be confirmed in future work.

7.3 Recommended Future Work 2

In the previous work in the thesis, we studied the effect of tuning the electronic structure of the materials to improve their water-splitting efficiency. This includes tailoring the spin state of the metal cations and tuning the metal and oxygen states. Recent studies also found out electron spin polarization to be an efficient way to boost the efficiency of water

electrocatalysts.¹⁴ This can be achieved by introducing an outside stimulator, for example, a magnet. After an exposure to magnetic field, the magnetic moments in ferromagnetic materials can be aligned, hence the spin state of the metal cation can be tuned. By magnetizing a ferromagnetic material, electronic structure of the bulk material can be tuned and thus further constrain the electronic structure of the surface-active species. Besides, the effect of magnetization stimulator on the interaction between the catalysts and the water surroundings can be uncovered as well. Here, antiferromagnetic (AFM) $\text{Na}_{0.75}\text{CoO}_2$ and ferromagnetic (FM) $\text{La}_{0.25}\text{Sr}_{0.75}\text{CoO}_3$ have been employed for the investigation of the magnetic stimulator on their OER efficiency.

7.3.1 Experimental details

$\text{Na}_{0.75}\text{CoO}_2$ and $\text{La}_{0.25}\text{Sr}_{0.75}\text{CoO}_3$ were synthesized by a solid-state method. Stoichiometric amounts of Na_2CO_3 and Co_3O_4 or La_2O_3 , SrCO_3 , Co_3O_4 were grinded and pressed into pellets. The pellets were sintered at 900 °C for 12 hours. XRD were conducted for the phase determination. Electrodes will be exposed to magnetic field prior to the electrochemical tests. CV studies will be conducted in 0.1/1 M CsOH/KOH/NaOH/LiOH for electrodes with or without magnetization.

7.3.2 Preliminary results

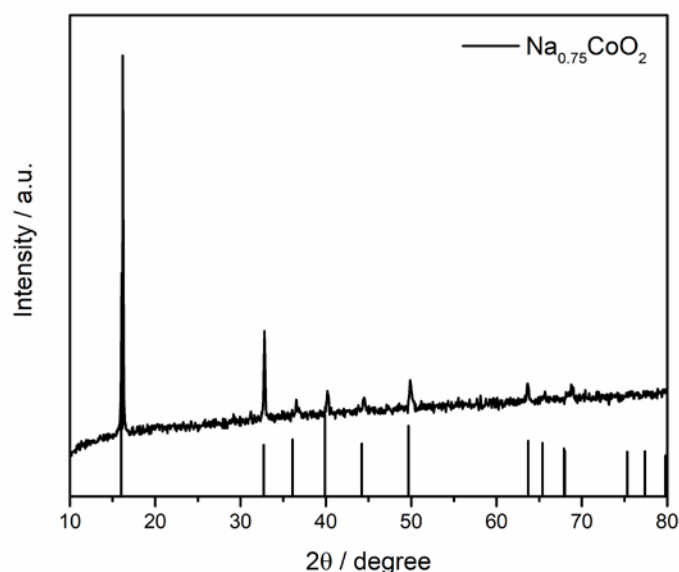


Figure 7.8 XRD pattern for $\text{Na}_{0.75}\text{CoO}_2$.

The crystal structures of $\text{Na}_{0.75}\text{CoO}_2$ were characterized by powder X-ray diffraction (XRD). As displayed in Figure 7.8, the diffraction peaks of the as-prepared $\text{Na}_{0.75}\text{CoO}_2$ match with that of the standard P63/mmc structure with alternative CoO_2 layers and CoO_6 octahedrons.

7.4 Recommended Future Work 3

In the previous work in the thesis, the physical origin of the electrolyte composition on the performance of the catalysts has been revealed. Transition metal oxides/hydroxides react with the alkaline solution in different ways as a function of the electrolyte composition. However, how the electronic and local structures of these materials vary during OER in electrolytes with different cations and impurities has to be explored. Fe impurities and different cation species are introduced to the OER of $\text{Zn}_{1-x}\text{Sr}_x\text{Co}_2\text{O}_4$. Electrochemical properties, surface and interfacial properties will be explored.

7.4.1 Experimental details

Spinel oxides $\text{Zn}_{1-x}\text{Sr}_x\text{Co}_2\text{O}_4$ were synthesized by sol gel methods, phase purity has been confirmed by X-ray diffraction (XRD). Electrochemical tests and pH dependent experiments were conducted in LiOH/NaOH/KOH with/without Fe impurities and different behaviors were observed.

7.4.2 Preliminary results

$\text{Zn}_{0.99}\text{Sr}_{0.01}\text{Co}_2\text{O}_4$ exhibits continuously increased OER currents along with cycling, and eventually shows better OER activity than that of ZnCo_2O_4 , indicating the formation of a new surface for $\text{Zn}_{0.99}\text{Sr}_{0.01}\text{Co}_2\text{O}_4$. It is due to the dissolution of highly soluble Sr^{2+} in alkaline solution, which triggers the oxidation of Co^{3+} active species to form (oxy)hydroxide on the surface. However, we will still need to study the electronic properties as well as the local structure of the new surface formed after OER reaction. Indeed, this new surface is certainly dynamic and interact with the electrolyte and its composition, as we could observe by adding 1000 ppm Fe impurities in the electrolyte. Indeed, with Fe impurities in these alkaline solutions, the OER activity of $\text{Zn}_{0.99}\text{Sr}_{0.01}\text{Co}_2\text{O}_4$ is highly boosted in KOH and NaOH while it remains low for LiOH (Figure 7.9). Hence, additional experiments are needed to understand the dynamics of the surface, especially the Co oxidation state and environment as well as the

incorporation of Fe impurities. For that, XANES and EXAFS are to be conducted for studying the electronic and local structure of these spinels during OER in electrolytes with different cations and impurities.¹⁵

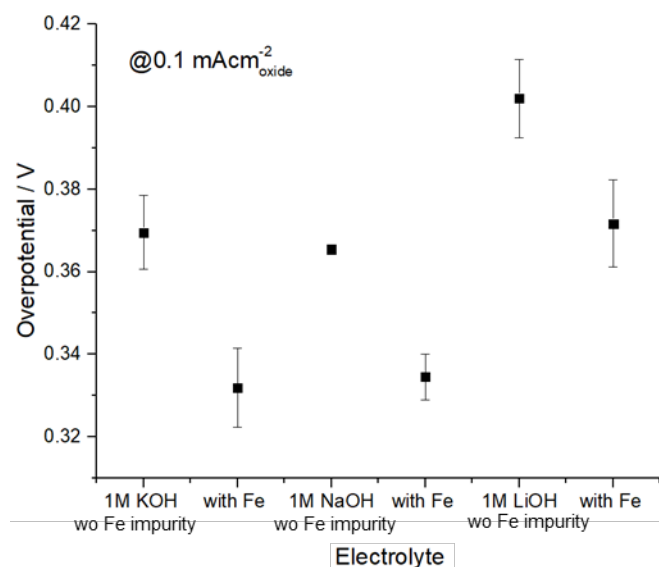


Figure 7.9 Summary of OER activity of $\text{Zn}_{0.99}\text{Sr}_{0.01}\text{Co}_2\text{O}_4$ in 1M LiOH/NaOH/KOH solution with and without Fe impurities.

7.5 References

- (1) Watanabe, E.; Zhao, W.; Sugahara, A.; Mortemard de Boisse, B.; Lander, L.; Asakura, D.; Okamoto, Y.; Mizokawa, T.; Okubo, M.; Yamada, A. Redox-Driven Spin Transition in a Layered Battery Cathode Material. *Chem. Mater.* **2019**, *31* (7), 2358–2365. <https://doi.org/10.1021/acs.chemmater.8b04775>.
- (2) Kim, J.-Y.; Park, J.-H.; Park, B.-G.; Noh, H.-J.; Oh, S.-J.; Yang, J. S.; Kim, D.-H.; Bu, S. D.; Noh, T.-W.; Lin, H.-J.; Hsieh, H.-H.; Chen, C. T. Ferromagnetism Induced by Clustered Co in Co-Doped Anatase TiO_2 Thin Films. *Phys. Rev. Lett.* **2003**, *90* (1), 017401. <https://doi.org/10.1103/PhysRevLett.90.017401>.
- (3) Prellier, W.; Fouchet, A.; Mercey, B. Oxide-Diluted Magnetic Semiconductors: A Review of the Experimental Status. *J. Phys.: Condens. Matter* **2003**, *15* (37), R1583–R1601. <https://doi.org/10.1088/0953-8984/15/37/R01>.
- (4) Joon, M. Electronic Structure and Magnetic Properties of Wurtzite CoO. *Journal of the Korean Physical Society* **2006**, *48* (6), 5.
- (5) Teruya, A.; Suzuki, F.; Aoki, D.; Honda, F.; Nakamura, A.; Nakashima, M.; Amako, Y.; Harima, H.; Uchima, K.; Hedo, M.; Nakama, T.; Ōnuki, Y. Fermi Surface and Magnetic Properties in Ferromagnet CoS_2 and Paramagnet CoSe_2 with the Pyrite-Type Cubic Structure. *J. Phys.: Conf. Ser.* **2017**, *807*, 012001. <https://doi.org/10.1088/1742-6596/807/1/012001>.

- (6) Nickel, E. H. The Application of Ligand-Field Concepts to an Understanding of the Structural Stabilities and Solid-Solution Limits of Sulphides and Related Minerals. *Chemical Geology* **1970**, *5* (4), 233–241. [https://doi.org/10.1016/0009-2541\(70\)90040-9](https://doi.org/10.1016/0009-2541(70)90040-9).
- (7) Bredow, T.; Gerson, A. R. Effect of Exchange and Correlation on Bulk Properties of MgO, NiO, and CoO. *Phys. Rev. B* **2000**, *61* (8), 5194–5201. <https://doi.org/10.1103/PhysRevB.61.5194>.
- (8) Gracia, J.; Sharpe, R.; Munarriz, J. Principles Determining the Activity of Magnetic Oxides for Electron Transfer Reactions. *Journal of Catalysis* **2018**, *361*, 331–338. <https://doi.org/10.1016/j.jcat.2018.03.012>.
- (9) Lin, H.-J.; Chin, Y. Y.; Hu, Z.; Shu, G. J.; Chou, F. C.; Ohta, H.; Yoshimura, K.; Hébert, S.; Maignan, A.; Tanaka, A.; Tjeng, L. H.; Chen, C. T. Local Orbital Occupation and Energy Levels of Co in Na_xCoO₂: A Soft x-Ray Absorption Study. *Phys. Rev. B* **2010**, *81* (11), 115138. <https://doi.org/10.1103/PhysRevB.81.115138>.
- (10) Chang, C. F.; Hu, Z.; Wu, H.; Burnus, T.; Hollmann, N.; Benomar, M.; Lorenz, T.; Tanaka, A.; Lin, H.-J.; Hsieh, H. H.; Chen, C. T.; Tjeng, L. H. Spin Blockade, Orbital Occupation, and Charge Ordering in La_{1.5}Sr_{0.5}CoO₄. *Phys. Rev. Lett.* **2009**, *102* (11), 116401. <https://doi.org/10.1103/PhysRevLett.102.116401>.
- (11) Istomin, S. Ya.; Tyablikov, O. A.; Kazakov, S. M.; Antipov, E. V.; Kurbakov, A. I.; Tsirlin, A. A.; Hollmann, N.; Chin, Y. Y.; Lin, H.-J.; Chen, C. T.; Tanaka, A.; Tjeng, L. H.; Hu, Z. An Unusual High-Spin Ground State of Co³⁺ in Octahedral Coordination in Brownmillerite-Type Cobalt Oxide. *Dalton Trans.* **2015**, *44* (23), 10708–10713. <https://doi.org/10.1039/C4DT03670K>.
- (12) Long, X.-H.; Wu, Y.-R.; Zhang, N.; Yu, P.-F.; Feng, X.-F.; Zheng, S.; Fu, J.-M.; Liu, X.-S.; Liu, N.; Wang, M.; Xu, L.-M.; Chen, J.-M.; Lee, J.-M. Charge Compensation and Capacity Fading in LiCoO₂ at High Voltage Investigated by Soft x-Ray Absorption Spectroscopy. *Chinese Phys. B* **2018**, *27* (10), 107802. <https://doi.org/10.1088/1674-1056/27/10/107802>.
- (13) Choi, H. C.; Lee, S. Y.; Kim, S. B.; Kim, M. G.; Lee, M. K.; Shin, H. J.; Lee, J. S. Local Structural Characterization for Electrochemical Insertion–Extraction of Lithium into CoO with X-Ray Absorption Spectroscopy. *J. Phys. Chem. B* **2002**, *106* (36), 9252–9260. <https://doi.org/10.1021/jp0205968>.
- (14) Garcés-Pineda, F. A.; Blasco-Ahicart, M.; Nieto-Castro, D.; López, N.; Galán-Mascarós, J. R. Direct Magnetic Enhancement of Electrocatalytic Water Oxidation in Alkaline Media. *Nat Energy* **2019**, *4* (6), 519–525. <https://doi.org/10.1038/s41560-019-0404-4>.
- (15) Yang, C.; Batuk, M.; Jacquet, Q.; Rouse, G.; Yin, W.; Zhang, L.; Hadermann, J.; Abakumov, A. M.; Cibir, G.; Chadwick, A. Revealing PH-Dependent Activities and Surface Instabilities for Ni-Based Electrocatalysts during the Oxygen Evolution Reaction. *ACS Energy Letters* **2018**, *3* (12), 2884–2890.

Conclusion

The hypotheses in the thesis are tested by experiments, characterizations, modeling and kinetic parameter extrapolations. This thesis regards the revealing of the OER mechanism by establishing the correlation between the material properties and the electrocatalytic properties. In the Chapter 4, the example of perovskite transition metal oxides $\text{LaCo}_{0.9}\text{Fe}_{0.1}\text{O}_3$ demonstrates how electronic structure can be modified such that the OER activity is tailored. Characterizations providing structural insights such as XRD, SEM, FTIR, SEM and SQUID aid the understanding of the bulk properties of the materials. DFT modeling facilitates the comprehension of the intrinsic electronic structure of $\text{LaCo}_{0.9}\text{Fe}_{0.1}\text{O}_3$. A link is built between the electrochemical performance of the material and its covalency of metal d band and O p band. In Chapter 5, both the electronic properties and the surface reconstructed properties have been probed by characterization techniques and DFT calculations. The novel OER mechanism involving surface reorganization is correlated with the intrinsic properties. In details, electrochemical studies, XAS, XRD, XPS, TEM-EDS, EELS and XMCD analyze the Ni agglomeration and the reconstruction with the participation of surface oxygen. This observed electrocatalytic performance is due to the more active O p -band compared with M d -band. In the Chapter 6, perovskite transition metal oxide LSCO and transition metal hydroxides $\text{CoOOH}/\text{Co}_{0.5}\text{Fe}_{0.5}\text{OOH}$ are found to exhibit different behaviors when tuning the electrolyte compositions, which include the concentration of the OH^- and the alkali cation species in the electrolyte. Different from that in Chapter 5 which employs electrochemical studies on the study of interfacial properties, here, kinetic parameters are extrapolated by the use of temperature dependent experiments. The pH dependence of LSCO and CoOOH owes to the increase in pre-exponential factors as a result of increased concentration of active sites or a change in the entropy of activation of the reaction. Instead, the cation dependence observed for $\text{Co}_{0.5}\text{Fe}_{0.5}\text{OOH}$ is attributed to the change in activation energy as a result of the modified formation enthalpies of the intermediates. From the listed studies in the thesis, we have reached out from the bulk of the catalysts, to the surface of the catalysts, finally to the interface between the catalysts and the electrolyte. The catalytic activity is well correlated with their intrinsic, surface and interfacial properties. The findings are not only meaningful for the understanding of OER for Co-based transition metal oxides/hydroxides, they are helpful for future design of highly active electrocatalysts.

Table des illustrations

Figure 2.1 (a) Oxygen electrochemistry application for energy storage and conversion. (b) Reaction formulas for OER, ORR, HOR and HER. The overpotentials of the reactions. The figures are adapted from Ref 1.	10
Figure 2.2 TOF of different oxides materials and the natural catalyst OEC. This figure is adapted from Ref 1.	12
Figure 2.3 Crystal structure of spinel structure oxides (e.g. ZnCo_2O_4), delafossite structure oxides (e.g. LiCoO_2), perovskite (e.g. LaCoO_3) and rock salt structure (CoO) with CoO_6	14
Figure 2.4 Structure of perovskite oxide.	14
Figure 2.5 Structure of spinel oxide. This figure is adapted from Ref 17.	15
Figure 2.6 Structure of layered hydroxides. This figure is adapted from Ref 23.	16
Figure 2.7 (a) Spatial arrangement of oxygen ligands with respect to the d orbitals in the octahedral crystal field. (b) degenerate d orbitals in octahedral crystal field. This figure is adapted from Ref 25.	17
Figure 2.8 Scheme of low spin state, intermediate spin state and high spin state of Co^{3+}	18
Figure 2.9 (a) Spatial arrangement of oxygen ligands with respect to the d orbitals in the tetrahedral crystal field. (b) degenerate d orbitals in tetrahedral crystal field. This figure is adapted from Ref 25.	18
Figure 2.10 Traditional mechanism of OER process in which the concerted proton–electron transfers are involved on the metal sites. The oxygen in blue are originated from electrolyte, whereas oxygen in red is the oxygen contributed from the oxide lattice. This figure is adapted from Ref 33.	19
Figure 2.11 Four steps CPET reactions.	19
Figure 2.12 Reaction free energies for four CPET steps. (left) This figure is adapted from Ref 34. Reaction free energy of real catalysts and ideal catalysts under three different OER potentials. (right) This figure is adapted from Ref 35.	20
Figure 2.13 Volcano plot. This figure is adapted from Ref 36.	21
Figure 2.14 (a) Correlation between OER activity and the occupation of e_g orbital for different perovskite materials. (b) adsorption energy of oxygen vs. e_g occupation. These figures are adapted from Ref 37.	21
Figure 2.15. Compression on z axis (left) and elongation on z axis (right). This figure is adapted from Ref 42.	22
Figure 2.16 Dissolution and re-deposition mechanism for BSCF82. This figure is adapted from Ref 52.	24
Figure 2.17 Evolved OER mechanisms which involve non-concerted proton–electron transfer. The illustration on the left involves OER that evolve $^{34}\text{O}_2$ and $^{36}\text{O}_2$ is evolved on the right. The same processes as in concerted proton-electron transfer have been marked in yellow and green. These figures are adapted from Ref 33.	25
Figure 2.18 Zaanen-Sawatzki-Allen (ZSA) framework for the electronic structure of transition metal oxides. These figures are adapted from Ref 26.	25
Figure 2.19 (a) (c) Metal cations as active sites without oxygen deficiency. (b) (d) Oxygen deficiency participates in the OER process. These figures are adapted from Ref 26.	26
Figure 2.20 pH dependent OER activities of LSCO and LaNiO_3 . . This figure is adapted from Ref 55.	27
Figure 2.21 Comparison between the concerted proton–electron transfer OER mechanism and the non-concerted proton-electron transfer OER mechanism. These reactions are adapted from Ref 57.	27

Figure 2.22 Activation energies as reported by Otagawa and Bockris for perovskites OER catalysts as a function of the OER current density measured at 300 mV overpotential. This figure is adapted from Ref 58.....	28
Figure 2.23 Two categories of cations and anions in the solutions. This figure is adapted from Ref 104.	30
Figure 3.1 Sol-gel methods for synthesis. This figure is adapted from Ref 1.....	40
Figure 3.2 The electrochemical setup for electrodeposition.	42
Figure 3.2 Experimental setup for the three-electrode cell. This figure is adapted from Ref 7.	43
Figure 3.3 Scheme of X-ray Diffraction. This figure is adapted from Ref 10.	46
Figure 3.4 Scheme of transmission mode of XAS measurement. This figure is adapted from Ref 14.	47
Figure 3.5 Three parts of XAS spectra depending on the energy of the incident photons. This figure is adapted from Ref ¹⁶	48
Figure 3.6 XAS spectrum. This figure is adapted from Ref 14.	48
Figure 3.7 Resonance for different element in XAS. This figure is adapted from Ref ¹⁶	49
Figure 3.8 Operations Schematic of FTIR spectrometer. This figure is adapted from Ref 18.	49
Figure 3.9 Stretching vibration and bending vibration of molecules after IR radiation. This figure is adapted from Ref 19.	50
Figure 3.10 Diagram of XMCD. This figure is adapted from Ref 20.	51
Figure 3.11 Working principles for TEM. This figure is adapted from Ref 22.	52
Figure 3.12 Schematic of electron energy loss spectrum. This figure is adapted from Ref 23.	53
Figure 3.13 Working principle for the SQUID. This figure is adapted from Ref 26.	54
Figure 4.1 XRD patterns of $\text{LaCo}_{1-x}\text{Fe}_x\text{O}_3$ ($x=0.00, 0.10, 0.25, 0.50, 0.75, 1.00$).	67
Figure 4.2 Perovskite structure (ABO_3) with rhombohedral distorted structure (a) and orthorhombic structure (b). A (La in green) represents the metal cation which accommodates at the corners of the unit cell. B (Co in blue and Fe in orange) represents the octahedrally coordinated transition metal cation which is at the centre of the unit cell. The negative oxygen ions occupy the face-centred positions.	68
Figure 4.3 SEM images of $\text{LaCo}_{1-x}\text{Fe}_x\text{O}_3$ ($x=0.00, 0.10, 0.25, 0.50, 0.75, 1.00$).	69
Figure 4.4 BET raw data of $\text{LaCo}_{1-x}\text{Fe}_x\text{O}_3$ ($x=0.00, 0.10, 0.25, 0.50, 0.75, 1.00$) and trend in specific surface area as Fe substitution increases.	70
Figure 4.5 FT-IR spectra of $\text{LaCo}_{1-x}\text{Fe}_x\text{O}_3$ ($x=0.00, 0.10, 0.25, 0.50, 0.75, 1.00$).	71
Figure 4.6 (a) The representative CV curves (the second cycle) of oxygen evolution reaction in 1.0 M KOH. The inset of (a) shows the Tafel plot of $\text{LaCo}_{0.90}\text{Fe}_{0.10}\text{O}_3$ (yellow line) for comparison with unsubstituted LaCoO_3 (red line) and benchmarked IrO_2 extracted from reference ²⁴ . (b) The specific current density for $\text{LaCo}_{1-x}\text{Fe}_x\text{O}_3$ at 1.63 V vs RHE.	73
Figure 4.7 (a) Normalised Co K-edge XANES spectra of $\text{LaCo}_{1-x}\text{Fe}_x\text{O}_3$ ($x = 0.00, 0.10, 0.25, 0.50, 0.75, 1.00$) with CoO and LiCoO_2 (Sigma Aldrich) as reference. The inset exhibits the zoomed in Co K-edge XANES spectra for LaCoO_3 (red line) and $\text{LaCo}_{0.9}\text{Fe}_{0.1}\text{O}_3$ (yellow line) from 7709 to 7712 eV. (b) Normalised Fe K-edge XANES spectra of $\text{LaCo}_{1-x}\text{Fe}_x\text{O}_3$ ($x=0.00, 0.10, 0.25, 0.50, 0.75, 1.00$) with Fe foil and Fe_2O_3 (Sigma Aldrich) as reference. The inset shows the zoomed in Fe K-edge XANES spectra for $\text{LaCo}_{1-x}\text{Fe}_x\text{O}_3$ from 7110 to 7120 eV.	75
Figure 4.8 (a) EXAFS $k^3\chi(R)$ spectra of $\text{LaCo}_{1-x}\text{Fe}_x\text{O}_3$ ($x=0.00, 0.10, 0.25, 0.50, 0.75$) at Co K-edge. (b) EXAFS $k^3\chi(R)$ spectra of $\text{LaCo}_{1-x}\text{Fe}_x\text{O}_3$ ($x=0.10, 0.25, 0.50, 0.75, 1.00$) at Fe K-edge.	76
Figure 4.9 100Oe Field-cooled M-T curves of $\text{LaCo}_{1-x}\text{Fe}_x\text{O}_3$ ($x=0.00, 0.10, 0.25, 0.50, 0.75, 1.00$) and the trend of Curie Temperature with the increase in Fe substitution.	78

Figure 4.10 Spin structure analyses of $\text{LaCo}_{1-x}\text{Fe}_x\text{O}_3$. ($x=0.00, 0.10, 0.25, 0.50, 0.75, 1.00$) (a) The temperature-dependence inverse susceptibilities for $\text{LaCo}_{1-x}\text{Fe}_x\text{O}_3$ samples. The inset are the plots for Co^{3+} LS ($t_{2g}^6 e_g^0, S = 0$) and Co^{3+} HS ($t_{2g}^4 e_g^2, S = 2$) in the octahedral ligand-field. (b) Curie constant for $\text{LaCo}_{1-x}\text{Fe}_x\text{O}_3$. ($x=0.00, 0.10, 0.25, 0.50, 0.75, 1.00$). (c) The ratio of HS Co^{3+} in $\text{LaCo}_{1-x}\text{Fe}_x\text{O}_3$ with $x=0.00, 0.10, 0.25, 0.50, 0.75$	79
Figure 4.11 Computed TDOS (total density of states) of LaCoO_3 with Co ions in low spin state (LS: $t_{2g}^6 e_g^0$) (a) and $\text{LaCo}_{0.9}\text{Fe}_{0.1}\text{O}_3$ with Co ions in higher spin state (b). Fermi level is denoted by vertical dashed line. Arrows corresponds to spin-up and spin-down spin projection. Insets show the zoomed in pDOS of LaCoO_3 and $\text{LaCo}_{0.9}\text{Fe}_{0.1}\text{O}_3$ from -1.5 eV to 1.5 eV relative to E_F . pDOS of the Co d states and O p states in LaCoO_3 (c) and $\text{LaCo}_{0.9}\text{Fe}_{0.1}\text{O}_3$ (d).....	81
Figure 5.1 (a) XRD patterns of $\text{ZnCo}_{2-x}\text{Ni}_x\text{O}_4$ ($x=0.0, 0.2, 0.4, 0.6, 0.8$); BET surface area of $\text{ZnCo}_{2-x}\text{Ni}_x\text{O}_4$ (inset). (b) Electronic structural characterization of $\text{ZnCo}_{2-x}\text{Ni}_x\text{O}_4$ ($x=0.0, 0.2, 0.4, 0.6, 0.8$) by XANES. Normalized Co K-edge XANES spectra (left panel) and Normalized Ni K-edge XANES spectra (right panel). (c) Geometric information characterization by Fourier transform of the EXAFS (FT-EXAFS). FT-EXAFS spectra and fitting for Co K-edge (left panel) and Ni K-edge (right panel).....	93
Figure 5.2 (a) Normalized Zn K-edge XANES spectra of $\text{ZnCo}_{2-x}\text{Ni}_x\text{O}_4$ ($x=0.0, 0.2, 0.4, 0.6, 0.8, 1.2, 1.6, 2.0$). The inset shows the white lines of $\text{ZnCo}_{2-x}\text{Ni}_x\text{O}_4$ ($x=0.0, 0.2, 0.4, 0.6, 0.8$) oxides. An increase in the intensity of F1 and decrease in F2 indicates the decreased degree of disorder in spinel structure. (b) FT-EXAFS $k^3\chi(R)$ spectra of $\text{ZnCo}_{2-x}\text{Ni}_x\text{O}_4$ ($x=0, 0.2, 0.4, 0.6, 0.8$) at Zn K edge.....	94
Figure 5.3 XRD patterns of ZnCo_2O_4 , $\text{ZnCo}_{0.8}\text{Ni}_{1.2}\text{O}_4$ and ZnNi_2O_4 . Peaks denoted by ‘*’ correspond to ZnO wurtzite structure and peaks indicated with ‘#’ refers to NiO rock-salt structure.....	95
Figure 5.4 Normalized Zn K-edge XANES spectra of $\text{ZnCo}_{2-x}\text{Ni}_x\text{O}_4$ ($x=0.0, 0.2, 0.4, 0.6, 0.8, 1.2, 1.6, 2.0$) (left panel). The inset shows the white lines of $\text{ZnCo}_{2-x}\text{Ni}_x\text{O}_4$ ($x=0.0, 0.2, 0.4, 0.6, 0.8$) oxides. An increase in the intensity of F1 and decrease in F2 indicates the increased degree of disorder in spinel structure. Normalized Co K-edge XANES spectra of $\text{ZnCo}_{2-x}\text{Ni}_x\text{O}_4$ ($x=0.0, 0.2, 0.4, 0.6, 0.8, 1.2, 1.6$) (middle panel). Normalized Ni K-edge XANES spectra of $\text{ZnCo}_{2-x}\text{Ni}_x\text{O}_4$ ($x=0.2, 0.4, 0.6, 0.8, 1.2, 1.6, 2.0$) (right panel).....	95
Figure 5.5 Electrochemical characterization on OER performance of $\text{ZnCo}_{2-x}\text{Ni}_x\text{O}_4$ ($x=0.0, 0.2, 0.4, 0.6, 0.8$). All data points and error bars were obtained by averaging the results of at least three independent measurements. (a) CV curves of the 1000 th cycle comparing to the 2 nd cycle of $\text{ZnCo}_{2-x}\text{Ni}_x\text{O}_4$ ($x=0.0, 0.2, 0.4, 0.6, 0.8$). The insets present the Tafel plot for surface-area-normalized $\text{ZnCo}_{2-x}\text{Ni}_x\text{O}_4$ ($x=0.0, 0.2, 0.4, 0.6, 0.8$) at the 2 nd cycle (top) and 1000 th cycle (bottom) compared with LaCoO_3 ⁶⁰ , LaNiO_3 ⁶⁰ , IrO_2 (100) extracted from IrO_2 ⁶¹ and IrO_2 ⁶² . (b) iR corrected potential (in RHE scale) of the 1000 th cycle comparing to the 2 nd cycle of $\text{ZnCo}_{2-x}\text{Ni}_x\text{O}_4$ ($x=0.0, 0.2, 0.4, 0.6, 0.8$) at $25 \mu\text{A cm}^{-2}_{\text{oxide}}$. (c) Evolutive CV curves for representative $\text{ZnCo}_{1.2}\text{Ni}_{0.8}\text{O}_4$ from 2 nd to 1000 th cycle in 1M KOH at 10 mV s^{-1} in between 0.904 and 1.624 V (vs. RHE). The insets show the redox peaks from 1.23 V to 1.5 V. (d) Evolution of the pseudocapacitive charge during cycling (0.904-1.624 V versus RHE) in 1M KOH (left axis) and the OER activity at 1.6V versus RHE (right axis) for $\text{ZnCo}_{1.2}\text{Ni}_{0.8}\text{O}_4$	97
Figure 5.6 Chronoamperometry of $\text{ZnCo}_{2-x}\text{Ni}_x\text{O}_4$ ($x=0.0, 0.2, 0.4, 0.6, 0.8$) after 100 th CV at an overpotential of 0.314 V (vs. RHE).....	98
Figure 5.7 a) Evolutive CV curves for representative ZnCo_2O_4 from 2 nd to 1000 th cycle in 1M KOH at 10 mV s^{-1} in between 0.904 and 1.624 V (vs. RHE). The insets show the redox peaks from 1.33 V to 1.59 V. b) Evolution of the pseudocapacitive charge during cycling (0.904-1.624 V versus RHE) in 1M KOH (left axis) and the OER activity at 1.6V versus RHE (right axis) for ZnCo_2O_4	98

Figure 5.8 Structural and compositional characterization of $\text{ZnCo}_{1.2}\text{Ni}_{0.8}\text{O}_4$ before and after OER cycling. (a) ABF image of pristine $\text{ZnCo}_{1.2}\text{Ni}_{0.8}\text{O}_4$ (left) and $\text{ZnCo}_{1.2}\text{Ni}_{0.8}\text{O}_4$ after thousand cycles of OER in 1M KOH at 10 mV/s between 0.904 and 1.624 V (vs. RHE) (right). The inset at the bottom right is the FFT pattern for the bulk which can be referred to Fd3m space group. (b) STEM-EDS image and analysis of pristine (left) and cycled (right) $\text{ZnCo}_{1.2}\text{Ni}_{0.8}\text{O}_4$	99
Figure 5.9 X-ray photoelectron spectra (XPS) survey of Zn, Co and Ni 2p regions for $\text{ZnCo}_{1.8}\text{Ni}_{0.2}\text{O}_4$ (a), $\text{ZnCo}_{1.6}\text{Ni}_{0.4}\text{O}_4$ (b), $\text{ZnCo}_{0.4}\text{Ni}_{0.6}\text{O}_4$ (c) and $\text{ZnCo}_{1.2}\text{Ni}_{0.8}\text{O}_4$ (d) surface before OER testing (black line) and after thousand cycles of OER (after OER) in 1M KOH at 10 mVs ⁻¹ between 0.904 and 1.624 V (vs. RHE).....	100
Figure 5.10 (a) EELS spectra of O K-edge and Ni L-edge along the scanning pathway are to detect the change in O electronic structures and charge distributions of metal cations. L3/L2 ratios of Ni edge calculated from Ni L-edge EELS spectra for pristine $\text{ZnCo}_{1.2}\text{Ni}_{0.8}\text{O}_4$ (b) and cycled $\text{ZnCo}_{1.2}\text{Ni}_{0.8}\text{O}_4$ (c). The ratios of L3/L2 for Ni edge before and after cycling have been determined by a Hartree–Slater cross section method ⁷⁴ . Lower L3/L2 corresponds to higher chemical states of the Ni cations. This indicates that there is surface Ni ²⁺ before OER, and these surface Ni cations acquire higher valence state after cycling.	101
Figure 5.11 X-ray photoelectron spectra (XPS) of Ni 2p regions for $\text{ZnCo}_{2-x}\text{Ni}_x\text{O}_4$ surface before OER testing and after thousand cycles of OER in 1M KOH at 10 mVs ⁻¹ between 0.904 and 1.624 V (vs. RHE). Fittings of experimental spectra obtained for $\text{ZnCo}_{2-x}\text{Ni}_x\text{O}_4$ are shown in coloured curves. Fittings of satellites are shown in dark blue colour.....	102
Figure 5.12 XPS of Ni 2p regions for $\text{ZnCo}_{1.2}\text{Ni}_{0.8}\text{O}_4$ surface before OER testing and after thousand cycles of OER in 1M KOH at 10 mVs ⁻¹ between 0.904 and 1.624 V (vs. RHE). Fittings of experimental spectra obtained for $\text{ZnCo}_{1.2}\text{Ni}_{0.8}\text{O}_4$ are shown in coloured curves. Fittings of satellites are shown in dark blue colour. Shaded area demonstrates the fitting of satellites. The satellite structure at 881eV is associated with a 2p ⁵ 3d ⁷ final state transformed from a 2p ⁶ 3d ⁷ state in the photoemission process, and the structure at 861eV is attributed to the 2p ⁵ 3d ⁸ L final state from 2p ⁶ 3d ⁸ . ^{69,70} Thus, the relatively strong satellite structure at the lower binding strength compared to that at higher binding strength is the result of increased Ni ³⁺ which gives rise to removal of electrons from valence levels to which charge transfer from the ligand is facilitated ^{75–77} . The broadening of main peaks for the Ni edge indicates the presence of delocalised electrons on 3d-2p states after OER. ¹⁰²	103
Figure 5.13 Soft XAS spectra at the Ni L _{2,3} -edge for $\text{ZnCo}_{1.2}\text{Ni}_{0.8}\text{O}_4$ before (red line) and after OER cycling (blue line).	104
Figure 5.14 XMCD spectra raised from the difference between the μ ⁺ and μ ⁻ soft XAS spectra at the Ni L _{2,3} -edge for $\text{ZnCo}_{1.2}\text{Ni}_{0.8}\text{O}_4$ before (bottom) and after OER cycling (top).....	105
Figure 5.15 OER activity (current normalized by surface area of oxide) of pristine $\text{ZnCo}_{2-x}\text{Ni}_x\text{O}_4$ at 1.6 V (versus RHE) after iR correction as a function of pH.	107
Figure 5.16 pH-dependent OER activity for pristine $\text{ZnCo}_{2-x}\text{Ni}_x\text{O}_4$. CV measurements for pristine ZnCo_2O_4 (a) and $\text{ZnCo}_{1.2}\text{Ni}_{0.8}\text{O}_4$ (b) from 0.1 M KOH (pH 13) to 1 M KOH (pH 14) recorded at 10 mV s ⁻¹ on the RHE scales after iR correction. Insets are the Tafel plots in different pH. Increasing the pH value from 13 to 14 leads to seven times greater intrinsic OER activity (OER activity normalised by the surface area of working electrode) for pristine ZnCo_2O_4 . The decreased Tafel slope along with increased pH, from 57.73 mV dec ⁻¹ to 48.59 mV dec ⁻¹ , indicates a change in reaction pathways when using KOH with different concentrations. [25] All other samples exhibit similar performance . CV measurements for pristine ZnCo_2O_4 (c) and $\text{ZnCo}_{1.2}\text{Ni}_{0.8}\text{O}_4$ (d) from 0.1 M KOH (pH 13) to 1 M KOH (pH 14) recorded at 200 mV s ⁻¹ on the SHE scales. Bottom panel shows the schematic for non-concerted proton-electron transfer of surface deprotonation of pristine ZnCo_2O_4 and $\text{ZnCo}_{1.2}\text{Ni}_{0.8}\text{O}_4$. The Pourbaix slopes obtained for these materials are quite different from	

Ni(OH) ₂ (-90 mV/pH) which also reconstructs to NiOOH under OER conditions, meaning that this deprotonation behaviour is very dependent on the oxide which is used to form the hydroxide.....	107
Figure 5.17 OER activity swept from low pH to high pH for pristine ZnCo _{2-x} Ni _x O ₄	108
Figure 5.18 OER activity swept from low pH to high pH comparing with activity swept from high pH to low pH in pH=13, pH =13.5 and pH=14 for pristine ZnCo _{2-x} Ni _x O ₄	109
Figure 5.19 OER activity swept from high pH to low pH for pristine ZnCo _{2-x} Ni _x O ₄	110
Figure 5.20 OER activity swept from high pH to low pH for pristine ZnCo ₂ O ₄ (a) and ZnCo _{1.2} Ni _{0.8} O ₄ (b). Tafel plots are shown in the insets.....	110
Figure 5.21 a) The schematic for the transition from pristine ZnCo ₂ O ₄ /ZnCo _{1.2} Ni _{0.8} O ₄ to CoOOH/NiOOH. b) OER activity swept from high pH to low pH (current normalized by surface area of oxide) of pristine ZnCo _{2-x} Ni _x O ₄ at 1.6 V (versus RHE) after iR correction as a function of pH.	111
Figure 5.22 OER activity swept from low pH to high pH comparing with activity swept from high pH to low pH in pH=13 (a), pH =13.5 (b) and pH=14 (c) for ZnCo ₂ O ₄ after 1000 th OER cycles.	111
Figure 5.23 (a) CV measurements for cycled ZnCo ₂ O ₄ from 0.1 M KOH (pH 13.12) to 1 M KOH (pH 13.98) recorded at 10 mV s ⁻¹ on the RHE scales after iR correction. Insets are the Tafel plots in different pH. (b) CV measurements for cycled ZnCo ₂ O ₄ from 0.1 M KOH (pH 13.12) to 1 M KOH (pH 13.98) recorded at 200 mV s ⁻¹ on the SHE scales. Bottom panels show the schematic for concerted proton-electron transfer of surface deprotonation of cycled ZnCo ₂ O ₄	112
Figure 5.24 OER activity swept from low pH to high pH comparing with activity swept from high pH to low pH in pH=13, pH =13.5 and pH=14 for ZnCo _{1.2} Ni _{0.8} O ₄ after 1000 th OER cycles.	112
Figure 5.25 (a) pH-dependent OER activity for cycled ZnCo _{1.2} Ni _{0.8} O ₄ . (b) The schematic for the transition from pristine ZnCo ₂ O ₄ /ZnCo _{1.2} Ni _{0.8} O ₄ to CoOOH/NiOOH. (c) The schematic for nonconcerted proton-electron transfer (2 H ⁺ :1e ⁻ ratio is shown as an example) of surface deprotonation of cycled ZnCo _{1.2} Ni _{0.8} O ₄ . (d) Energy of lowest unoccupied molecular orbital (LUMO) versus number of Ni in octahedral site. Insets are the schematic plots of models with one Zn atom in tetrahedral site, three Co or Ni atoms in octahedral site.	114
Figure 5.26 Top panel shows the crystal structures of Ni substituted ZnCo ₂ O ₄ . ZnCo _{2-x} Ni _x O ₄ (x≤0.8) possesses a spinel structure with Zn accommodating tetrahedron (red), Co (grey) and Ni (pink) occupying an octahedron. ZnCo _{2-x} Ni _x O ₄ (x>0.8) has phase separation into wurtzite, spinel and rock-salt structures. Bottom left panel shows the schematic representation of M _{Oh} d-band and O p-band for ZnCo _{2-x} Ni _x O ₄ (x=0, 0.2) with M _{Oh} d-band centre higher than O p-band centre. Bottom right panel is the schematic representation of M _{Oh} d-band and O p-band for ZnCo _{2-x} Ni _x O ₄ (x=0.4, 0.6, 0.8) with O p-band centre higher than M _{Oh} d-band centre. (a) Formation energy of ZnCo _{2-x} Ni _x O ₄ (x=0, 0.2, 0.4, 0.6, 0.8, 1.4, 1.6, 2.0) relative to ZnCo ₂ O ₄ and O p-band centre relative to M _{Oh} d-band centre of ZnCo _{2-x} Ni _x O ₄ (x=0, 0.2, 0.4, 0.6, 0.8, 1.4, 1.6, 2.0). Three regions are distinguished with the increased amount of x ratio: stable region for ZnCo _{2-x} Ni _x O ₄ (x=0, 0.2 and 0.4); unstable region for ZnCo _{2-x} Ni _x O ₄ (x=0.6 and 0.8) which undergoes significant surface reconstruction during OER cycles; for ZnCo _{2-x} Ni _x O ₄ with x>0.8, too high the formation energy or O p-band centre relative to M _{Oh} d-band centre results in very unstable phase and non-existent spinel structure.....	116
Figure 5.27 Electronic density of states (DOS) of ZnCo ₂ O ₄ (top panel), ZnCo _{1.6} Ni _{0.4} O ₄ (middle panel) and ZnCo _{1.2} Ni _{0.8} O ₄ (bottom panel).....	117
Figure 5.28 The schematics in the bottom middle show the adsorbates evolution mechanism (AEM) for ZnCo _{2-x} Ni _x O ₄ (x=0, 0.2 and 0.4) and the lattice-oxygen participated evolution	

mechanism (LOM) for $\text{ZnCo}_{2-x}\text{Ni}_x\text{O}_4$ ($x=0.6$ and 0.8). Red and black atoms are from the lattice and the solvent, respectively.....	118
Figure 6.1 (a) Potentiostatic measurements performed for $\text{La}_{0.6}\text{Sr}_{0.4}\text{CoO}_3$ at 25°C in 0.1 M KOH with a rotation rate of 1600 rpm and (b) Tafel slopes obtained by potentiostatic measurements compared to the one obtained for the same electrode using CV scan performed at 10 mV/s .	132
Figure 6.2 a) CV Measurements of LaCoO_3 from 10 to 60°C with an increment of 10°C . b) Averaged CV curves obtained from taking the average OER kinetic currents between forward and backward scans in order to remove the capacitive current contribution. c) Averaged Tafel plots by taking the average OER kinetic currents between forward and backward scans. Tafel slopes ($\sim 75\text{mVdec}^{-1}$) are labelled. d) Extrapolation of activation energy and pre-exponential factor from $\ln j$ vs $1000/T$ curve.....	134
Figure 6.3 Activation energy and pre-exponential factor at $\eta=0\text{mV}$ for $\text{La}_{1-x}\text{Sr}_x\text{CoO}_3$ vs OER exchange current density in 0.1M KOH at 20°C .	136
Figure 6.4. CV measurements for LaCoO_3 (a), $\text{La}_{0.6}\text{Sr}_{0.4}\text{CoO}_3$ (c), CoOOH (e) and $\text{Co}_{0.5}\text{Fe}_{0.5}\text{OOH}$ (g) at 20°C with a rotation speed gradually increased from 400 rpm , to 900 , 1600 and 2500 rpm . CV measurements for LaCoO_3 (b), $\text{La}_{0.6}\text{Sr}_{0.4}\text{CoO}_3$ (d), CoOOH (f) and $\text{Co}_{0.5}\text{Fe}_{0.5}\text{OOH}$ (h) at 20°C with a rotation speed gradually decreased from 1500 rpm to 1600 , 900 and 400 rpm . Tafel plots and Tafel slopes are shown in insets. These measurements demonstrate that no mass transport limitations are measured for these electrodes under these conditions, making valid the assumption that the measured current is the kinetics one.....	138
Figure 6.5 (a) Cyclic voltammetry (CV) measurements for LaCoO_3 electrode measured at 10 mV/s in 0.1 M KOH from 10 to 60°C with an increment of 10°C . (b) Extrapolation of the apparent activation energy and the pre-exponential factor from the Arrhenius plot $\ln(j)$ vs $1000/T$. (c) Schematic illustration for the effect of Sr^{2+} substitution into LaCoO_3 on the activation barrier for the OER. (d) Apparent activation energies and pre-exponential factors extrapolated at $\eta=400\text{mV}$ vs. RHE for the $\text{La}_{1-x}\text{Sr}_x\text{CoO}_3$ series as a function of the OER activity at $\eta = 400\text{mV}$ vs. RHE measured in 0.1 M KOH at 20°C .	141
Figure 6.6 Pre-exponential factors plotted as a function of the apparent activation energies extrapolated at $\eta = 400\text{mV}$ for the $\text{La}_{1-x}\text{Sr}_x\text{CoO}_3$ series in 0.1 , 0.3 and 1M KOH from Figure 6.5d and Figure 6.7a.....	143
Figure 6.7 Apparent activation energies and pre-exponential factors as a function of the OER activity measured at 20°C at $\eta = 400\text{mV}$ (a) in 0.1 , 0.3 and 1 M KOH for the $\text{La}_{1-x}\text{Sr}_x\text{CoO}_3$ series, (b) measured for $\text{La}_{0.5}\text{Sr}_{0.5}\text{CoO}_{3-\delta}$ (LSC05) 0.1 , 0.3 and 1 M KOH and LiOH and (c) measured for $\text{La}_{0.5}\text{Sr}_{0.5}\text{CoO}_{3-\delta}$ (LSC05) in 1 M LiOH , NaOH , KOH and CsOH .	145
Figure 6.8 Activation energy and pre-exponential factor at $\eta=400\text{mV}$ for $\text{La}_{1-x}\text{Sr}_x\text{CoO}_3$ vs activity at $\eta = 400\text{mV}$ in 0.1M LiOH and KOH at 20°C .	145
Figure 6.9 Cation dependence studies of $\text{La}_{0.5}\text{Sr}_{0.5}\text{CoO}_3$ in 0.1M LiOH , NaOH , KOH and CsOH . Activation energy and pre-exponential factor at $\eta = 400\text{mV}$ for $\text{La}_{0.5}\text{Sr}_{0.5}\text{CoO}_3$ vs activity at $\eta = 400\text{mV}$ in 0.1M LiOH , NaOH , KOH and CsOH at 20°C	146
Figure 6.10 (a) CV curves for CoOOH measured at 20°C and (b) corresponding apparent activation energies and pre-exponential factors as a function of the OER activity at 20°C and $\eta = 400\text{mV}$ in 0.1 , 0.3 and 1 M LiOH and KOH . (c) CV curves for CoOOH measured at 20°C and (b) corresponding apparent activation energies and pre-exponential factors as a function of the OER activity at 20°C and $\eta = 400\text{mV}$ in 1 M LiOH , NaOH , KOH and CsOH	147
Figure 6.11(a) CV curves for $\text{Fe}_{0.5}\text{Co}_{0.5}\text{OOH}$ measured at 20°C and (b) corresponding apparent activation energies and pre-exponential factors as a function of the OER activity at 20°C and $\eta = 400\text{mV}$ in 0.1 , 0.3 and 1 M LiOH and KOH . (c) CV curves for $\text{Fe}_{0.5}\text{Co}_{0.5}\text{OOH}$ measured at 20°C and (b) corresponding apparent activation energies and pre-exponential	

factors as a function of the OER activity at 20°C and $\eta = 400\text{mV}$ in 1 M LiOH, NaOH, KOH and CsOH.	148
Figure 6.12 OER activity at $\eta=400\text{mV}$ vs. RHE for $\text{Fe}_{0.5}\text{Co}_{0.5}\text{OOH}$ measured in 1 M LiOH, NaOH, KOH, CsOH and TMAOH as a function of (a) the cation hydration enthalpy obtained from ref ³⁰ and (b) the B coefficients from the Jones-Dole equation for the different cations as obtained from ref ³⁰	151
Figure 7.1 XRD patterns for CoO and CoS_2	161
Figure 7.2 Electrochemical studies of CoO and CoS_2 in 0.1M KOH.	162
Figure 7.3 Co L-edge for CoO and CoS_2 before and after OER.	162
Figure 7.4 Spin state and electron configuration for pristine CoO (a) and CoS_2 (b). Crystal structures for CoO (Co-O bond length=2.13 Å) (c) and CoS_2 (Co-S bond length=2.33 Å) (d).	163
Figure 7.5 DOS of LaCoO_3 , ZnCo_2O_4 , CoO and CoS_2	164
Figure 7.6 Spin state and electron configuration for CoO and CoS_2 after OER.	164
Figure 7.7 O K-edge for CoO and CoS_2 before and after OER.	165
Figure 7.8 XRD pattern for $\text{Na}_{0.75}\text{CoO}_2$	166
Figure 7.9 Summary of OER activity of $\text{Zn}_{0.99}\text{Sr}_{0.01}\text{Co}_2\text{O}_4$ in 1M LiOH/NaOH/KOH solution with and without Fe impurities.	168

Table des tableaux

Table 2.1 Oxides used as catalysts materials.....	5
Table 4.1 Effective magnetic moment (μ_{eff}) for different spin states of Co^{3+} ions in $\text{LaCo}_{1-x}\text{Fe}_x\text{O}_3$ ($x=0.00, 0.10, 0.25, 0.50, 0.75$) (LS: low spin; HS: high spin).....	73
Table 5.1 Summary of lattice parameter of $\text{ZnCo}_{2-x}\text{Ni}_x\text{O}_4$ ($x=0, 0.2, 0.4, 0.6, 0.8$).....	89

Résumé :

Le développement d'électrocatalyseurs efficaces pour la réaction de libération d'oxygène (OER) est important pour améliorer l'efficacité globale du processus d'électrolyse de l'eau. Les oxydes / hydroxydes de métaux de transition présentent une activité et une stabilité raisonnables lorsqu'utilisés dans un milieu alcalin. Ils ont le potentiel de remplacer les oxydes à base d'Ir et de Ru. Comprendre la réaction d'OER pour les oxydes / hydroxydes de métaux de transition dans les électrolytes alcalins aide à la conception d'électrocatalyseurs peu coûteux et très efficaces. Avec trois travaux différents sur les oxydes / hydroxydes à base de Co, cette thèse approfondit la compréhension des propriétés de surface des matériaux et des propriétés interfaciales sur la cinétique de la réaction d'OER. Tout d'abord, la substitution au fer régule par exemple la configuration des cations métalliques dans LaCoO_3 . Cela ajuste la covalence de la liaison oxygène $2p$ – métal $3d$ et améliore les performances. Deuxièmement, la substitution au Ni dans ZnCo_2O_4 modifie la position relative du centre de la bande O $2p$ et du centre de la bande métallique dans un environnement octaédrique M_{Oh} . Cela modifie la stabilité et la possibilité pour l'oxygène du réseau de participer à la réaction de dégagement d'oxygène. Enfin, en étudiant les séries $\text{La}_{1-x}\text{Sr}_x\text{CoO}_3$, CoOOH et CoOOH contenant Fe, l'impact de l'électrolyte sur les paramètres de la cinétique de réaction a été exploré. Avec une meilleure compréhension de la façon dont les propriétés des matériaux et l'environnement dynamique influencent l'activité et le mécanisme des OER, nous pouvons obtenir des catalyseurs de OER plus efficaces pour une meilleure infrastructure énergétique.

Mots clés : [les oxydes / hydroxydes à base de Co; OER ; électrolytes alcalins; des propriétés des matériaux; des propriétés de surface des matériaux; des propriétés interfaciale]

[Understanding the oxygen evolution reaction (OER) for Co based transition metal oxides / hydroxides in alkaline electrolytes]

Abstract :

The development of efficient electrocatalysts to lower the overpotential of oxygen evolution reaction (OER) is of fundamental importance in improving the overall efficiency of fuel production by water electrolysis. Among a plethora of catalysts being studied on, transition metal oxides / hydroxides that exhibit reasonable activity and stability in alkaline electrolyte have been identified as catalysts to potentially overpass the activity of expensive Ir- and Ru- based oxides. Understanding the OER for transition metal oxides / hydroxides in alkaline electrolytes paves the way for better design of low cost and highly efficient electrocatalysts. This dissertation, with three different work on Co-based oxides / hydroxides, studies and deepens the understanding of the bulk properties, surface properties of materials and interfacial properties on OER. Firstly, with Fe substitution, it addresses tuning the e_g configuration of metal cations in LaCoO_3 where adjusting the metal $3d$ oxygen $2p$ covalency can bring benefits to the OER performance. Secondly, with Ni substitution in ZnCo_2O_4 , it demonstrates a change in relative position of O p -band and M_{Oh} d -band centre which induces a change in stability as well as the possibility for lattice oxygen to participate in the OER. Finally, with $\text{La}_{1-x}\text{Sr}_x\text{CoO}_3$ series, CoOOH and Fe-containing CoOOH as examples, the impact of the electrolyte has been explored by the study of reaction kinetics parameters. With a better understanding of how material properties and dynamic environment influence the OER activity and mechanism, we can obtain more efficient OER catalysts for better energy infrastructure.

Keywords : [transition metal oxides / hydroxides; OER; alkaline electrolyte; bulk properties of materials; surface properties of materials; interfacial properties]